



HAL
open science

Control and transport of matter waves in an optical lattice

Nathan Dupont

► **To cite this version:**

Nathan Dupont. Control and transport of matter waves in an optical lattice. Quantum Physics [quant-ph]. Université Toulouse 3 - Paul Sabatier, 2022. English. NNT : . tel-03997401v4

HAL Id: tel-03997401

<https://theses.hal.science/tel-03997401v4>

Submitted on 5 Aug 2024

HAL is a multi-disciplinary open access archive for the deposit and dissemination of scientific research documents, whether they are published or not. The documents may come from teaching and research institutions in France or abroad, or from public or private research centers.

L'archive ouverte pluridisciplinaire **HAL**, est destinée au dépôt et à la diffusion de documents scientifiques de niveau recherche, publiés ou non, émanant des établissements d'enseignement et de recherche français ou étrangers, des laboratoires publics ou privés.



Distributed under a Creative Commons Attribution 4.0 International License



THÈSE

En vue de l'obtention du
DOCTORAT DE L'UNIVERSITÉ DE TOULOUSE
Délivré par l'Université Toulouse 3 - Paul Sabatier

Présentée et soutenue par
Nathan DUPONT

Le 15 décembre 2022

**Contrôle et transport d'ondes de matière dans un réseau
optique : Contrôle optimal, effet ratchet et étude de l'émergence
d'un ordre supercristallin**

Ecole doctorale : **SDM - SCIENCES DE LA MATIERE - Toulouse**

Spécialité : **Physique**

Unité de recherche :

LCAR - Laboratoire Collisions Agrégats Réactivité

Thèse dirigée par

David GUERY-ODELIN

Jury

Mme Caroline CHAMPENOIS, Rapporteur

M. Jérôme BEUGNON, Rapporteur

M. Éric SURAUD, Examineur

M. Nathan GOLDMAN, Examineur

M. David GUERY-ODELIN, Directeur de thèse

Contents

List of Figures	iii
Remerciements	vii
General introduction	1
I Methods for the study of wave function dynamics in a one-dimensional periodic potential	7
1 Elements of theory for the study of a wave function in a one-dimensional potential	9
Introduction	11
1.1 Classical particle in a one-dimensional periodic potential	11
1.2 Wave function in a time-independent sine potential	18
1.3 Wave function in a time-dependent sine potential	24
1.4 Quantum states in the phase space	28
Conclusion	35
2 Experimental setup	37
Introduction	39
2.1 Bose-Einstein condensation	39
2.2 Experimental sequence for Bose-Einstein condensation	40
2.3 Observing the system	46
2.4 The one-dimensional optical lattice	49
Conclusion	57
II Control and transport of the BEC one-body wave function in the optical lattice	59
3 Quantum optimal control of matter waves in a one-dimensional optical lattice	61
Introduction	63
3.1 Optimal-control formalism	65
3.2 Controlling momentum distributions	74
3.3 Wave function control	79
3.4 An application to quantum simulation	91

Conclusion	95
4 Non-diffusive Hamiltonian ratchet	97
Introduction	99
4.1 Designing a non-diffusive Hamiltonian ratchet in classical mechanics	102
4.2 Quantum ratchet transport along regular classical trajectories	108
4.3 Experimental ratchet transport of matter waves	112
Conclusion	118
III Beyond the one-body wave function	119
5 Emergence of a tunable supercrystalline order in a Floquet-Bloch system	121
Introduction	123
5.1 Modulation regime and typical observations	125
5.2 An effective tight-binding model	126
5.3 Experimental results	140
5.4 Discussion on the realized state	146
Conclusion	149
General conclusion	151
IV Appendices	157
A Rubidium 87 D₂ line	159
B Dipole beams preparation and control	161
C Lattice beams preparation and control	163
D Effect of the control duration in our QOC protocol	167
E Additional optimal control preparations	169
E.1 Momentum distribution control from the resting BEC	169
E.2 Control of the relative phases between three momentum components	169
E.3 Squeezed and rotated Gaussian states	170
F Résumé du manuscrit en français	173
Bibliography	197

List of Figures

1.1	One-dimensional sine potential and corresponding phase space	14
1.2	Construction of a stroboscopic phase portrait	15
1.3	Examples of stroboscopic phase portraits	16
1.4	Subperiod evolution of a stroboscopic phase portrait	17
1.5	Band structures and Bloch eigenstates	22
1.6	Band structure and quasi-energy spectra	27
1.7	Wigner representation of Bloch eigenstates in the phase space of the static sine potential	30
1.8	Husimi representation of Bloch eigenstates in the phase space of the static sine potential	32
1.9	Husimi representations of Floquet-Bloch states	35
2.1	Sketch of the old and new dipole beam geometries	44
2.2	Schematic of absorption imaging	47
2.3	Imaging axes	48
2.4	Adiabatic lattice loading and matter wave diffraction	52
2.5	Calibration of the optical lattice depth from Kapitza-Dirac diffraction	54
2.6	Calibration of the optical lattice depth from a sudden lattice translation	56
2.7	Sketch of the band-mapping technique	57
	“Hello World” written with matter diffraction	61
3.1	Schematic of a gradient ascent iteration for the computation of a discretized control field	72
3.2	Non-unicity of the control fields for the preparation of a given target	74
3.3	Controlling momentum distributions: single momentum components	76
3.4	Controlling momentum distributions: two-component equiprobable and arbitrary momentum superpositions	78
3.5	Control and measurement of the phase between two momentum components	81
3.6	Preparations of Bloch eigenstates and superpositions thereof	83
3.7	Quantum state reconstruction in a Bloch system by likelihood maximization	87
3.8	Experimental preparation and measurement of non-squeezed Gaussian states	88
3.9	Evolution of the momentum distribution of superpositions of Gaussian states in the static lattice	89
3.10	Experimental preparation and measurement of squeezed Gaussian states	90

3.11	Evolution of the momentum distribution of a highly squeezed state in the static lattice	91
3.12	Initial states for dynamical tunneling	93
3.13	Quantum-optimal control applied to dynamical tunneling experiments	95
4.1	Diagram of a mechanical rotating ratchet	99
4.2	Parameter maps for initial guess determination in the search for ratchet modulation parameters	106
4.3	Classical non-diffusive ratchet trajectory	107
4.4	Subperiod evolution of the stroboscopic phase portrait and ratcheting island . . .	108
4.5	Ratcheting Floquet state and influence of the effective Planck constant	111
4.6	Floquet state mixing phenomenon illustrated on the ratcheting Floquet state . .	112
4.7	Semi-classical non-diffusive ratchet transport from the ground state	114
4.8	Experiments of ratchet transport from the ground state of the lattice	116
4.9	Ratchet transport experiments of ratcheting Floquet state prepared by QOC . .	117
5.1	Non-resonant modulation in the one-body wave function framework	126
5.2	Experimental protocol and nucleation of decimals peaks	127
5.3	Partial fits of Floquet spectra with the two-level tight-binding model	130
5.4	Typical results of the two-band tight-binding model with interactions for realistic parameters	138
5.5	Predictions from the two-band tight-binding model with interactions	139
5.6	Measurement of the quasi-momentum of the decimals peaks through band-mapping	141
5.7	Instability displacement with the modulation frequency	142
5.8	Measurement of the nucleation time of the instability	144
5.9	Survival time of the nucleated pattern	145
5.10	Instability nucleation through amplitude modulation of the lattice	146
5.11	Structure of the reduced one-body density matrix after nucleation of the instability	148
5.12	Correlations and coherence after nucleation of the instability	149
6.1	Summary figure of my PhD work	152
A.1	Rubidium 87 D ₂ line	159
B.1	Legend for the optical diagram	161
B.2	Optical diagram for the dipole beams	162
C.1	Bode plot for the amplitude modulation of the lattice	164
C.2	Optical diagram for the lattice beams	165
D.1	Effect of the control duration	167
E.1	Experimental preparation of the plane wave with momentum $p = 6 \hbar k_L$ from the resting BEC	170
E.2	Preparation of three-momentum component states	171
E.3	Preparation and measurement of rotated squeezed Gaussian states	171

F.1	Exemples de portraits de phase stroboscopiques	177
F.2	Structure de bande et spectres de quasi-énergie	178
F.3	Représentations de Husimi d'états de Floquet-Bloch	179
F.4	Chargement adiabatique du réseau optique et diffraction d'onde de matière	181
F.5	“Controlé” écrit avec des diffractions d'ondes de matière	183
F.6	Reconstruction d'un état quantique dans un système de Bloch par maximisation de la vraisemblance	184
F.7	Préparation expérimentale et reconstruction d'états gaussiens comprimés	185
F.8	Évolution sous-stroboscopique d'un portrait de phase stroboscopique d'un système présentant un effet <i>ratchet</i> régulier	188
F.9	Influence de la constante de Planck effective sur le transport <i>ratchet</i>	189
F.10	Transport <i>ratchet</i> semi-classique et non-diffusif à partir de l'état fondamental du réseau optique	190
F.11	Protocole expérimental et observation typique de nucléation d'ordres décimaux	192
F.12	Résultats de l'étude de la stabilité du système pour des paramètres de modèle réalistes	193
F.13	Déplacement de l'instabilité avec la fréquence de modulation	194

Remerciements

Ce manuscrit retrace le travail de recherche auquel j'ai eu la chance de prendre part au sein de l'équipe Atomes Froids du LCAR de février 2019 à décembre 2022. S'il m'arrive de dire "je" pour y narrer cette aventure, qu'on reste assuré du réel travail d'équipe que requièrent l'obtention, l'analyse et la compréhension des résultats j'y présente. Hors du laboratoire, vous êtes pareillement nombreux à avoir participé à mon épanouissement lors de ces années passées à Toulouse. Aussi, je tiens à remercier ceux qui, directement ou indirectement, par leur travail ou¹ leur amitié, ont contribué à la bonne réalisation de ce doctorat.

En premier lieu, merci aux membres de mon jury Jérôme Beugnon, Caroline Champenois, Nathan Goldman et Éric Suraud pour votre temps, l'intérêt que vous avez porté à mon manuscrit et la bienveillance qui transparait dans vos rapports et dont vous avez fait montre lors de la soutenance. Les échanges que nous y avons eu constituent pour moi une conclusion enrichissante à ce travail de thèse, et ils demeureront un riche souvenir de ce rite de passage.

Merci ensuite aux trois chercheurs qui ont rendu possible ce doctorat : à David, pour ton solide encadrement et ta remarquable disponibilité malgré tes charges et activités de recherche transversales. Je loue ton intuition physique ainsi que ta passion communicative pour la recherche, et je te suis grandement reconnaissant pour ton soutien dans mes projets. À Juliette pour ton expertise expérimentale, ta bienveillance et ta pédagogie si précieuse à mon arrivée dans l'équipe. Enfin à Bruno, modèle de rigueur ! L'intérêt que je portais à ma thèse s'est vu décuplé lorsque tu as rejoins le groupe, et je te remercie pour ta patience et ton aide qui m'auront permis de m'approprier toujours davantage les sujets sur lesquels nous avons travaillé. Je conserverai un excellent souvenir de nos sessions de désossage d'antiques boîtiers électroniques, ainsi que de nos divers et longs échanges, fussent-ils scientifiques ou non.

Vous formez un solide et beau trio, et je me sais heureux d'avoir pu réaliser ce doctorat avec vous. Je vous tiens et garderai chacun en très haute estime.

Je remercie grandement les autres membres, de passage comme moi, du groupe Atomes Froids : merci à Maxime A. pour ta pédagogie et ton goût pour la physique atomique expérimentale que tu as si bien su me transmettre. Merci à Gabriel C., fervent condisciple de Michel Dumas, pour ces grands et nombreux moments de partage autour et hors de la science, à "travailler sérieusement sans se prendre au sérieux". Tu m'as beaucoup appris, et j'ai grandement apprécié travailler avec toi ! Merci à Lucas pour m'avoir épaulé sur la deuxième moitié de ma thèse, et pour le cruciverbisme méridien (remerciant en passant Philippe Dupuis !). Merci enfin à Floriane et Nicolas pour votre application, vos relectures zélées de codes et surtout pour votre sympathie. La rapidité avec laquelle vous vous êtes approprié l'expérience et les formalismes

¹Un "ou" bien-sûr inclusif !

théoriques propres à nos sujets de recherche m'impressionnent et m'assurent que la relève est amplement assurée ! On aura, par sous-ensembles, formé de fines équipes à la hauteur des exigences de transmission de savoir nécessaire à ce que continue de tourner sans trop faillir une expérience d'une telle technicité, et je suis fier d'avoir été, grâce à vous, un petit maillon de cette jolie chaîne.

Je remercie sincèrement Maxime Martinez, Bertrand Georgeot, Gabriel Lemarié, Olivier Giraud, Denis Ullmo, Peter Schlagheck et Dominique Sugny, avec qui nous avons collaboré au travers des différents sujets de recherche abordés durant mon doctorat.

Merci aux membres du LCAR, un laboratoire dans lequel il fait bon travailler, et notamment à Jean-Marc, Christine, Carole, Anna, Stéphane, Alexandre et Baptiste, ainsi qu'aux collègues doctorants et post-doctorants Qi, Ashley, Tanguy, Romain, Léo, Julien A., Olivier T. et Julie R.. C'a été un réel plaisir de vous côtoyer au quotidien !

Plus largement à l'échelle de feu l'IRSAMC et de la FÉRMI, je remercie chaleureusement Nicolas Destainville pour m'avoir, en 2018, accueilli en stage au LPT. C'est par cette introduction au milieu de la recherche que j'ai pris goût au travail de laboratoire et que s'est confirmé mon souhait de faire de la recherche fondamentale. Je remercie également Patricia, Nicolas E., Xavier et Sylvain. Un immense merci à Maxime M. pour tes qualités de chercheur et d'ami, et particulièrement pour les soirées pizzas (et celle à manger des lentilles, d'accord, un chouïa trop cuites), les longues discussions nocturnes, et ta promesse tenue de m'emmener voir une étape du Tour ! Merci à Nicolas M. et Théo pour les groupes de musique blues-jazz manouche-trad' irlandaise (oui) et ces nombreuses discussions captivantes sur la bande-dessinée, l'Histoire et autres sciences. Merci aussi à Julie C., Faedi, Ulysse, Agustin, Claire, Naimo, Denis R., Thomas B. et Thomas R., Hugo, Jordan, Benjamin E. et Benjamin R., Olivier G., Bhupen, Ravi, Noam, Julien H., Sasank, Juraj, Jeanne, Maen, Élise, Martin, Vincent et à tous les autres doctorants et post-doctorants de la FÉRMI avec qui j'ai eu la chance d'interagir durant cette thèse.

Merci à l'École Doctorale Sciences de la Matière, et notamment à Éric Benoist et Jérôme Cuny pour votre implication et votre disponibilité.

Merci à Gabriel C., Maxime M., Ulysse, Maud T., Corentin, Tanguy, Anaïs, Pierre, Sébastien, Sarah et Sophie pour les après-midi *binge watching* de séries, jeux de société et les goûters de crêpes !

Merci du fond du cœur à Christine, François, Damien et Mélitta pour vos accueils toujours chaleureux, les copieux repas et ces randonnées dans les Pyrénées, tous grandement appréciés durant mes cinq années passées à Toulouse.

Merci à ma famille pour leur simple et inconditionnel soutien depuis le début.

Enfin, un immense merci à Amélie, pour ta douceur au quotidien et ton infailible accompagnement lors de la rédaction de ce manuscrit. Vivement le prochain chapitre en Belgique !

Bruxelles, 15 février 2023.

General introduction

The use of light and magnetic fields to control the external degrees of freedom of atoms (their position and speed) has revolutionized the field of atomic physics. Benefiting from the development of lasers in the 1960s, techniques of laser trapping and cooling [1, 2, 3] have resulted in unprecedented control abilities of atomic particles, to such an extent that, in 1997, S. Chu, C. Cohen-Tannoudji and W. Phillips were awarded the Nobel Prize in Physics for their contributions to the development of these experimental techniques. Using them, one is able to cool gases of atoms near the absolute zero, at temperatures where the unusual laws of quantum physics begin to prevail. An emblematic example of this is Bose-Einstein condensation. Through this quantum phase transition first described by A. Einstein around 1925 [4, 5], a bosonic gas goes from an ensemble of particles classically described by Maxwell-Boltzmann statistics to a macroscopically populated matter wave whose evolution is governed by quantum mechanics: a Bose-Einstein condensate (BEC).

Bose-Einstein condensation was achieved for the first time in 1995, 70 years later, in the groups of E. Cornell and C. Wieman [6] and in that of W. Ketterle [7], from the combination of laser and evaporative coolings. This experimental achievement, rewarded by the Nobel prize in 2001, marked the birth of the field of quantum gases which has been constantly growing ever since. Ultracold quantum gases, which may be bosonic or fermionic, constitute very versatile platforms for the experimentalist to study and harness quantum mechanics:

- Using laser and magnetic fields, one is able to realize a wide variety of potentials [8, 9] in which to study the evolution of quantum systems. It is for instance possible to manipulate single atoms in optical tweezers [10, 11] and realize controllable periodic Bloch potential using *e.g.* optical lattices [12] or spatial light modulators [13, 14].
- Effective Hamiltonians [15, 16] can be designed in Floquet systems, where one periodically modulates the potentials in order to design specific energy level structures and dynamics. Such Floquet engineering is for example an approach to create artificial magnetism for neutral atoms [17, 18].
- A powerful tool provided by ultracold atoms is the ability to tune the strength and sign of short-range interatomic interactions using magnetic fields and Feshbach resonances [19]. Also, a strong experimental effort has recently been devoted to the realization and control of systems with longer-range interactions, such as dipolar gases [20, 21, 22] and Rydberg atom ensembles [23, 24, 25].

This high degree of control offered by quantum gas setups is of particular interest in the fields of quantum simulation and quantum metrology.

Quantum simulation [26, 27] consists in using a highly controllable quantum system to simulate the model Hamiltonian of another one, less controllable or more difficult to characterize. This idea was first suggested by R. Feynman in 1982 [28], and, since then, quantum simulation has been implemented on many platforms, such as superconducting circuits [29], photonic systems [30], trapped ions [31] and ultracold neutral atoms [32, 33, 34]. We are here interested in this last platform, on which in the last twenty years, major experiments of quantum simulation with ultracold atoms were realized. One can cite the three-dimensional implementation of the Bose-Hubbard model, on which the phase transition between a superfluid and a Mott insulator could be observed [35], the realization of the Anderson localization in one [36, 37], two [38, 39] and three-dimensional [40, 41, 42] systems with simulated disorder, and the Berezinskii-Kosterlitz-Thouless transition in two-dimensional gases [43, 44].

Another field of application that benefits from the great controllability offered by quantum gases is quantum metrology. There, a key example of the advantage of manipulating fully a quantum system is given by the use of squeezed states, which allow to reach sensitivities closer to the fundamental limits intimately related to Heisenberg uncertainty principle [45, 46]. This is famously the case of squeezed photonic states, used to enhanced spectroscopy [47] and interferometry experiments [48, 49], but there is also a long going theoretical and experimental effort to take advantage of squeezing with matter for enhanced matter wave interferometry [50, 51, 52, 53, 54, 55].

All these applications call for the development of new optimization methods to control and manipulate quantum states in cold atom systems. Several modern approaches have been proposed for this purpose, among which we can cite quantum feedback [56], shortcut to adiabaticity [57], machine learning [58] and optimal control theory [59, 60].

The Cold Atoms research group in which I did my PhD at *Laboratoire Collisions, Agrégats et Réactivité* (LCAR, Toulouse) takes part in the effort to develop techniques to control ultracold atom systems. My PhD work reported in this manuscript deals with both the development of such methods and their application to quantum simulation studies in a Floquet-Bloch system (periodic in space and time). The LCAR Cold Atoms group developed an ultracold atom experiment producing BECs of ^{87}Rb that are placed in a far-detuned one-dimensional optical lattice. Along the axis of the lattice, the atoms experience a sine potential whose depth and position can be arbitrarily controlled in time by the means of acousto-optic modulators. This system constitutes a powerful and versatile platform to develop new methods for the control of quantum states, as well as to experimentally study the dynamics of matter waves in a sine potential with controllable time dependencies, in a regime of weakly interacting particles.

Summary of my work and outline of this manuscript

This manuscript presents the research work in which I participated from 2019 to 2022 in the Cold Atoms group at LCAR. It is divided into three parts: a first part introducing theoretical, numerical and experimental methods required for the studies presented in the thesis, a second

part featuring results about the control and transport of quantum states apprehended in the one-body wave function formalism and a third part presenting a study beyond one-body physics in our system. New results are presented in the parts two and three of this thesis. There, a detailed introduction on the addressed subject is given in the beginning of the corresponding chapter.

Part 1 - Methods for the study of wave function dynamics in a one-dimensional periodic potential. The first part, made up of two chapters, is dedicated to the introduction of methods to study the dynamics of wave functions in a one-dimensional periodic potential whose parameters can be periodically modulated in time. **Chapter 1** consists in reminders of theoretical concepts and numerical tools for the study of such one-dimensional Floquet-Bloch systems. I then present in **Chapter 2** the BECs experiment and the controllable optical lattice used to implement this system in the laboratory, and with which the results presented in the following parts were obtained.

Part 2 - Control and transport of the BEC one-body wave function in the optical lattice. The second part of this manuscript features two research works where the evolution of the atomic state is described by the Schrödinger equation and the formalism introduced in Chap. 1. In **Chapter 3**, I present the experimental implementation of a quantum-optimal control protocol in our experiment: by continuously shifting the optical lattice in an optimal way, we demonstrate our ability to prepare arbitrary momentum distributions and motional quantum states for the BECs in the lattice. This allowed us to prepare squeezed Gaussian states up to more than four times narrower in position than the ground state of the optical lattice, a state that would be unattainable using standard adiabatical methods. To characterize the states that we prepare, we implemented a quantum state tomography based on likelihood maximization which I then detail. I conclude this chapter with the presentation of a concrete application of quantum-optimal control to a simulation of dynamical tunneling in a Floquet system. **Chapter 4** features a study (both numerical and experimental) of the ratchet effect, which consists in the emergence of a directed current of particles in a potential periodic in space and time. I begin with a classical mechanics study in which I show how to design an integrable ratchet effect in a Hamiltonian system by correlating the modulations of amplitude and phase of a symmetric sine potential. I then consider quantum mechanics in this system, and detail how quantum transport along the ratcheting classical trajectories depends, in a non-monotonous way, on the effective Planck constant. Following these studies, we experimentally realized this system, and I report on the observation of non-diffusive ratchet transport of matter waves in the optical lattice.

Part 3 - Beyond the one-body wave function. The last part of this manuscript is composed of **Chapter 5**, featuring a study of the emergence of a supercrystalline order that results from interatomic interactions in the modulated optical lattice. In the experiments presented in this chapter, we load the atoms in the ground state of the lattice before modulating its phase at a frequency that couples the ground band to an excited band, that coupling being not resonant for

the initial state. In this configuration, we show how two-body collisions occurring between atoms of the ground state lead to the appearance of atomic population at symmetric quasi-momenta through four-wave mixing, at a position in the Brillouin zone that can be tuned by Floquet engineering the quasi-energy spectrum of the system. This produces a new periodicity in the distribution of atoms in the lattice, larger and non-commensurable with the lattice spacing.

The work presented in Chap. 3 results from a collaboration with Prof. D. Sugny from the *Laboratoire Interdisciplinaire de Carnot Bourgogne* (Dijon), and the work presented in Chap. 5 results from a collaboration with Prof. P. Schlagheck from the CESAM research unit at the University of Liège.

List of publications

I present a list of the publications of our group to which I contributed during my thesis:

- [61] M. Arnal, G. Chatelain, M. Martinez, N. Dupont, O. Giraud, D. Ullmo, B. Georgeot, G. Lemarié, J. Billy, and D. Guéry-Odelin. *Chaos-assisted tunneling resonances in a synthetic Floquet superlattice*, Science Advances (2020),
- [62] G Chatelain, N Dupont, M Arnal, V Brunaud, J Billy, B Peaudecerf, P Schlagheck, and D Guéry-Odelin. *Observation and control of quantized scattering halos*, New Journal of Physics (2020),
- [63] N. Dupont, G. Chatelain, L. Gabardos, M. Arnal, J. Billy, B. Peaudecerf, D. Sugny, and D. Guéry-Odelin. *Quantum State Control of a Bose-Einstein Condensate in an Optical Lattice*, PRX Quantum (2021),
- [64] N. Dupont, F. Arrouas, L. Gabardos, N. Ombredane, J. Billy, B. Peaudecerf, D. Sugny, and D. Guéry-Odelin. *Phase-space distributions of Bose-Einstein condensates in an optical lattice: Optimal shaping and reconstruction*, currently under review (2022).
- [65] N. Dupont, L. Gabardos, F. Arrouas, B. Peaudecerf, J. Billy, and D. Guéry-Odelin. *Matter wave transport from non-diffusive Hamiltonian ratchet effect*, In preparation (2022).
- [66] N. Dupont, L. Gabardos, F. Arrouas, G. Chatelain, M. Arnal, J. Billy, P. Schlagheck, B. Peaudecerf, and D. Guéry-Odelin, *Emergence of a tunable supercrystalline order in a Floquet-Bloch system*, In preparation (2022)

I detail in this manuscript the results presented in the last four works listed above: [63] and [64] are adressed in Chap. 3, [65] in Chap. 4 and [66] in Chap. 5. Experimental details about our results on chaos-assisted tunneling [61] and quantized scattering halos [62] can be found in the theses of M. Arnal [67] and G. Chatelain [68], previous PhD students of the group.

Part I

Methods for the study of wave function dynamics in a one-dimensional periodic potential

Chapter 1 - Elements of theory for the study of a wave function in a one-dimensional potential

Si vous me savez peu de gré de ce que je vous dis, sachez-m'en beaucoup de ce que je ne vous dis pas.

Denis Diderot (Jacques le Fataliste et son maître, ca. 1778)

Contents

Introduction	11
1.1 Classical particle in a one-dimensional periodic potential	11
1.1.1 Basics on analytical mechanics	11
1.1.2 Phase space of the one-dimensional sine potential	12
1.1.3 Symmetries of the phase space.	18
1.2 Wave function in a time-independent sine potential	18
1.2.1 Bloch's theorem in one dimension	19
1.2.2 The central equation for the sine potential and the band structure	20
1.2.3 Quantum state evolution in a Bloch system	23
1.3 Wave function in a time-dependent sine potential	24
1.3.1 Time-dependent sine potential: general case	24
1.3.2 Time-periodic Hamiltonians : Floquet formalism	25
1.4 Quantum states in the phase space	28
1.4.1 Wigner and Husimi representations and the effective Planck constant	29
1.4.2 Floquet states representation in the phase space	34
Conclusion	35

Introduction

The goal of this first chapter is to briefly recapitulate elements of theory, concepts and numerical tools used to study one-body wave functions in one-dimensional periodic potentials without interactions. The methods that we recall will then be used throughout this manuscript. Some of the developments presented in this chapter are inspired from [69].

1.1 Classical particle in a one-dimensional periodic potential

In this first section, we present some reminders on analytical mechanics. The main objective is to introduce the notion of phase space, and the construction of the stroboscopic phase portrait of a one-dimensional system periodically modulated in time. In the end of this first chapter, after discussing quantum dynamics in a one-dimensional sine potential, we revisit the notion of phase space to introduce the phase space representation of a quantum state (Sec. 1.4).

1.1.1 Basics on analytical mechanics

Lagrangian mechanics. We consider a classical system with N degrees of freedom. In the Lagrangian formulation of analytical mechanics, the state of the system is completely described by N independent generalized coordinates $\mathbf{q} = (q_1, \dots, q_N)$ and their time derivatives $\dot{\mathbf{q}} = (\dot{q}_1, \dots, \dot{q}_N)$. The dynamics of the system is ruled by the Lagrangian

$$L(\mathbf{q}, \dot{\mathbf{q}}, t) = T - V, \quad (1.1)$$

with T and V being respectively the kinetic and potential energies. Given an initial condition $(\mathbf{q}(t_0), \dot{\mathbf{q}}(t_0))$, the classical trajectory $\mathbf{q}(t)$ that the system will follow over the time interval $[t_0, t_1]$ is, among all the possible trajectories, the one that minimizes the action S , a functional of $\mathbf{q}(t)$ that reads

$$S[\mathbf{q}(t), t_0, t_1] = \int_{t_0}^{t_1} L(\mathbf{q}, \dot{\mathbf{q}}, t) dt. \quad (1.2)$$

The minimization of S leads to N Euler-Lagrange equations:

$$\frac{d}{dt} \left(\frac{\partial L}{\partial \dot{q}_i} \right) - \frac{\partial L}{\partial q_i} = 0, \quad (1.3)$$

which in turn gives N equations of motion.

Hamiltonian mechanics. To introduce the phase space of the system, we switch to the Hamiltonian formulation of analytical mechanics by introducing the generalized momenta $\mathbf{p} = (p_1, \dots, p_N)$ and the Hamiltonian H through the Legendre transformation:

$$p_i = \frac{\partial L}{\partial \dot{q}_i}, \quad H(\mathbf{q}, \mathbf{p}, t) = \sum_{i=1}^N \dot{q}_i p_i - L. \quad (1.4)$$

From the Hamiltonian, the equations of motion are given by the Hamilton equations:

$$\frac{dq_i}{dt} = \frac{\partial H}{\partial p_i} \quad \text{and} \quad \frac{dp_i}{dt} = -\frac{\partial H}{\partial q_i}. \quad (1.5)$$

For a particle of mass m , a Cartesian coordinate system, a kinetic energy $T(\dot{\mathbf{q}}) = m\dot{\mathbf{q}}^2/2$ and a potential $V(\mathbf{q}, t)$ that does not depend on the velocities $\dot{\mathbf{q}}$, the Hamiltonian is

$$H(\mathbf{q}, \mathbf{p}, t) = T(\mathbf{p}) + V(\mathbf{q}, t), \quad (1.6)$$

where the generalized momenta are the usual momenta $\mathbf{p} = m\dot{\mathbf{q}}$.

Phase space. In the Hamiltonian formalism, the state of the system at a given time t_0 is a point $(\mathbf{q}(t_0), \mathbf{p}(t_0))$ in the *phase space* of the system. In this space of dimension $2N$, the conservation of the mechanical energy constrains trajectories $(\mathbf{q}(t), \mathbf{p}(t))$ on a hypersurface of dimension $2N - 1$. For such a constant Hamiltonian system, the determinism of the dynamics implies that there cannot be intersection of trajectories in the phase space, since then the state at the hypothetical crossing would have multiple possible evolutions.

Integrability of a dynamical system. The dynamics of an Hamiltonian system is fully integrable if there are as many conserved and independent constants of motion as there are degrees of freedom [70, 71, 69]. As we will see for the time-independent sine-potential in one dimension, the phase space of an integrable system only displays regular trajectories. On the other hand, irregular chaotic trajectories can emerge in the phase space of systems with fewer constants of motion than degrees of freedom. As for most of the dynamical systems studied in this thesis, the majority of physical systems present a mixed dynamics, with the coexistence of integrable and chaotic trajectories.

1.1.2 Phase space of the one-dimensional sine potential

The Hamiltonian that will interest us in most of this manuscript is the Hamiltonian for the one-dimensional sine potential of spatial period d whose depth and position can be varied along time:

$$H(x, p, t) = \frac{p^2}{2m} - A(t) \times \frac{V_0}{2} \cos\left(\frac{2\pi x}{d} + \varphi(t)\right). \quad (1.7)$$

with $A(t)$ a dimensionless scaling function of order 1. In this section, we study the classical dynamics in this system by successively considering the case where H is time-independent, the case where it is time-dependent and the special case where H is periodic in time.

Time-independent sine potential. We first consider the time-independent Hamiltonian with modulation functions $A(t) = 1$ and $\varphi(t) = 0$ in Eq. (1.7):

$$H(x, p) = \frac{p^2}{2m} - \frac{V_0}{2} \cos\left(\frac{2\pi x}{d}\right), \quad (1.8)$$

which corresponds to the Hamiltonian of the simple pendulum. To represent the phase space of the system, the general strategy is to compute¹ several trajectories $(x(t), p(t))$ for several initial conditions (x_0, p_0) using the Hamilton equations (1.5). However, as the time-independent Hamiltonian (1.8) conserves the mechanical energy, we can circumvent the explicit numerical integration of individual trajectories, evaluate the Hamiltonian over the discretized two-dimensional space (x, p) and display lines of iso-mechanical energy. These lines (also called orbits, which we draw in Fig. 1.1) correspond to trajectories $(x(t), p(t))$ of a classical particle described by the Hamiltonian (1.8). As the ordinate p of a point informs on the time evolution of its abscissa x , orbits are followed in a given direction (clockwise in a (x, p) plot where x and p are defined as increasing to the right and upwards respectively, as in Fig. 1.1).

We display the separatrix, the limit trajectory of infinite period that separates periodic trajectories bounded within a site of the potential from unbounded trajectories that travel between sites. We define the momentum $p_{\text{sep}} = \sqrt{2mV_0}$ of the separatrix in $x = 0$. We note that, displaying the position in units of d and the momentum in units of p_{sep} , the phase space of Fig. 1.1(b) describes the classical dynamics of the Hamiltonian (1.8) for all specific parameters m , V_0 and d . As we discuss in Sec. 1.4, this scaling invariance of the dynamics does not hold in the quantum case.

In this manuscript, we use different sets of characteristic quantities to scale the dynamics. In Fig. 1.1, the (x, p) phase space is plotted with respect to x/d and p/p_{sep} . In a following paragraph concerning time-modulated potentials, the time scale in the scaling of the momentum is proportional to the period of modulation. A summary on our two main dynamical scalings is presented at the end of this chapter (p. 33).

¹In the work presented in this manuscript, we use the Runge-Kutta ‘‘RK4’’ method to integrate classical dynamics.

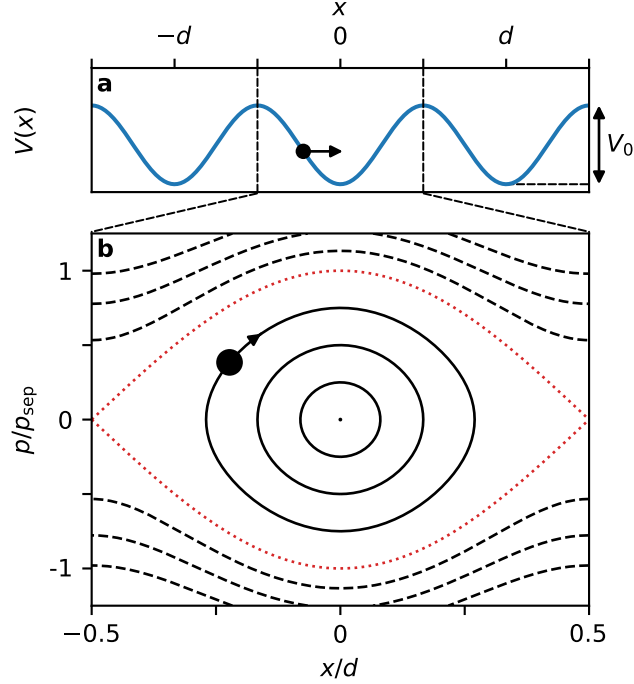


Figure 1.1 | One-dimensional sine potential and corresponding phase space. (a) One dimensional sine potential over three spatial cells (solid blue line). We draw a particle moving in the potential (black marker and arrow). (b) (x, p) phase space over one spatial cell, with bounded trajectories (plain black lines), unbounded trajectories (dashed black lines) and the separatrix (dotted red line). We mark the phase space coordinate of the particle in panel (a) (black marker) with the direction of its evolution (black arrow).

Time-dependent sine potential. The situation becomes more complicated for time-dependent systems. First of all, the mechanical energy is not conserved anymore. Even in one dimension, we have fewer constant(s) of motion than degree(s) of freedom, so we lose the certainty of having integrable dynamics. Furthermore, in the general case of time-dependent Hamiltonians $H(x, p, t)$, one cannot simply adjoin integrated trajectories in the (x, p) plane in order to display the phase space of the system. Indeed, as the states in (x_0, p_0, t_1) and (x_0, p_0, t_2) generally experience different potentials $V(x_0, t_1)$ and $V(x_0, t_2)$, they evolve along different trajectories. A naive (x, p) plot of the trajectories would result in crossing trajectories artifacts. Therefore, for a time-dependent system, one has to consider the (x, p, t) phase space, with an additional effective dimension.

Periodically time-modulated sine potential. A specific type of time-dependent systems that interests us in this manuscript is the case of the periodically modulated sine potential in one dimension, with a Hamiltonian of the form $H(x, p, t + T) = H(x, p, t)$ (with T the modulation period). Here, the periodicity of the Hamiltonian allows for a valid and informative representation of the (x, p, t) phase space in the (x, p) plane. To compare trajectories when the potential is identical, one only displays the states $(x(t), p(t))$ of the system at times $t = t_0 + nT$. As depicted in Fig. 1.2(a) for one trajectory, this amounts to only considering the trajectories when they

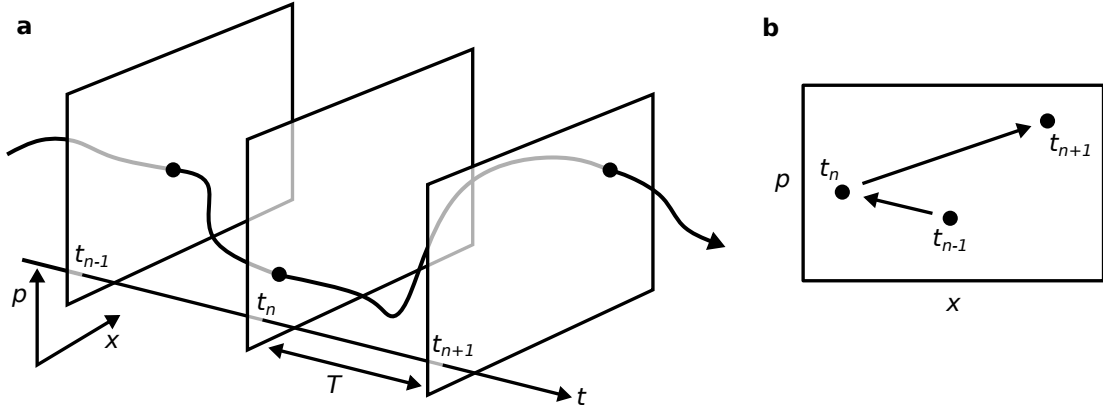


Figure 1.2 | Construction of a stroboscopic phase portrait. (a) Intersections (blue dots) between a trajectory (blue solid line) of the (x, p, t) phase space and the planes (x, p, t_n) with $t_n = t_0 + nT$ (see text). (b) Resulting stroboscopic phase portrait. Figure inspired from [69].

intersect the planes $(x, p, t_0 + nT)$, with $0 \leq t_0 < T$ and $n \in \mathbb{N}$. The resulting plot (Fig. 1.2(b)) is called the *stroboscopic phase portrait* and is an example of Poincaré section, a method to represent the phase space of a system in a subspace of lower dimensionality [69].

We now give examples of stroboscopic phase portraits. We consider the time-dependent Hamiltonian (1.7) whose depth and position reference are modulated periodically: $A(t + T) = A(t)$ and $\varphi(t + T) = \varphi(t)$. We define the dimensionless units

$$\tilde{x} = \frac{2\pi}{d} x, \quad \tilde{t} = \frac{2\pi}{T} t, \quad \tilde{p} = \frac{d\tilde{x}}{d\tilde{t}} = \frac{T}{md} p \quad \text{and} \quad \tilde{H} = \frac{T^2}{md^2} H. \quad (1.9)$$

From Eqs. (1.7) and (1.9), the dimensionless Hamiltonian reads:

$$\tilde{H}(\tilde{x}, \tilde{p}, \tilde{t}) = \frac{\tilde{p}^2}{2} - A(\tilde{t}) \times \gamma \cos(\tilde{x} + \varphi(\tilde{t})) \quad (1.10)$$

with the scaled potential amplitude $\gamma = V_0 T^2 / 2md^2$. In Fig. 1.3, we consider two cases:

(a) The offset² modulation of amplitude with one harmonic:

$$\begin{aligned} A(\tilde{t}) &= 1 + \varepsilon_0 \cos(\tilde{t}) \\ \varphi(\tilde{t}) &= 0 \end{aligned} \quad (1.11)$$

²In Chap. 2, we present the experimental realization of the systems discussed in this chapter. We then see how experimental constraints require $|A(\tilde{t})| > 0$, which explain the form of $A(\tilde{t})$ in Eq. (1.11), with $0 \leq \varepsilon_0 \leq 1$ in the experiment.

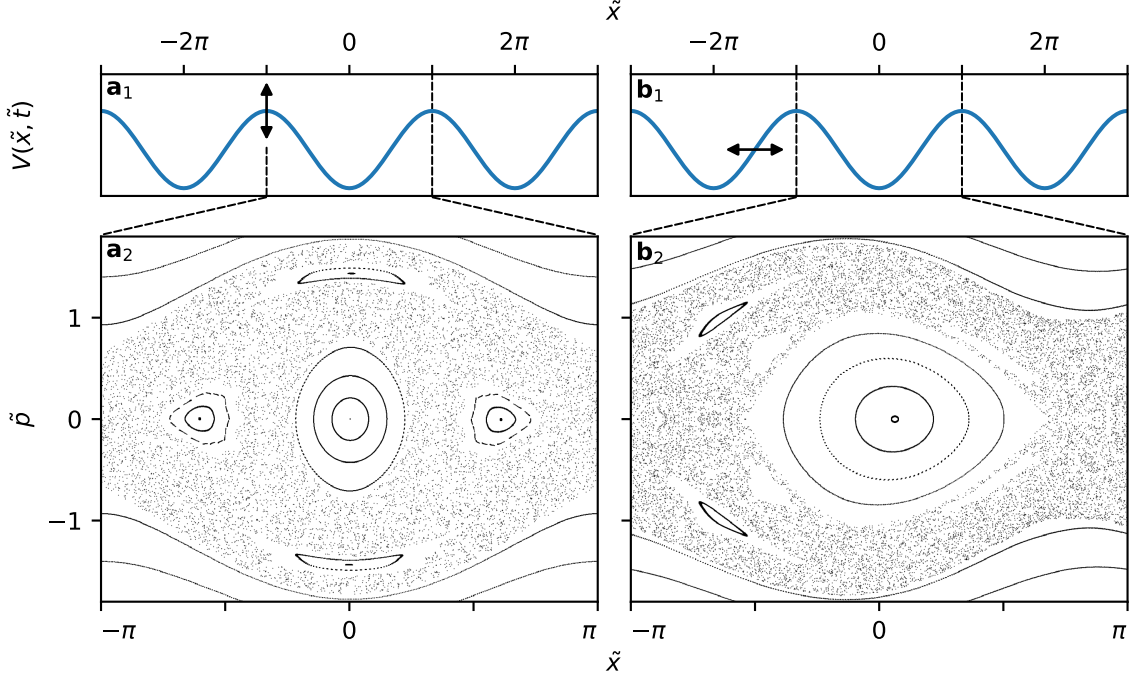


Figure 1.3 | Examples of stroboscopic phase portraits. Top: periodically modulated potentials over three spatial periods. Bottom: stroboscopic phase portraits. **(a)** Modulation of the depth of the potential, *i.e.* Eq. (1.10) for the modulation functions (1.11), with $\gamma = 0.375$, $\varepsilon_0 = 0.24$ and a subperiod time of stroboscopic observation $\tilde{t}_0 = 0$ (see text). **(b)** Modulation of the position reference of the potential, *i.e.* Eq. (1.10) for the modulation functions (1.12), with $\gamma = 0.44$, $\varphi_0 = 2\pi/24 = 15^\circ$ and a subperiod time of stroboscopic observation $\tilde{t}_0 = 0$.

(b) The phase modulation with one harmonic:

$$\begin{aligned} A(\tilde{t}) &= 1 \\ \varphi(\tilde{t}) &= \varphi_0 \cos(\tilde{t}) \end{aligned} \tag{1.12}$$

In the stroboscopic phase portraits of Fig. 1.3(a₂,b₂), we see three kinds of trajectories:

- We first have trajectories that live on closed lines inscribed inside one another. These regions of various shapes are called *regular islands* and consist of sections of inscribed tori³ made of surfaces of regular trajectories in the (x, p, t) phase space.
- At large dimensionless momentum ($|\tilde{p}| \gtrsim 1$ in Fig. 1.3), we see the unbounded trajectories that we already encountered in the case of the static potential (Fig. 1.1(b)), with enough mechanical energy to only be slightly perturbed by the modulation.
- Finally, inside the unbounded trajectories and surrounding the regular islands is the *chaotic sea*, a region of irregular trajectories that ergodically span all the accessible region of the phase space.

³They are also called KAM tori [71], for A. Kolmogorov [72], V. Arnold [73] and J. Moser [74]. A classical trajectory cannot cross a KAM torus by virtue of determinism.

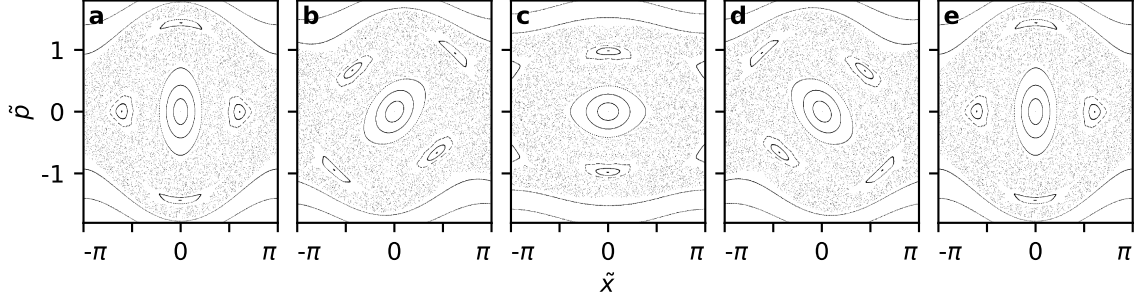


Figure 1.4 | Subperiod evolution of a stroboscopic phase portrait. (a-e) Stroboscopic phase portraits of the same Hamiltonian (1.10) in the amplitude modulation case of Eq. (1.11). The difference between the panels is the reference time \tilde{t}_0 of the stroboscopic observations, with $\tilde{t}_0 = 0, \pi/2, \pi, 3\pi/2$ and 2π for (a) to (e) resp.

The phase portraits of Fig. 1.3 give examples of mixed dynamics, with the coexistence of regular and chaotic trajectories. The degree of chaos (*i.e.* the ratio of phase space area between the chaotic sea and the regular islands) depends on the strength of the modulations [75, 69].

The stroboscopic phase portraits of Fig. 1.3 correspond to the specific choice of subperiod observation time $\tilde{t}_0 = 0$ (in accordance with our definitions of the modulation functions $A(\tilde{t})$ and $\varphi(\tilde{t})$ in Eqs (1.11) and (1.12) ; see Fig.1.2 and the explanation of the construction of a stroboscopic phase portrait). This parameter can be varied to inform on the sub-stroboscopic evolution of the system. We illustrate this procedure in Fig. 1.4, where we draw, for different times $0 \leq \tilde{t}_0 \leq 2\pi$, the stroboscopic phase portraits in the case of the amplitude modulation of the sine potential (Fig. 1.3(a)). In Fig. 1.4, we can discriminate between two kinds of regular islands: the islands that are linked to a given site of the potential (*e.g.* the three islands on the $\tilde{p} = 0$ axis at $\tilde{t}_0 = 0$) and the islands that travel to neighboring sites between periods (*e.g.* the two islands in $(\tilde{x}, \tilde{p}) \approx (0, \pm 1.25)$ at $\tilde{t}_0 = 0$). In the dimensionless units (1.9), the average momentum of any trajectory from a given regular island is the same rational number⁴:

$$\langle \tilde{p}_{\text{reg}} \rangle = \lim_{n \rightarrow \infty} \frac{1}{n \times 2\pi} \int_0^{n \times 2\pi} \tilde{p}_{\text{reg}}(\tilde{t}) d\tilde{t} = w \in \mathbb{Q}, \quad (1.13)$$

for $\tilde{p}_{\text{reg}}(\tilde{t})$ the scaled momentum of a trajectory in the regular island. The number w is the *winding number* [76, 71] of the regular island, which corresponds to the number of sites traveled per modulation period. This observation is at the heart of Chap. 4, where, through the correlation of the amplitude and phase modulations (Eqs. (1.11) and (1.12)), we engineer a transporting regular island (*i.e.* with a winding number $w \neq 0$) that passes by $(x, p) = (0, 0)$.

⁴In the evaluation of this average, the necessity of the limit comes from the quasi-periodicity of trajectories in regular islands. With the exception of the trajectory at the center of a regular island, the result $\langle \tilde{p}_{\text{reg}} \rangle = w \in \mathbb{Q}$ is in general only obtained asymptotically.

1.1.3 Symmetries of the phase space.

The symmetries of the phase space reflect the symmetries of the Hamiltonian. The two relevant symmetries for our dynamical study are the spatial symmetry S_x and the time-reversal symmetry S_t :

$$S_x : \begin{matrix} x \rightarrow -x \\ t \rightarrow t \end{matrix}, \quad \text{and} \quad S_t : \begin{matrix} x \rightarrow x \\ t \rightarrow -t \end{matrix} \quad (1.14)$$

with each symmetry transformation implying $p \rightarrow -p$. At time t , a given Hamiltonian $H(x, p, t)$ with trajectories $(x(t), p(t))$ has the symmetry S if the symmetric trajectories $S(x(t), p(t))$ are solutions of the symmetric equations of motion deduced from $S(H(x, p, t))$.

For instance, the amplitude modulation of Eq. (1.11) never breaks the spatial symmetry $S_{\tilde{x}}$ of the Hamiltonian (1.10). Therefore, the stroboscopic phase portraits in Fig. 1.4 have the central symmetry $(\tilde{x}, \tilde{p}) \rightarrow (-\tilde{x}, -\tilde{p})$ for all observation times \tilde{t}_0 . Moreover, the amplitude modulation being a function of $\cos(\tilde{t})$, the Hamiltonian has the symmetry $S_{\tilde{t}}$ only at times $\tilde{t}_0 = n\pi$ with $n \in \mathbb{N}$, which corresponds to the instants when the stroboscopic phase portraits have the axial symmetry $(\tilde{x}, \tilde{p}) \rightarrow (\tilde{x}, -\tilde{p})$ (Fig. 1.4(a,c,e)). The same analysis for the phase modulation (1.12) confirms the fact that the stroboscopic phase portrait of Fig. 1.3(b) displays the symmetry $S_{\tilde{t}}$ but not $S_{\tilde{x}}$ at $\tilde{t}_0 = 0$.

This concludes our reminders on classical mechanics. We now turn to the quantum regime for the study of a wave function in the sine-potential system.

1.2 Wave function in a time-independent sine potential

We first consider the case of a quantum particle in the static potential

$$V(x) = -\frac{V_0}{2} \cos\left(\frac{2\pi x}{d}\right). \quad (1.15)$$

We define characteristic quantities that we use throughout this manuscript:

- the wave number of the sine potential $k_L = 2\pi/d$,
- the characteristic energy $E_L = \hbar^2 k_L^2 / 2m = h^2 / 2md^2$,
- the corresponding frequency $\nu_L = E_L / h = h / 2md^2$,

with h the Planck constant. In the following, we express the depth V_0 of the potential in units of E_L through the dimensionless parameter $s_0 = V_0 / E_L$. In Chap. 2, we discuss the experimental implementation of the potential (1.15) and we give the numerical values

of these quantities. In the experiment, realistic accessible values for s_0 are in the range $[0, 40]$.

When working with optical lattices, an energy scale commonly found in the literature is the recoil energy $E_r = \hbar^2/8md^2 = E_L/4$, which is the kinetic energy acquired by an initially resting atom of mass m when absorbing of a photon with wave number $k_L/2$. The realistic range for experimental lattice depths given in the previous paragraph corresponds to $V_0 \leq 160E_r$.

The quantum treatment of periodic potentials falls under the study of wave functions in crystalline structures. A major result in this field is Bloch's theorem, that we briefly present in the one-dimensional case.

1.2.1 Bloch's theorem in one dimension

We want to determine the eigenvectors of a generic one-dimensional Hamiltonian:

$$\hat{H} = \frac{\hat{p}^2}{2m} + \hat{V}(x) \quad (1.16)$$

with $\hat{p} = -i\hbar\partial/\partial x$ and a spatially periodic potential $\hat{V}(x+d) = \hat{V}(x)$. We define the plane waves $|\chi_r\rangle$, eigenstate of the momentum operator \hat{p} with eigenvalue $r\hbar k_L$:

$$\langle x|\chi_r\rangle = \chi_r(x) = \frac{e^{irk_L x}}{\sqrt{d}} \quad (1.17)$$

with a normalization over one site of the potential. Since \hat{H} is left invariant by the discrete spatial translation $x \rightarrow x - d$, it commutes with the spatial translation operator $\hat{T}_d = e^{-id\hat{p}/\hbar}$. Consequently, one can look for a basis of states in which \hat{H} and \hat{T}_d are diagonal operators, *i.e.* a common set of eigenstates for \hat{H} and \hat{T}_d . Bloch's theorem [77, 78, 79] states that these eigenstates are the product of a plane wave $\chi_{q/k_L}(x)$ and a function with the periodicity of the potential. They are functions of the form:

$$\psi_q(x) = u_q(x)e^{iqx}, \quad (1.18)$$

where the wave number q will be referred to as the quasi-momentum⁵, and $u_q(x+d) = u_q(x)$. Considering smooth enough potentials $V(x)$, the functions $u_q(x)$ can be expressed as their Fourier series:

$$u_q(x) = \sum_{\ell \in \mathbb{Z}} c_{q,\ell} \frac{e^{i\ell k_L x}}{\sqrt{d}} = \sum_{\ell \in \mathbb{Z}} c_{q,\ell} \chi_\ell(x), \quad (1.19)$$

⁵Even though the quantity associated to q that is homogeneous to a momentum is rather $\hbar q$.

with $c_{q,\ell} \in \mathbb{C}$. From Eqs. (1.18) and (1.19), the Bloch eigenstates can be written as

$$\psi_q(x) = \sum_{\ell \in \mathbb{Z}} c_{q,\ell} \frac{e^{i(\ell k_L + q)x}}{\sqrt{d}} = \sum_{\ell \in \mathbb{Z}} c_{q,\ell} \chi_{\ell + q/k_L}(x), \quad (1.20)$$

as well as any state evolving in the potential at given quasi-momentum q , since the basis of the Bloch eigenstates spans the Hilbert space for all q . We refer to the coefficients $c_{q,\ell} \in \mathbb{C}$ as the plane wave coefficients of a state, with the normalization condition $\sum_{\ell} |c_{q,\ell}|^2 = 1$. Within a subspace of fixed q , a state in a Bloch system is fully defined by the infinite set of its plane wave coefficients, and we see from Eq. (1.20) that it consists of a comb of plane waves with momenta $p = \hbar(\ell k_L + q)$ (with $\ell \in \mathbb{Z}$). We see that a phenomenological interpretation for the quasi-momentum is that it is the quantity that sets the *momentum reference of the plane wave comb* in the rest frame of the potential. Furthermore, Eq. (1.20) implies that quantum states at a given quasi-momentum in Bloch systems are periodic under the discrete quasi-momentum translation $q \rightarrow q + k_L$ (with $c_{q+m k_L, \ell} = c_{q, \ell}$ for $m \in \mathbb{Z}$ in the plane wave expansion of a given state $\psi_q(x)$). This defines the *first Brillouin zone*, the relevant quasi-momentum cell in which to study the dynamics of a system, that we define as $-0.5 < q/k_L \leq 0.5$.

In the following, we write $|\psi_q\rangle$ an arbitrary state at quasi-momentum q , and $|\phi_{q,n}\rangle$ the n^{th} Bloch eigenstate at quasi-momentum q (where the index n sorts the states by increasing eigenvalues ; see below).

1.2.2 The central equation for the sine potential and the band structure

The central equation. We now go back to the specific case of a wave function in a sine potential:

$$V(x) = -s_0 \frac{E_L}{2} \cos(k_L x). \quad (1.21)$$

From Bloch's theorem, we look for the eigenstates of this system in the form of Bloch waves $\phi_{q,n}(x) = \sum_{\ell} c_{q,\ell}^{(n)} \chi_{\ell + q/k_L}(x)$. Combining Eqs (1.16), (1.20) and (1.21), the time-independent Schrödinger equation leads to the *central equation*:

$$\begin{aligned} \hat{H} \phi_{q,n}(x) &= E_{q,n} \phi_{q,n}(x) \\ \left(\ell + \frac{q}{k_L} \right)^2 c_{q,\ell}^{(n)} - \frac{s_0}{4} \left(c_{q,\ell-1}^{(n)} + c_{q,\ell+1}^{(n)} \right) &= \frac{E_{q,n}}{E_L} c_{q,\ell}^{(n)}, \end{aligned} \quad (1.22)$$

with $E_{q,n}$ the eigenenergy associated with the Bloch eigenstate $|\phi_{q,n}\rangle$. We see that the Hamiltonian for the sine potential is tridiagonal in the basis of the plane waves, as it couples the plane wave $|\chi_{\ell}\rangle$ to the plane waves $|\chi_{\ell \pm 1}\rangle$. For given parameters (s_0, q) , its diagonalization gives the

Bloch eigenstates and the associated eigenenergies. This is done numerically. As the Hilbert space dimension of this continuous system is infinite, ℓ needs to be truncated to $|\ell| \leq \ell_{\max}$, an upper bound for the plane waves of highest kinetic energy considered. For a given problem, ℓ_{\max} is determined by making sure that the plane waves with the highest kinetic energy contributing to the dynamics are taken into account (*i.e.* by ensuring that the choice of a greater ℓ_{\max} results in the same dynamics). The resulting Hilbert space dimension is $d_{\text{H}} = 2\ell_{\max} + 1$. To model realistic situations in the experimental optical lattice (see Chap. 2), our simulations are typically done with $d_{\text{H}} \sim 30$.

The band structure. For a given s_0 , the spectrum of the Hamiltonian as a function of the quasi-momentum gives the *band structure*. In this thesis, we adopt the nomenclature ($s, p, d, f \dots$) for the bands of eigenenergy $n = (0, 1, 2, 3 \dots)$. In Fig. 1.5, we draw the band structures for two non-zero potential depths, and we show examples of Bloch eigenstates by displaying their plane wave coefficients $c_{q,\ell}$ and their spatial density of probability $|\phi_{q,n}(x)|^2$. We make a series of remarks:

- We define the parity operator \hat{P} , whose action on an arbitrary state in the position representation is

$$\hat{P}\psi_q(x) = \psi_q(-x). \quad (1.23)$$

For a symmetric potential $V(x) = V(-x)$, the Hamiltonian commutes with \hat{P} . Therefore,

$$\phi_{-q,n}(x) = \phi_{q,n}(-x). \quad (1.24)$$

Consequently, we have $c_{q,\ell}^{(n)} = \pm c_{-q,-\ell}^{(n)}$, and moreover $c_{q,\ell}^{(n)} = \pm c_{q,-\ell}^{(n)}$ for $q \in \{0, 0.5\}$. This is illustrated in Fig. 1.5(b,c,d,g,h).

- For a Bloch system left invariant by the time-reversal symmetry S_t (1.14) (such as the time-independent sine potential that we consider), the band structure is symmetric around $q = 0$, so we have $E_{q,n} = E_{-q,n}$ [79] (see Fig. 1.5(a,e)).
- Comparing the two ground states in Fig. 1.5(d) and (h), we see that, as the depth of the potential increases, the envelope of the c_ℓ gets wider and the probability dispersion of the spatial density gets narrower. This illustrates the uncertainty principle $\Delta x \Delta p \geq \hbar/2$ between the two incompatible observables x and p . At the end of this chapter, we briefly discuss the uncertainty principle when we consider the representation of a wave function in the phase space (Sec. 1.4). This phenomenon is also highlighted in Chap. 3, where we perform state squeezing in the optical lattice.
- Figure 1.5(f,g) shows two states at $q \neq 0$. We see how the momentum reference of the plane wave comb is translated accordingly. In Chap. 5, we study the emergence of states

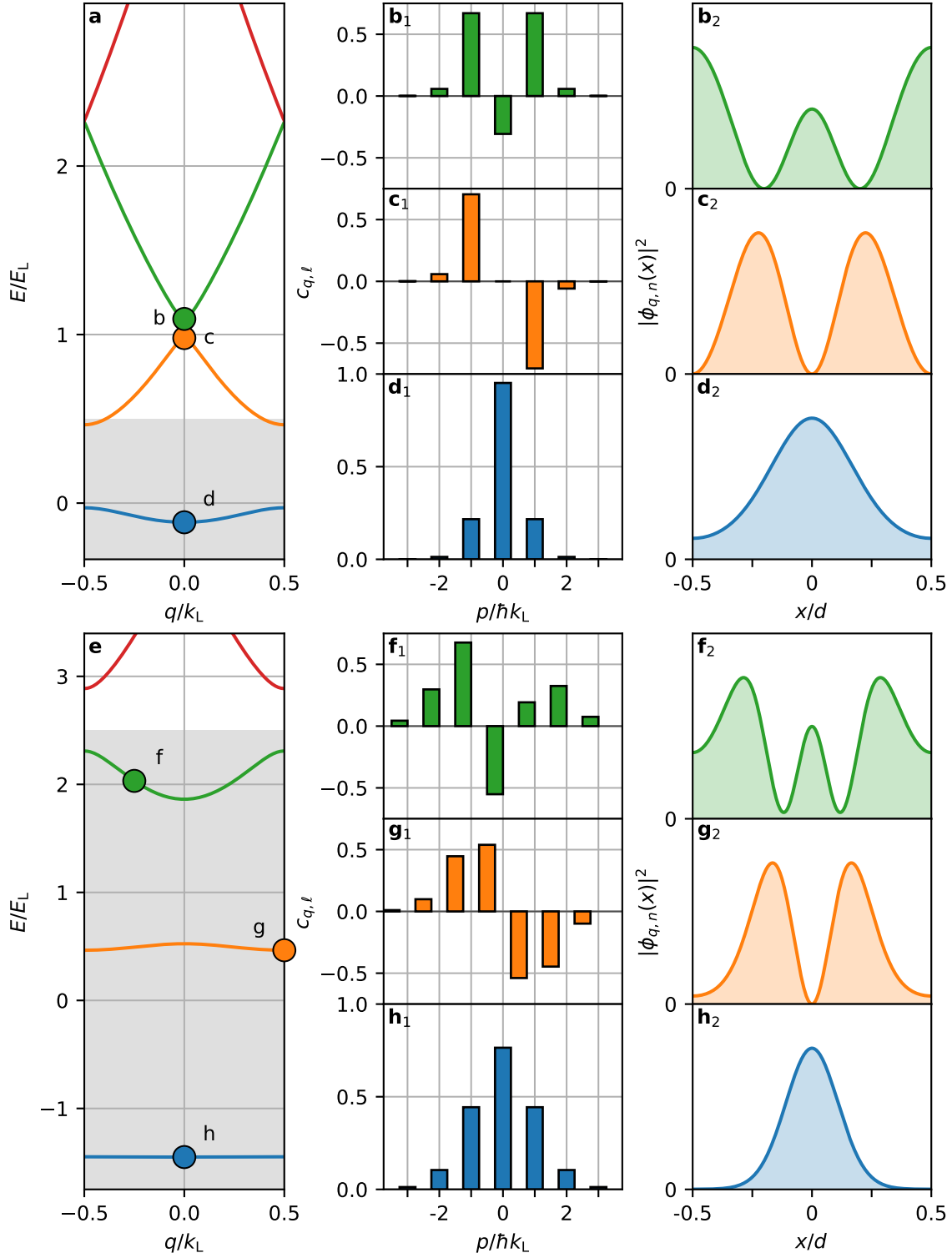


Figure 1.5 | Band structures and Bloch eigenstates. (a,e) Band structures in the first Brillouin zone obtained from Eq. (1.22) with $s_0 = 1$ (a) and $s_0 = 5$ (e). The bands s , p , d and f are in blue, orange, green and red. The grey shaded areas indicate the energies below the maximum potential energy $V(\pm d/2) = s_0 E_L/2$. (b,c,d,f,g,h)₁ Plane wave coefficients c_ℓ as a function of the plane waves momenta p in the rest frame of the potential for the Bloch eigenstates identified on panels (a,e). (b,c,d,f,g,h)₂ Spatial densities of probability for the Bloch eigenstates identified on panels (a,e).

coexisting at different quasi-momenta in a modulated optical lattice. The signature of the phenomenon is the population of plane waves on translated momentum comb.

The limit $s_0 \rightarrow 0$. In the absence of potential ($s_0 = 0$), the Hamiltonian in Eq. (1.22) is diagonal in the basis of the plane waves. This is expected since the plane waves are the eigenstates of the momentum operator \hat{p} . The band structure then simply becomes $E_{q,n} \rightarrow E_{q,\ell}/E_L = (\ell + q/k_L)^2$, *i.e.* the parabolic relation of dispersion for the free particle. In this situation, we get pairs of degenerate eigenstates at $q/k_L = 0$ and $q/k_L = 0.5$ as there then exist two relative integer values of ℓ such that $\ell + q/k_L$ takes the same value (with the exception of $\ell = 0$ at $q = 0$). This has experimental consequences when performing a band-mapping (see Sec. 2.4.3).

1.2.3 Quantum state evolution in a Bloch system

In the absence of interactions, the dynamics of a wave function is ruled by the time-dependent Schrödinger equation:

$$i\hbar \frac{\partial}{\partial t} \psi_q(x, t) = \hat{H}(t) \psi_q(x, t). \quad (1.25)$$

From time t_0 to t , the evolution of a state $\psi_q(x, t_0)$ is given by

$$\psi_q(x, t) = \hat{U}(t, t_0) \psi_q(x, t_0). \quad (1.26)$$

The evolution operator $\hat{U}(t, t_0)$ is a unitary operator that satisfies the Schrödinger equation

$$i\hbar \frac{\partial}{\partial t} \hat{U}(t, t_0) = \hat{H}(t) \hat{U}(t, t_0). \quad (1.27)$$

The solution of this equation reads

$$\hat{U}(t, t_0) = \hat{\mathcal{T}} \exp \left\{ \frac{-i}{\hbar} \int_{t_0}^t \hat{H}(t') dt' \right\}. \quad (1.28)$$

where $\hat{\mathcal{T}}$ is the time-ordering operator. For a time-independent periodic potential, it simplifies into

$$\begin{aligned} \hat{U}(t, t_0) &= e^{-i\hat{H} \times (t-t_0)/\hbar} \\ &= \sum_{n \in \mathbb{N}} e^{-iE_{q,n}(t-t_0)/\hbar} |\phi_{n,q}\rangle \langle \phi_{n,q}|. \end{aligned} \quad (1.29)$$

We see that it is straightforward to obtain the evolution of an arbitrary state in the time-independent sine potential (1.21) from its expansion on the Bloch eigenstates:

$$\begin{aligned} |\psi_q(t_0)\rangle &= \sum_{n \in \mathbb{N}} d_{q,n}(t_0) |\phi_{q,n}\rangle \\ \Rightarrow \hat{U}(t, t_0) |\psi_q(t_0)\rangle &= \sum_{n \in \mathbb{N}} d_{q,n}(t) |\phi_{q,n}\rangle \end{aligned} \quad (1.30)$$

with $d_{q,n}(t) = e^{-iE_{q,n}(t-t_0)/\hbar} d_{q,n}(t_0)$.

In Chap. 2, we present a method to calibrate the depth of our optical lattice that consists in probing the eigenenergies $E_{q,n}$ by triggering an out-of-equilibrium evolution in the sine potential.

1.3 Wave function in a time-dependent sine potential

1.3.1 Time-dependent sine potential: general case

Let us now consider the case of a sine potential whose depth and phase reference can be arbitrarily varied in time:

$$V(x, t) = -A(t) \times s_0 \frac{E_L}{2} \cos(k_L x + \varphi(t)). \quad (1.31)$$

The diagonal and off-diagonal matrix elements of the Hamiltonian in the central equation (1.22) become

$$\langle \chi_{\ell+q/k_L \pm 1} | \frac{\hat{H}(t)}{E_L} | \chi_{\ell+q/k_L} \rangle = -\frac{A(t)s_0 e^{\mp i\varphi(t)}}{4}. \quad (1.32)$$

We cannot develop further in the case of arbitrary functions $A(t)$ and $\varphi(t)$. We can however make numerical simulations to study a given dynamics, for instance by iteratively constructing the evolution operator from a series of Hamiltonians considered constant over a small enough time intervals δt :

$$\hat{U}(t, t_0) = \lim_{\delta t \rightarrow 0} \prod_{n=0}^{\lfloor (t-t_0)/\delta t \rfloor} \exp \left\{ \frac{-i\hat{H}(t - n\delta t) \times \delta t}{\hbar} \right\}. \quad (1.33)$$

with $\lfloor \cdot \rfloor$ denoting the integer part. In Chap. 3, we show how the optical lattice can be continuously moved in space in order to bring an initial state to a given target state. The quantum

optimal control algorithm used for the determination of the control field $x_0(t)$ notably relies on Eq. (1.33) to integrate the dynamics in the lattice.

In the next section, we address the specific case of time-periodic modulations of the sine potential (1.31).

1.3.2 Time-periodic Hamiltonians : Floquet formalism

We consider a potential that is periodically modulated in time:

$$V(x, t) = V(x, t + T). \quad (1.34)$$

Floquet operator, Floquet states and quasi-energies. In this system, a natural basis [80, 16] over which to decompose a state to study its evolution is the set of Floquet states $\{|\varphi_m^{(t_0)}\rangle\}$, the eigenstates of the evolution operator from t_0 to $t_0 + T$ (*i.e.* a one-period evolution). This operator, called the Floquet operator, reads

$$U_F^{(t_0)} = U(t_0 + T, t_0) = \hat{\mathcal{T}} \exp\left\{\frac{-i}{\hbar} \int_{t_0}^{t_0+T} \hat{H}(t) dt\right\}, \quad (1.35)$$

with the subperiod reference time $0 \leq t_0 < T$. As the evolution operator is unitary, its eigenvalues are complex numbers with norm one:

$$U_F^{(t_0)} |\varphi_m^{(t_0)}\rangle = \lambda_m |\varphi_m^{(t_0)}\rangle = e^{-i\epsilon_m T/\hbar} |\varphi_m^{(t_0)}\rangle. \quad (1.36)$$

where we have defined the *quasi-energies* ϵ_m given by $\epsilon_m = -\arg\{\lambda_m\}\hbar/T$. We see that the quasi-energies are periodic under the translation

$$\epsilon_m \rightarrow \epsilon_m + \frac{2\pi\hbar}{T} = \epsilon_m + h\nu, \quad (1.37)$$

with $h\nu$ the energy of one phonon at the frequency $\nu = 1/T$. Therefore, we only consider the quasi-energies in the interval $-h\nu/2 < \epsilon_m \leq h\nu/2$. This “quasi-energetic Floquet cell” is the translation of the Brillouin zone in the time domain [16]. For a given Floquet potential (Eq. (1.34)), two useful properties (see [16]) are that:

- the Floquet states for a different time reference t_1 can be determined from the Floquet states $|\varphi_m^{(t_0)}\rangle$ by propagating them from t_0 to t_1 , *i.e.*

$$|\varphi_m^{(t_1)}\rangle = \hat{U}(t_1, t_0) |\varphi_m^{(t_0)}\rangle, \quad (1.38)$$

- the quasi-energies ϵ_m of $U_F^{(t_0)}$ do not depend on the reference time t_0 .

From the Floquet states and their associated quasi-energies, we rewrite the Floquet operator (1.35)

$$\left(\hat{U}_F^{(t_0)}\right)^n = \sum_{m \in \mathbb{N}} e^{-in \times \epsilon_m T / \hbar} \left| \varphi_m^{(t_0)} \right\rangle \left\langle \varphi_m^{(t_0)} \right| \quad (1.39)$$

for $n \in \mathbb{N}$ modulation periods. Comparing Eqs. (1.29) and (1.39), we see that, in the Floquet formalism, the discrete, stroboscopic dynamics of a quantum system with a time periodic Hamiltonian is analogous to the continuous dynamics with a time independent Hamiltonian ; the quasi-energies and the Floquet states playing the role of the eigenenergies and the Bloch eigenstates. A potential that is both periodic in space and time is called a *Floquet-Bloch potential*.

Quasi-energy spectrum. The analog of the band structure for a Floquet-Bloch Hamiltonian is the quasi-energy spectrum (or Floquet spectrum) as a function of the quasi-momentum. As examples, we draw in Fig. 1.6 two quasi-energy spectra (computed from Eqs. (1.32) and (1.33)) for the amplitude modulated Floquet-Bloch potential

$$V(x, t) = -[1 + \varepsilon_0 \cos(2\pi\nu t)] s_0 \frac{E_L}{2} \cos(k_L x), \quad (1.40)$$

with parameters $s_0 = 4$, $\nu = 3.2 \nu_L$ and the two amplitudes of modulation $\varepsilon_0 = 0$ and $\varepsilon_0 = 0.15$. For $\varepsilon_0 = 0$ (Fig. 1.6(b)), we are actually in the situation of the static potential, so the Floquet states are simply the Bloch eigenstates, with the eigenenergies correspondence

$$\epsilon_n \equiv E_n \bmod (h\nu) + \Delta\epsilon \quad (1.41)$$

(the dependence on q is implicit, and $\Delta\epsilon$ is an arbitrary offset of all the quasi-energies corresponding on the arbitrary global phase in Eq. (1.36)). This equivalence modulo the phononic energy $h\nu$ (Eq. (1.37)) is well illustrated by the comparison between the band structure of the static potential (Fig. 1.6(a)) and the quasi-energy spectrum in absence of modulation (Fig. 1.6(b)). We see that the quasi-energy spectrum consists of superimposed slices of the band structure with energy height $h\nu$. In the absence of modulation (Fig. 1.6(b)), the quasi-energy levels cross at the quasi-momenta where the Bloch bands in the band structure are separated by $k \times h\nu$ with $k \in \mathbb{N}^*$. The integer k is directly the order of the phononic transition implied. For $\varepsilon_0 > 0$ (Fig. 1.6(c)), the inter-band couplings induced by the modulation of the potential leads to Bloch eigenstates hybridizations (see below), with quasi-energy bands displaying avoided crossings whose width increases with the modulation amplitude.

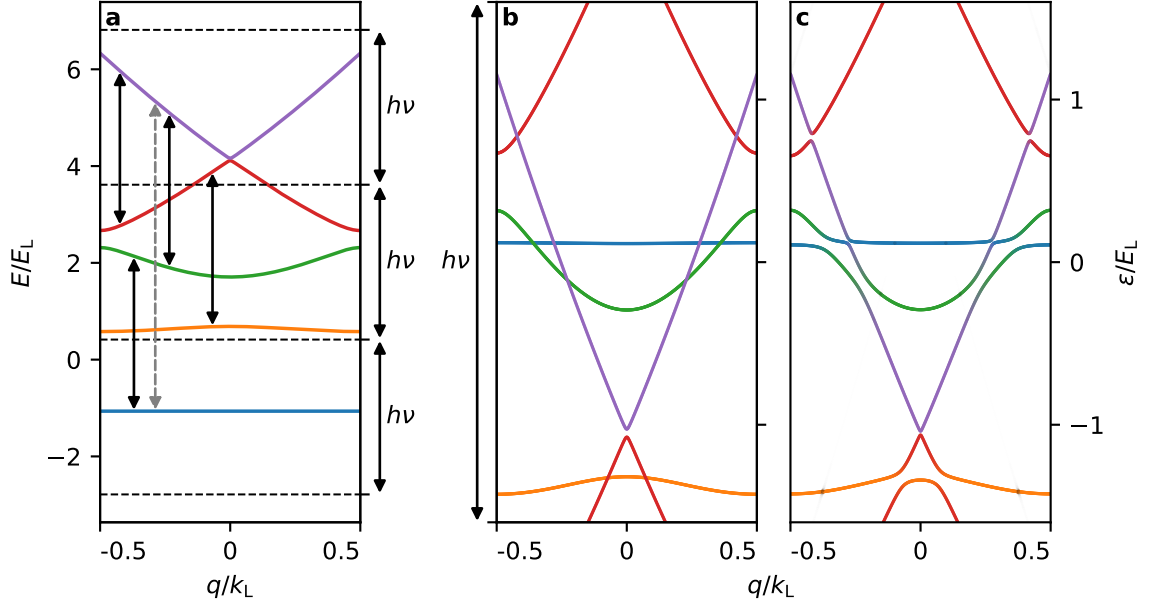


Figure 1.6 | Band structure and quasi-energy spectra. (a) Band structure (plain colored lines) of the static sine potential for $s_0 = 4$. The s , p , d , f and g bands are in blue, orange, green, red and purple respectively. The arrows are placed at the quasi-momenta where the Bloch bands are separated by an energy $|E_{i,q} - E_{j,q}| = k \times h\nu$ (see text), with $k = 1$ (plain back arrow) and $k = 2$ (dotted grey arrow). Arrows are only shown for $q < 0$ for the figure to remain legible. The horizontal dashed lines correspond to the energy period in the quasi-energy spectra (b,c) (see text). (b,c) Quasi-energy spectra for the time-periodic potential (1.40) for two different amplitudes of modulation ε_0 and other parameters $s_0 = 4$ and $\nu = 3.2\nu_L$. The amplitudes of modulation are $\varepsilon_0 = 0$ (b) and $\varepsilon_0 = 0.15$ (c).

Identification of the relevant Floquet states. The static band structure of Fig. 1.6(a) has been obtained numerically in a Hilbert space of truncated dimension d_H (in this case $d_H = 31$, see Sec. 1.2.2). After the diagonalization of the Hamiltonian, one can directly identify the n^{th} Bloch eigenstate as it is the state corresponding to the n^{th} greatest eigenenergy. The amplitude modulated sine potential (1.40) is also a continuous system with an infinite Hilbert space dimension. As for the static case, the Floquet spectra of Fig. 1.6(b,c) have been obtained working with a basis of the d_H plane waves (from Eqs. (1.32) and (1.33) with $d_H = 31$). Therefore, for each quasi-momentum considered in Fig. 1.6(b,c), we actually have d_H states, with no obvious ordering between the quasi-energies $-h\nu/2 < \epsilon_m \leq h\nu/2$ (which are moreover defined up to an arbitrary offset). To identify relevant Floquet states, an efficient method is to sort them by their overlap with known states. We use this method, in Fig. 1.6(b,c) where, for all the quasi-momenta considered, we only display the quasi-energies of the $N = 5$ Floquet states maximally alike the first five Bloch eigenstates. Furthermore, the color⁶ $C_m^{(\varphi)}$ with which we draw the quasi-energy ϵ_m of a given Floquet state $|\varphi_{q,m}\rangle$ is the weighted average of the colors $C_n^{(\phi)}$ associated to the first five Bloch bands $|\phi_{q,n}\rangle$, with weights corresponding to the overlaps between the Bloch eigenstates and the Floquet state considered:

⁶For instance encoded in RGB: $C_i = [r_i, g_i, b_i]$ with $0 \leq r_i, g_i, b_i \leq 1$.

$$C_m^{(\varphi)} = \sum_{n=1}^N C_n^{(\phi)} |\langle \phi_{q,n} | \varphi_{q,m} \rangle|^2 \quad (1.42)$$

Doing so, the above-mentioned hybridization of Bloch eigenstates induced by the modulation of the potential can directly be observed at the avoided crossings of Fig. 1.6(c), through which the color of a Floquet band smoothly transitions between the colors associated with the two static Bloch bands.

1.4 Quantum states in the phase space

In Fig. 1.5, we have drawn band structures and represented typical Bloch eigenstates both in the p and x representations. In this section, we discuss the endeavor of giving both informations at once, *i.e.* representing the quantum state of a one-dimensional system in the (x, p) phase space.

In the beginning of this chapter (Sec. 1.1), we recalled that the state of a classical system at a given time is a point in the position-momentum phase space of the system. In the quantum regime, the position and momentum of a particle are not defined point-wise. Instead, if the state of a particle is defined by the ket $|\psi\rangle$, the Born rule states that the probability of finding the particle between x and $x + dx$ is $|\langle x|\psi\rangle|^2 dx = |\psi(x)|^2 dx$, and the probability of finding the particle with a momentum between p and $p + dp$ is $|\langle p|\psi\rangle|^2 dp = |\psi(p)|^2 dp$. Moreover, the wave function $\psi(x)$ and $\psi(p)$ for a particle in a given state are related by the Fourier transform:

$$\psi(p) = \int_{-\infty}^{\infty} \frac{\psi(x) e^{-ixp/\hbar}}{\sqrt{2\pi\hbar}} dx \quad (1.43)$$

with the Heisenberg uncertainty relation between the standard deviation⁷ Δx of $\psi(x)$ and the standard deviation Δp of $\psi(p)$:

$$\Delta x \Delta p \geq \frac{\hbar}{2}. \quad (1.44)$$

This inequality implies that the minimal “area” $\Delta x \Delta p$ of a state in the phase space is typically \hbar , and corroborates that a wave function cannot be described by a vector in the phase space.

⁷For an observable \hat{A} , we have $\Delta A = \sqrt{\langle \hat{A}^2 \rangle_\psi - \langle \hat{A} \rangle_\psi^2}$,

1.4.1 Wigner and Husimi representations and the effective Planck constant

Wigner representation. To represent a quantum state $|\psi\rangle$ in the phase space, E. Wigner [81] introduced the function $W_\psi(x, p) : \mathbb{R}^2 \mapsto \mathbb{R}$:

$$W_\psi(x, p) = \frac{1}{\pi\hbar} \int_{-\infty}^{\infty} \psi^*(x+u)\psi(x-u) \exp\left\{-i\frac{2pu}{\hbar}\right\} du. \quad (1.45)$$

such that its integration along the x axis *or* the p axis (called the marginal distributions) yields the density of probability:

$$\begin{aligned} \int_{\Omega_p} W_\psi(x, p) dp &= |\psi(x)|^2 \\ \int_{\Omega_x} W_\psi(x, p) dx &= |\psi(p)|^2 \end{aligned} \quad (1.46)$$

where $\Omega_{x,p}$ are the intervals over which $\psi(x)$ and $\psi(p)$ are normalized (in the case of our sine potential, we work with $\Omega_x = [-d/2, d/2]$ and $\Omega_p = (-\infty, \infty)$). However, it is known that the Wigner function can take negative values [82], so one speaks of a *quasiprobability distribution*. For a state $\psi_q(x)$ in the subspace of quasi-momentum q written over the basis of the plane waves in an infinite sine potential (Eq. (1.20)), the Wigner function reads [83]:

$$W_{\psi_q}(x, p) = \begin{cases} \frac{1}{2\pi} \sum_{\ell \in \mathbb{Z}} c_\ell^* c_{m-\ell} e^{-i(2\ell-m)k_L x}, & p/\hbar = q + \frac{m}{2}k_L \\ 0, & \text{elsewhere} \end{cases} \quad (1.47)$$

with $m \in \mathbb{Z}$. We note that $W_{\psi_q}(x, p)$ takes non-zero values for integer and half integer values of $p - \hbar q$, whereas $|\psi_q(p)|^2$ is non-zero only for integer values of $p - \hbar q$ (Sec. 1.2.1). In Fig. 1.7, we plot the Wigner representations and marginal distributions of the first two Bloch eigenstates for a lattice of depth $s_0 = 3$ at quasi-momentum $q = 0$. We see that the contribution of $W_{\psi_q}(x, p)$ for half integer values of p cancels out when integrating along x for the evaluation of the marginal distribution $|\psi_q(p)|^2$, as could also be deduced from (1.47).

Husimi representation. The alternative to the Wigner representation that we choose to use in this manuscript is the Husimi representation [84] commonly used for dynamical studies in the semi-classical regime (see below). The Husimi function $Q_\psi(x, p) : \mathbb{R}^2 \mapsto [0, 1]$ can be expressed as

$$Q_\psi(x, p) = \frac{1}{2\pi\hbar} |\langle g(x, p) | \psi \rangle|^2. \quad (1.48)$$

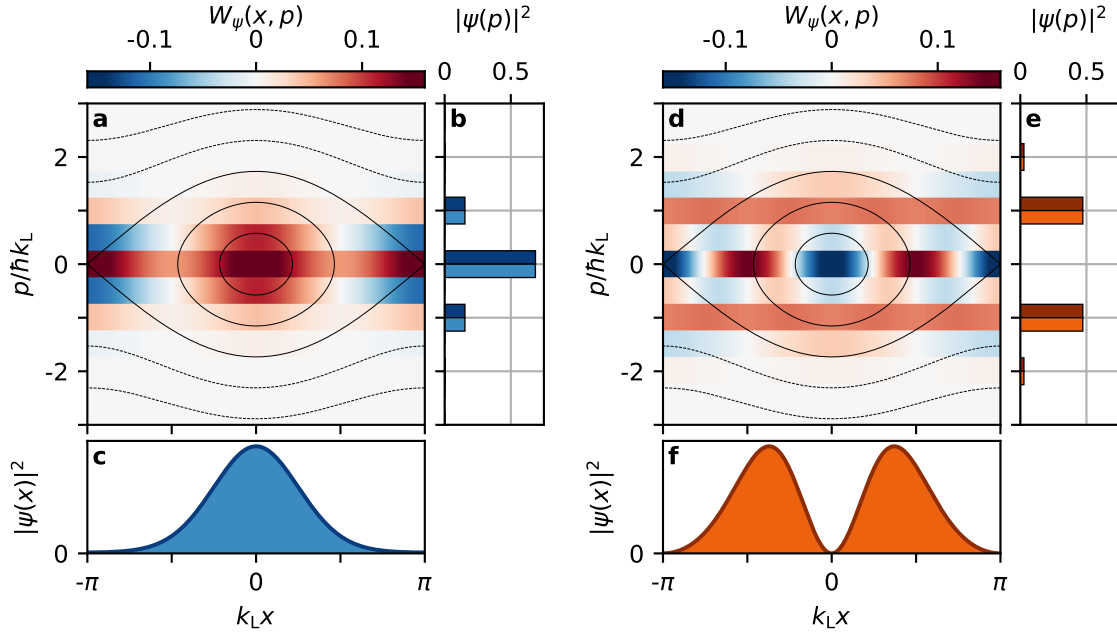


Figure 1.7 | Wigner representation of Bloch eigenstates in the phase space of the static sine potential (1.21) (a) Wigner representation $W_\psi(x, p)$ (Eq. (1.45)) of the ground state $|\psi\rangle = |\phi_{q,n=0}\rangle$ at depth $s_0 = 3$ and quasi-momentum $q = 0$. For visibility, the resulting horizontal stripes are plotted with width $\hbar k_L/2$ but are in reality infinitesimally thin. (b) Densities of probability in the momentum representation obtained either from the marginal distribution of $W_\psi(x, p)$ (dark blue bars) or directly from the known plane wave coefficients (light blue bars). (c) Densities of probability in the position representation obtained either from the marginal distribution of $W_\psi(x, p)$ (dark blue line) or directly from the Fourier series of $\psi(x)$ (Eq. (1.20)) with the known plane wave coefficients (curve delimiting the light blue area). (d,e,f) Same as (a,b,c) for the first excited state $|\psi\rangle = |\phi_{q=0,n=1}\rangle$. The classical trajectories are plotted in black lines.

i.e. the evaluation of the overlap between $|\psi\rangle$ and a Gaussian state $|g(x, p)\rangle$ centered in $(\langle \hat{x} \rangle_{g(x,p)}, \langle \hat{p} \rangle_{g(x,p)}) = (x, p)$. In the position representation, this state can be written

$$\langle x | g(x_0, p_0) \rangle = \frac{1}{\sqrt[4]{2\pi(\Delta x)^2}} \exp \left\{ -\frac{(x - x_0)^2}{4(\Delta x)^2} + i \frac{x p_0}{\hbar} \right\}. \quad (1.49)$$

The Gaussian state $|g(x_0, p_0)\rangle$ is a state that minimizes the uncertainty inequality (1.44), with $\Delta p = \hbar/2\Delta x$. The evaluation of $Q_\psi(x, p)$ (1.48) informs on the probability of measuring the particle described by the state $|\psi\rangle$ in a typical phase space area of $\sim \hbar$ around the point (x, p) , with normalization $\iint Q_\psi(x, p) dx dp = 1$. There is however a somewhat arbitrary choice that needs to be made on the standard deviation Δx of the Gaussian state in the Husimi function (1.48). In the case of a harmonic oscillator of angular frequency ω , one usually takes the ground state of the system, *i.e.* a Gaussian state with standard deviation $\Delta x = \sqrt{\hbar/2m\omega}$. In the case of the sine potential, we make a similar choice by taking the ground state of the harmonic oscillator that approximates the bottom of each site of the potential. At depth s_0 , the corresponding angular frequency is $\omega_0 = \sqrt{s_0} \times 2\pi\nu_L$ (see Sec. 1.2). The plane wave coefficients of this periodic Gaussian state are [85]:

$$c_{q,\ell}(x_0, p_0) = \left(\frac{2}{\pi\sqrt{s_0}} \right)^{1/4} \exp \left\{ -i(\ell k_L + q)x_0 - \frac{(\ell\hbar k_L + \hbar q - p_0)^2}{\sqrt{s_0}(\hbar k_L)^2} \right\} \quad (1.50)$$

with standard deviations $\Delta x = s^{-1/4}k_L^{-1}$ and $\Delta p = s^{1/4}\hbar k_L/2$, verifying the uncertainty relation (1.44). Such Husimi representations are shown in Fig. 1.8.

Equation (1.50) only yields normalized states $|g_q(x_0, p_0)\rangle = \sum_{\ell} c_{q,\ell}(x_0, p_0)|\chi_{\ell+q/k_L}\rangle$ when the standard deviation Δp of the envelope of the plane wave coefficients is far greater than the spacing $\hbar k_L$ of the momentum comb:

$$\Delta p \gg \hbar k_L \Leftrightarrow s \gg 1. \quad (1.51)$$



At depth $s_0 \geq 5$, one can compute that the error of normalization is at most

$$\left| \sum_{\ell \in \mathbb{Z}} |c_{q,\ell}(x_0, p_0)|^2 - 1 \right| \leq 3.25 \cdot 10^{-5}. \quad (1.52)$$

As a precaution, we systematically renormalize the states obtained from the definition (1.50).

The effective Planck constant. In Fig. 1.8, we plot, alongside trajectories from classical dynamics, the Husimi functions of the first two Bloch eigenstates in the sine potential for the two depths $s_0 = 3$ and $s_0 = 20$. We see that, while the classical trajectories scaled by k_L^{-1} and p_{sep} do not depend on the parameters of the potential, the effect of the variation of the depth of the potential is well visible on the quantum states' extent in the phase space. The difference in behavior between the classical and quantum descriptions can be shown formally: we once again consider the one-dimensional Hamiltonian

$$H(x, p) = \frac{p^2}{2m} - \frac{s_0 E_L}{2} \cos(k_L x) \quad (1.53)$$

and the dimensionless units

$$\tilde{x} = \frac{x}{x_0}, \quad \tilde{p} = \frac{p}{p_0} \quad \text{and} \quad \tilde{t} = \frac{p_0 t}{m x_0} = \frac{t}{t_0}, \quad (1.54)$$

with the scalings

$$x_0 = k_L^{-1} \quad \text{and} \quad p_0 = p_{\text{sep}} = \sqrt{2m s_0 E_L} = \hbar k_L \sqrt{s_0}. \quad (1.55)$$

The scaled Hamiltonian is

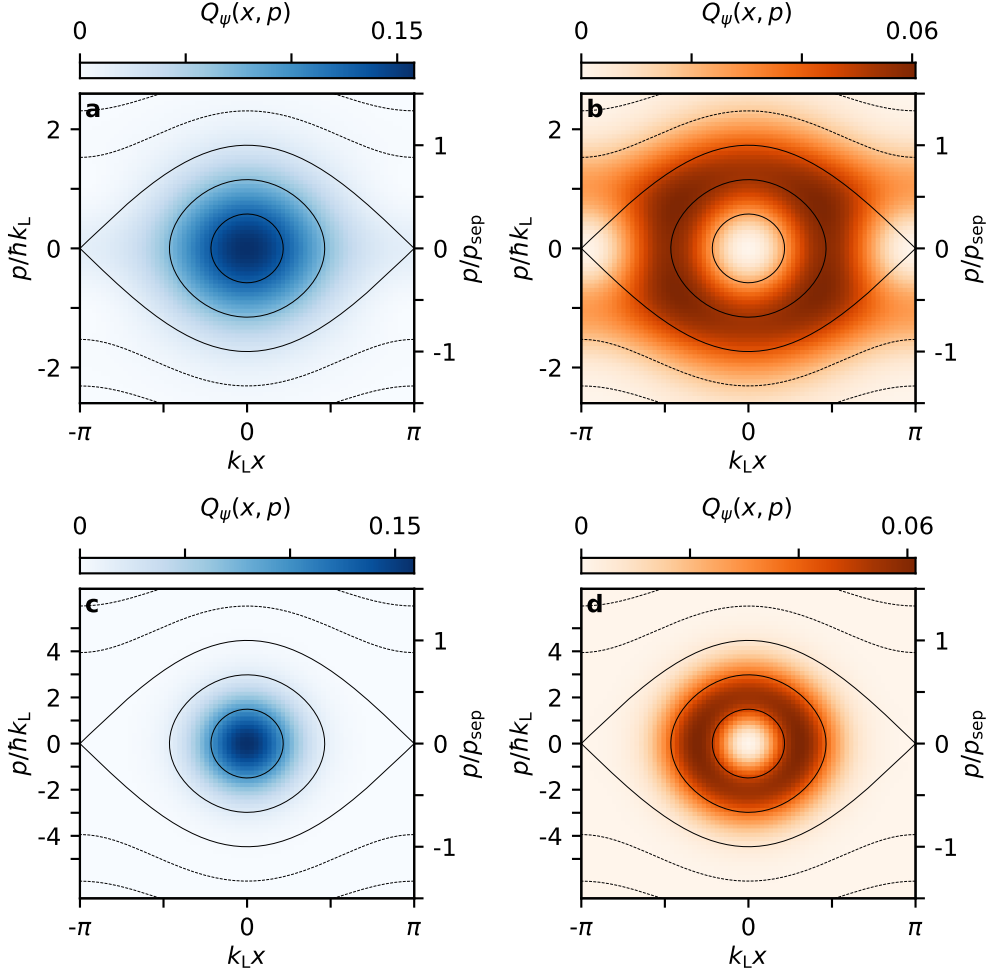


Figure 1.8 | Husimi representation of Bloch eigenstates in the phase space of the static sine potential (1.21). (a-b) Husimi representation $Q_\psi(x, p)$ of the first two Bloch eigenstates $|\psi\rangle = |\phi_{q,n=0,1}\rangle$ in a sine potential of depth $s_0 = 3$ at $q = 0$. (c-d) Same as (a,b) in a sine potential of depth $s_0 = 20$. The classical trajectories are plotted in black lines. Please note that two momentum axes are presented on each side of the panels: the first one on the left is in absolute units of $\hbar k_L$, and the second one on the right is relative to a given classical trajectory (in this case the separatrix, see Fig. 1.1). Having fixed here the *relative* momentum axes, classical trajectories are invariant under variation of the depth of the potential, whereas Husimi representations of the shown states display important differences, especially in extent. These scaling behaviors are embedded in the notion of the effective Planck constant (see text).

$$\tilde{H}(\tilde{x}, \tilde{p}) = \frac{\tilde{p}^2}{2} - \frac{1}{4} \cos(\tilde{x}) \quad (1.56)$$

with $\tilde{H} = Hm/p_0^2 = H/(2s_0 E_L)$. One can verify that the Hamilton equations (1.5) hold:

$$\frac{d\tilde{x}}{d\tilde{t}} = \frac{\partial \tilde{H}}{\partial \tilde{p}} \quad \text{and} \quad \frac{d\tilde{p}}{d\tilde{t}} = -\frac{\partial \tilde{H}}{\partial \tilde{x}}. \quad (1.57)$$

The resulting equations of motion describe the scaled classical dynamics for the Hamilto-

nian (1.56) which now depends on zero parameter. This demonstrates the scaling invariance of the classical dynamics (see Fig. 1.8). However, if we now consider the quantum dynamics, the scaled Schrödinger equation reads:

$$i \frac{\hbar}{x_0 p_0} \frac{\partial |\psi\rangle}{\partial \tilde{t}} = \left(\frac{\tilde{p}^2}{2} - \frac{1}{4} \cos(\tilde{x}) \right) |\psi\rangle \quad (1.58)$$

We see that the reduced Planck constant is scaled by an action parameter $S_0 = x_0 p_0$. This leads to define an effective Planck constant:

$$\hbar_{\text{eff}} = \frac{\hbar}{S_0}, \quad (1.59)$$

a tunable parameter that sets the typical extent of quantum states in the scaled phase space (Fig. 1.8), as well as the prevalence and timescales of quantum phenomena in the system (such as tunneling between the sites of the potential).

For the time-independent sine potential, we find in the end, with our choice of scaling,

$$\hbar_{\text{eff}} = \frac{1}{\sqrt{s_0}}. \quad (1.60)$$

Scaling of the time-independent sine potential

$$\begin{aligned} H(x, p) &= \frac{p^2}{2m} - s_0 \frac{E_L}{2} \cos(k_L x) \\ \rightarrow \tilde{H}(\tilde{x}, \tilde{p}) &= \frac{\tilde{p}^2}{2} - \frac{1}{4} \cos(\tilde{x}) \end{aligned} \quad (1.61)$$

with

$$\tilde{x} = k_L x, \quad \tilde{p} = \frac{p}{p_{\text{sep}}} = \frac{p}{\hbar k_L \sqrt{s_0}}, \quad \tilde{t} = 4\pi\nu_L \sqrt{s_0} t, \quad \text{and} \quad \tilde{H} = \frac{H}{2s_0 E_L}. \quad (1.62)$$

- The scaled classical dynamics does not depend on any parameter.
- The scaled quantum dynamics depends on

$$\hbar_{\text{eff}} = \frac{1}{\sqrt{s_0}}. \quad (1.63)$$

The same procedure can be followed to scale the dynamics of the periodically modulated sine potential (see p. 15). In this case, it is the frequency of modulation that tunes \hbar_{eff} , and thus the “quantumness” of the dynamics.

Scaling of the sine potential periodically modulated in depth and position

$$H(x, p, t) = \frac{p^2}{2m} - A(t) \times s_0 \frac{E_L}{2} \cos(k_L x + \varphi(t)) \quad \begin{array}{l} A(t+T) = A(t) \\ \varphi(t+T) = \varphi(t) \\ T = \nu^{-1} \end{array} \quad (1.64)$$

$$\rightarrow \tilde{H}(\tilde{x}, \tilde{p}, \tilde{t}) = \frac{\tilde{p}^2}{2} - A(\tilde{t}) \times \gamma \cos(\tilde{x} + \varphi(\tilde{t}))$$

with

$$\tilde{x} = k_L x, \quad \tilde{p} = \frac{T}{md} p, \quad \tilde{t} = \frac{2\pi}{T} t, \quad \text{and} \quad \tilde{H} = \frac{T^2}{md^2} H. \quad (1.65)$$

The classical dynamics depends on

$$A(\tilde{t}), \quad \varphi(\tilde{t}) \quad \text{and} \quad \gamma = s_0 \left(\frac{\nu_L}{\nu} \right)^2. \quad (1.66)$$

The quantum dynamics depends, in addition, on

$$\hbar_{\text{eff}} = 2 \frac{\nu_L}{\nu}. \quad (1.67)$$

One can vary \hbar_{eff} in a fixed scaled stroboscopic phase space (with a fixed γ (1.66)) by tuning ν and adjusting $s_0 = 4\gamma/\hbar_{\text{eff}}^2$ accordingly.

1.4.2 Floquet states representation in the phase space

In this final section, we combine the notions of stroboscopic phase portraits (Sec. 1.1.2), Floquet states (Sec. 1.3.2) and Husimi function (Sec. 1.4.1) to give an example of phase space representation of Floquet states. We define the semi-classical regime ($\hbar_{\text{eff}} \rightarrow 0$), in which the extent of the quantum states gets much smaller than the area of the regular islands in the stroboscopic phase portrait. In this regime, the Floquet states can be divided between states localized on regular islands and states spread over the chaotic sea [86, 87]. We illustrate this phenomenon in Fig. 1.9, in the case of the amplitude-modulated potential (Eq. (1.11)) and for a small value of \hbar_{eff} .

For finite values of \hbar_{eff} , coupling can occur between Floquet states, resulting in new states that can span both regular and chaotic regions of the phase space. This mechanism is discussed in Chap. 4, in which we determine optimal values of \hbar_{eff} for the transport of matter waves via a transporting regular island in the phase space. The quantum coupling between regular and chaotic regions of the phase space is also at the origin of chaos-assisted tunneling (CAT) [88, 89]. During my thesis, we made the first observations of CAT resonances [61] with matter waves. I do not present this work in this manuscript, as it is already detailed in previous theses, focusing on both the experimental [67, 68] and theoretical aspects [69] of the study. We however re-address this subject at the end of Chap. 3, where we apply a state-control protocol to the study of dynamical tunneling (of which CAT is a particular case).

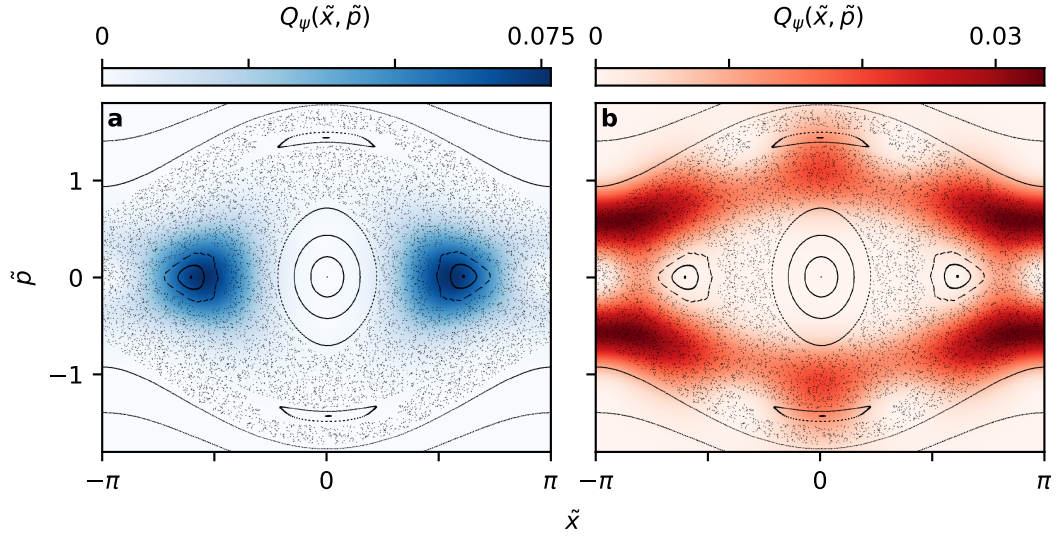


Figure 1.9 | Husimi representations of Floquet-Bloch states in the amplitude-modulated potential (1.11) with parameters $\gamma = 0.375$, $\varepsilon_0 = 0.24$ and $\hbar_{\text{eff}} = 0.2$. (a) A Floquet state localized on regular islands. (b) A Floquet state spread over the chaotic sea.

Conclusion

In this first chapter, I briefly introduced concepts and numerical tools for the study of wave functions in a time-periodic potential. During my thesis, I have worked with Bose-Einstein Condensates placed in a controllable one-dimensional optical lattice for the simulation of this system. The next chapter is dedicated to the presentation of the experiment.

Chapter 2 - Experimental setup

C'était l'époque des diodes, on en foutait sous tous les boutons, ça s'vendait comme des p'tits pains.

Karim Debbache (CROSSED - 11 - WarGames, 2013)

Contents

Introduction	39
2.1 Bose-Einstein condensation	39
2.2 Experimental sequence for Bose-Einstein condensation	40
2.2.1 Magneto-optical traps	41
2.2.2 Magnetic trapping and micro-wave evaporation	42
2.2.3 Dipole trapping and evaporation	43
2.2.4 Characterization of the hybrid trap at the end of the evaporative cooling	45
2.3 Observing the system	46
2.3.1 Absorption imaging	46
2.3.2 Time-of-flight	48
2.4 The one-dimensional optical lattice	49
2.4.1 Adiabatic loading of the lattice ground state	51
2.4.2 Optical lattice calibration	53
2.4.3 Band-mapping	55
Conclusion	57

Introduction

In the first chapter, we recalled elements of theory to study the dynamics of a wave function in a sine potential. In this chapter, we describe the ultracold atom setup used at LCAR to realize this system with Bose-Einstein condensates (BECs) of ^{87}Rb in a one-dimensional optical lattice. We start with a brief introduction on Bose-Einstein condensation. We then present our experimental sequence for the obtention of BECs and how we access the atomic momentum distribution. We conclude with a description of the optical lattice, its control, and common experimental techniques that are used in the experiments presented in the following chapters of this manuscript.

2.1 Bose-Einstein condensation

In this section, we briefly introduce concepts and quantities relative to Bose-Einstein condensation. For details and derivations of these results, see *e.g.* [90, 91].

Bose-Einstein condensation is a quantum phase transition first predicted for massive particles in seminal works of A. Einstein in 1924 [4] and 1925 [5]. In an ideal gas of N bosons, there exists a critical temperature T_C below which a macroscopic number N_0 of particles condenses into the ground state $|\psi_0\rangle$ of the trap in which they are confined. In the zero temperature limit (see below), all the particles indexed by i are in the ground state $|\psi_0\rangle$ of the system, and the BEC state is

$$|\Psi\rangle = \bigotimes_{i=1}^N |\psi_0^{(i)}\rangle. \quad (2.1)$$

In a gas of density n , the average distance between particles is $l = n^{-1/3}$. Bose-Einstein condensation occurs when the typical extent of the particle wave functions becomes of the order of l . For particles of mass m in a gas at temperature T , this typical wave function size is given by the thermal de Broglie wavelength

$$\Lambda_T = \sqrt{\frac{2\pi\hbar^2}{mk_B T}}, \quad (2.2)$$

with k_B the Boltzmann constant. The condition for Bose-Einstein condensation is thus $\Lambda_T \geq l$, and T_C is defined as the temperature under which this condition is met. In order to reach this regime, one needs to cool the gas while keeping the atomic density high enough for Λ_T to become greater than l .

For a dilute (see below) gas of N bosons in a three-dimensional harmonic trap with average frequency $\bar{\Omega} = (\Omega_x\Omega_y\Omega_z)^{1/3}$, it can be shown [90] that, in the semi-classical limit where $k_B T \gg$

$\hbar\Omega_j$ (with $j = x, y, z$; *i.e.* when the level spacing in the harmonic potential is much smaller than the thermal energy), T_C is approximately given by:

$$k_B T_C \approx 0.94 \hbar \bar{\Omega} N^{1/3}, \quad (2.3)$$

with a number of condensed atoms

$$N_0(T) \approx N \left[1 - \left(\frac{T}{T_C} \right)^3 \right], \quad \text{for } T < T_C. \quad (2.4)$$

The experimental setup presented in this chapter produces BECs of $N \approx 5 \cdot 10^5$ atoms in a three-dimensional harmonic trap with average angular frequency $\bar{\Omega} \approx 2\pi \times 36$ Hz (see Sec. 2.2.4). From Eq. (2.3), the critical temperature is approximately

$$T_C \approx 130 \text{ nK}. \quad (2.5)$$

Working at temperatures $T \lesssim T_C$, the above-mentioned semi-classical limit is valid, since $\hbar\bar{\Omega}/k_B \sim 1$ nK.

Experimentally, Bose-Einstein condensation was first achieved in 1995, more than 70 years after its prediction, in the group of E. Cornell and C. Wieman with ^{87}Rb [6] and in the group of W. Ketterle with ^{23}Na [7]. In 2001, they were awarded the Nobel Prize in Physics for this experimental achievement. Since then, the number of research groups working with quantum gases has exploded [92].

The version of the experimental setup used for the studies presented in this manuscript is in operation at LCAR since 2016. Previous PhD students of the group have extensively detailed in their thesis [93, 94, 67, 68] the construction of the experiment as well as the physics behind the different cooling steps towards Bose-Einstein condensation. In this manuscript, I choose to simply list the steps that compose the cooling sequence, with brief descriptions and updated key figures. During my thesis, we modified the geometry of the dipole trap in which the BECs are finally obtained. In the corresponding section (Sec. 2.2.3), I describe and characterize this new configuration.

2.2 Experimental sequence for Bose-Einstein condensation

We start with a vapor of Rb atoms in a vacuum chamber [93]. Our atomic cooling sequence for the obtention of BECs is composed of three main phases:

(2.2.1) - an initial cooling stage in magneto-optical traps,

(2.2.2) - a first step of forced evaporation, by selectively inducing micro-wave transitions in a strong magnetic gradient,

(2.2.3) - a second step of forced evaporation in a dipole trap (with a remaining low magnetic gradient).

In the section dedicated to each phase, we begin with general considerations about the cooling process involved, followed by a paragraph with specific experimental details.

Note on evaporative cooling. The last two cooling steps are based on evaporative cooling [95, 96]: through elastic collisions in a trap of given depth, particles sometimes acquire enough energy to leave the trap, so the total energy of the gas decreases. Further elastic collisions lead to the thermalization of the ensemble at a lower temperature. In the experiment, we perform forced evaporation, which consists in actively facilitating the loss of the most energetic atoms (see Secs. 2.2.2 and 2.2.3). In our case, given the relatively low energy of the colliding bosons, collisions occur in s -waves [90, 97, 68]. In this case, the cross section of collisions is $\sigma = 8\pi a_s^2$, where the s -wave scattering length a_s describes the effective range of inter-particle interaction¹. Furthermore, we work in the regime of dilute Bose gases, meaning that the average distance between particles is much larger than the s -wave scattering length ($na_s^3 \ll 1$).

2.2.1 Magneto-optical traps

A magneto-optical trap (MOT) combines Doppler cooling, with laser beams slightly red-detuned from an atomic resonance, and Zeeman shifts induced by a magnetic field gradient to create a non-conservative trap in which the atoms are cooled and confined [90, 100]. We work with the D₂ line² of ⁸⁷Rb, between the two atomic levels 5²S_{1/2} and 5²P_{3/2}. The cooling transition is between the states $|F = 2\rangle \rightarrow |F' = 3\rangle$ and this two-state cycle is closed by a repumping beam tuned on the $|F = 1\rangle \rightarrow |F' = 2\rangle$ transition.

Experimental details. Our MOT setup is composed of a two-dimensional MOT (made by the SYRTE lab (Paris)) that feeds a home-made three-dimensional MOT at the center of a rectangular glass cell. For the 3D MOT, the intensity of the six cooling beams is ~ 2 mW/cm², and a magnetic field gradient of $b' \approx 13$ G/cm is created by two coils (located on the cell sides [93], along the x axis of the cell shown in Fig. 2.1) in which current flows in opposite directions. The 3D MOT is loaded during 5 s, and we get³ a cloud of $N \sim 4 \cdot 10^9$ atoms at $T \sim 400$ μ K. After a dark MOT [101, 67] and an optical molasses [102, 90, 67], we shut down

¹For the atomic state in which the atoms are when we perform evaporative cooling (see below), we have $a_s \approx 5.23$ nm [98, 99].

²We present details of this line in App. A. For more information, see [99].

³The amount of atoms in the MOT saturates absorption images (see Sec. 2.3) and these numbers are estimates. Reliable references are taken for a shortened 3D MOT loading time. After 1 s (instead of 5), we have $N \approx 1.9 \cdot 10^9$ atoms at $T \approx 300$ μ K

the magnetic gradient and the repumping beams for 5 ms. The atoms accumulate in the three m_F levels of the state $|F = 1\rangle$. At this stage, we have $N \sim 4 \cdot 10^9$ atoms at $T \lesssim 100 \mu\text{K}$.

2.2.2 Magnetic trapping and micro-wave evaporation

The second cooling step consists in capturing the atoms in a quadrupole magnetic trap and selectively transferring the most energetic atoms toward a non-trapped state [95, 103]. In a magnetic field $\mathbf{B}(\mathbf{r})$, an atom in the state $|F, m_F\rangle$ experiences the potential

$$U_{\text{mag}}(\mathbf{r}) = g_F m_F \mu_B |\mathbf{B}(\mathbf{r})|, \quad (2.6)$$

where g_F is the Landé g -factor (dependent on the state considered, see App. A) and $\mu_B = 9.27 \cdot 10^{-24} \text{ J/T}$ is the Bohr magneton. We generate a magnetic quadrupole field (see below), which near the field zero can be written as

$$\mathbf{B}(x, y, z) = b' \begin{pmatrix} x/2 \\ y/2 \\ -z \end{pmatrix}. \quad (2.7)$$

with gravity along $-\mathbf{e}_z$. The atoms that we capture are in the low-field-seeking state $|F = 1, m_F = -1\rangle$ (with $g_F = -1/2$ for $F = 1$), and we work with the transition toward the non-trapped high-field-seeking state $|F = 2, m_F = -1\rangle$ (with $g_F = 1/2$ for $F = 2$). In the absence of magnetic field, the micro-wave frequency associated with this transition is $\nu_0 \approx 6.835 \text{ GHz}$ [99]. As in the MOT, the gradient of the quadrupole makes the energy levels of the different m_F states spatially dependent. This allows us to tune the frequency of the micro-waves shone on the atoms to only induce the transition at a controlled distance from the center of the trap, in regions only explored by the most energetic atoms. This forced evaporation, followed by a subsequent thermalization, causes the temperature of the atom cloud to decrease, as described above (p. 41).

Experimental details. This second phase happens in a conservative quadrupole trap produced by three pairs of water-cooled coils in the anti-Helmholtz configuration where current⁴ flows in opposite direction. They are located above and below the glass cell [93], along the z axis of the cell (Fig. 2.1). The coils withstand 160 A of current, which corresponds to a total maximum gradient of $\approx 300 \text{ G/cm}$. Among the atoms falling from the 3D MOT, only the ones in the low-field-seeking state $|F = 1, m_F = -1\rangle$ are captured⁵. To match the size of the expanding cloud falling during 5 ms from the 3D MOT, the initial gradient of magnetic field is set to $\approx 60 \text{ G/cm}$. A compensation coil allows to adjust the position of the magnetic field zero along the y

⁴The six coils are powered by six SM 15-200D supplies by Delta Elektronika.

⁵As Bose-Einstein condensation is achieved reliably on the experiment, increasing the number of atoms captured in the quadrupole trap through spin polarization is not required.

axis of the cell (Fig. 2.1). In 500 ms, we load $1.2 \cdot 10^9$ atoms at a temperature that has increased to $T \approx 170 \mu\text{K}$. To increase the interatomic collision rate for the evaporation, we compress adiabatically the cloud by ramping the gradient of magnetic field to $\approx 250 \text{ G/cm}$ in 200 ms. The temperature rises to $T \approx 220 \mu\text{K}$. During 8.5 s, we then shine micro-waves on the atoms, at a frequency swept from 6.720 to 6.818 GHz⁶. At this stage, we have $N \approx 7 \cdot 10^7$ atoms at $T \approx 40 \mu\text{K}$.

Majorana losses [90, 93] near the magnetic field zero at the center of the quadrupole (2.7) prevent us from pushing the cooling further with this method. The final cooling step is then performed in an optical dipole trap.

2.2.3 Dipole trapping and evaporation

For the third and final cooling stage, the atoms are loaded in an optical dipole trap. The dipole force results from the interaction between an atom and a light beam of inhomogeneous intensity, which is *far-detuned* from an atomic transition. Considering a light beam of intensity $I(\mathbf{r})$ and optical frequency ν , the dipole potential [8, 79] experienced by the atom is proportional to $I(\mathbf{r})$ and inversely proportional to the frequency detuning $\Delta = \nu - \nu_0$ (where ν_0 is the frequency associated to the atomic transition considered):

$$U_{\text{dip}}(\mathbf{r}) \propto \frac{I(\mathbf{r})}{\Delta}. \quad (2.8)$$

Depending on the sign of Δ , the resulting dipole force $\mathbf{F} = -\nabla V(\mathbf{r})$ is either attractive or repulsive. In the experiment, we work with linearly polarized Gaussian beams (see below) of wavelength $\lambda = 1064 \text{ nm}$, *i.e.* red-detuned from the D_2 line of ^{87}Rb ($\lambda_0 \approx 780.2 \text{ nm}$, see App. A). This creates an attractive force towards the intensity maxima. In this situation, Eq. (2.8) becomes $U_{\text{dip}}(\mathbf{r}) = \zeta I(\mathbf{r})$, with $\zeta \approx -2.1 \cdot 10^{-36} \text{ J}/(\text{W}/\text{m}^2)$ [104]. Finally, the intensity of a Gaussian beam propagating along the x axis is:

$$I(x, y, z) = \frac{2P}{\pi w^2(x)} \exp\left\{-\frac{2(y^2 + z^2)}{w^2(x)}\right\}, \quad (2.9)$$

where P is the power of the beam and $w(x)$ is the distance to the x axis at which the intensity is $1/e^2$ times its value on the axis⁷. The end of the evaporation takes place in a dipole trap made of crossing red-detuned laser beams, whose powers are decreased in time to force the evaporation [93].

⁶For the generation of the micro-wave, see [93]. The final frequency $\nu_f = 6.818 \text{ GHz}$ cuts the depth of the quadrupole trap to $h|\nu_f - \nu_0| \approx k_B \times 580 \mu\text{K}$, with h the Planck constant and $\nu_0 = 6.83 \text{ GHz}$ the frequency associated to the transition between the levels in the absence of magnetic field (*i.e.* in the center of the trap).

⁷This distance is $w(x) = w_0 \sqrt{1 + \left(\frac{x}{x_R}\right)^2}$, with w_0 the beam waist and $x_R = \pi w_0^2 / \lambda$ the Rayleigh length.

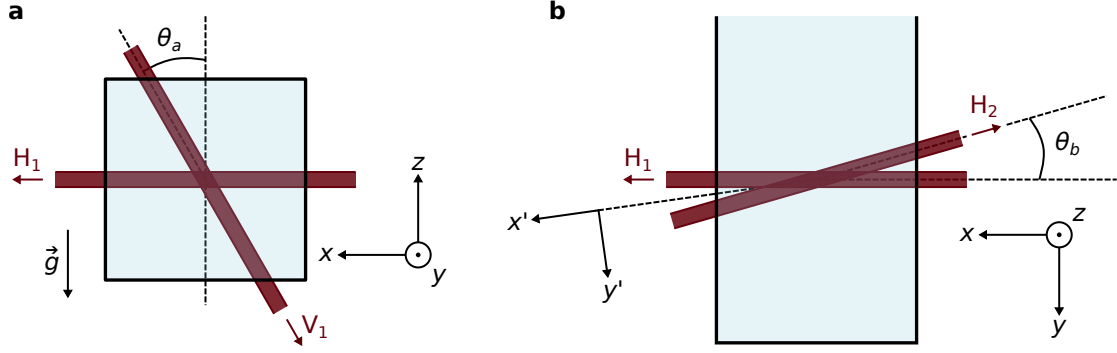


Figure 2.1 | Sketch of the old and new dipole beam geometries. The dark red rectangles represent the dipole beams and the pale blue rectangle represents the glass cell (neither the beam sizes nor their divergence is to scale with the size of the cell). To prevent reflections, the incidence angle of the horizontal beam H_1 on the uncoated cell is $\sim 1^\circ$ [93]. **(a)** Old geometry illustrated with an axial section of the cell. The angle between the recycled vertical beam V_1 and the z axis was $\theta_a \approx 30^\circ$. **(b)** New geometry illustrated in the horizontal plane. The angle between the two independent horizontal beams H_1 and H_2 is $\theta_b \approx 16^\circ$, so the principal axes x' and y' of the resulting trap make an angle $\theta' \approx 8^\circ$ with x and y .

Experimental details. After the micro-wave evaporation, we decompress the cloud by lowering the magnetic gradient from $b' \approx 250$ G/cm to $b' \approx 22$ G/cm in 1.1 s. This final gradient compensates approximately 72% of gravity, and the atoms slowly fall into a dipole trap positioned approximately $200 \mu\text{m}$ below the center of the quadrupole [17]. The dipole trap is made of two crossed Gaussian beams⁸ of wavelength $\lambda = 1064$ nm. Figure 2.1 shows the previous and new geometries of the dipole trap.

Previous configuration - An horizontal beam H_1 (with waist $w_0 = 75 \mu\text{m}$ and initial power $P_0 = 10.3$ W) went through the cell a first time. It was recycled into a vertical beam V_1 ($w_0 = 35 \mu\text{m}$, $P_0 = 6$ W) that went back through the cell in its (x, z) plane from top to bottom. This recycled beam made an angle $\theta \approx 30^\circ$ with the vertical axis. In this recycled configuration, only the intensity of H_1 was locked with a PID⁹ controller acting on the power of the radio-frequency (RF) driving the acousto-optic modulator (AOM) of this beam.

New configuration - Two independent beams $H_{1,2}$ ($w_0 = 45 \mu\text{m}$, $P_0 = 4$ W) intersect in the horizontal plane with an angle $\theta \approx 16^\circ$. The reasons for the change are an increased volume for the dipole trap as well as the ability to independently diagnose the individual effect of the two beams on the atoms (which was impossible in the recycled configuration). In this configuration, both the intensities of H_1 and H_2 are controlled with PIDs. To minimize the reflection on the uncoated cell, the polarization of both beams is horizontal (*i.e.* in the (x, y) plane of the cell). To prevent interferences between the beams, we work with opposite AOM diffraction orders ± 1 to detune the beams frequencies by about 80 MHz (see App. B for details).

⁸See App. B for technical details and the optical diagram for the preparation of the dipole beams.

⁹PID: proportional–integral–derivative

We load $N \approx 1.2 \cdot 10^7$ atoms at $T \approx 40 \mu\text{K}$ into the resulting hybrid trap (composed of the dipole trap, the magnetic trap and gravity). We force the evaporation by lowering the power of the dipole beams using the smooth power law [105]

$$P(t) = P_0 \left(1 + \frac{t}{\tau}\right)^{-\alpha}, \quad (2.10)$$

with $\tau = 1.75$ s and $\alpha = 4$. After 5.4 s of evaporation, the depth of the dipole trap is reduced by a factor $P_0/P_f \approx 275$ and Bose-Einstein condensation is achieved. The experiment produces BECs of $N \approx 5 \cdot 10^5$ ^{87}Rb atoms¹⁰ in the lowest hyperfine level $|F = 1, m_F = -1\rangle$ every 22 s. Such a BEC is shown in Fig. 2.2(c).

2.2.4 Characterization of the hybrid trap at the end of the evaporative cooling

At the end of the evaporative cooling, the BEC is in a hybrid trap made of

- the two dipole beams with powers $P_f \approx 20$ mW,
- the quadrupole (2.7) with a magnetic gradient $b' \approx 22$ G/cm and whose center is located approximately 200 μm above the crossed dipole trap,
- the gravitational potential.

We locally approximate this hybrid trap with the three-dimensional harmonic potential

$$U_{\text{hyb}}(x', y', z) \simeq \frac{1}{2}m [\Omega_{x'}^2(x')^2 + \Omega_{y'}^2(y')^2 + \Omega_z^2 z^2], \quad (2.11)$$

where $(x', y', z) = (0, 0, 0)$ is the center of the crossed dipole trap and the primed x' and y' lie along the principal axes of the trap, *i.e.* at an angle $\theta' \approx 8^\circ$ with x and y (see Fig. 2.1(b)). To measure the angular frequencies Ω_j , we trigger out-of-equilibrium evolutions¹¹ and measure the periods of oscillation in the corresponding directions (we present the method for the observation of the system in the next section 2.3). We find

$$\Omega_{x'} = 2\pi \times (10.4 \pm 0.2) \text{ Hz}, \quad (2.12)$$

$$\Omega_{y'} = 2\pi \times (68 \pm 4) \text{ Hz},$$

$$\Omega_z = 2\pi \times (66 \pm 2) \text{ Hz},$$

with an average angular frequency $\bar{\Omega} = (\Omega_x \Omega_{y'} \Omega_{z'})^{1/3} \approx 2\pi \times 36$ Hz.

¹⁰For information, we made BECs of up to $N = 2 \cdot 10^5$ atoms every 30 s with the previous dipole trap geometry.

¹¹We make three independent experiments where we trigger oscillations by pulsing current into coils approximately placed along the right axis, *i.e.* one of the 3D MOT coils to measure $\Omega_{x'}$, the compensation coil for $\Omega_{y'}$ and one of the magnetic trap coils for Ω_z (see Sec. 2.2).

Life time in the hybrid trap and reduction of the number of atoms in the BECs. We measure the life time in the hybrid trap by monitoring the number of atoms (see following section) in the hybrid trap during a holding time at the end of the evaporation. During this holding time, we observe a spontaneous evaporation leading to an exponential decrease of the number of atoms in the BECs. We measure a characteristic time of $\tau \approx 20$ s for this exponential atomic loss. This method can be used to artificially reduce the number of atoms in the BECs for experiments that require a control on that parameter. This is the case in Sec. 3.4 and 5.

2.3 Observing the system

2.3.1 Absorption imaging

In this section, we explain how we access the atomic density distribution using absorption imaging. Its principle is the following: in due time, we illuminate the atoms with a laser beam that is resonant with an atomic transition and light is absorbed. From the shadow of the cloud, we determine its position and size (Fig. 2.2). The number of atoms in the cloud is deduced from the fraction of light absorbed.

As depicted in Fig. 2.2, we consider a resonant beam traveling along a fictitious z axis. In the regime where the beam intensity is low compared to the atomic saturation intensity, the intensity that remains after passing through the cloud is given by the Beer-Lambert law:

$$I_{\text{out}}(x, y) = I_{\text{in}}(x, y) e^{-\sigma_0 n_c(x, y)} \quad (2.13)$$

where $I_{\text{in}}(x, y)$ is the initial intensity, σ_0 is the cross section of absorption and $n_c(x, y) = \int n(x, y, z) dz$ is the atomic column density traversed by the light. By taking pictures with and without atoms, we respectively access $I_{\text{out}}(x, y)$ and $I_{\text{in}}(x, y)$. From Eq. (2.13), the column density simply reads

$$n_c(x, y) = \frac{1}{\sigma_0} \text{OD}(x, y), \quad (2.14)$$

with the optical density $\text{OD}(x, y) = \ln\{I_{\text{in}}(x, y)/I_{\text{out}}(x, y)\}$. The number of atoms in a cloud is $N = \iint n_c(x, y) dx dy$. On the example of Fig. 2.2(c), we measure a BEC of $N = 5.11 \cdot 10^5 \pm 3\%$ atoms over 10 realizations (where the uncertainty corresponds to one standard deviation of the statistics).

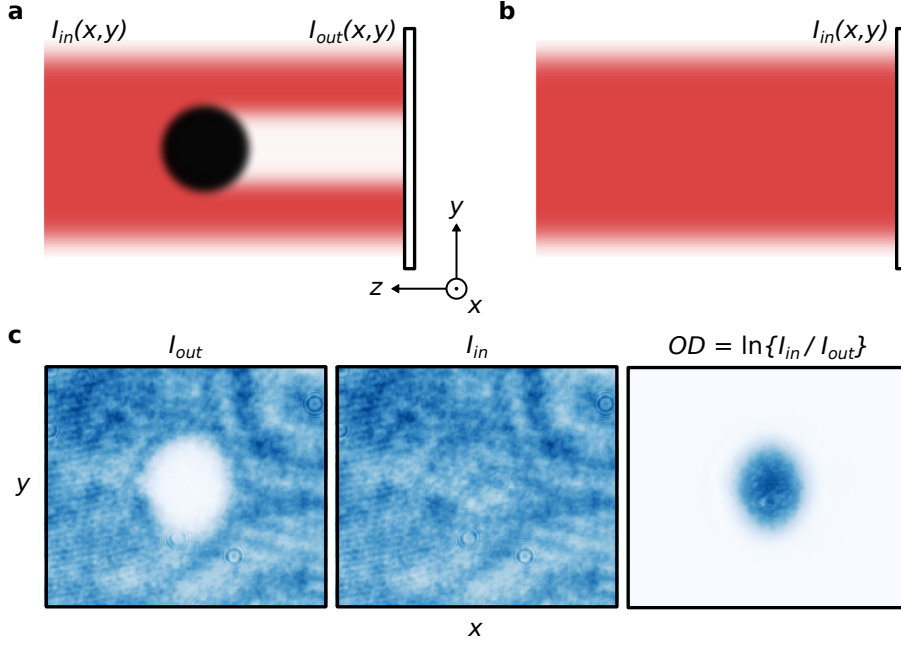


Figure 2.2 | Schematic of absorption imaging. (a) We illuminate the atom cloud (black disk) with a resonant beam (red area), light is absorbed (white area) and $I_{out}(x, y)$ is measured by taking an image on the screen (thin white rectangle). (b) $I_{in}(x, y)$ is measured by taking an image shortly after without the cloud. (c) Experimental example of $I_{in}(x, y)$, $I_{out}(x, y)$ and the resulting optical density when performing the absorption image of a BEC after a 35 ms time-of-flight (see Sec. 2.3.2). The coordinate system (x, y, z) is that of the imagery axis and does not correspond to the coordinate system of the cell (see Fig. 2.3). Figure inspired from [69].

Experimental details. The frequency of the imaging beam is tuned on the transition $|F = 2\rangle \rightarrow |F' = 3\rangle$ (*i.e.* the cooling transition in the MOT, see Sec. 2.2.1 and App. A). We recall that, after the MOT stage, the atoms are in the state $|F = 1\rangle$. Before imaging the cloud, we repump the atoms in the state $|F = 2\rangle$ by shining the repumping beam for a few ms. For ^{87}Rb atoms equally distributed in the five m_F levels of this state and an imaging beam with linear polarization and wavelength $\lambda \approx 780$ nm, the cross section of absorption is $\sigma_0 \approx 0.136 \mu\text{m}^2$ [61]. To correct imperfections (extraneous light, defaults on the optical path, etc.), we take three images¹²: (i) a first image with the atoms and the imaging beam (I_{atoms}), (ii) an image of the imaging beam without the atoms (I_{beam}) and (iii) a background image ($I_{background}$) without the beam. We compute the OD with $I_{in} = I_{beam} - I_{background}$ and $I_{out} = I_{atoms} - I_{background}$. Figure 2.2(c) shows examples of I_{in} , I_{out} and the resulting OD when performing the absorption image of a BEC after time-of-flight (see Sec. 2.3.2).

Three imaging setups (see Fig. 2.3) are installed on the experiment to observe the atoms along different axes during the experimental sequence:

¹²Images are taken using a CCD camera A102f from Basler. The screen is made of 1392×1040 square pixels with side $6.45 \mu\text{m}$. The signal is a photoelectron count per pixel proportional to the imaging beam intensity at that point.

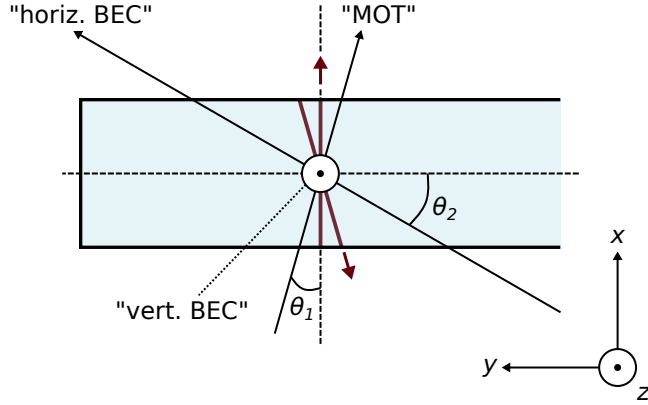


Figure 2.3 | Imaging axes in the horizontal plane (with a 90° rotation from Fig. 2.1(b)). The identified angles are $\theta_1 \approx 16^\circ$ and $\theta_2 \approx 30^\circ$. The “vert. BEC” imaging beam goes through the dipole cross from the bottom to the top of the cell. The red lines and arrows indicate the crossed dipole trap with the direction of propagation of the beams and the pale blue rectangle represents the cell (not to scale).

- the “MOT” axis, in the horizontal plane, with magnification $M \approx 0.33$,
- the “horizontal BEC” axis, in the horizontal plane, with magnification $M \approx 2.5$,
- the “vertical BEC” axis, with magnification $M \approx 4.2$. This axis was added during my thesis to visualize the new crossed dipole trap.

Every experimental image presented in this manuscript is taken with the “horizontal BEC” imaging axis.

2.3.2 Time-of-flight

The observation of the atoms in the experiment is generally performed after a time-of-flight (TOF): after a sudden switch-off of all trapping potentials, the atom cloud starts to fall due to gravity, with a constant expansion in the center of mass frame that carries information on the *in situ* velocity distribution. We take an absorption image after a time t_{TOF} .

For a thermal atomic ensemble ($T \gg T_c$, see Sec. 2.1) described by the Maxwell-Boltzmann statistics, the standard deviation of the cloud size along a given axis x following a TOF is

$$\Delta x(t_{\text{TOF}}) = \sqrt{\Delta x_0^2 + (\Delta v_x t_{\text{TOF}})^2}. \quad (2.15)$$

with Δx_0 and Δv_x the *in situ* standard deviations of the position and velocity respectively. By measuring the expansion of a thermal cloud as t_{TOF} increases, Eq. (2.15) allows to access the cloud temperature T , as the slope of $\Delta x^2(t_{\text{TOF}}^2)$ is proportional to T according to the equipartition theorem:

$$\frac{1}{2}m\Delta v_x^2 = \frac{1}{2}k_B T. \quad (2.16)$$

Moreover, after sufficiently long TOF ($t_{\text{TOF}} \gg \Delta x_0/\Delta v_x$), one can neglect the initial size of the cloud, and the final density distribution reflects directly the velocity distribution of the cloud before the TOF.

For quantum gases, TOF imagery allows to dilute the clouds whose observation is made difficult by their small size and high optical density. In a similar way as for the thermal case, one measures a momentum density of probability when observing the system after a sufficiently long ballistic TOF. For a BEC composed of atoms condensed in the state $|\psi\rangle$, one even statistically samples $|\langle p|\psi\rangle|^2$ in a single TOF measurement of the system (see for instance next section 2.4).

2.4 The one-dimensional optical lattice

In this last section, we describe our one-dimensional optical lattice and introduce experimental methods that we frequently use in the rest of this manuscript to study matter waves dynamics in the optical lattice.

An optical lattice is a periodic dipole potential (Eq. (2.8)) resulting from a spatially periodic variation of light intensity. Our one-dimensional optical lattice results from the interference of two Gaussian beams (Eq. (2.9)) with the same wavelength and linear polarization, that are counterpropagating along the x axis (see below). Neglecting the divergence of the beams¹³, their electric fields along the x axis are the real part of the phasors

$$\underline{\mathbf{E}}_1(x, t) = \underline{E}_0 e^{i(-kx - \omega t - \varphi_1)} \mathbf{e}_\perp \quad \text{and} \quad \underline{\mathbf{E}}_2(x, t) = \underline{E}_0 e^{i(kx - \omega t - \varphi_2)} \mathbf{e}_\perp, \quad (2.17)$$

where $k = 2\pi/\lambda$ is the wavenumber of the laser beams and \mathbf{e}_\perp is a constant unitary vector in the (y, z) plane. The light intensity resulting from the interference of these fields is proportional to the square modulus of the total field $\underline{\mathbf{E}} = \underline{\mathbf{E}}_1 + \underline{\mathbf{E}}_2$:

$$\begin{aligned} I(x) &\propto |\underline{\mathbf{E}}(x, t)|^2 = 4 |\underline{E}_0|^2 \cos^2\left(kx + \frac{\varphi}{2}\right) \\ &= 2 |\underline{E}_0|^2 \cos\left(\frac{2\pi x}{\lambda/2} + \varphi\right) + 2 |\underline{E}_0|^2 \end{aligned} \quad (2.18)$$

with $\varphi = \varphi_1 - \varphi_2$ the phase difference between the beams. We see that the step of the periodic variation of intensity is $d = \lambda/2$. Dropping the constant term that stems from the linearization of the quadratic cosine, we finally get the attractive dipole potential for the lattice

¹³*e.g.* near the focal point, for values of x small compared to the Rayleigh length x_R of the beams (see below).

$$V(x) = -\frac{V_0}{2} \cos(k_L x + \varphi), \quad (2.19)$$

where we used the wave number of the periodic potential $k_L = 2\pi/d$ defined in Chap. 1. V_0 is proportional to the maximum intensity of the lattice standing wave of Eq. (2.18). Controlling the intensity and the relative phase φ of the interfering beams, we get the sine potential studied in Chap. 1:

$$V(x, t) = -A(t) \times s_0 \frac{E_L}{2} \cos(k_L x + \varphi(t)). \quad (2.20)$$

Experimental details. We here briefly present the experimental implementation of this controlled one-dimensional optical lattice. Technical details and the optical diagram for the preparation of the beams can be found in App. C. The two beams for the lattice are obtained from the same laser source with wavelength $\lambda = 1064$ nm. They are counterpropagating along the x axis of the cell and focused on the crossed dipole trap, with waist $w_0 = 150$ μm and a maximum power $P = 2.3$ W. Using four synchronized arbitrary waveform generators and three AOMs (see App. C), we are able to continuously control $A(t)$ and $\varphi(t)$ in Eq. (2.20).

We remark that, by only controlling the intensity of the lattice beams, we have $0 \leq A(t) \leq s_{\text{max}}/s_0$ in Eq. (2.20), where s_{max} is the maximum lattice depth achievable ($s_{\text{max}} \approx 40$ for our setup).

Given the atomic mass m of ^{87}Rb and the lattice spacing d :

$$m \approx 1.443 \cdot 10^{-25} \text{ kg} \quad \text{and} \quad d = \lambda/2 = 532 \text{ nm}, \quad (2.21)$$

we evaluate the characteristic lattice quantities defined in the previous chapter (sec. 1.2):

- $k_L = 2\pi/d \approx 11.81 \cdot 10^6 \text{ m}^{-1}$,
- $E_L = \hbar^2 k_L^2 / 2m \approx 5.375 \cdot 10^{-30} \text{ J}$,
- $\nu_L = E_L/h \approx 8111.3 \text{ Hz}$.

Our one-dimensional optical lattice constrains the dynamics along the x axis into lattice sites associated with the harmonic oscillator frequency $\nu = \sqrt{s_0} \nu_L$ (see Sec. 1.4.1). This frequency is to be compared with the frequencies (2.12) of the three-dimensional hybrid trap in which the atoms are held. We see that, regardless the lattice depth, the typical timescales for the dynamics in the lattice ($T \approx 123 \mu\text{s}/\sqrt{s_0}$) are much smaller than the timescales in the hybrid trap ($T_j = 2\pi/\Omega_j > 15$ ms). As the typical duration of the experiments presented in this manuscript is ~ 1 ms, the dynamics along the x axis is uncoupled from the dynamics along the perpendicular axes, which allows us to assume a one-dimensional system in our studies. In

particular in the following, we consider along the x axis only the shared wave function (2.1) of a BECs evolving in the time-dependent Bloch system (2.20), *i.e.* Bloch waves (see Chap. 1)

$$\psi_q(x, t) = \sum_{\ell \in \mathbb{Z}} c_{q, \ell}(t) |\chi_{\ell+q/k_L}\rangle, \quad (2.22)$$

with the plane waves defined in Sec. 1.2.1 as $\langle x | \chi_{\ell+q/k_L} \rangle = e^{i(\ell k_L + q)x} / \sqrt{d}$.

We now present a series of established experimental techniques when working with ultracold atoms in optical lattices.

2.4.1 Adiabatic loading of the lattice ground state

The first technique we present is a protocol to load the ground state of the static lattice. For a given lattice depth s_0 , this state is the Bloch eigenstate $|\phi_{q=0, n=0}^{(s_0)}\rangle$ associated to the lowest eigenenergy $E_{q=0, n=0}^{(s_0)}$ (see Sec.1.2.1). Initially, the BEC state is the resting plane wave that corresponds to the ground state of a lattice of null depth $|\chi_0\rangle = |\phi_{0,0}^{(s_0=0)}\rangle$, and we want to drive this state to $|\phi_{0,0}^{(s_0)}\rangle$. One can do so adiabatically¹⁴ by ramping up the lattice depth s_0 with a timescale τ much larger than the largest timescales of the system given its energy levels [106]. This smallest timescale is the period associated to the transition towards the plane waves of second lowest kinetic energy $|\chi_{\pm 1}\rangle$, which have an energy difference E_L with the BEC. The timescale in comparison to which the lattice loading needs to be slow is $h/E_L = \nu_L^{-1} \approx 123 \mu\text{s}$. To this end, we ramp up the lattice depth $s(t) = A(t) \times s_0$ with the smooth amplitude function

$$A(t) = (\kappa + 1) \left(\frac{t}{\tau}\right)^\kappa - \kappa \left(\frac{t}{\tau}\right)^{\kappa+1}. \quad (2.23)$$

Experimentally, we use the characteristic loading time $\tau = 1 \text{ ms}$ (sufficiently large in comparison to h/E_L) and slope parameter $\kappa = 11$. The lattice depth follows the loading curve (2.23) during the interval $0 \leq t \leq t_{\text{load}} = \tau$, such that $0 \leq A(t) \leq 1$.

We show in Fig. 2.4 an experiment of adiabatic lattice loading. The matter wave diffraction observed in Fig. 2.4(e) illustrates how the TOF measurement of BEC in an optical lattice (*i.e.* a Bloch wave (2.22)) amounts to sampling its momentum distribution: during the TOF expansion, the planes waves separate into spatially resolved momentum components¹⁵, with a momentum difference $\Delta p = \hbar k_L = h/d$. When we shine the imaging beam, an atom is measured in the plane wave ℓ with probability $|c_{q, \ell}|^2$, which we access by measuring the fraction of atoms in the ℓ^{th} momentum component. In the specific case of Fig.2.4, we adiabatically load the ground state of the lattice, and we see that the relative atomic populations in the momentum orders are in

¹⁴The term ‘‘adiabatic’’ must be understood in the quantum sense of an eigenstate follow-up as a parameter of the system is varied. On the other hand, a diabatic process projects the initial state onto several non-degenerate eigenstates of the final system.

¹⁵In the form of diffraction orders that we often refer to as ‘‘momentum orders’’.

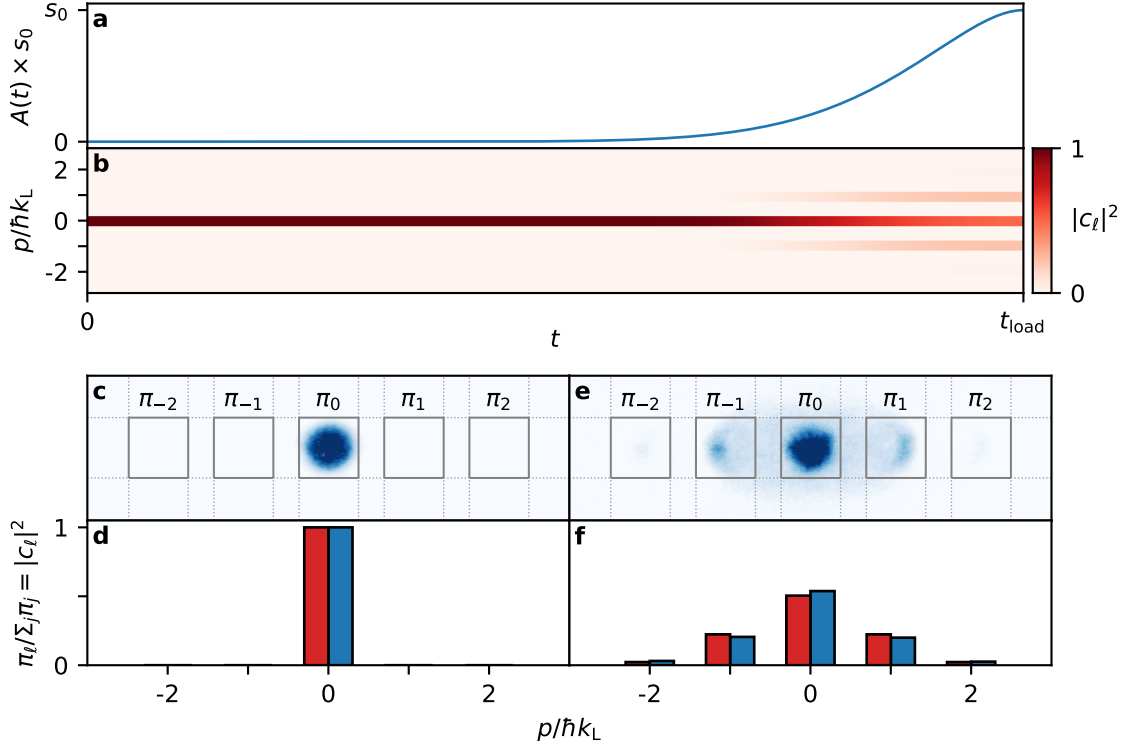


Figure 2.4 | Adiabatic lattice loading and matter wave diffraction. (a) Lattice depth curve (2.23) to adiabatically load the ground state of the lattice of depth s_0 (see text). (b) Numerical simulation of the lattice loading showing the momentum distribution as a function of time. (c) Experimental TOF absorption image of the BEC before loading the lattice. The grey rectangles delimit the regions in which the plane wave populations are extracted (see (e), Sec. 2.3 and text for details). (d) Bar diagram comparing the experimental (blue) and numerical (red) plane wave populations (*i.e.* momentum distribution). (e) Experimental TOF absorption image at the end of the loading. (f) Experimental (blue) and numerical (red) momentum distributions. The lattice depth, determined after the loading (see Sec. 2.4.2), is $s_0 = 8.06 \pm 0.10$. The duration of the TOF is $t_{\text{TOF}} = 35$ ms and the colormaps for the OD on panels (c,e) are truncated to 0.8 of their respective maximum value in order to see details.

agreement with a numerical computation (see Sec. 1.2.2) of momentum distribution $|\langle p | \phi_{0,0}^{(s_0)} \rangle|^2$ of the ground state (where the experimental s_0 is determined in the next section).

The method of adiabatic lattice loading is limited to the preparation of the ground state of the lattice. In the next chapter (Chap. 3), we apply quantum optimal control to extend the range of quantum states reachable in an optical lattice.

Note on measurement of the momentum component population. Here, the plane wave population is extracted from a count of the atoms in the rectangular regions shown in Fig. 2.4(c,e). In Fig. 2.4(e), we see atomic signal between the diffraction orders 0 and ± 1 . This signal comes from scattering halos populated by pairs of atoms undergoing a two-body collision at the beginning of the TOF [107, 62] (see also Fig. 2.5 where this phenomenon is more obvious). As the momentum distribution of the atoms in the periodic lattice is quantized (see Chap. 1), these halos (that also expand during the TOF) are seen in between the diffraction orders (mostly in

between the most populated ones). During my thesis, we have studied these halos and developed a protocol to observe them between given momentum orders. This method, which relies on a sudden lattice shift followed by a precisely timed evolution in the lattice in order to populate given momentum orders, is detailed in our publication [62] as well as in a previous thesis [68]. This study is at the root of our initiative to implement quantum-optimal control on the experiment, which is the subject of the next chapter of this manuscript. Importantly, scattering halos can make the extraction of momentum distributions more complicated as (i) momentum orders are depopulated during the process [68] and (ii) the counting region associated to a given order can be polluted by scattering atoms coming from adjacent orders. This latter effect can be mitigated by subtracting to each order population the halo signal measured in the two lateral regions between that order and its neighbors.

2.4.2 Optical lattice calibration

In Sec. 2.4 (with details in App. C), we presented the optical lattice with its amplitude and phase control by the mean of three AOMs. The experiments of quantum state preparation and transport in the optical lattice that we present in the next two chapters require to know the depth s_0 of the optical lattice with great precision (typically a few percents). In this section, we introduce two methods to measure the lattice depth.

Kapitza-Dirac diffraction. The first method that we use relies on pulsing the lattice of unknown depth on the BEC [108]. For a sufficiently short pulse (see below), one can consider that the atoms get their momentum affected by the potential without enough time to start accumulating a displacement. This is the Raman-Nath approximation [109, 110], notably used for efficient computation of the dynamics in the kicked-rotor [111], a simple yet powerful model to study quantum chaos. Formally, one neglects the kinetic terms in the Hamiltonian when integrating the time-dependent Schrödinger equation during the pulse. In the position representation, we have

$$i\hbar \frac{\partial}{\partial t} \psi(x, t) \simeq \hat{V}(x) \psi(x, t) \quad \Rightarrow \quad \psi(x, t) \simeq \exp\left\{ \frac{it}{\hbar} \times s_0 \frac{E_L}{2} \cos(k_L x) \right\} \psi(x, 0) \quad (2.24)$$

with $\psi(x, 0) = \chi_0(x) = 1/\sqrt{d}$ the initial wave function just before pulsing the lattice. To compute this phase impression, we use the Jacobi-Anger identity:

$$e^{iz \cos(\theta)} = \sum_{n=-\infty}^{\infty} i^n J_n(z) e^{in\theta}, \quad (2.25)$$

where $J_n(z)$ are the Bessel functions of the first kind. The evolution (2.24) becomes

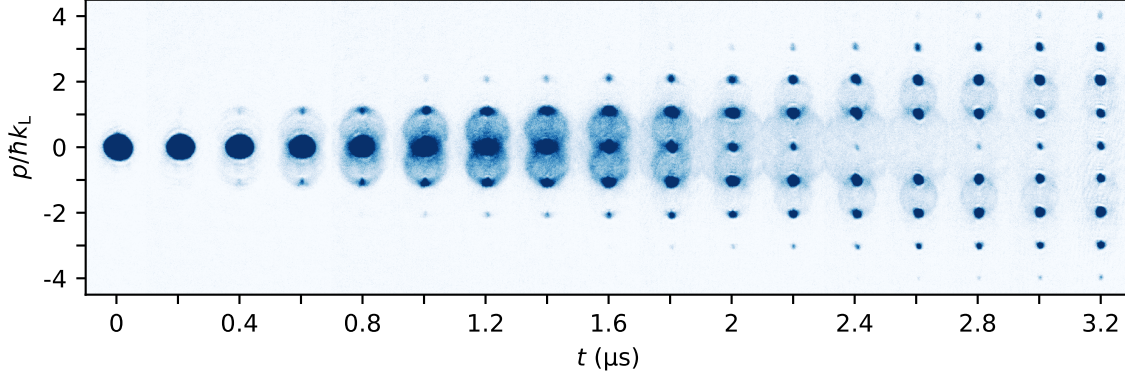


Figure 2.5 | Calibration of the optical lattice depth from Kapitza-Dirac diffraction. Horizontal stack of experimental TOF absorption images as the duration of the Raman-Nath pulse increases.

$$\psi(x, t) \simeq \sum_{\ell \in \mathbb{Z}} i^\ell J_\ell(\pi \nu_L s_0 t) \frac{e^{i\ell k_L x}}{\sqrt{d}} = \sum_{\ell \in \mathbb{Z}} c_\ell(t) \chi_\ell(x) \quad (2.26)$$

with plane wave coefficients $c_\ell(t) = i^\ell J_\ell(\pi \nu_L s_0 t)$.

A quick method to estimate the lattice depth s_0 is to experimentally determine the first pulse time τ_0 for which the zeroth plane wave is totally depleted (*i.e.* a complete depletion of the zeroth momentum order). Once this time is found, and knowing the first zero $z_0 \approx 2.405$ of $J_0(z)$, we get

$$\begin{aligned} |c_0(\tau_0)|^2 = 0 &\Leftrightarrow |J_0(\pi \nu_L s_0 \tau_0)|^2 = 0 \\ &\Leftrightarrow s_0 = \frac{z_0}{\pi \nu_L \tau_0} \approx \frac{94.38 \mu\text{s}}{\tau_0} \end{aligned} \quad (2.27)$$

Figure 2.5 shows experimental Kapitza-Dirac diffraction of matter wave in an optical lattice of fixed depth for an increasing pulse duration. We see that the zeroth momentum order is depleted for $\tau_0 \approx 2.6 \mu\text{s}$, which gives a lattice depth $s_0 \approx 36.3$ according to Eq. (2.27).

In Eqs.(2.24), (2.26) and (2.27), we made the approximation that the lattice is pulsed for a duration negligible compared to the time needed for the atoms to start moving in the potential. In a semi-classical picture, a lower bound for this timescale is approximately given by the period T_0 of the harmonic oscillator that approximates the bottom of the lattice sites. In the previous chapter (see Sec. 1.4.1), we found the frequency of this harmonic oscillator to be $\nu_0 = \sqrt{s_0} \nu_L$.

We have $T_0 \propto s_0^{-1/2}$ while $\tau_0 \propto s_0^{-1}$ (Eq. (2.27)). These scalings are favorable for this first lattice calibration, which works if s_0 is large enough for the Raman-Nath approximation

to hold up to τ_0 [94]. We state the following condition for the validity of this calibration method:

$$\frac{\tau_0}{T_0} \approx \frac{z_0}{\pi\sqrt{s_0}} \ll 1 \Leftrightarrow \sqrt{s_0} \gg 1 \quad (2.28)$$

This calibration technique is a fast way to estimate the depth of a sufficiently deep lattice. For more precision (notably for $s_0 < 10$ where most of the experiments presented in this manuscript are performed), we use a second method that relies on fitting an out-of-equilibrium evolution of the atoms in the lattice.

Oscillation of the translated ground state. A second, longer but more precise method has been proposed by our group and published before my thesis [112, 113]. It consists in loading the ground state (Sec. 2.4.1) of the lattice of unknown depth s_0 before applying a sudden phase translation φ_0 such that the atoms are placed on the flank of the lattice wells and start oscillating. In the quantum picture, the translated ground state¹⁶ is projected onto the Bloch eigenstates of the lattice and its evolution is totally determined by this projection according to Eq. (1.29). Using s_0 as an adjustable parameter¹⁷, we perform a least-square fit of the experimental evolution of the atomic momentum distribution. In Fig. 2.6, we show an example of lattice calibration with the experimental data and numerical fit. The lattice depth determined with the experiment of Fig. 2.6 was used in Fig. 2.4 to compare the experimental loading of the ground state with the numerical simulation. This lattice calibration method is used before and after each experiment presented in the rest of this manuscript (to verify that the lattice depth, which notably depends on the lattice beams alignment, has not shifted).

A strength of this method is that, given the adiabatic loading of the lattice, we can infer with confidence that the initial state is the shifted ground state of the lattice of unknown depth. In Chap. 3 about quantum-optimal control, in order to certify our quantum state preparation protocol, we revisit this method of parameter determination through an evolution in the static lattice. However, the point of view is there reversed, as the unknown parameter is the initial quantum state that begins to evolve in a static lattice of previously calibrated depth.

2.4.3 Band-mapping

Band-mapping is a well established experimental technique for cold atoms in optical lattices [107, 114, 79], by which the weights of a state on the different Bloch bands are mapped on

¹⁶We recall (see Sec. 1.2.1) the expression of the translation operator $\hat{T}_{\Delta x} = e^{-i\Delta x \hat{p}/\hbar}$ with $\hat{p}|\chi_r\rangle = r\hbar k_L|\chi_r\rangle$. The translation of a state $|\psi\rangle$ in a Bloch system reads $\hat{T}_{\Delta x}|\psi\rangle = \sum_{\ell} c_{\ell} e^{-i\Delta x \ell k_L} |\chi_{\ell}\rangle$ with $c_{\ell} = \langle \chi_{\ell} | \psi \rangle$. According to our expression of the lattice potential (2.19), a phase shift φ_0 translates the lattice by a distance $\Delta x = -\varphi_0/k_L$ in the laboratory frame of reference which translates an arbitrary state $|\psi\rangle$ by a distance $-\Delta x = \varphi_0/k_L$ in the lattice.

¹⁷For each lattice depth considered, the Bloch eigenstates and eigenenergies are computed numerically as described in Sec. 1.2.2.

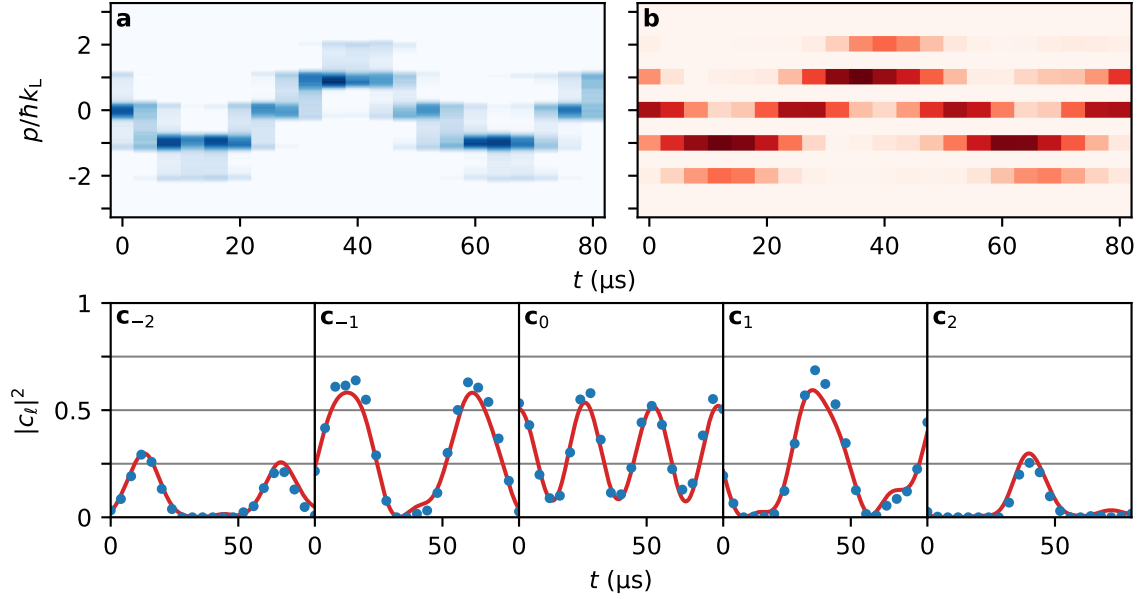


Figure 2.6 | Calibration of the optical lattice depth from a sudden lattice translation. (a) Stack of experimental integrated TOF absorption images as a function of the holding time showing the momentum evolution of the initial state (which was the ground state up until the sudden lattice shift) in the translated lattice. (b) Numerical evolution at the lattice depth that fits (a). (c) Relative plane wave populations (with panel (c_ℓ) featuring |c_ℓ|²) as a function of time, with experimental data of (a) (blue points) and fitting numerical simulation of (b) (solid red line). The known parameter was the initial lattice phase translation $\varphi_0 = 30^\circ$ and we measured $s_0 = 8.06 \pm 0.10$.

the plane wave populations. It consists in an adiabatic unloading of the lattice, during which a state $|\psi_q\rangle$ has the norm of its Bloch coefficients $|\langle\phi_{q,n}|\psi_q\rangle|$ conserved (with $|\phi_{q,n}\rangle$ the n^{th} Bloch eigenstate at quasi-momentum q). For degenerate Bose gases resolved in quasi-momentum, this method allows to access the probability distribution of a state over the basis of the Bloch waves. In $q/k_L = 0$ and $q/k_L = 0.5$ however¹⁸, the closings of the gaps lead to eigenstate degeneracies that mix the information for two consecutive bands (with the exception of the ground state at $q/k_L = 0$). In the end, an atom initially in the n^{th} Bloch band at quasi-momentum q ends up in the plane wave(s) of reduced momentum

$$p/\hbar k_L = \begin{cases} \frac{q}{k_L} + \text{sgn}(q) (-1)^n \left\lfloor \frac{n+1}{2} \right\rfloor, & q \notin \{0, 0.5\} \\ \pm \left(\frac{q}{k_L} + (-1)^n \left\lfloor \frac{n+1}{2} \right\rfloor \right), & q \in \{0, 0.5\} \end{cases} \quad (2.29)$$

where the integer part $\lfloor \cdot \rfloor$ and the factors $(-1)^n$ and $\text{sgn}(q)$ stem from the unfolding of the band structure. We draw in Fig. 2.7 an example for three different states in $q/k_L = 0$ (blue), $q/k_L = 0.5$ (green) and $q/k_L \notin \{0, 0.5\}$ (yellow) before and after a fictitious band-mapping protocol.

This method is used in Chap. 5 where we study the emergence of unstable modes in the

¹⁸We recall that we express the quasi-momentum in the first Brillouin zone $q/k_L \in (-0.5, 0.5]$, see Sec. 1.2.1.

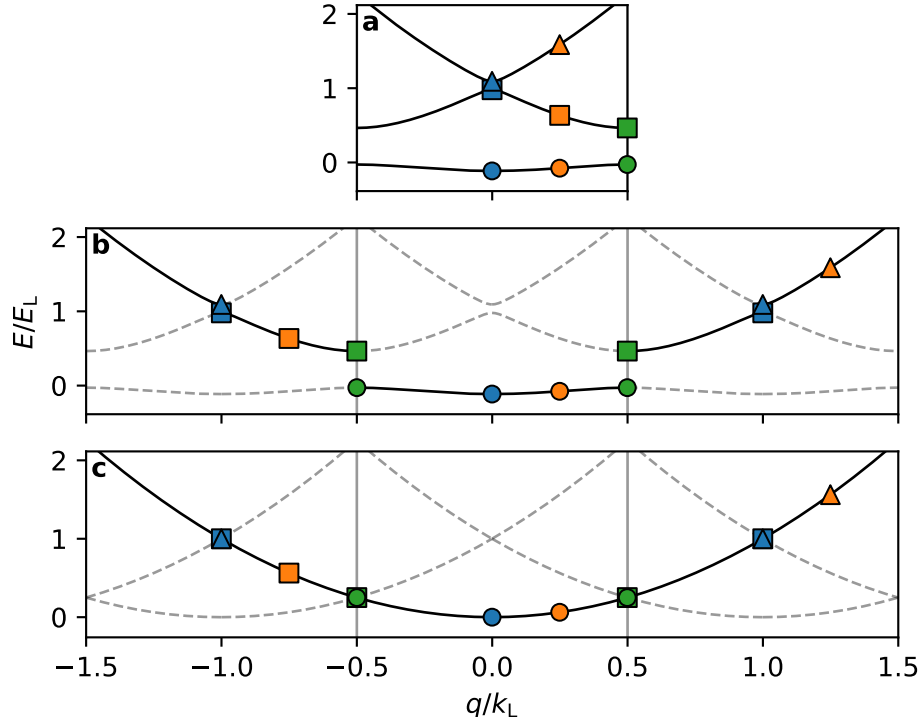


Figure 2.7 | Sketch of the band-mapping technique. (a) Band structure of a static one-dimensional optical lattice at depth $s_0 = 1$ (solid lines). (b) Equivalent, unfolded representation of the same band structure (solid and dotted lines). (c) Unfolded representation of the band structure of a lattice of depth $s_0 = 0$ (solid and dotted lines) *i.e.* relation of dispersion of the free particle (solid line). We draw three hypothetical states resolved in quasi-momentum: the blue and yellow states are superpositions of the first three Bloch states in $q/k_L = 0$ and $q/k_L = 0.25$ respectively, and the green state is a superposition of the first two Bloch states in $q = 0.5$. Between the three superpositions considered, only the yellow state in $q/k_L \notin \{0, 0.5\}$ has the norm of all its Bloch coefficients unambiguously accessible through band-mapping.

Brillouin zone of the phase-modulated optical lattice. These instabilities lead to the population of states coexisting at different quasi-momenta, which we highlight through band-mapping.

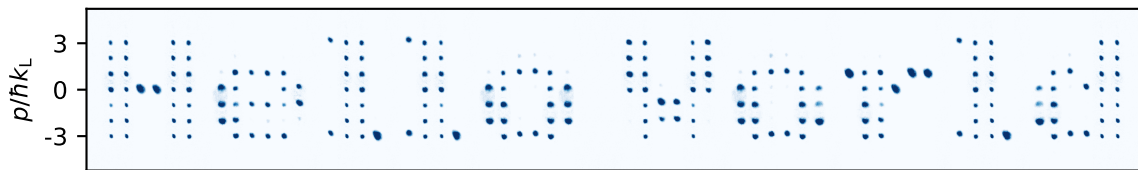
Conclusion

This brief presentation of the experimental setup concludes this first part of methods. Once again, I redirect an unfulfilled reader to the theses of my predecessors [93, 94, 115, 67, 68] where the experimental setup has been more detailed. The next parts of this manuscript present results obtained on the ultracold atom experiment described in this chapter and that will be apprehended in the theoretical and numerical framework discussed in Chap. 1.

Part II

Control and transport of the BEC one-body wave function in the optical lattice

Chapter 3 - Quantum optimal control of matter waves in a one-dimensional optical lattice



Horizontal stack of 54 independent momentum distributions (see Sec. 3.2)

Contents

Introduction	63
3.1 Optimal-control formalism	65
3.1.1 Introduction to optimal control in the classical case	65
3.1.2 Application to one-dimensional Bloch systems	67
3.1.3 Numerical method for control field computation	70
3.1.4 Numerical results, local optima and control duration	73
3.2 Controlling momentum distributions	74
3.2.1 Fidelities between momentum distributions	74
3.2.2 Preparing single momentum components	75
3.2.3 Preparing arbitrary superpositions of momentum components	78
3.3 Wave function control	79
3.3.1 Control of the relative phases between two momentum components	79
3.3.2 Preparation of Bloch eigenstates and superpositions thereof	80
3.3.3 Quantum state reconstruction by likelihood maximization	82
3.3.4 Non-squeezed Gaussian states	86
3.3.5 Squeezed Gaussian states	89
3.4 An application to quantum simulation	91
3.4.1 Introduction to dynamical tunneling	92
3.4.2 Experimental results	94
Conclusion	95

Introduction

In the first part of this manuscript, we recalled basics of quantum mechanics to study wave function dynamics in a one-dimensional Floquet-Bloch system (Chap. 1), and we presented our experimental setup, in which we place BECs in a controllable one-dimensional optical lattice (Chap. 2) to implement this system in the laboratory. This setup is simple and therefore a powerful system on which to develop methods of quantum state manipulation, notably for quantum simulation, as we will show in this chapter. To perform the simulation of a quantum system [26, 27], one has to engineer the Hamiltonian to be studied, prepare the system in the desired initial state and in due time measure the state of system. In this chapter, we present research work that we undertook in 2021, which is part of the development and implementation of techniques to face the last two of the above-mentioned requirements: initial state preparation and final state measurement.

Quantum state control. The preparation of a desired quantum state generally calls for manipulating a quantum dynamical system by means of external time-dependent parameters. In practice, it amounts to steering that system from a state easily provided by an experimental setup to the desired one with high fidelity, and in a reasonable, or even minimum time, while satisfying experimental constraints and limitations. Several approaches have been developed for quantum state control, allowing to reach states unachievable by adiabatical means. We can cite the use of composite pulses [116, 117], shortcuts to adiabaticity [57] or machine-learning schemes [58]. Another approach, which we use in this chapter, is the application of optimal-control theory to control quantum systems.

Optimal-control theory, of which we introduce the formalism in Sec. 3.1, arguably goes back to the Brachistochrone problem, submitted by J. Bernouilli in 1696 to the mathematicians of his time [118]. Considering a system that can, more generally, be controlled with external parameters, optimal-control theory is a mathematical framework with which one can compute the optimal variation of control parameters in order for the system to follow optimal trajectories that minimize some cost function. The evolution of this field is intertwined with the genesis of analytical mechanics in the 18th century, before the crowning contributions of L. Pontryagin [119] in the 1950s and later R. Bellman [120]. Applications of optimal control could hardly be more diverse, with examples in aerospace with satellite maneuvering [121, 122], communication protocols in computer science [123], finance [124] and biology [125].

Quantum optimal control (QOC) is the application of optimal-control theory to quantum systems [126], with proposals and implementations *e.g.* in the fields of quantum chemistry, quantum information, magnetic resonance and NV-centers, (see [59, 60] and references therein). QOC is well suited for quantum state control of cold and ultracold atoms for interferometry [127, 128, 129] and quantum simulation [130, 131]. We present in this chapter the implementation of QOC in our experiment, where we use the time variation of the phase of the optical lattice (Sec. 2.4) as our single control parameter in order to control the motional state $|\psi_{q,\ell}\rangle = \sum_{\ell} c_{q,\ell} |\chi_{\ell+q/k_L}\rangle$ of BECs in the lattice. We prepare firstly momentum probability distributions (targeting sets of real elements $\{|c_{q,\ell}|^2\}$, *i.e.* regardless the relative phases between

coefficients $c_{q,\ell}$), before fully addressing specific quantum states in the Hilbert space of our Bloch system (targeting sets of complex amplitudes $\{c_{q,\ell}\}$).

Observation of the system and certification of the preparation. When performing measurement on a quantum system, one never accesses the wave function of the system, but rather a possible outcome of the measurement of an observable with a probability distribution given by the squared modulus of the wave function. This is well illustrated by our TOF measurement, through which we access the momentum distribution of the BEC in the lattice, *i.e.* the set $\{|c_{q,\ell}|^2\}$ of the squared moduli of the plane wave amplitude (see Sec. 2.4.1). Such a measurement, based on a single observation of the system, is sufficient to evaluate a fidelity to a target defined purely as a momentum probability distribution, but cannot ensure proper quantum state preparation. Indeed, to certify our ability to prepare a given quantum state $|\psi_{q,\ell}\rangle$ associated to a unique set $\{c_{q,\ell}\}$ of complex coefficients, we need to access all the information of these measured coefficients $c_{q,\ell}$, that is both their norm $|c_{q,\ell}|$ and phase $\arg\{c_{q,\ell}\}$. Full quantum state tomography [132] is a matter of great relevance to quantum simulation and computation. Several methods to solve that problem have been put forward, using *e.g.* mappings from the motional state to internal degrees of freedom [133, 134, 135], while recent proposals in the context of many-body systems exploit randomized measurements [136] or neural networks [137]. In our case, we reconstruct the motional state of the BECs in the lattice with a maximum likelihood iterative method inspired by quantum optics [138, 139, 140, 141], using measurements of the subsequent evolution of the prepared state in the static lattice potential.

This chapter is organized as follow: in the first section 3.1, we give an introduction to the basics of optimal-control theory, we detail the application of QOC to our one-dimensional Bloch system, and we present our numerical approach to compute the lattice phase curve for the preparation of a given target. The second section features experimental results on the preparation of readily-observable momentum distributions (Sec. 3.2). In the third section, we target specific quantum states and detail the state reconstruction algorithm (Sec. 3.3). To conclude, we present in the Sec. 3.4 an application of our QOC implementation to the quantum simulation of dynamical tunneling [142, 89, 61] in the depth-modulated optical lattice. Some of the developments in Sec. 3.1 are inspired from [68, 143].

The research work presented in this chapter results from a collaboration with Prof. Dominique Sugny from the *Laboratoire Interdisciplinaire de Carnot Bourgogne* (Dijon), who specializes in the application of optimal control to quantum systems. It has lead to the publications:

- [63] N. Dupont, G. Chatelain, L. Gabardos, M. Arnal, J. Billy, B. Peaudecerf, D. Sugny and D. Guéry-Odelin, *Quantum State Control of a Bose-Einstein Condensate in an Optical Lattice*, PRX Quantum, 2:040303, (2021)
- [64] N. Dupont, F. Arrouas, L. Gabardos, N. Ombredane, J. Billy, B. Peaudecerf, D. Sugny and D. Guéry-Odelin. *Phase-space distributions of Bose-Einstein condensates in an optical lattice: Optimal shaping and reconstruction*, currently under review (2022)

3.1 Optimal-control formalism

3.1.1 Introduction to optimal control in the classical case

Optimal-control theory deals with systems described by parameterized equations of evolution:

$$\dot{\mathbf{x}}(t) = \mathbf{f}(\mathbf{x}(t), \mathbf{u}(t), t), \quad (3.1)$$

with the initial condition $\mathbf{x}(0) = \mathbf{x}_0$ and a given scalar cost functional $J[\mathbf{x}(t), \mathbf{u}(t), t]$ (see below). In Eq. (3.1),

- $\mathbf{x}(t) \in \mathbb{R}^n$ is the state vector of the system (for a classical system, it can for example be phase space coordinates, with $n = 2N$ if there are N degrees of freedom ; Sec. 1.1),
- \mathbf{f} is a function encapsulating the evolution (*e.g.* the Hamilton equations for a dynamical system),
- $\mathbf{u}(t) \in \mathbb{R}^m$ are m time-dependent control parameters used to drive the initial state \mathbf{x}_0 to a target state \mathbf{x}_T (with $m \neq n$ in general).

The optimal-control problem is to determine the control $\mathbf{u}(t)$ over the time interval $0 \leq t \leq t_c$ (with t_c the control duration, a parameter let free for now) that drives \mathbf{x}_0 into $\mathbf{x}(t_c) \simeq \mathbf{x}_T$ while minimizing the cost J . This cost can generally be written

$$J[\mathbf{x}(t), \mathbf{u}(t), t] = \phi(\mathbf{x}(t_c), t_c) + \int_0^{t_c} f_0(\mathbf{x}(t), \mathbf{u}(t), t) dt \quad (3.2)$$

where the first term accounts for the cost in reaching the target, and in the time required, and the second term is a cost functional dependent on the path $\mathbf{x}(t)$ and resource $\mathbf{u}(t)$ to reach the final state (it can for example be a resource cost of the form $\int_0^{t_c} |\mathbf{u}(t)|^2 dt$).

Pontryagin maximum principle. To solve such optimal-control problems, L. Pontryagin introduced in 1956 what is now referred to as the Pontryagin maximum principle (PMP). We here state this principle without demonstration (for more information, see [119, 144, 143]). We start by introducing a scalar, Hamiltonian-like function H_P , named Pontryagin Hamiltonian, that can be written as

$$H_P(\mathbf{x}(t), \mathbf{p}(t), \mathbf{u}(t), t) = -f_0(\mathbf{x}(t), \mathbf{u}(t), t) + \mathbf{p}(t) \cdot \mathbf{f}(\mathbf{x}(t), \mathbf{u}(t), t), \quad (3.3)$$

where the adjoint momentum-like¹ vector $\mathbf{p}(t) \in \mathbb{R}^n$ is nothing but a time-dependent Lagrange multiplier. This adjoint state has its evolution governed by Hamilton equations deduced from the Pontryagin Hamiltonian:

$$\dot{\mathbf{x}} = \frac{\partial H_P}{\partial \mathbf{p}} \quad \text{and} \quad \dot{\mathbf{p}} = -\frac{\partial H_P}{\partial \mathbf{x}}. \quad (3.4)$$

The PMP states that optimal controls² $\mathbf{u}^*(t)$, that minimize the cost, maximize H_P along the trajectory:

$$H_P(\mathbf{x}(t), \mathbf{p}(t), \mathbf{u}^*(t), t) = \max_{\mathbf{u}(t)} \{H_P(\mathbf{x}(t), \mathbf{p}(t), \mathbf{u}(t), t)\} \quad \text{for } 0 \leq t \leq t_c, \quad (3.5)$$

or, equivalently

$$\left. \frac{\partial H_P}{\partial \mathbf{u}} \right|_{\mathbf{u}=\mathbf{u}^*} = 0 \quad \text{for } 0 \leq t \leq t_c. \quad (3.6)$$

Solving an optimal-control problem amounts to solving Eq. (3.6) for $\mathbf{u}^*(t)$. However, we so far do not have enough information to evaluate H_P and $\mathbf{p}(t)$. One tackles a given problem depending on the constraints that enter the definition of the cost function (3.2) [143, 68]. This leads to the definition of a series of cases:

(i) If neither $\mathbf{x}(t_c)$ nor t_c are fixed, we set

$$\mathbf{p}(t_c) = - \left. \frac{\partial \phi(\mathbf{x}(t), t)}{\partial \mathbf{x}} \right|_{t=t_c} \quad \text{and} \quad \left. \frac{\partial \phi(\mathbf{x}(t), t)}{\partial t} \right|_{t=t_c} = H_P(\mathbf{x}(t_c), \mathbf{p}(t_c), \mathbf{u}(t_c), t_c). \quad (3.7)$$

(ii) If $\mathbf{x}(t_c)$ is fixed and t_c is free, we set

$$\left. \frac{\partial \phi(\mathbf{x}(t), t)}{\partial t} \right|_{t=t_c} = H_P(\mathbf{x}(t_c), \mathbf{p}(t_c), \mathbf{u}(t_c), t_c). \quad (3.8)$$

(iii) If, on the contrary, t_c is fixed and $\mathbf{x}(t_c)$ is free, we set

$$\mathbf{p}(t_c) = - \left. \frac{\partial \phi(\mathbf{x}(t), t)}{\partial \mathbf{x}} \right|_{t=t_c} \quad (3.9)$$

(iv) Finally if both $\mathbf{x}(t_c)$ and t_c are fixed, Eqs. (3.3) and (3.4) contain enough information to solve for $\mathbf{u}^*(t)$ in Eq. (3.6).

¹We stress that \mathbf{p} is a mathematical construction, adjoint vector to the state vector \mathbf{x} . In the classical dynamics example taken above, we have $\mathbf{x} = (q_1, \dots, q_N, p_1, \dots, p_N)^T$, comprising itself the true generalized momenta p_i (Sec. 1.1).

²We consider the case where there are no constraints on $\mathbf{u}(t)$.

Our constraints. In our case, we will only require for the final state $\mathbf{x}(t_c)$ to reach \mathbf{x}_T the most accurately possible in a fixed amount of time t_c and regardless of the path taken. This puts us in the third case detailed above, with a cost function that becomes

$$J[\mathbf{x}(t), \mathbf{u}(t), t] \rightarrow J(\mathbf{x}(t_c)) = \phi(\mathbf{x}(t_c)) = -\mathcal{F}(\mathbf{x}_T, \mathbf{x}(t_c)), \quad (3.10)$$

where $\mathcal{F}(\mathbf{x}_T, \mathbf{x}(t_c))$ is a fidelity to the target to be *maximized*. Thus, we need to determine $\mathbf{u}^*(t)$ from the system composed of Eqs. (3.4) and (3.6) with the boundary conditions $\mathbf{x}(0) = \mathbf{x}_0$ (defined as our initial state) and $\mathbf{p}(t_c)$ (Eq. (3.9)). However, this task is generally not easy. We therefore proceed using an iterative algorithm. One can show that the transformation $\mathbf{u}(t) \rightarrow \mathbf{u}(t) + \delta\mathbf{u}(t)$ with $\delta\mathbf{u}(t) = \varepsilon \partial H_P / \partial \mathbf{u}$ (with ε a small positive parameter) increases the fidelity [143], with $\mathbf{u}^*(t)$ a fixed point of the transformation (according to Eq. (3.6)). In our implementation, we use a numerical iterative gradient-ascent method based on this property. The procedure is detailed in Sec. (3.1.3).

3.1.2 Application to one-dimensional Bloch systems

In order to apply the previous discussion to the control of BECs in the optical lattice, we need to get expressions for the state vector, adjoint vector (with its final condition) and $\partial H_P / \partial \mathbf{u}$ in our system. In the experiment, the atoms experience the controllable lattice potential

$$V(x, t) = -A(t)s_0 \frac{E_L}{2} \cos(k_L x + \varphi(t)). \quad (3.11)$$

In Sec. 1.2, we recalled Bloch's theorem in one dimension, from which it follows that a quantum state at a given quasi-momentum q in a one-dimensional potential of period d is uniquely expanded over the basis of the plane waves as

$$|\psi_q(t)\rangle = \sum_{\ell \in \mathbb{Z}} c_{q,\ell}(t) |\chi_{\ell+q/k_L}\rangle, \quad (3.12)$$

with $\langle x | \chi_{\ell+q/k_L} \rangle = e^{i(\ell k_L + q)x} / \sqrt{d}$ and $k_L = 2\pi/d$. We state the uniqueness of this expansion with the isomorphism

$$|\psi_q(t)\rangle \leftrightarrow \mathbf{C}_q(t) = \begin{pmatrix} \vdots \\ c_{q,\ell}(t) \\ \vdots \end{pmatrix}. \quad (3.13)$$

In the following, we represent an arbitrary state $|\psi_q(t)\rangle$ using its associated coefficient vector $\mathbf{C}_q(t)$, and we drop the explicit dependence on q . In vector form, the time-dependent Schrödinger equation reads

$$i\dot{\mathbf{C}}(t) = M(u(t))\mathbf{C}(t), \quad (3.14)$$

with $M(u(t)) = H(u(t))/E_L$ (see Eqs. (1.22) and (1.32)) and $u(t)$ is a parameter of the controlled lattice potential (3.11). In the experiments presented in Secs. 3.2, 3.3 and 3.4, the control parameter $u(t)$ is the lattice phase $\varphi(t)$, and the control is performed in a lattice of constant depth ($A(t) = 1$). In what follows, we keep a general narrative with the parameter $u(t)$ as long as our development allows it.

The formalism of optimal-control theory is introduced for real-valued state vectors. We connect our quantum state $\mathbf{C}(t)$ to the real vector $\mathbf{X}(t)$ defined as

$$\mathbf{X}(t) = \begin{pmatrix} \operatorname{Re}\{\mathbf{C}(t)\} \\ \operatorname{Im}\{\mathbf{C}(t)\} \end{pmatrix} = \begin{pmatrix} \operatorname{Re} \left\{ \begin{matrix} \vdots \\ c_\ell(t) \\ \vdots \end{matrix} \right\} \\ \operatorname{Im} \left\{ \begin{matrix} \vdots \\ c_\ell(t) \\ \vdots \end{matrix} \right\} \end{pmatrix}. \quad (3.15)$$

We get a real-valued vector $\mathbf{X}(t) \in \mathbb{R}^{2d_H}$, with d_H the Hilbert space dimension (see Sec. 1.2.2). The evolution equation for $\mathbf{X}(t)$ in the form of (3.1) is obtained from the Schrödinger equation (3.14):

$$\dot{\mathbf{X}}(t) = \begin{pmatrix} \operatorname{Im}\{M(u(t))\} & \operatorname{Re}\{M(u(t))\} \\ -\operatorname{Re}\{M(u(t))\} & \operatorname{Im}\{M(u(t))\} \end{pmatrix} \mathbf{X}(t) = \mathbf{f}(\mathbf{X}(t), u(t)). \quad (3.16)$$

Following optimal-control formalism, we define the Pontryagin Hamiltonian for this problem:

$$H_P = \mathbf{P}(t) \cdot \mathbf{f}(\mathbf{X}(t), u(t)) = \mathbf{P}^T(t) \times \mathbf{f}(\mathbf{X}(t), u(t)), \quad (3.17)$$

where we have denoted the matrix product with \times . In a similar way as the relation (3.15) between $\mathbf{X}(t)$ and $\mathbf{C}(t)$, we associate a complex-valued vector $\mathbf{D}(t)$ to the adjoint state $\mathbf{P}(t)$:

$$\mathbf{P}(t) = \begin{pmatrix} \operatorname{Re}\{\mathbf{D}(t)\} \\ \operatorname{Im}\{\mathbf{D}(t)\} \end{pmatrix}. \quad (3.18)$$

From Eqs (3.17) and (3.18), the Pontryagin Hamiltonian for the one-dimensional Bloch system becomes

$$\begin{aligned}
H_P &= \operatorname{Re}\{\mathbf{D}\} \operatorname{Re}\{\dot{\mathbf{C}}\} + \operatorname{Im}\{\mathbf{D}\} \operatorname{Im}\{\dot{\mathbf{C}}\} \\
&= \operatorname{Re}\left\{ \left(\operatorname{Re}\{\mathbf{D}^T\} - i \operatorname{Im}\{\mathbf{D}^T\} \right) \times \left(\operatorname{Re}\{\dot{\mathbf{C}}\} + i \operatorname{Im}\{\dot{\mathbf{C}}\} \right) \right\} \\
&= \operatorname{Re}\left\{ \mathbf{D}^\dagger \times \dot{\mathbf{C}} \right\}.
\end{aligned} \tag{3.19}$$

where the time dependence is implicit. Using Eq. (3.14), we finally get for H_P :

$$\begin{aligned}
H_P &= \operatorname{Im}\left\{ \mathbf{D}^\dagger(t) M(u(t)) \mathbf{C}(t) \right\} \\
\Rightarrow \frac{\partial H_P}{\partial u} &= \operatorname{Im}\left\{ \mathbf{D}^\dagger(t) \frac{\partial M(u(t))}{\partial u} \mathbf{C}(t) \right\}
\end{aligned} \tag{3.20}$$

Finally, the boundary condition $\mathbf{D}(t_c)$ is obtained from the evolution of $\mathbf{P}(t)$ given by the Hamilton equations applied to H_P . Using Eqs. (3.16) and (3.17):

$$\begin{aligned}
\dot{\mathbf{P}} &= - \left(\frac{\partial H_P}{\partial \mathbf{X}} \right)^\top = \left[\mathbf{P}^\top \begin{pmatrix} -\operatorname{Im}\{M(u(t))\} & -\operatorname{Re}\{M(u(t))\} \\ \operatorname{Re}\{M(u(t))\} & -\operatorname{Im}\{M(u(t))\} \end{pmatrix} \right]^\top \\
&= \begin{pmatrix} \operatorname{Im}\{M(u(t))\} & \operatorname{Re}\{M(u(t))\} \\ -\operatorname{Re}\{M(u(t))\} & \operatorname{Im}\{M(u(t))\} \end{pmatrix} \mathbf{P}
\end{aligned} \tag{3.21}$$

where we have used the fact that $M(u(t)) = H(u(t))/E_L$ is Hermitian³. We get that $\mathbf{D}(t)$ evolves as $\mathbf{C}(t)$:

$$i\dot{\mathbf{D}}(t) = M(u(t))\mathbf{D}(t), \tag{3.22}$$

with a final condition obtained from Eqs. (3.9) and (3.10):

$$\begin{aligned}
\mathbf{P}^\top(t_c) &= + \left. \frac{\partial \mathcal{F}}{\partial \mathbf{X}} \right|_{t=t_c} \\
\Rightarrow \mathbf{D}(t_c) &= \left. \frac{\partial \mathcal{F}}{\partial \mathbf{C}^\top} \right|_{t=t_c},
\end{aligned} \tag{3.23}$$

The adjoint state $\mathbf{D}(t)$ is evaluated for all time $0 \leq t \leq t_c$ by propagating its final state (3.23) backward in time using Eq. (3.22). We also need to define the fidelity function \mathcal{F} to the target

³Which implies for our development $\operatorname{Re}\{M^\top\} = \operatorname{Re}\{M\}$ and $\operatorname{Im}\{M^\top\} = -\operatorname{Im}\{M\}$.

$|\psi_T\rangle \leftrightarrow \mathbf{C}_T$. This choice depends on the states targeted (see below). For most of our targets, we will use the quantum fidelity between pure states

$$\mathcal{F}(|\psi_T\rangle, |\psi(t)\rangle) = |\langle\psi_T|\psi(t)\rangle|^2 = \left| \mathbf{C}_T^\dagger \times \mathbf{C}(t) \right|^2. \quad (3.24)$$

With the expressions for the state $\mathbf{C}(t)$ and its adjoint $\mathbf{D}(t)$, their boundary condition (a free choice for \mathbf{C}_0 and Eq. 3.23 for $\mathbf{D}(t_c)$), the knowledge that they both evolve according to Schrödinger equation (Eqs. (3.14) and (3.22)) and the expression for $\partial H_P/\partial u$ along the trajectory (Eq. (3.20)), we have all the ingredients to iteratively compute control fields.

3.1.3 Numerical method for control field computation

As discussed in the previous section, our control parameter in the studies presented thereafter is the lattice phase $\varphi(t)$. We now explicit this choice with $u(t) \rightarrow \varphi(t)$. For numerical computation, we discretize the time vector $t \rightarrow t_n = t_0, t_1, \dots, t_N$ during the state preparation, with $t_0 = 0$ and $t_N = N\Delta t = t_c$ (with Δt a small time interval ; see below). The lattice phase $\varphi(t)$ is defined constant by part over Δt (see Fig. 3.1 below), and we write $\varphi(t_n) = \varphi_n$. The evolution operator from t_{n-1} to t_n is

$$U(t_n, t_{n-1}) = U_n = \exp\left\{ \frac{-i\Delta t H_n}{\hbar} \right\} = \exp\{-i2\pi\nu_L \Delta t M_n\}, \quad (3.25)$$

where we have used $H(t_n) = H_n = E_L M_n = h\nu_L M_n$. We want to drive an initial state $\mathbf{C}(0)$ to a target \mathbf{C}_T . We start with the initialization of the control field $\varphi_n^{(0)}$ (an initial guess), which prepares a certain final state

$$\mathbf{C}^{(0)}(t_c) = U_N^{(0)} U_{N-1}^{(0)} \dots U_2^{(0)} U_1^{(0)} \mathbf{C}(0), \quad (3.26)$$

that has a fidelity $\mathcal{F}^{(0)}$ to the target. If we vary of the control field $\varphi_n \rightarrow \varphi_n + \delta\varphi_n$, the variation of fidelity is

$$\delta\mathcal{F} = \sum_{n=1}^N \frac{\partial\mathcal{F}}{\partial\varphi_n} \delta\varphi_n \quad (3.27)$$

The heart of the gradient ascent method [145, 146, 147] that we use is to choose $\delta\varphi_n$ so that $\delta\mathcal{F} \geq 0$ in order for \mathcal{F} to increase. We see that if we modify the control field with the corrections

$$\delta\varphi_n = \varepsilon \frac{\partial\mathcal{F}}{\partial\varphi_n}, \quad (3.28)$$

with $\varepsilon > 0$, we make sure to have $\delta\mathcal{F} \geq 0$ since the right-hand-side of Eq. (3.27) becomes $\sum_n \varepsilon (\partial\mathcal{F}/\partial\varphi_n)^2$ where each term is greater than or equal to zero. As we will see below, the corrections (3.28) correspond to the general control field corrections $\delta\mathbf{u}(t) = \varepsilon \partial H_P / \partial \mathbf{u}$ discussed at the end of Sec. 3.1.1.

We now show how one can compute $\delta\mathcal{F}/\delta\varphi_n$. As the fidelity only depends on the final state reached $\mathbf{C}(t_c)$ (for a fixed target), the dependence of \mathcal{F} on the control field φ_n is that of $\mathbf{C}(t_c)$. The resulting complex derivative reads⁴

$$\begin{aligned} \frac{\partial\mathcal{F}}{\partial\varphi_n} &= \frac{\partial\mathbf{C}^\dagger(t_c)}{\partial\varphi_n} \frac{\partial\mathcal{F}}{\partial\mathbf{C}^\dagger(t_c)} + \frac{\partial\mathcal{F}}{\partial\mathbf{C}(t_c)} \frac{\partial\mathbf{C}(t_c)}{\partial\varphi_n} \\ &= 2 \operatorname{Re} \left\{ \frac{\partial\mathbf{C}^\dagger(t_c)}{\partial\varphi_n} \frac{\partial\mathcal{F}}{\partial\mathbf{C}^\dagger(t_c)} \right\}. \end{aligned} \quad (3.29)$$

The first factor in the argument of the real-part function is

$$\begin{aligned} \frac{\partial\mathbf{C}^\dagger(t_c)}{\partial\varphi_n} &= \mathbf{C}_0^\dagger U_1^\dagger \dots U_{n-1}^\dagger \frac{\partial U_n^\dagger}{\partial\varphi_n} U_{n+1}^\dagger \dots U_N^\dagger \\ &\simeq i2\pi\nu_L \Delta t \mathbf{C}_0^\dagger U_1^\dagger \dots U_{n-1}^\dagger \frac{\partial M_n}{\partial\varphi_n} U_{n+1}^\dagger \dots U_N^\dagger \end{aligned} \quad (3.30)$$

where we expanded $U_n \simeq \mathbb{1}_{d_H} - i2\pi\nu_L \Delta t M_n$ (arguing that Δt is a small time interval) and used $M_n^\dagger = M_n$. As the second factor in the argument of the real-part function in Eq. (3.29), we recognize the boundary condition $\mathbf{D}(t_c) = \mathbf{D}_N$ (Eq. (3.23)). Equation (3.29) thus becomes⁵

$$\begin{aligned} \frac{\partial\mathcal{F}}{\partial\varphi_n} &\simeq 2 \operatorname{Re} \left\{ i2\pi\nu_L \Delta t \mathbf{C}_0^\dagger U_1^\dagger \dots U_{n-1}^\dagger \frac{\partial M_n}{\partial\varphi_n} U_{n+1}^\dagger \dots U_N^\dagger \mathbf{D}_N \right\} \\ &\simeq -4\pi\nu_L \Delta t \operatorname{Im} \left\{ \mathbf{C}_{n-1}^\dagger \frac{\partial M_n}{\partial\varphi_n} \mathbf{D}_n \right\} = 4\pi\nu_L \Delta t \operatorname{Im} \left\{ \mathbf{D}_n^\dagger \frac{\partial M_n}{\partial\varphi_n} \mathbf{C}_{n-1} \right\}, \end{aligned} \quad (3.31)$$

where we have propagated \mathbf{C}_0^\dagger forward up to \mathbf{C}_{n-1}^\dagger , and \mathbf{D}_N backward up to \mathbf{D}_n . From Eqs. (3.27) and (3.28), we see that doing this operation for all n such that $0 \leq t_n \leq t_c$ gives the corrections to be applied to each φ_n to increase the fidelity.

In Eq. (3.31), we recognize a discrete version of the derivative of the Pontryagin Hamiltonian with respect to the control parameter (3.20). Our gradient ascent (3.28) is effectively performed by iteratively modifying the control field with the corrections

⁴with $z + z^* = 2 \operatorname{Re}\{z\}$; $z \in \mathbb{C}$.

⁵with $\operatorname{Re}\{iz\} = -\operatorname{Im}\{z\}$ and $\operatorname{Im}\{z^*\} = -\operatorname{Im}\{z\}$.

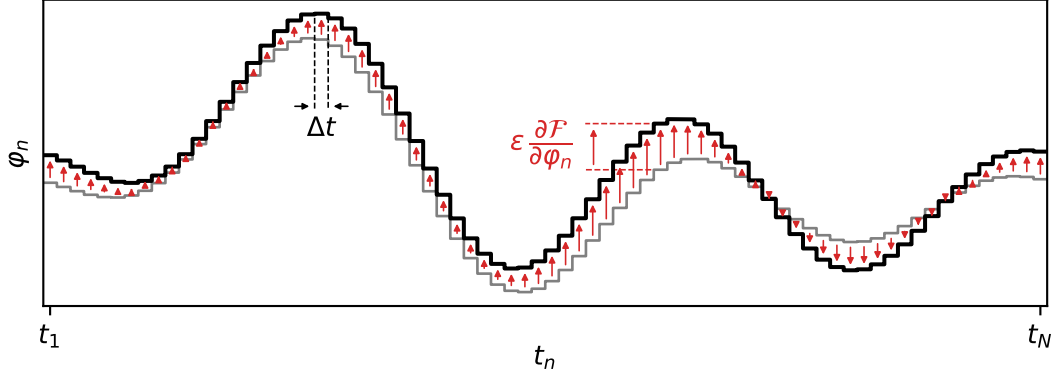


Figure 3.1 | Schematic of a gradient ascent iteration for the computation of a discretized control field showing the field φ_n at time t_n at the current step (gray line) and at the next step (black line), after applying the corrections $\delta\varphi_n$ (red arrows). Our discretization convention is such that the evolution operator $U(\varphi_n)$ transforms C_{n-1} into C_n .

$$\delta\varphi_n = \varepsilon 4\pi\nu_L \Delta t \operatorname{Im} \left\{ \mathbf{D}_n^\dagger \frac{\partial M_n}{\partial \varphi_n} C_{n-1} \right\} \simeq \varepsilon' \frac{\partial H_P}{\partial \varphi_n} \quad (3.32)$$

as prescribed by optimal-control theory through the PMP (Sec. 3.1.1). The small positive parameter ε is initialized to 1 and then slightly adjusted following a line-search method [147]. Our numerical approach is summarized in a list of concrete steps in the following box, and an iteration of this algorithm is schematically depicted in Fig. 3.1.

Iterative gradient-ascent algorithm

0. Set a initial state C_0 , a target C_T , a fidelity function and a control duration^a t_c (we state typical values for this parameter in the next section 3.1.4). Set also a break condition on the fidelity or the number of iterations.
1. Initialize a guess field $\varphi_n^{(0)}$.
2. Propagate C_0 forward to obtain C_n for all n using the time dependent Schrödinger equation (Eqs. (3.26) and (3.25)).
3. Evaluate the adjoint state at final time \mathbf{D}_N using Eq. (3.23) and propagate it backward up to $t = 0$ using Schrödinger equation to obtain \mathbf{D}_n for all n .
4. Compute the corrections $\delta\varphi_n$ for all n using Eq. (3.32) and the integration of C_n and \mathbf{D}_n . Transform $\varphi_n \rightarrow \varphi_n + \delta\varphi_n$.
5. Repeat from step 2 (with a possible adaptation of the correction amplitude ε) until reaching the desired fidelity or the maximum number of iterations.

^aWhich needs to be discretized into a number N of sufficiently small time steps Δt in order for the approximation done in Eq. (3.30) to be valid, as well as for the time-discretized fidelity gradient (3.31) to approximate the gradient of the Pontryagin Hamiltonian (3.20) in the continuous-time limit.

3.1.4 Numerical results, local optima and control duration

We now present numerical results of control field computation using the algorithm presented in the previous section. As an example, we target, in the subspace of quasi-momentum $q = 0$, the state

$$|\psi_T\rangle = \frac{1}{\sqrt{2}}(|\chi_{-3}\rangle + |\chi_3\rangle) \quad (3.33)$$

i.e. the superposition of plane waves with momenta $(-3, 3) \hbar k_L$ and a relative phase $\arg\{c_{-3}/c_3\} = 0$. Our initial state for the control is the ground state of the lattice at depth $s_0 = 5$ (a parameter that is fixed during the QOC preparation). We use the quantum fidelity (3.24), with a break condition of $\mathcal{F} > 0.995$ for the algorithm. Here, and in the following of this manuscript, we define $|\psi_{\text{QOC}}\rangle$ as the theoretical state obtained from the numerical propagation of the initial state with the optimized control field. Results are shown in Fig. 3.2 for two different resulting control fields for the preparation of the state (3.33). The control fields have been obtained from two different initial guesses, from which, in both cases, the gradient ascent algorithm has converged to an optimal control (which means that we effectively get $\mathcal{F} > 0.995$). This illustrates the general fact in optical-control theory that if there exist multiple local optima for the control parameter with respect to the cost function, a gradient-based approach may only converge towards one of these optima depending on the initialization of the control field [126, 143]. In this case, both optimal control fields $\varphi(t)$ give a satisfactory result, which mean that the local fidelity maxima near our two initializations were such that $\mathcal{F} \approx 1$.

Remark on the control duration. In our numerical approach of this optical-control problem, we fix the control duration t_c . This quantity has to be large enough for the target to become reachable, and preferably from a vast region of control field initialization (see previous paragraph). In our system, the evolution of the atoms in the lattice is governed by the band structure (Sec. 1.2.2). As our initial state is the ground state of the optical lattice, we define as the relevant timescale the period T_0 associated to the transition between the two lowest bands s and p at the center of the Brillouin zone ($q = 0$):

$$T_0(s_0) = \frac{h}{E_{0,1}^{(s_0)} - E_{0,0}^{(s_0)}}, \quad (3.34)$$

with $E_{q,n}^{(s_0)}$ the n^{th} Bloch eigenenergy at quasi-momentum q and lattice depth s_0 . For $t_c \ll T_0$, not enough time is given for the atomic state to eventually evolve toward the target. For $t_c \gg T_0$, it is easier for the numerical algorithm to converge. The problem then becomes an experimental one, as experimental fluctuations have more time to accumulate and limit the fidelity of the preparation. We present a brief study of the control duration effect on experimental preparations in App. D. In our experiments, we typically use control durations of a few T_0 (mainly 1.5 to

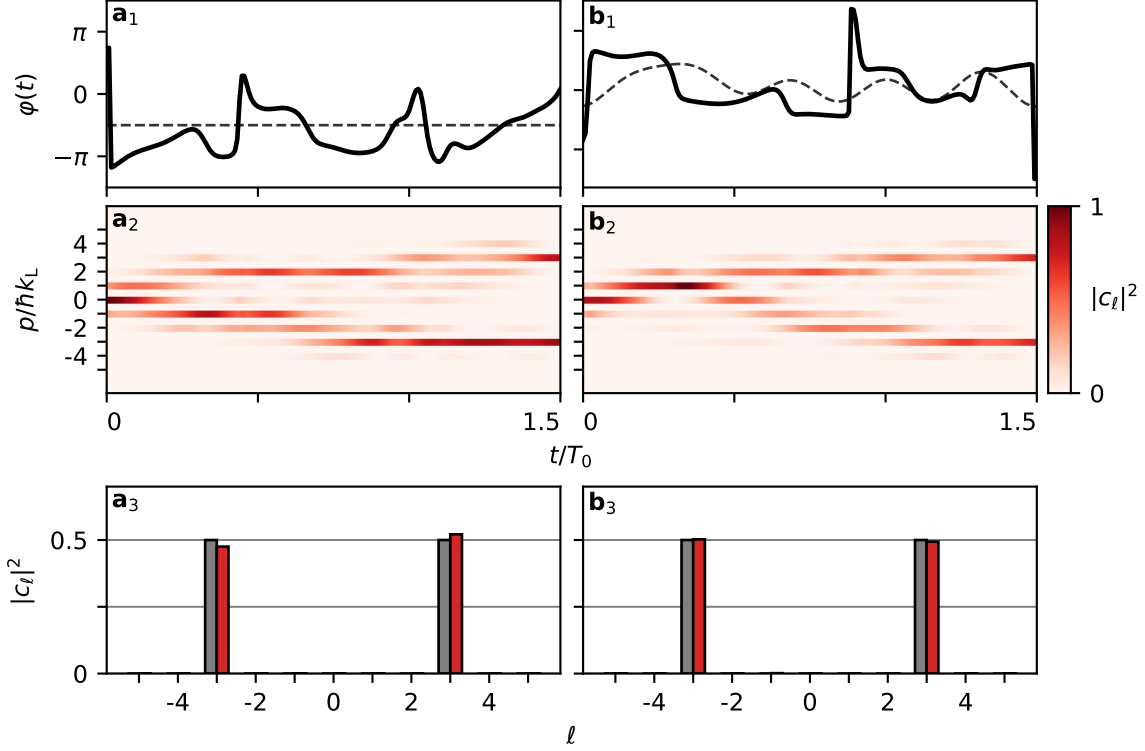


Figure 3.2 | Non-unicity of the control fields for the preparation of a given target. (a₁,b₁) Examples of lattice phase evolutions as a function of time optimized by optimal-control theory (solid black line) for the preparation of $|\psi_T\rangle$ (3.33), starting from two different initial guesses (dashed black line). (a₂,b₂) Corresponding numerical evolutions of momentum distribution. (a₃,b₃) Comparisons between the momentum distribution of $|\phi_{\text{QOC}}\rangle$ (red bars) and the target (grey bars). Resulting numerical quantum fidelities (Eq. (3.24)) are $\mathcal{F} \gtrsim 0.996$ for (a,b). The lattice depth is $s_0 = 5$ and time is given in units of $T_0(s_0 = 5) \approx 62 \mu\text{s}$ (see text).

$2T_0$). Most of the results presented in this chapter are obtained with lattice depths around $s_0 = 5$, for which $T_0 \approx 62 \mu\text{s}$.

3.2 Controlling momentum distributions

We now turn to experimental results. In first sets of experiments, we control the momentum distribution $|\langle p|\psi\rangle|^2$ of BECs in the optical lattice. We start by introducing two new fidelity definitions, which are less restrictive than (3.24) given our targets.

3.2.1 Fidelities between momentum distributions

Our goal in this first section of results is to target given momentum distributions $\{|c_\ell|^2\}$ at quasi-momentum $q = 0$. As our targets only depend on the norms $\{|c_\ell|\}$, we note that it is unnecessarily restrictive to require the preparation of a specific state whose c_ℓ coefficients have imposed relative phases. Indeed, a given momentum distributions $\{|c_\ell|^2\}$ is achieved if we

drive our initial state to the Hilbert subspace composed of the infinitely large number of states whose plane wave coefficient norms are $\{|c_\ell|\}$. We define two fidelities, less restrictive than the quantum fidelity (3.24), that allow to compute control fields towards this subspace:

$$\mathcal{F}^{(\alpha)}(\{|c_\ell|\}, \{|d_\ell|\}) = 1 - \frac{1}{2} \sum_{\ell \in \mathbb{Z}} (|c_\ell| - |d_\ell|)^2 \quad (3.35)$$

$$\mathcal{F}^{(\beta)}(\{|c_\ell|\}, \{|d_\ell|\}) = \left(\sum_{\ell \in \mathbb{Z}} |c_\ell| |d_\ell| \right)^2, \quad (3.36)$$

with c_ℓ, d_ℓ the plane wave coefficients of the two states between which the fidelities are computed, and $0 \leq \mathcal{F}^{(\alpha, \beta)} \leq 1$ for normalized states $\sum_\ell |c_\ell|^2 = \sum_\ell |d_\ell|^2 = 1$. This duplicity of definition for the fidelity between momentum distributions is fortuitous: for the results presented in the following sections 3.2.2 and 3.2.3, control fields have been computed with the first definition $\mathcal{F}^{(\alpha)}$ (3.35). For the treatment of the experimental data, we however use the second definition $\mathcal{F}^{(\beta)}$ (3.36), as it corresponds to the quantum fidelity (3.24) in the specific case of complex phase matching between the two states coefficients of the two states⁶. We have verified that the results of momentum distribution presented in the following could have been obtained with either definition, whether for the control field calculation or data treatment.



The choice for the fidelity function impacts steps 3 and 5 of our iterative gradient-ascent algorithm (p. 72), namely the final condition for the adjoint state and the break condition.

Experimental results of momentum distribution control are shown in the next two sections. In Sec. 3.2.2, we present preparations of single momentum components. In Sec. 3.2.3, we present equiprobable superpositions of two momentum components and an arbitrarily populated momentum state.

3.2.2 Preparing single momentum components

We first target momentum distributions given by $\{|c_\ell|^2\} = \{\delta_{m, \ell}\}$, with m the reduced momentum $p/\hbar k_L$ of the targeted plane waves. Results are shown in Fig. 3.3 for $m = 0, 2, 4, 10$ and quantitative details can be found in Table 3.1. The measured experimental fidelities are very close to the numerical ones, and both show a similar trend, with slowly decreasing values as we go from low momentum targets to high momentum targets (see Table 3.1). At the same time, the control phase gets more complex, as seen in Fig.3.3(d). To reach high single momentum states, such as $p = 10 \hbar k_L$ (Fig.3.3(d)) we increase the time of the control ramp to ensure the convergence of the algorithm. We note that we reach momenta much higher than the separatrix momentum $p_{\text{sep}} = \sqrt{s_0} \hbar k_L$ (Sec. 1.1.2), which corresponds to the classical limit with a sudden lattice shift [62].

⁶Given the coefficient norms of two states, $\mathcal{F}^{(\beta)}$ (3.36) is therefore an upper bound of \mathcal{F} (3.24).

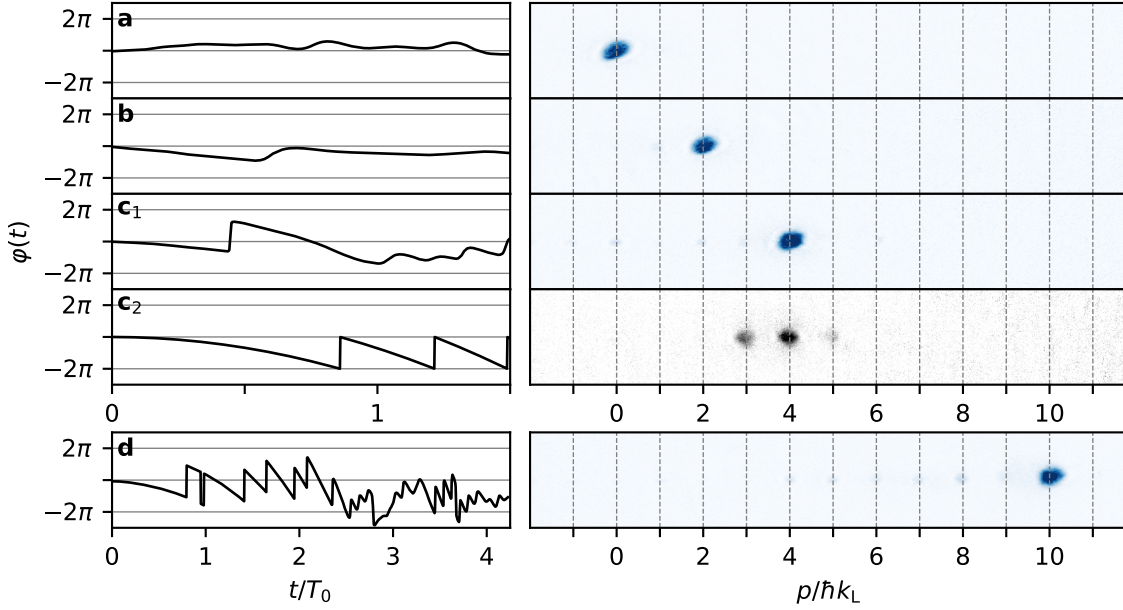


Figure 3.3 | Controlling momentum distributions: single momentum components. Left: Control field as a function of time. Right: TOF absorption images, where the OD colormaps have been truncated to 0.5 of their maximum respective value (which saturates the center of the mainly populated orders) to reveal preparation defects. **(a,b,c₁,d)** QOC preparations. **(c₂)** Lattice acceleration (see text). See Table 3.1 for details.

We stress that, as any image of atoms featured in this thesis, the ODs shown in panels (a,b,c₁,d) are TOF absorption images of BECs directly dropped from the optical lattice (in this case, once the propagation procedure has been applied). Strikingly, the usual momentum quantization induced by the lattice periodicity imprinted in the wave function is suppressed. While this is expected as we target single plane waves, these experiments interestingly amount to the realization of a blazed grating for matter waves (in direct analogy with optics), as the measured momentum distributions correspond to an *in situ* constant phase gradient $\Delta\phi(x) = mk_L x$ across the lattice sites (see for instance [90]).

Preparing the single plane wave with momentum $m \times \hbar k_L$ corresponds to accelerating all the atoms of the BEC up to that momentum. We can compare our QOC method to the more standard protocol of accelerating the lattice to impart momentum to the atoms. In Fig. 3.3(c₂), we illustrate this comparison in the case of $m = 4$, where we uniformly accelerate the lattice up to a velocity of $4\hbar/md$ for the same amount of time t_c and lattice depth s_0 used for the corresponding QOC experiment of Fig. 3.3(c₁). After the acceleration, the fidelity to the target state, *i.e.* the single momentum state $p = 4\hbar k_L$, is only $\mathcal{F}_{c_2}^{(\beta)} = 0.49 \pm 0.03$, which is much lower than the one obtained using the QOC method ($\mathcal{F}_{c_1}^{(\beta)} = 0.89 \pm 0.01$, see Table 3.1). This is clearly visible on the experimental absorption image of Fig. 3.3(c₂), with atomic population on the neighboring momentum orders. One could argue that the fidelity to the target state using the acceleration method can be increased by working adiabatically and performing Bloch oscillations [148, 149, 79]. Numerical simulations show however that reaching a fidelity $\mathcal{F}^{(\beta)} > 90\%$ to a given single momentum state requires low lattice depths $s_0 < 1$ and that the adiabaticity condition [79] then

Fig. 3.3	a	b	c	d
s_0	5.1 ± 0.2	5.2 ± 0.2	5.2 ± 0.2	5.1 ± 0.2
t_c/T_0	1.5	1.5	1.5	4.25
m	0	2	4	10
$\mathcal{F}_{\text{num}}^{(\beta)}$	0.99	0.99	0.89	0.87
$\mathcal{F}_{\text{exp}}^{(\beta)}$	0.94 ± 0.01	0.94 ± 0.01	0.89 ± 0.01	0.74 ± 0.05

Table 3.1 | Detail table related to the preparation of single momentum components. This table refers to Fig. 3.3. s_0 is the lattice depth, t_c/T_0 is the control duration rescaled by the period T_0 (Eq. (3.34), see text) and m is the momentum (rescaled by $\hbar k_L$) of the targeted plane wave. The fidelity $\mathcal{F}^{(\beta)}$ is defined in Eq. (3.36). $\mathcal{F}_{\text{num}}^{(\beta)}$ is evaluated between the target and $|\psi_{\text{QOC}}\rangle$. $\mathcal{F}_{\text{exp}}^{(\beta)}$ is evaluated between the target and the state experimentally prepared by the application of optimal control fields (with an average over 10 realizations, and an uncertainty corresponding to one standard-deviation).

leads to a generally much longer control time t_c (see below). The control time will also grow linearly with the momentum of the targeted state, reaching $t_c = 1.7$ ms for the $p = 4 \hbar k_L$ state considered in our comparison (to be compared with $t_c = 1.5 T_0 \approx 92 \mu\text{s}$ using QOC). Such long control times also mean that the atoms move much further away from the center of the trap (Sec. 2.2.4) during the lattice acceleration, with expected deleterious effects as this additional potential is not taken into account by our model. In Table 3.2, we summarize the results of the comparison between QOC and adiabatic acceleration for several momentum orders. We conclude that the QOC method is both a fast and accurate procedure to populate single momentum states with a high fidelity.

m		2	4	8	10
$\mathcal{F}_{\text{exp}}^{(\beta)}$		0.94 ± 0.01	0.89 ± 0.01	0.76 ± 0.04	0.74 ± 0.05
QOC	$s_0 (\pm 0.2)$	5.2	5.2	5.1	5.1
	$t_c (\mu\text{s})$	91.7	91.7	260	260
Acc	s_0	0.75	1.1	2.1	2.3
	$t_{\text{acc}} (\mu\text{s})$	$1.7 \cdot 10^3$	$1.7 \cdot 10^3$	$1.2 \cdot 10^3$	$1.4 \cdot 10^3$

Table 3.2 | QOC versus adiabatic lattice acceleration. Comparison of the control time t_c required to reach a given single momentum target ($p = m \times \hbar k_L$) with the same fidelity using either our QOC protocol or an adiabatical Bloch oscillation scheme with a uniformly accelerated lattice (“Acc”). $\mathcal{F}_{\text{exp}}^{(\beta)}$ refers to the experiments Fig. 3.3(b,c₁,d) as well a preparation of the 8th plane wave not featured in Fig. 3.3. We indicate the lattice depth s_0 at which the experiments were performed (for the QOC case), or which would be required (for the accelerated case).

The comparison between the control fields $\varphi(t)$ in both methods (QOC and lattice acceleration) also sheds light on the way the optimal phase is designed: the artificially-made folded quadratic growth pattern in the control phase for the acceleration method (Fig. 3.3(c₂)) can also be found in the QOC phases, for instance in Fig. 3.3(c₁,d). In the case of panel (c₁), the optimal control field $\varphi(t)$ can be interpreted as a first acceleration stage towards the targeted momentum state (for $t/T_0 < 0.75$), and a second “correction” stage to reduce the population in unwanted momentum states.

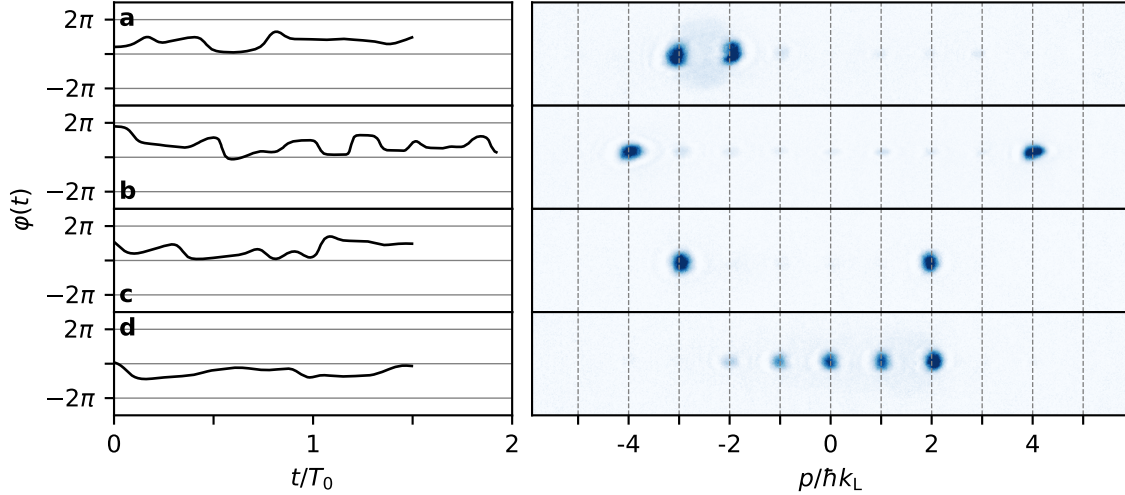


Figure 3.4 | Controlling momentum distributions: two-components equiprobable and arbitrary momentum superpositions. Left: Control field as a function of time. Right: TOF absorption images, where the OD colormaps have been truncated to 0.5 of their maximum respective value (which saturates the center of the mainly populated orders) to reveal preparation defects. See Table 3.3 for details.

3.2.3 Preparing arbitrary superpositions of momentum components

In this last section of results concerning momentum distribution control, we shape the lattice phase $\varphi(t)$ to realize arbitrary momentum superpositions. Results are shown in Fig. 3.4, with details in Table 3.3. We begin with equiprobable superpositions of two momentum states, varying their relative momentum. We show the case of neighboring momentum states (Fig. 3.4(a)), opposite momentum states (Fig. 3.4(b)) and an arbitrary pair of momentum states (Fig. 3.4(c)). We also prepare an arbitrary momentum distribution corresponding to an “ascending staircase” distribution $(|c_{-2}|^2, |c_{-1}|^2, |c_0|^2, |c_1|^2, |c_2|^2) = (1, 2, 3, 4, 5)/15$ (Fig. 3.4(d)). In each case shown, we achieve good experimental fidelities to the ideal target (larger than 88 %, see Table 3.3), slightly below the corresponding numerical fidelities.

To further demonstrate the robustness and versatility of our QOC method for the preparation of momentum distributions, we prepared all the $2^7 = 128$ equal-weight superpositions of momenta between $p = -3\hbar k_L$ and $p = 3\hbar k_L$ in the lattice of depth $s_0 \approx 5$. As an amusing way of presenting the results, we constructed an alphabet by concatenating the resulting TOF absorption images, allowing us to write words and sentences. An example of such a printout is shown in the beginning of this chapter (p. 61).

All experimental results of QOC featured in this chapter are obtained with the ground state of the lattice as the initial state for the control. The arbitrariness of this choice is illustrated in App. E, where we show an experiment of momentum distribution control with the resting BEC ($c_\ell = \delta_{0,\ell}$) as the initial state.

We recall that the targets in this section were defined regardless the relative phases between their c_ℓ coefficients. In the next section, we experimentally target specific quantum states, and

Fig. 3.4	a	b	c	d
s_0	4.6 ± 0.2	5.0 ± 0.1	4.6 ± 0.2	5.1 ± 0.1
t_c/T_0	1.5	1.5	≈ 2	1.5
$\{m\}$	$\{-3, -2\}$	$\{-4, 4\}$	$\{-3, 2\}$	$\{-2, -1, 0, 1, 2\}$
$\{ c_m ^2\}$	—	$\{0.5, 0.5\}$	—	$\{1, 2, 3, 4, 5\}/15$
$\mathcal{F}_{\text{num}}^{(\beta)}$	0.95	0.92	0.98	0.99
$\mathcal{F}_{\text{exp}}^{(\beta)}$	0.88 ± 0.03	0.93 ± 0.01	0.93 ± 0.02	0.94 ± 0.01

Table 3.3 | Detail table related to the preparation of two-component equiprobable and arbitrary momentum superpositions. This table refers to Fig. 3.4. s_0 is the lattice depth, t_c/T_0 is the control duration reduced by the period T_0 (Eq. (3.34), see text), $\{m\}$ is the set of momenta of the targeted components (reduced by $\hbar k_L$) and $\{|c_m|^2\}_T$ are the square moduli of the corresponding coefficients. The fidelity $\mathcal{F}^{(\beta)}$ is defined in Eq. (3.36). $\mathcal{F}_{\text{num}}^{(\beta)}$ is evaluated between the target $|\psi_{\text{QOC}}\rangle$. $\mathcal{F}_{\text{exp}}^{(\beta)}$ is evaluated between the target and the state experimentally prepared by the application of optimal control fields (with an average over 10 realizations, and an uncertainty corresponding to one standard-deviation).

present how we manage to assess the prepared states.

3.3 Wave function control

In this second section of results, we tackle the preparation of specific quantum states $|\psi\rangle = \sum_{\ell} c_{q,\ell} |\chi_{\ell+q/k_L}\rangle$. To compute control fields, we therefore use the usual fidelity between pure quantum states $\mathcal{F} = |\langle\psi|\phi\rangle|^2$. The difficulty now lies in the measurement of the prepared complex wave function in order to certify our preparation protocol. Our general procedure to deduce the prepared quantum states is to hold them in the static lattice after the preparation. We then use the data of their evolution in the optical lattice as information to identify the state. In the following, we first show that we can prepare and identify superpositions of two momentum components with an arbitrary relative phase (Sec.3.3.1) and specific eigenstates of the lattice potential as well as eigenstate superpositions (Sec.3.3.2). We then turn to the more general preparation of arbitrary states in the system, through the target of Gaussian states (for which we develop a systematic reconstruction method) that we translate and superpose (Sec. 3.3.4) or squeeze (Sec. 3.3.5) in the (x, p) phase space of each lattice site.

3.3.1 Control of the relative phases between two momentum components

To prepare a given quantum state in our Bloch system, we need to control the complex phase of each⁷ coefficient $c_{q,\ell}$. We first demonstrate this control by targeting the simple momentum superposition

$$|\psi_T^{(\Delta\phi)}\rangle = \frac{1}{\sqrt{2}} \left(|\chi_1\rangle + e^{i\Delta\phi} |\chi_{-1}\rangle \right). \quad (3.37)$$

⁷Actually each coefficient minus one, since states are defined up to a global phase.

For several target values of the relative phase $\Delta\phi = j \times \pi/8$ (with $j \in \{0, 1, \dots, 15\}$) we compute an optimal-control ramp that prepares the corresponding superposition $|\psi_{\text{QOC}}^{(\Delta\phi)}\rangle$ with numerical quantum fidelity $\mathcal{F}_{\text{num}} > 0.995$. With each ramp, we also evaluate the prepared relative phase $\Delta\phi_{\text{prep}} = \arg\{c_{-1}/c_1\}$ from a simulation of the optimal control preparation. To measure the relative phase $\Delta\phi_{\text{meas}}$ of the experimentally prepared superpositions, we use the subsequent evolutions of the momentum distribution in the static lattice. These evolutions are measured over an extra $110 \mu\text{s}$ ($\approx 1.75 T_0$). Results are shown in Fig. 3.5.

For each of the five evolutions presented, we see that the initial momentum distributions (at $t = 0$) are the same, which is the expected superposition $(-1, 1) \hbar k_{\text{L}}$ given the addressed state (3.37). The subsequent evolutions then strongly differ depending on the prepared relative phase $\Delta\phi_{\text{prep}}$. This allows us to measure relative phases $\Delta\phi_{\text{meas}}$ with precision by fitting, on the experimental data, numerical evolutions of the ideal state (3.37) with the relative phase $\Delta\phi$ as the adjustable parameter. This procedure is illustrated in Fig. 3.5(c₂-c₂). In Fig. 3.5(f), we compare the prepared and measured relative phases. The good agreement between the two (see the caption of Fig. 3.5 for details) demonstrates our ability to engineer the phase of momentum superpositions reliably. The residual mismatch may be attributed to at least two different effects: on the first hand, lattice depth fluctuations has a double deleterious effect on this experimental scheme, as they impact both the QOC preparations and the subsequent evolutions. On the other hand, the adjustments of wave function dynamics performed here suffer from only having the relative phase $\Delta\phi$ as adjustable parameter. Indeed, we here effectively assume that the prepared states at the beginning of the evolution were always the ideal state (3.37), with an equal-weight superposition of the sole momentum components $(-1, 1) \hbar k_{\text{L}}$. Even if the preparations were ideal, we know for a fact that this is inaccurate, as the numerical fidelities to the targets only are $\mathcal{F} \gtrsim 0.995$. This necessarily limits the measurement potential of our fit. Later in this chapter (Sec. 3.3.3), we overcome this limitation with a reconstruction method that only require a constant lattice depth s_0 as an assumption.

We have also performed similar experiments with three-momentum superpositions and different relative phases. These experiments are presented in App. E.

3.3.2 Preparation of Bloch eigenstates and superpositions thereof

To further demonstrate our ability to prepare quantum states with specific relative phases between their c_ℓ coefficients, we target two Bloch eigenstates of the static lattice and two given superpositions of Bloch eigenstates. Our target are computed from the diagonalization of the static lattice Hamiltonian in the basis of the plane waves (see Sec. 1.2.2). Writing $|\phi_{q,n}^{(s_0)}\rangle$ the n^{th} Bloch eigenstate (ranked by increasing eigenenergies) at quasi-momentum q and lattice depth s_0 , we target the states⁸ (with indices corresponding to the panels of Fig. 3.6)

⁸The specific depth values indicated for these targets correspond to the depths calibrated before each experiment (Sec. 2.4.2).

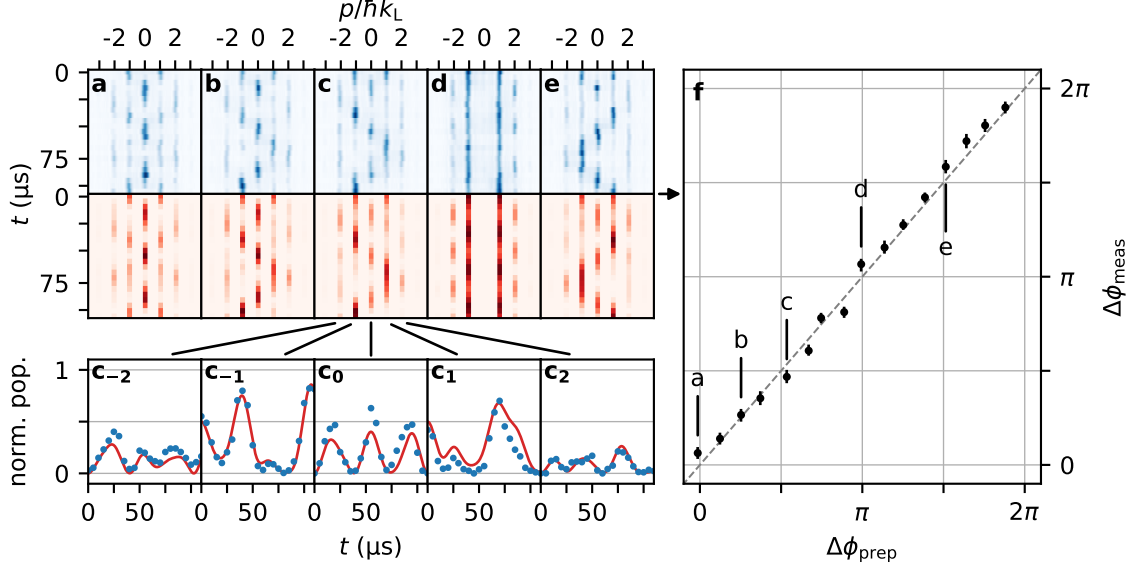


Figure 3.5 | Control and measurement of the phase between two momentum components. (a-e) Top: stacks of integrated experimental images (blue) showing the evolution of the momentum distribution during a 110 μs holding time in a static lattice after applying a control field $\varphi(t)$ preparing the momentum superposition $|\psi_{\Delta\phi}\rangle$ of momentum components $(-1, 1) \hbar k_L$ (Eq. (3.37)) with an expected relative phases $\Delta\phi_{\text{prep}} = 3^\circ, 46^\circ, 96^\circ, 184^\circ$ and 276° . Bottom: numerical propagation (red) in a static lattice of the same momentum superposition with a relative phase adjusted by least-squares fitting of the experimental data, yielding respectively $\Delta\phi_{\text{meas}} = (11 \pm 6)^\circ, (48 \pm 7)^\circ, (84 \pm 6)^\circ, (192 \pm 7)^\circ$ and $(285 \pm 6)^\circ$. (c₋₂-c₂) Detail of the evolution of momentum populations in (c), with panel (c_ℓ) featuring the ℓth momentum component, and showing the experimental data (blue dots) and numerical propagation of the superposition $|\psi_{\Delta\phi_{\text{meas}}}\rangle$ with relative phase $\Delta\phi_{\text{meas}}$ determined by least-square fitting (continuous red line). (f) Measured relative phase $\Delta\phi_{\text{meas}}$ as a function of QOC prepared relative phase $\Delta\phi_{\text{prep}}$ for data (a-e) and more. All data shown were obtained for a calibrated lattice depth $s_0 \approx 5$. The error bars represent the 95 % confidence interval for the fitted value of $\Delta\phi_{\text{meas}}$. The grey dotted line is of slope one.

$$\begin{aligned}
|\psi_{\text{T}}^{(b)}\rangle &= |\phi_{q=0,n=1}^{(s_0=8.15)}\rangle \\
|\psi_{\text{T}}^{(c)}\rangle &= |\phi_{q=k_L/4,n=2}^{(s_0=8.26)}\rangle \\
|\psi_{\text{T}}^{(e)}\rangle &= \frac{1}{\sqrt{2}} \left(|\phi_{q=0,n=1}^{(s_0=5.60)}\rangle + |\phi_{q=0,n=3}^{(s_0=5.60)}\rangle \right) \\
|\psi_{\text{T}}^{(f)}\rangle &= \frac{1}{\sqrt{2}} \left(|\phi_{q=k_L/4,n=0}^{(s_0=5.66)}\rangle + |\phi_{q=k_L/4,n=1}^{(s_0=5.66)}\rangle \right).
\end{aligned} \tag{3.38}$$

Expectations. In the case of the one-eigenstate targets $|\psi_{\text{T}}^{(b,c)}\rangle$, we expect to observe no evolution of the momentum distributions as we target steady states of the system. For the two eigenstate superpositions $|\psi_{\text{T}}^{(e,f)}\rangle$, we are preparing the two-level superposition:

$$|\psi_q(t=0)\rangle = \frac{1}{\sqrt{2}} \left(|\phi_{q,n}^{(s_0)}\rangle + |\phi_{q,m}^{(s_0)}\rangle \right), \tag{3.39}$$

whose evolution can be written as (Sec. 1.2.3)

$$|\psi_q(t)\rangle = \frac{e^{-iE_{q,n}^{(s_0)}t/\hbar}}{\sqrt{2}} \left(|\phi_{q,n}^{(s_0)}\rangle + e^{-i(E_{q,m}^{(s_0)} - E_{q,n}^{(s_0)})t/\hbar} |\phi_{q,m}^{(s_0)}\rangle \right). \quad (3.40)$$

We therefore expect to detect only one frequency of evolution $\nu_{q,n,m}^{(s_0)} = |E_{q,m}^{(s_0)} - E_{q,n}^{(s_0)}|/\hbar$. We compute $\nu_{(e)} \approx 33 \mu\text{s}$ and $\nu_{(f)} \approx 59 \mu\text{s}$.

For these expectations to hold, the eigenstates that go into our target definitions (3.38) need indeed to be eigenstates (see below). While this is directly the case when targeting $|\psi_T^{(b,e)}\rangle$ (as we apply our QOC protocol in the subspace of quasi-momentum $q = 0$), we need, in the case of $|\psi_T^{(c,f)}\rangle$, to put our preparations in the subspace $q = k_L/4$ after the QOC stage. A state associated with a particle of mass m initially in the subspace of quasi-momentum q is projected onto the subspace of quasi-momentum q' by instantaneously giving it a speed $v = \hbar(q' - q)/m$ with respect to the Bloch system in which it evolves. In the experiment, we induce this instantaneous speed shift by putting the lattice at speed $v = -\hbar(q' - q)/m$ with a linear lattice phase curve once the QOC preparation is done⁹.

We present the results of these experiments in Fig. 3.6. The control duration is $t_c = 1.5 T_0$ and we obtain control fields with numerical fidelities $\mathcal{F} \gtrsim 0.99$. In Fig. 3.6(b,c,e,f), we compare the evolutions of the states prepared experimentally and the theoretical states $|\psi_{\text{QOC}}\rangle$ prepared numerically. As expected, the plane wave populations for the one-eigenstate preparations do not evolve in time (Fig. 3.6(b,c)), demonstrating that we have indeed generated eigenstates. For the eigenstate superpositions (Fig. 3.6(e,f)), we strikingly observe the evolution of *all* momentum orders with mainly one frequency in each case (one can contrast these with *e.g.* Fig. 3.5(c)). The observed frequency are in agreement with our expectations (see above).

We point out that similar experiments of eigenstate preparations were performed in one, two and three dimensions with control sequences of pulsed lattices [130].

We have so far demonstrated quantum state control with simple two-momentum component superpositions (Sec. 3.3.1) and here with the preparation of lattice eigenstates. To prove our ability to prepare arbitrary quantum states, we need a systematic state reconstruction method to measure our preparations.



In the rest of this chapter, we work in the subspace of quasi-momentum $q = 0$.

3.3.3 Quantum state reconstruction by likelihood maximization

We present in this section the implementation of an iterative likelihood maximization method that allows us to systematically reconstruct prepared states from their evolution in the static lattice after the preparation. As we will see, a strength of this method is that no

⁹For the targets $|\psi_T^{(c,f)}\rangle$, the lattice is given a speed of $v = -\hbar k_L/4m \approx -2.158 \text{ mm/s}$ after the QOC stage.

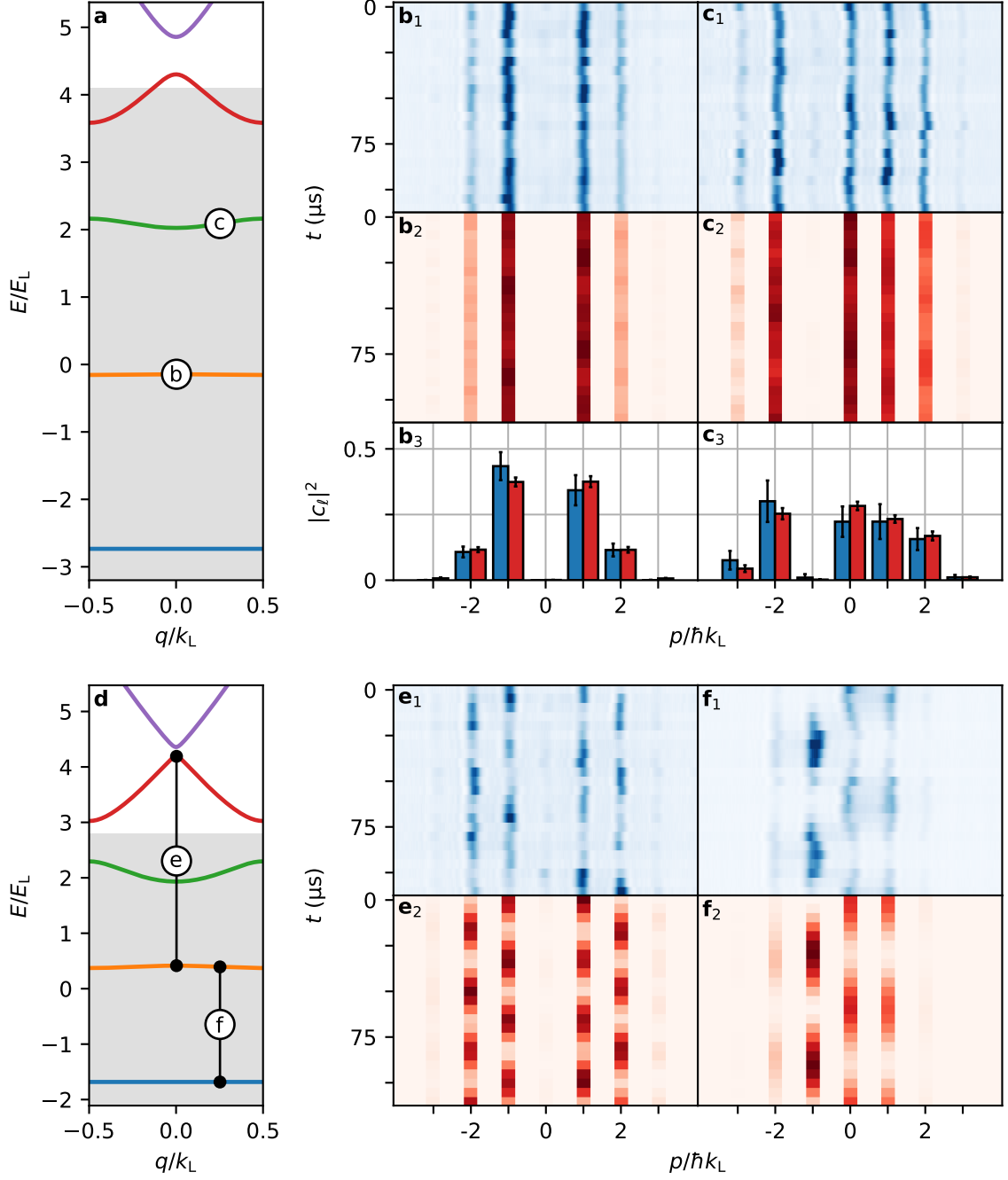


Figure 3.6 | Preparations of Bloch eigenstates and superpositions thereof. (a,d) Lattice band structures (color lines) for the two depths $s_0 = 8.2$ (a) and $s_0 = 5.6$ (d) over one Brillouin zone, and identification of the eigenstates targeted in panels (b,c) and eigenstate superpositions targeted in panels (e,f) (black annotations). The grey areas indicates the energies below the maximum potential energy of the lattice. (b) Preparation of the eigenstate of the p band at quasi-momentum $q = 0$ for $s_0 = 8.15 \pm 0.30$. (b₁) Experimental data showing the evolution of the prepared state in the lattice. (b₂) Numerical evolution of $|\psi_{\text{QOC}}\rangle$. (b₃) Time-averaged experimental (blue) and theoretical (red) momentum distributions. The error bars represent the standard deviation along the evolution. (c) Same as (b) but for the eigenstate on the d band at quasi-momentum $q/k_L = 0.25$ for $s_0 = 8.26 \pm 0.10$. (e) Same as (b) but for the equal-weight superposition of eigenstates of the p and f bands at quasi-momentum $q = 0$ for $s_0 = 5.60 \pm 0.15$. (f) Same as (b) but for the equal-weight superposition of eigenstates of the s and p bands at quasi-momentum $q/k_L = 0.25$ for $s_0 = 5.66 \pm 0.15$. This experimental figure can be compared with the theoretical figure 1.5 p. 22.

assumption is made about the state to be reconstructed (as opposed to the evolution fits shown in Sec. 3.3.1). The only details needed by the algorithm are “contextual”, namely the lattice depth s_0 and the data time stamps corresponding to the evolution data fed to the algorithm. We start with reminders on measurement in quantum mechanics [150], and we then present the reconstruction algorithm that we use in the following section. Let $\hat{\rho}$ be the density matrix¹⁰ associated to the state of a system that we want to reconstruct from a set of measurements.

Projective measurement. We consider the projective measurement of the physical quantity a associated with the observable operator \hat{A} with eigenvalues and eigenvectors $\{a_i, |a_i\rangle\}$. When measuring \hat{A} on $\hat{\rho}$, one gets the result a_i with probability

$$\pi_i = \text{tr}\left\{\hat{P}_i\hat{\rho}\right\} \quad \text{and the state becomes} \quad \hat{\rho} \rightarrow \hat{\rho}' = \frac{\hat{P}_i\hat{\rho}\hat{P}_i}{\pi_i}, \quad (3.41)$$

where $\hat{P}_i = |a_i\rangle\langle a_i|$ is the projector on the corresponding eigenstate, with $\sum_i \hat{P}_i = \mathbb{1}$. This ideal projective measurement scheme is also referred to as von Neumann measurement [150].

Generalized measurement. We can describe a more general measurement that is not based on projectors anymore. We consider a set of operator \hat{M}_i (named Kraus operators) acting on the system, the only condition being $\sum_i \hat{M}_i^\dagger \hat{M}_i = \mathbb{1}$. When measuring the state of the system, we get the result i with probability

$$\pi_i = \text{tr}\left\{\hat{\rho}\hat{M}_i^\dagger \hat{M}_i\right\} \quad \text{and the state becomes} \quad \hat{\rho} \rightarrow \hat{\rho}' = \frac{\hat{M}_i\hat{\rho}\hat{M}_i^\dagger}{\pi_i}. \quad (3.42)$$

Projective measurement is a special case of generalized measurement where the Kraus operators M_i are projectors. We define the positive operator-valued measure (POVM) formed by the set of operators $\hat{E}_i = \hat{M}_i^\dagger \hat{M}_i$ (which are not necessarily projectors).

We now consider an unknown state $\hat{\rho}$, prepared a large number of times, on which have been performed a set of measurements of the POVM $\{E_i\}$. We are given the frequencies f_i (with $\sum_i f_i = 1$) with which the results i were obtained. Reconstructing $\hat{\rho}$ consists in finding the theoretical state most likely to have produced these results. This state $\hat{\rho}_{\text{ML}}$ is the one that maximizes the likelihood function \mathcal{L} defined as

$$\mathcal{L}[\hat{\rho}] = \prod_i \text{tr}\left\{\hat{\rho}\hat{E}_i\right\}^{f_i} \quad \text{and} \quad \hat{\rho}_{\text{ML}} = \arg \max_{\hat{\rho}} \{\mathcal{L}[\hat{\rho}]\} \quad (3.43)$$

However, finding $\hat{\rho}$ is a tedious endeavor, as one needs to set all the matrix elements of $\hat{\rho}_{\text{ML}}$. Precisely, in a Hilbert space of dimension d_{H} , symmetric density matrices have d_{H} real numbers

¹⁰For a one-body pure state $|\psi\rangle$, one has $\hat{\rho} = |\psi\rangle\langle\psi|$. As will be explained below, we will however not restrict our analysis to pure states. In general, one rather has $\hat{\rho} = \sum_i p_i |\psi_i\rangle\langle\psi_i|$, where p_i is a classical probability for the state defined by $\hat{\rho}$ to be measured in the state $|\psi_i\rangle$, with $\sum_i p_i = 1$.

on the diagonal, and $d_{\text{H}}(d_{\text{H}} - 1)/2$ complex numbers as unique off-diagonal coefficients, which amounts to $(d_{\text{H}})^2$ real number to determine. We therefore turn to a numerical iterative process to reconstruct $\hat{\rho}_{\text{ML}}$.

Iterative maximum likelihood algorithm and application to our case. The algorithm that we implement to reconstruct $\hat{\rho}_{\text{ML}}$ is inspired from quantum optics [138, 140, 141] with recent implementations on matter wave systems [151, 152]. We consider a POVM $\{E_i\}$, with the experimental frequency f_i for the measure i , and a guess density matrix $\hat{\rho}$. The algorithm is based on the definition of an operator $\hat{R}[\hat{\rho}]$:

$$\hat{R}[\hat{\rho}] = \sum_i \frac{f_i}{\text{tr}\{\hat{\rho}\hat{E}_i\}} \hat{E}_i, \quad (3.44)$$

and the transformation

$$\hat{\rho} \rightarrow \hat{\rho}' = \frac{\hat{R}[\hat{\rho}] \hat{\rho} \hat{R}[\hat{\rho}]}{\text{tr}\{\hat{R}[\hat{\rho}] \hat{\rho} \hat{R}[\hat{\rho}]\}}. \quad (3.45)$$

We remark that if $\hat{\rho}$ is the maximum likelihood density matrix $\hat{\rho}_{\text{ML}}$, we have $\pi_i = \text{tr}\{\hat{\rho}_{\text{ML}}\hat{E}_i\} \approx f_i$, implying that $\hat{R}[\hat{\rho}_{\text{ML}}] \approx \sum_i \hat{E}_i = \mathbb{1}$. Thus $\hat{\rho}_{\text{ML}}$ is left unchanged by the transformation (3.45), with $\mathcal{L}[\hat{\rho}'] \geq \mathcal{L}[\hat{\rho}]$ [140]. The iterative application of the transformation (3.45) thus yields a series of density matrices that have increasing likelihood with respect to the experimental data.

Concretely, we measure in our case the relative plane wave atomic populations $|c_\ell(t)|^2$ of the prepared state evolving in the static lattice during a time interval $t \in [t_c, t_c + t_{\text{rec}}]$ with a number N_t of measurement times (unless specified otherwise, we use $t_{\text{rec}} = 100 \mu\text{s}$ and $N_t = 21$ time steps). Considering all the evolution data as our measurement ensemble, an atom is measured at time t in the plane wave ℓ with frequency

$$f_i = f_{\ell,t} = \frac{1}{N_t} |c_\ell(t)|^2. \quad (3.46)$$

As we intend to use these measurements to reconstruct the state prepared at t_c , the elements of the POVM are therefore

$$\hat{E}_i = \hat{E}_{\ell,t} = \frac{1}{N_t} \hat{U}^\dagger(t, t_c) |\chi_\ell\rangle \langle \chi_\ell| \hat{U}(t, t_c), \quad (3.47)$$

with $\hat{U}(t, t_c)$ the evolution operator in the static lattice potential from t to t_c . This allows to define the operator \hat{R} (3.44) for a given density matrix. With these expressions, we implement the algorithm summarized in the following box.

Summary of the iterative maximum likelihood algorithm

1. Set an initial guess state $\hat{\rho}^{(i=0)}$.
2. At iteration i , construct $R[\hat{\rho}^{(i)}] = \sum_j f_j E_j / \text{tr}\{\hat{\rho}^{(i)} E_j\}$.
3. Transform $\hat{\rho}^{(i)} \rightarrow \hat{\rho}^{(i+1)} = R[\hat{\rho}^{(i)}] \hat{\rho}^{(i)} R[\hat{\rho}^{(i)}] / \text{tr}\{R[\hat{\rho}^{(i)}] \hat{\rho}^{(i)} R[\hat{\rho}^{(i)}]\}$.
4. Iterate from step 2 until $\mathcal{L}[\hat{\rho}^{(i+1)}] - \mathcal{L}[\hat{\rho}^{(i)}] \approx 0 \Leftrightarrow \hat{\rho}^{(i+1)}$ converged to $\hat{\rho}_{\text{ML}}$.

As our initial guess for the one-body density matrix, we set $\hat{\rho}^{(0)} = \mathbb{1}_{d_{\text{H}}}/d_{\text{H}}$, with $d_{\text{H}} = 2\ell_{\text{max}} + 3$ chosen as the cut-off dimension of the Hilbert space in order to avoid boundary effects, ℓ_{max} being the highest diffraction order at which some signal is experimentally detected (for the experiments presented in the following section, we have $2 \leq \ell_{\text{max}} \leq 6$). Our choice for $\hat{\rho}^{(0)}$ is the state that maximizes the von Neumann entropy¹¹, which corresponds to the most unbiased guess with no assumption on the state to be reconstructed. Finally, two indicators are computed to certify the preparation: the fidelity of $\hat{\rho}_{\text{ML}}$ to the numerically propagated state $\mathcal{F}_{\text{exp}} = \langle \psi_{\text{QOC}} | \hat{\rho}_{\text{ML}} | \psi_{\text{QOC}} \rangle$ and the purity $\gamma = \text{tr}\{\hat{\rho}_{\text{ML}}^2\}$ which is an indicator of our preparation reproducibility over the realizations used for the reconstruction (see next paragraph). We illustrate the quantum state reconstruction process in Fig.3.7 with an experimental example taken from the next section.

Note on the framework shift and the introduction of density matrices. Beside the reconstruction formalism, one can apprehend the shift from working with kets to working with one-body density matrices as the need to introduce mixed states in order for the reconstructed evolution to have a chance to match the experimental data. Indeed, we recall that our experimental data along time are the preparation of several states $|\psi_j(t_c)\rangle$ identical to the extent of our experimental abilities and evolved for increasing times (before being destructed for the momentum distributions measurement, see Sec. 2.3). Thus, one can expect the theoretical state whose evolution maximizes the likelihood with the experimental data to be a state resulting of some statistical mix of the states $|\psi_j\rangle$, with a purity γ quantifying the reproducibility of the preparation.

In the following, we apply this state reconstruction scheme to evaluate the preparation of translated Gaussian states, superpositions of Gaussian states and squeezed Gaussian states using our QOC protocol.

3.3.4 Non-squeezed Gaussian states

In this section, we prepare and reconstruct non-squeezed Gaussian states centered at arbitrary positions in phase space. As already introduced in Sec. 1.4.1 where we introduced the Husimi representation of a state in the (x, p) phase space, we define non-squeezed Gaussian states in our Bloch system as the Gaussian states that have the same (x, p) aspect ratio as the

¹¹The von Neumann entropy reads $S = -\text{tr}\{\hat{\rho} \ln \hat{\rho}\}$.

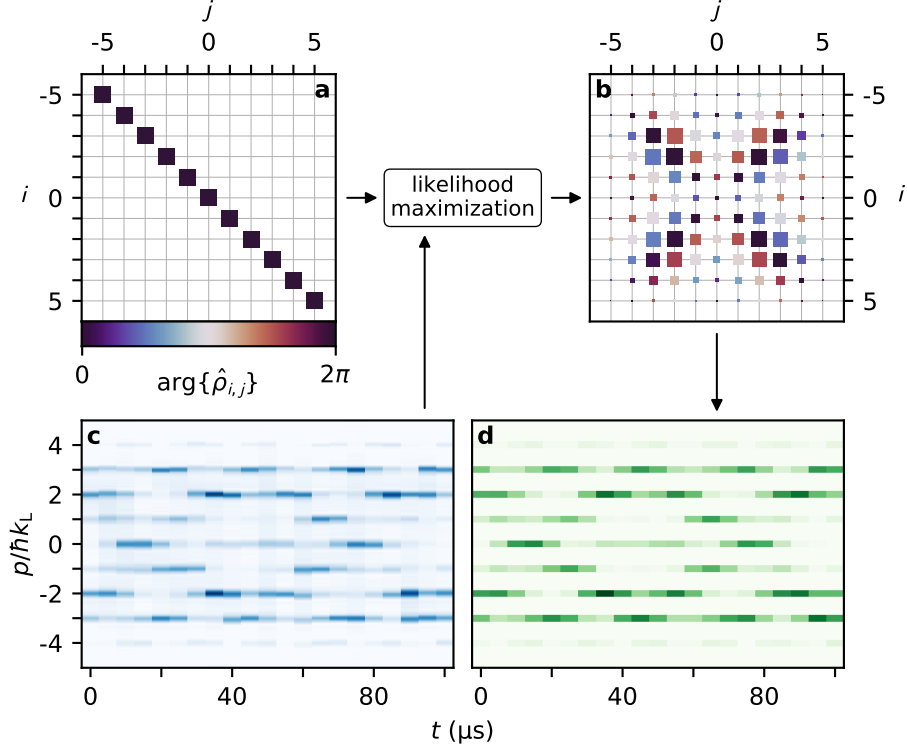


Figure 3.7 | Quantum state reconstruction in a Bloch system by likelihood maximization. (a-b) Density matrices $\hat{\rho}$ with $\arg\{\hat{\rho}_{i,j}\}$ color coded and $|\hat{\rho}_{i,j}|$ size coded (not to scale between panels). (a) Identity matrix $\mathbb{1}_{d_H}/d_H$ ($d_H = 11$) as the initial guess. (b) Density matrix of maximum likelihood $\hat{\rho}_{\text{ML}}$. (c) Stack of experimental integrated absorption images taken during the evolution of the prepared state in the static lattice at $s = 5.5 \pm 0.5$. (d) Diagonal terms of the numerical propagation of $\hat{\rho}_{\text{ML}}$, whose evolution maximizes the likelihood of results in (c). These data correspond to the experiment of Fig. 3.8(d) (see below).

ground state of the harmonic oscillator that approximates the bottom of each lattice well. We here denote as $|g(u, v)\rangle$ this state displaced in phase space by $(u, v) = (k_L \langle \hat{x} \rangle_{g(u,v)}, \langle \hat{p} \rangle_{g(u,v)} / \hbar k_L)$. In this system of coordinates, Eq. (1.50) for the plane wave coefficients of this state becomes

$$c_\ell(u, v) = \left(\frac{2}{\pi \sqrt{s_0}} \right)^{1/4} e^{iuv/2} e^{-ilv} e^{-(l-v)^2/\sqrt{s_0}}. \quad (3.48)$$

We write Δx_0 and Δp_0 the position and momentum standard deviation for this non-squeezed state. We have $k_L \Delta x_0 = s^{-1/4}$ and $\Delta p_0 / \hbar k_L = s^{1/4}/2$.

To present the results for the preparations of such phase space distributions, we compare the Husimi function $Q_{\hat{\rho}}(u, v) = \langle g(u, v) | \hat{\rho} | g(u, v) \rangle / 2\pi$ (see Sec. 1.4.1) of the numerically prepared states $\hat{\rho}_{\text{QOC}} = |\psi_{\text{QOC}}\rangle \langle \psi_{\text{QOC}}|$ and corresponding density matrices $\hat{\rho}_{\text{ML}}$ reconstructed from experimental data. We show results of non-squeezed state preparations in Fig. 3.8(a-c) with quantitative details in Table 3.4. We see that we are able to prepare non-squeezed Gaussian states with high fidelity to numerical simulations ($\mathcal{F}_{\text{exp}} \geq 0.86$) and great purity ($\gamma \geq 0.93$). As discussed in the previous section, our experimental reconstruction data comes from several

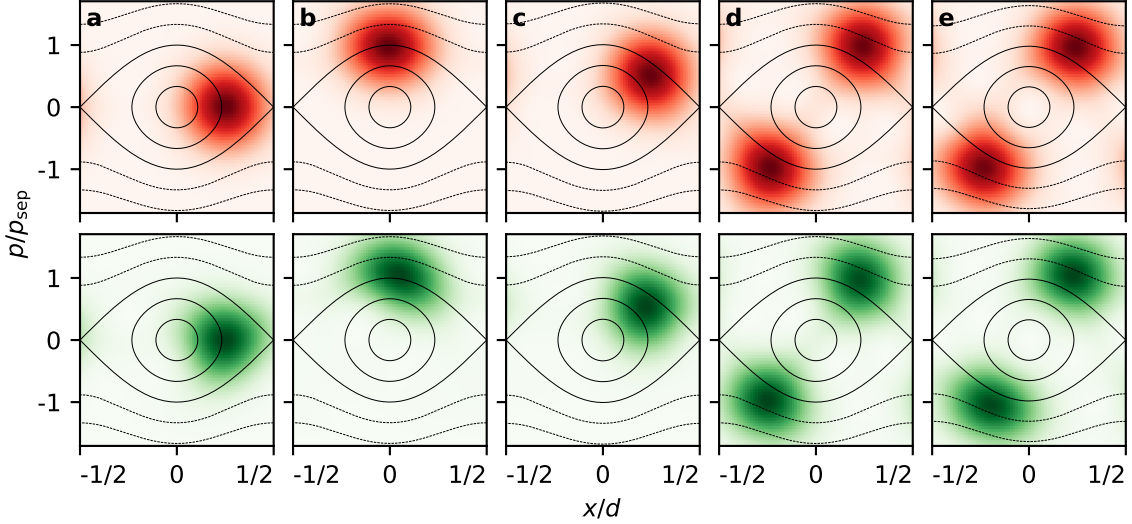


Figure 3.8 | Experimental preparation and measurement of non-squeezed Gaussian states. (a-e) Husimi representations in the phase space of the static lattice. Top (red): states $|\psi_{\text{QOC}}\rangle$ numerically prepared by optimal control. Bottom (green): density matrices $\hat{\rho}_{\text{ML}}$ reconstructed from experimental data by likelihood maximization. The relative phases in the superpositions (d,e) are respectively 0 and π (see text). The colormap value for each Husimi function extends from 0 to its maximum value. See Table 3.4 for associated experimental parameters and figures of merit.

Fig. 3.8	a	b	c	d	e
u	$\pi/2$	0	$\pi/2$	$\pm\pi/2$	$\pm\pi/2$
v	0	\sqrt{s}	$\sqrt{s}/2$	$\pm\sqrt{s}$	$\pm\sqrt{s}$
\mathcal{F}_{exp}	0.95	0.86	0.93	0.89	0.91
γ	0.95	0.96	0.93	0.82	0.91
s	5.50 ± 0.25	5.49 ± 0.20	5.57 ± 0.20	5.5 ± 0.5	5.30 ± 0.25

Table 3.4 | Parameters used for the preparation of non-squeezed Gaussian states and figures of merit obtained from their reconstruction. For all experiments $\mathcal{F}_{\text{num}} > 0.995$ and $t_c = 1.75 T_0$. This table refers to Fig. 3.8.

independent initial states evolved for different durations before measurement. We thus attribute the eventual decrease in purity to experimental fluctuations. In Fig. 3.8(d,e), we realize even and odd superpositions of non-squeezed Gaussian states, that is

$$|\psi_{\text{T}}^{(\Delta\phi)}\rangle = \frac{1}{\sqrt{2}} \left(|g(u, v)\rangle + e^{i\Delta\phi} |g(-u, -v)\rangle \right), \quad (3.49)$$

with $\Delta\phi = 0, \pi$ for (d,e) respectively. While very little difference is observed between the Husimi functions¹² of the two superpositions realized (both for $|\psi_{\text{QOC}}\rangle$ and $\hat{\rho}_{\text{ML}}$), the differences between their momentum evolutions (shown in Fig. 3.9) allow to unambiguously identify the prepared states. This allows us to iteratively reconstruct density matrices $\hat{\rho}_{\text{ML}}^{(\text{d})}$ and $\hat{\rho}_{\text{ML}}^{(\text{e})}$ with good purity

¹²The apparent similitude between the Husimi functions of the Gaussian state superpositions realized is a known feature of the Husimi quasi-distribution of probability [153].

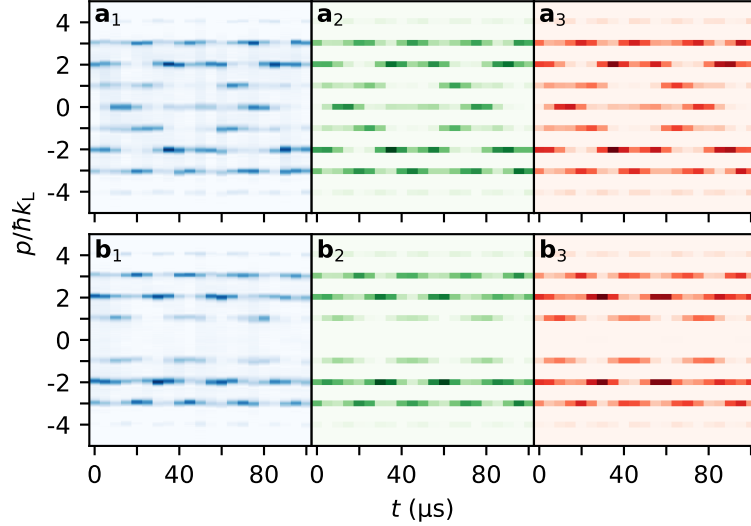


Figure 3.9 | Evolution of the momentum distribution of superpositions of Gaussian states in the static lattice. Top panels (a) correspond to the even superposition of Fig. 3.8(d). Bottom panels (b) correspond to the odd superposition of Fig. 3.8(e). (a₁-b₁) Stacks of experimental integrated absorption images taken during the evolution of the prepared states in the static lattice. (a₂-b₂) Numerical evolution of the diagonal terms of the density matrices reconstructed from (a₁-b₁). (a₃-b₃) Numerical evolution of the numerically prepared states $|\psi_{\text{QOC}}\rangle$. See Table 3.4 for details.

($\gamma \geq 0.82$) and consistency with numerical simulations: $\mathcal{F}_{\text{exp}}^{(d)} = 0.89$ and $\mathcal{F}_{\text{exp}}^{(e)} = 0.91$ (see Table 3.4). This is further confirmed by the very low cross fidelities $\mathcal{F}(|\psi_{\text{QOC}}^{(d)}\rangle, \hat{\rho}_{\text{ML}}^{(e)}) = 0.026$ and $\mathcal{F}(|\psi_{\text{QOC}}^{(e)}\rangle, \hat{\rho}_{\text{ML}}^{(d)}) = 0.042$ (as the targets for Fig. 3.8(d,e) are orthogonal). To our knowledge, there is no adiabatic method for preparing such superpositions of translated Gaussian states in the lattice.

3.3.5 Squeezed Gaussian states

In this last section of experimental results about wave function control, we apply our preparation and reconstruction procedures to the squeezing of Gaussian states. We define the x -squeezing parameter as the ratio of standard deviations $\xi = \Delta x / \Delta x_0 = (\Delta p / \Delta p_0)^{-1}$, with Δx_0 and Δp_0 the non-squeezed standard deviations (see previous section). Including ξ in the definition of our Gaussian states, Eq. (3.48) becomes

$$c_\ell^{(\xi)}(u, v) = \left(\frac{2\xi^2}{\pi\sqrt{s_0}} \right)^{1/4} e^{iuv/2} e^{-ilu} e^{-\xi^2(l-v)^2/\sqrt{s_0}}. \quad (3.50)$$

For the squeezed Gaussian state $|g^{(\xi)}\rangle$ at lattice depth s_0 , position and momentum standard deviations are given by $k_L \Delta x = \xi s_0^{(-1/4)}$ and $\Delta p / \hbar k_L = s_0^{1/4} / 2\xi$. In our periodic system, the upper bound on ξ is infinite and is reached when only a single diffraction order ℓ is populated (we have shown results up to $|\ell| = 10$ in Sec. 3.2.2). Figure 3.10 and Table 3.5 display results of squeezed Gaussian states positioned at the center of the phase space ($(u, v) = (0, 0)$) for $1/\xi$

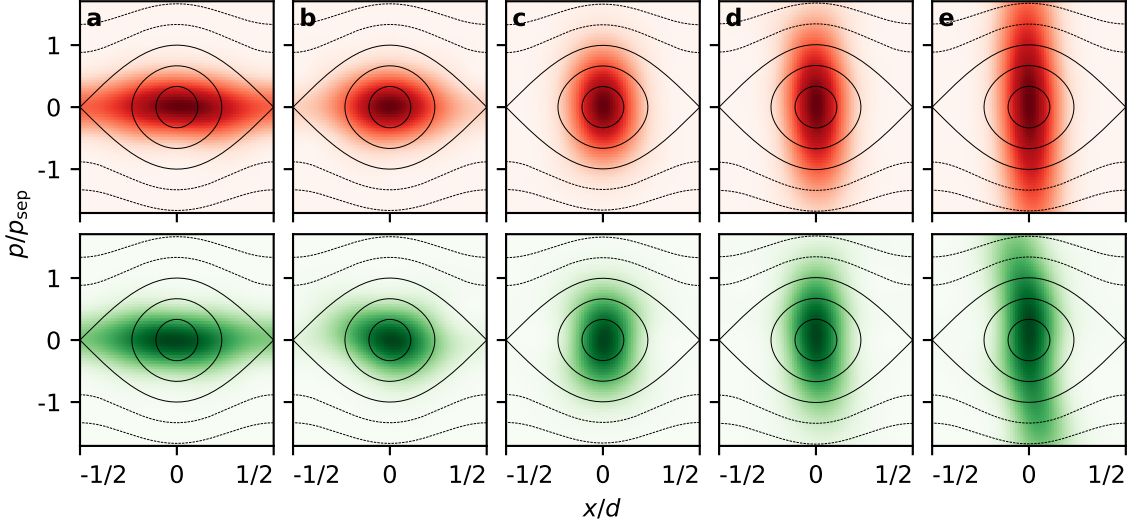


Figure 3.10 | Experimental preparation and measurement of squeezed Gaussian states. (a-e) Husimi representations in the phase space of the static lattice. Top (red): states $|\psi_{\text{QOC}}\rangle$ numerically prepared by optimal control. Bottom (green): density matrices $\hat{\rho}_{\text{ML}}$ reconstructed from experimental data by likelihood maximization. The colormap value for each Husimi function extends from 0 to its maximum value. See Table 3.5 for details.

Fig. 3.10	a	b	c	d	e
$1/\xi$	0.44	0.62	1.65	2.75	4.34
\mathcal{F}_{num}	— > 0.995 —		—	0.980	0.965
\mathcal{F}_{exp}	0.99	0.96	0.98	0.93	0.75
γ	1.00	1.00	1.00	0.92	0.72
s	5.49 ± 0.20	5.49 ± 0.20	5.45 ± 0.40	5.57 ± 0.20	5.62 ± 0.25
t_c/T_0	— 1.75 —		—	—	2
$t_{\text{rec}} (\mu\text{s})$	— 100 —		—	—	125

Table 3.5 | Parameters used for the preparation of squeezed Gaussian states and figures of merit obtained from their reconstruction. For all experiments $(u, v) = (0, 0)$.

ranging from 0.44 to 4.34. Up to $1/\xi = 2.75$, we prepare and reconstruct states with good fidelities and purities ($\mathcal{F}_{\text{exp}} \geq 0.93$ and $\gamma \geq 0.92$, see Fig. 3.10(a-d)). For the highly squeezed state $1/\xi = 4.34$ of Fig.3.10(e), we increase t_c to $2T_0$ in order for the QOC algorithm to converge to a control field giving a reasonable numerical fidelity \mathcal{F}_{num} . This is due to the complexity of the target state which consists in the superposition of 13 significantly populated momentum components ($|c_{|q|<7}|^2 > 0.025$) with as many complex coefficients to control. This large number of populated momentum components also makes the reconstruction more challenging, requiring a Hilbert space of dimension $d_{\text{H}} = 15$, with $15^2 = 225$ real parameters to determine in order to find $\hat{\rho}_{\text{ML}}$ (Sec. 3.3.3). To help the algorithm set this many parameters, we increase the amount of information we give it by increasing the duration of the evolution after the QOC preparation to $t_{\text{rec}} = 125 \mu\text{s}$ with $N_t = 26$ time steps. The simultaneous population of many momentum components also affects the reconstruction in that it reduces the signal-to-noise

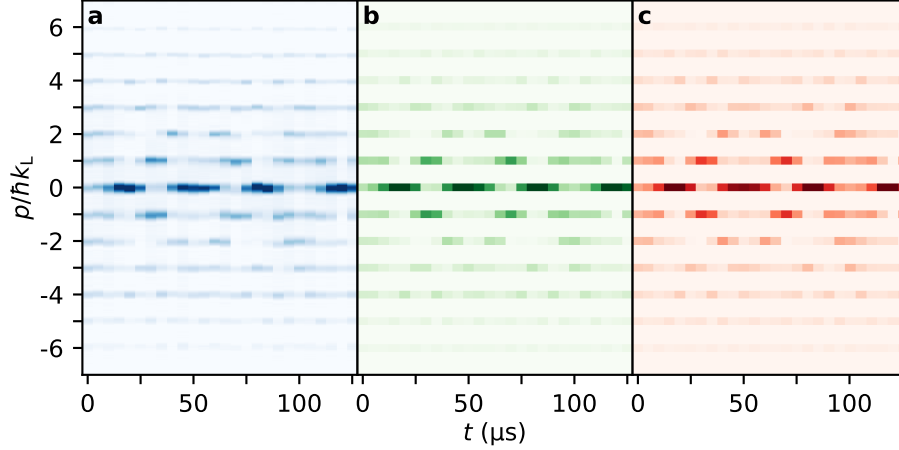


Figure 3.11 | Evolution of the momentum distribution of a highly squeezed state in the static lattice. (a) Stack of experimental integrated absorption images taken during the evolution of the prepared state in the static lattice. (b) Numerical evolution of the diagonal terms of the density matrix reconstructed from (a). (c) Numerical evolution of the state $|\psi_{\text{QOC}}\rangle$ obtained by optimal control. (b,c) correspond to the evolutions of the states presented in Fig. 3.10(e). See Table 3.5 for details.

ratio due to the lower number of atoms per diffraction peak. We illustrate this by drawing in Fig. 3.11 the momentum evolutions of the experimental, reconstructed and numerical states during their evolution in the lattice, where one sees an important loss of signal-to-noise ratio in experimental data as the magnitude of the considered momentum increases. Nevertheless, we achieve a fidelity $\mathcal{F}_{\text{exp}} = 0.75$ even in that extreme case, and all the Husimi functions of Fig. 3.10 show qualitatively very good agreement between $\hat{\rho}_{\text{ML}}$ and $|\psi_{\text{QOC}}\rangle$ for the squeezing of Gaussian states.

Interestingly, one can consider the effective lattice depth s_{eff} at which the ground state matches the squeezed Gaussian state (3.50) generated at depth s_0 with squeezing parameter ξ . Comparing Eqs. (3.48) and (3.50), one finds $s_{\text{eff}} = s_0/\xi^4$. In that sense, Fig.3.10(e) shows the realization of the ground state of a lattice of effective depth $s_{\text{eff}} \approx 2000$ in our lattice of depth $s_0 = 5.62$. This is, to our knowledge, the first realization of such a state, the production of which is technically impossible with adiabatic methods. To give an idea, the laser for the lattice in our experiment (see Sec. 2.4 and App. C) has a maximum power of 15 W, which corresponds for our setup to a maximum lattice depth of $s_0 \approx 40$. With the same setup, we thus would require a laser of about 750 W to produce a lattice depth of $s_0 \approx 2000$.

We also targeted Gaussian states both squeezed and rotated in the (x, p) plane. Target state definition and results for those experiments are presented in App. E.

3.4 An application to quantum simulation

We conclude this chapter with an example of application of our QOC protocol to quantum simulation, namely the production of the initial state for the study of dynamical tunneling in

an amplitude-modulated one-dimensional optical lattice.

3.4.1 Introduction to dynamical tunneling

As we discussed in the first chapter of this manuscript (Sec. 1.1.2), the mixed stroboscopic phase portrait of a periodically driven dynamical system features classical trajectories that are either quasi-periodic (regular) or chaotic (resulting respectively in continuous lines or spread points in the phase portrait, see *e.g.* Fig. 3.12(a₂)). In such a system, quantum particles can undergo dynamical tunneling, which consists in oscillating from one region of regular trajectories to another, crossing classically impassable Kolmogorov-Arnold-Moser surfaces (see Sec. 1.1.2 and [89]). Dynamical tunneling occurs when two non-degenerate Floquet states (Sec. 1.3.2) span the same regular regions of phase space, with a tunneling oscillation frequency proportional to the quasi-energy difference between the two states in the quasi-energy spectrum [142, 89].

In previous experiments with cold atoms in optical lattices, dynamical tunneling was studied with an initial sudden shift of the lattice to bring the ground state of the system in one of the tunnel-coupled regular regions (a representation of this approach is shown in Fig. 3.12(a) for the parameters of the dynamical tunneling experiment performed here ; see below). Although this method provides evidence of the phenomenon [154, 155, 61], more than one frequency is observed in the tunneling signal as the initial states are only partially projected in the subspace of the two relevant Floquet states that carries the dynamical tunneling of interest. Moreover, the visibility of the oscillations is limited by the unequal-weight projection onto these states. We here apply QOC as a way to optimize the initial state for the observation of dynamical tunneling. Our goal is to compare the tunneling signal between the two methods.

Following the dynamical scaling for periodically modulated potentials summarized p. 34, the Hamiltonian that we study is that of the amplitude-modulated potential¹³:

$$\tilde{H}(\tilde{x}, \tilde{p}, \tilde{t}) = \frac{\tilde{p}^2}{2} - \gamma [1 + \varepsilon_0 \cos(\tilde{t})] \cos(\tilde{x}), \quad (3.51)$$

which generates the mixed phase space of Fig. 3.12(a_{1,b}) for the parameters $(\gamma, \varepsilon_0) = (0.25, 0.1)$. We focus on the center of the stroboscopic phase portrait, where a classical particle, stroboscopically observed every two periods of modulation, is bound to the lateral harmonic-oscillator-like region it started in (see Fig. 3.13(a)). We fix $\hbar_{\text{eff}} = 0.355$ (which corresponds to the experimental parameters $s_0 = 7.93$ and $\nu = 45.697$ kHz, see p. 34) for the dynamical tunneling timescale to be compatible with the two-period stroboscopic sampling¹⁴. Our optimal-control target is the state that maximizes the visibility of the tunneling oscillation, that is the equal-weight superposition of the two main Floquet states $|\varphi_A\rangle$ and $|\varphi_B\rangle$ in the central regular region of the stroboscopic phase portrait. Once the Floquet states are obtained through diagonalization of the Floquet

¹³Note that γ is the scaled depth of the potential, and no longer the purity of a density matrix.

¹⁴For $\hbar_{\text{eff}} = 0.355$, numerical simulations give a dynamical tunneling period of approximately $20T$ where $T = 1/\nu$ is the period of modulation of the potential. As the system is observed every 2 periods, we thus expect to sample the tunneling signal with approximately 10 measures per tunneling period, which is satisfactory.

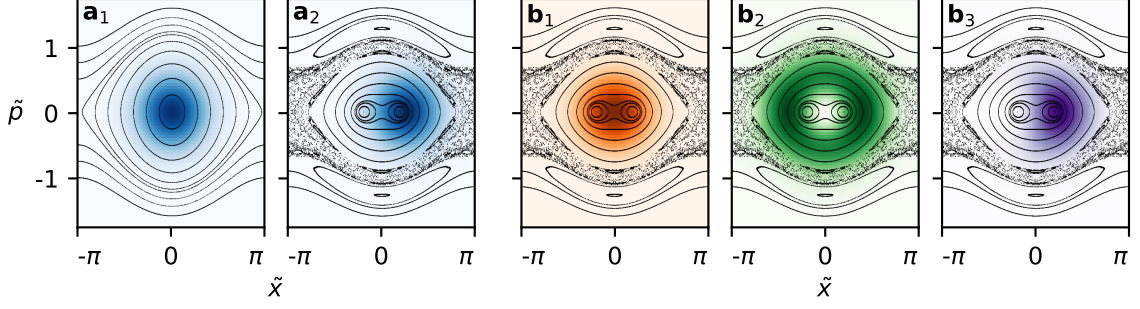


Figure 3.12 | Initial states for dynamical tunneling. Husimi representations and underlying classical phase spaces for (a) the states involved in the translation method and (b) the relevant Floquet states (see text). **(a₁)** Lattice ground state $|\phi_{n=0}\rangle$. **(a₂)** Translation of the ground state $\hat{T}_{\Delta\tilde{x}_R}|\phi_{n=0}\rangle$ just after the start of the modulation. **(b₁)** One of the relevant Floquet state $|\varphi_A\rangle$. **(b₂)** The other relevant Floquet state $|\varphi_B\rangle$. **(b₃)** The ideal superposition of Floquet states $|\psi(\theta_R)\rangle$. See text for the definitions of these states. The colormap for each Husimi function extends from 0 to its maximum value. Parameters are $(\gamma, \varepsilon_0, \hbar_{\text{eff}}) = (0.25, 0.1, 0.355)$.

operator (*i.e.* the evolution operator over one modulation period, see 1.3.2), we identify $|\varphi_{A,B}\rangle$ from their overlap with a non-squeezed Gaussian state (Eq. (3.48)) translated in the center of one of the lateral harmonic-oscillator-like region of the stroboscopic phase portrait. We show the Husimi functions of $|\varphi_{A,B}\rangle$ in Fig. 3.12(b₁, b₂). The theoretical state that maximizes the visibility of the tunneling oscillation reads

$$|\psi(\theta)\rangle = \frac{1}{\sqrt{2}} \left(|\varphi_A\rangle + e^{i\theta} |\varphi_B\rangle \right) \quad (3.52)$$

where the relative phase θ between the Floquet states $|\varphi_A\rangle$ and $|\varphi_B\rangle$ fixes the initial condition for the oscillation between the two lateral regular regions. We arbitrarily fix a starting point in the right region, so we set $\theta = \theta_R$ defined as

$$\theta_R = \arg \max_{\theta} \left\{ \left\langle \hat{x} \right\rangle_{\psi(\theta)} \right\} \quad (3.53)$$

Our optimal-control target is thus $|\psi(\theta_R)\rangle$. We draw the Husimi distribution of this state in Fig. 3.12(b₃). Finally, in order to compare the QOC approach with the signal obtained from the translated¹⁵ ground state $\hat{T}_{\Delta\tilde{x}}|\phi_{n=0}\rangle$, we determine the optimal translation distance $\Delta\tilde{x}_R$ as the one that maximizes the overlap between $\hat{T}_{\Delta\tilde{x}}|\phi_{n=0}\rangle$ and the ideal state $|\psi(\theta_R)\rangle$:

$$\Delta\tilde{x}_R = \arg \max_{\Delta\tilde{x}} \left\{ \left| \langle \psi(\theta_R) | \hat{T}_{\Delta\tilde{x}} | \phi_{n=0} \rangle \right|^2 \right\}. \quad (3.54)$$

For our modulation parameters, we find a maximum overlap $|\langle \psi(\theta_R) | \hat{T}_{\Delta\tilde{x}_R} | \phi_{n=0} \rangle|^2 \approx 0.91$ for the translation method. The Husimi distributions of the states $|\phi_{n=0}\rangle$ and $\hat{T}_{\Delta\tilde{x}_R}|\phi_{n=0}\rangle$ are

¹⁵See Sec. 1.2.1 for an expression of the translation operator.

shown in Fig. 3.12(a).

3.4.2 Experimental results

For the experiment without QOC, the ground state is translated by a distance $\Delta\tilde{x}_R$ by applying a sudden phase shift $\varphi_0 = \Delta\tilde{x}_R$ (which spatially translates the lattice by a quantity $-\Delta\tilde{x}_R/k_L$, see Eq. (3.11)) right between the lattice loading and the beginning of the amplitude modulation. For the QOC experiment, we choose the ground state of the static lattice as our initial state for the QOC preparation. The amplitude modulation begins immediately after the QOC stage. Our control parameter remains the phase of the lattice $\varphi(t)$, with a control duration set to $t_c = 1.75 T_0$. The QOC algorithm (p. 72) converges to a control field reaching numerical fidelity $\mathcal{F}_{\text{num}} > 0.995$.

In this dynamical tunneling experiment, the tunneling takes place between two region of the x axis, separated by a fraction of the lattice step $d = 532$ nm. Our imagery setup (Sec. 2.3) cannot spatially resolve the phenomenon *in-situ*. The trick is to transfer the spatial information along the momentum axis using the sub-stroboscopic dynamics (see Fig. 1.4). To do so, after evolution in the modulated potential, and before TOF measurement, we modulate the potential during an additional half-period to perform a $\pi/2$ -rotation around the center of the phase space and convert the population in the right (resp. left) regular region of the lattice well into negative (resp. positive) momentum components accessible through TOF [61]. This phase portrait rotation technique is illustrated in Fig. 3.13(a-b).

Figure 3.13(c-j) compares the results of dynamical tunneling experiments when the initial state is either approximated by a translation of the ground state (Fig.3.13(c-f)) or targeted by our optimal control method (Fig.3.13(g-j)). The spectral content of the oscillations is clearly refined when the two-Floquet state superposition is prepared, resulting in a greater signal-to-noise ratio for the measurement of the atomic tunneling frequency.

Chaos-assisted tunneling. Our application of QOC to dynamical tunneling is inspired from the study [61] of chaos-assisted tunneling (CAT) [88, 89] that we performed in 2020 in collaboration with M. Martinez, G. Lemarié and B. Georgeot from the *Laboratoire de Physique Théorique* (Toulouse) and O. Giraud and D. Ullmo from the *Laboratoire de Physique Théorique et Modèles Statistiques* (Paris). CAT is a type of dynamical tunneling where the tunneling between the two regular region is carried by two Floquet states mainly located on these regions, as well as by a third Floquet state delocalized over the chaotic sea (see Fig. 1.9 for an example of such a state). Under the variation of an external parameter of the system (*e.g.* the frequency of modulation), CAT resonances were predicted [88], associated with a non-monotonic variation of the tunneling frequencies in that three-level system. In our publication [61], we were the first to unambiguously observe such a resonance of CAT with matter wave. I recall that, while I chose not to present in my manuscript this research axis in which I participated, details of this study can be find in the thesis of M. Arnal [67], G. Chatelain [68] and M. Martinez [69].

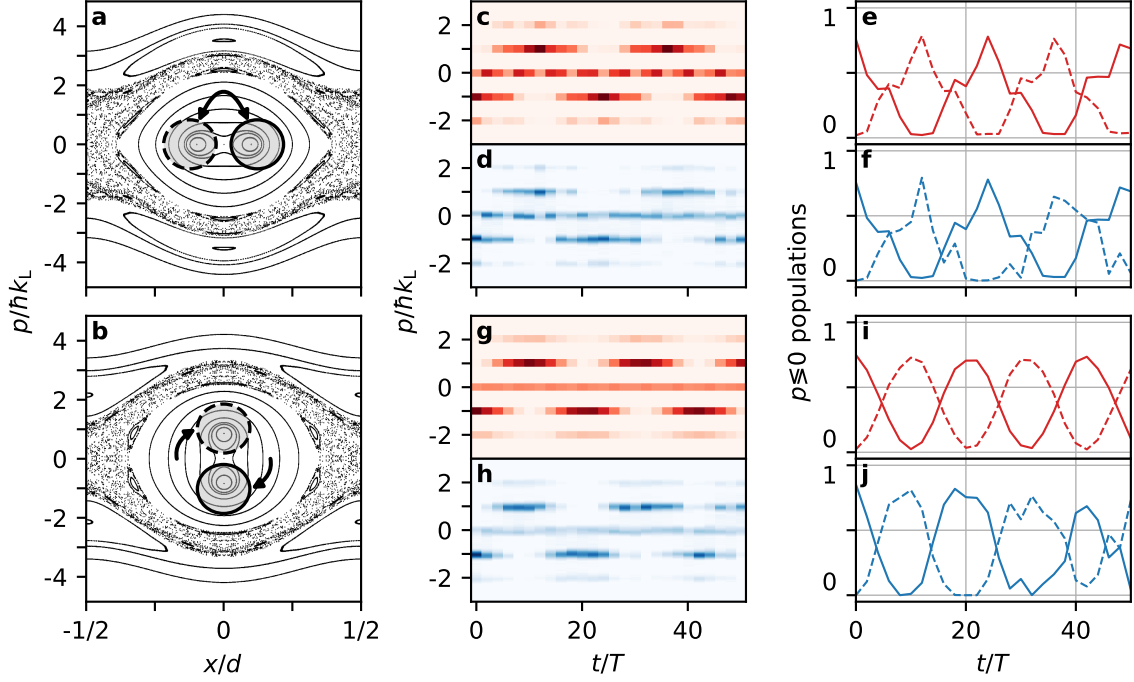


Figure 3.13 | Quantum-optimal control applied to dynamical tunneling experiments. (a) Stroboscopic phase portrait for the amplitude-modulated potential (3.51) with the initially populated region (gray area with black solid line border) and the coupled regular region that gets populated through dynamical tunneling (gray area with black dashed line border). (b) Same as (a) after the $\pi/2$ -phase space rotation (see text). (c-f) Results for the initially translated ground state. (g-j) Results with the initial state obtained from optimal control. (c,g) Numerical evolution of the momentum distribution. (d,h) Corresponding stack of experimental integrated absorption images. (e,i) Numerical and (f,j) experimental evolutions of the negative (solid line) and positive (dashed line) momentum populations, originating from the regions identified in (a,b) with the matching contouring line-style.

Importantly, in our experiments on CAT [61], we observed that a large number of atoms in the BECs happens to have a deleterious effect on the time during which dynamical tunneling signals could be observed¹⁶. In [61], we indeed have had to measure signals over up to hundreds of modulation periods of the potential, and reducing the number of atoms in the BECs by a factor of 10 had a salutary effect on this experiment. Since then, the modification of the dipole trap geometry on our experiment (Sec. 2.2.3) has led to the setup regularly producing BECs with up to five times more atoms. We thus point out that similar reduction of the number of atoms in the BECs were performed for the experiment of this section, where we worked with BECs of $N \approx 5 \cdot 10^4$ atoms, *i.e.* 10 times less than what the experiment produces. The protocol to reduce the number of atoms in the BECs is discussed in Sec. 2.2.4.

Conclusion

In this chapter, we discussed the successful implementation of quantum-optimal control

¹⁶We attribute this phenomenon to the interactions between atoms, but the exact mechanism is still unclear.

(QOC) in our experiment to control the motional state of BECs in a one-dimensional optical lattice. QOC allows us to target states either unreachable by adiabatical means or in comparatively much shorter time.

In a first set of experiments, we established our ability to prepare given momentum distributions in the lattice. In a second step, we demonstrated full and reliable control of the external quantum state in which we prepare the atoms. We applied this control for the preparation of specific states in the phase space of the system. Such state control is a great tool for quantum simulation, notably in the semi-classical regime (Sec. 1.4.2) where quantum dynamics is strongly related to the underlying structures in the classical phase space. We concluded this chapter with an example of application of QOC for quantum simulation in a study of dynamical tunneling in the depth-modulated optical lattice. In this last example, we demonstrated our ability to target Floquet states of a given time-periodic Hamiltonian.

Quantum state control raises the question: How does one certifies proper state preparation? In our first experiments of momentum distribution preparation, the information was readily accessible through TOF imaging. We however required dedicated protocols when we targeted a broader range of quantum states (associated with sets of *complex* coefficients). Our general approach was to use data from the subsequent evolution of the prepared state in the static lattice as information to infer this prepared state. For simple momentum superposition targets, this was achieved through least-square analysis. To reconstruct the quantum state in the general case, we implemented a full quantum state tomography using a maximum-likelihood iterative approach, which allowed us to characterize our experimental states and confirm the success of the optimal-control preparation.

Chapter 4 - Non-diffusive Hamiltonian ratchet

[...] because we pull up the shades and let the light out, because we cool off on the earth and get heat from the sun, the ratchets and pawls that we make can turn one way. This one-wayness is interrelated with the fact that the ratchet is part of the universe. It is part of the universe not only in the sense that it obeys the physical laws of the universe, but its one-way behavior is tied to the one-way behavior of the entire universe. It cannot be completely understood until the mystery of the beginnings of the history of the universe are reduced still further from speculation to scientific understanding.

Richard Feynman (The Feynman Lectures on Physics, Vol. 1, Chap. 46, 1963)

Contents

Introduction	99
4.1 Designing a non-diffusive Hamiltonian ratchet in classical mechanics	102
4.1.1 Hamiltonian system considered and statement of the problem	102
4.1.2 Search for modulation parameters	104
4.1.3 Results of classical mechanics	106
4.2 Quantum ratchet transport along regular classical trajectories	108
4.2.1 A Floquet system	108
4.2.2 Influence of the effective Planck constant and Floquet state mixing	110
4.3 Experimental ratchet transport of matter waves	112
4.3.1 Transport from the ground state	113
4.3.2 Preparation of the ratcheting Floquet state using quantum-optimal control	116
Conclusion	118

Introduction

A ratchet is a mechanical device that constrains the movement of a system in a defined direction. Its mechanism is schematically depicted in its rotating configuration in Fig. 4.1: if we apply torque on the gear, the combined effect of the pawl and the axial asymmetry of the tothing prevents the gear from rotating counterclockwise. Ratchets are widespread mechanisms that are part of many common devices, such as pendulum clocks, ratchet wrenches or bicycle freewheels.

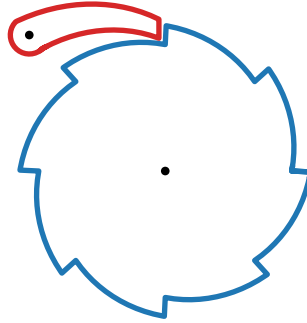


Figure 4.1 | Diagram of a mechanical rotating ratchet. Both the red pawl and the blue gear can rotate around their fixed black pivots.

In physics, ratchet became a subject of interest with G. Lippmann around 1900 [156, 157]. In a thought experiment, he considers a molecular size device that produces work from thermal noise using a ratchet mechanism to rectify the isotropy of Brownian motion. The first arguments against this setup apparently violating the second law of thermodynamics came from M. von Smoluchowski in 1912 [158], saying that as the ratchet part of the system also undergoes Brownian motion, it cannot consistently direct movement. In 1962, R. Feynman revisits the idea in the 46th chapter of his Lectures in Physics [159, 160], showing that for such a system to work, the ratchet must be held at a lower temperature than the rest of the machine, with heat flowing irreversibly between the parts (this ratchet system being *in fine* an intricate Carnot heat engine).

More abstractly, one defines the ratchet effect as the emergence of a directed current¹

$$J = \lim_{T \rightarrow \infty} \frac{1}{T} \int_0^T \dot{x}(t) dt \neq 0, \quad (4.1)$$

for a particle in a potential that is periodic in space and time:

$$V(x + d, t) = V(x, t + T) = V(x, t). \quad (4.2)$$

¹We restrict ourselves to the one dimensional case.

The ratchet effect is an intriguing phenomenon², as it directly follows from the spatial periodicity of $V(x, t)$ that no net force derives globally from such potentials:

$$\langle F(x, t) \rangle_{d, T} = \frac{1}{dT} \iint_{d, T} -\frac{\partial V(x, t)}{\partial x} dx dt = 0. \quad (4.3)$$

The operating mechanism of the ratchet effect is well understood, and relies minimally on the fact that systems featuring this effect are out of equilibrium, with time-dependent potentials that break specific space and time symmetries [161, 162, 163, 164]. Among such systems, we can distinguish two families of ratchets:

- (i) On one hand, Brownian ratchets [165, 166] consist in systems submitted to stochastic forces with a potential that rectifies the isotropy of Brownian motion [167] into a directed transport (in the fashion of the Lippmann-von Smoluchowski-Feynman ratchet). Interestingly, Brownian ratchets are thought to be the principle of operation of molecular motors [168, 169, 170, 171], as for instance for the kinesin [172], a motor protein found in eukaryotic cells. They are usually studied in the overdamped regime to account for the strong dissipation in biological media [166, 173]
- (ii) On the other hand, one has deterministic ratchets, for which the classical dynamics is captured by the phase space of the systems (Sec. 1.1.2). Deterministic ratchets are either dissipative³ or Hamiltonian [76, 182, 163].

We focus in this chapter on Hamiltonian ratchets.

As we have seen in Chap. 1, Hamiltonian systems under moderate temporal driving exhibit a mixed dynamics, with a phase space displaying islands of regular trajectories embedded in a chaotic sea of non-integrable ones. A fundamental property of chaotic systems briefly addressed in Sec. 1.1.2 is *ergodicity*, which corresponds to the fact that a classical trajectory $(\mathbf{q}_c(t), \mathbf{p}_c(t))$ (Sec. 1.1.2) initialized in a chaotic region of phase space (index “c”) will eventually span all this chaotic region uniformly [69]. Considering a physical quantity $f(\mathbf{q}, \mathbf{p})$, ergodicity formally means

$$\lim_{T \rightarrow \infty} \frac{1}{T} \int_0^T f(\mathbf{q}_c(t), \mathbf{p}_c(t)) dt = \frac{1}{V_{\Pi_c}} \int_{\Pi_c} f(\mathbf{q}, \mathbf{p}) d\mathbf{q} d\mathbf{p} \quad (4.4)$$

$$\langle f(\mathbf{q}_c(t), \mathbf{p}_c(t)) \rangle_t = \langle f(\mathbf{q}, \mathbf{p}) \rangle_{\Pi_c},$$

where Π_c stands for the considered chaotic region of phase space and V_{Π_c} its hyper-volume. Put in words, ergodicity means that a trajectory from a given chaotic region of phase space is, in

²We add that particles are usually considered starting at rest in the reference frame of the potential, and the emerging asymptotic current J (Eq. (4.1)) is also measured with respect to that reference frame. In other words, neither particles launched at high speed in unbounded phase space trajectories (Sec. 1.1.2) nor particles bound to a potential of the form (4.2) that travels linearly at $v = d/T$ are experiencing ratchet effect.

³A few references on research about dissipative deterministic ratchet: [174, 175, 176, 177, 178, 179, 180, 181]

time, representative of all trajectories from that chaotic region. Going back to one-dimensional Hamiltonian ratchets, the physical quantity $f(x(t), p(t))$ that goes into the definition of the asymptotic current J (Eq. (4.1)) is the speed $\dot{x}(t) = p(t)/m$. From the ergodicity principle (4.4), we have, for a trajectory initialized in a chaotic region Π_c ,

$$J = \frac{1}{m} \langle p_c(t) \rangle_t = \frac{1}{m} \langle p \rangle_{\Pi_c}. \quad (4.5)$$

From the right-hand side of this last equation, we see that the emergence of a non-zero asymptotic current (*i.e.* the ratchet effect) can result from the contribution of trajectories belonging to chaotic regions having a non-zero momentum barycentre. As a matter of fact, studies on Hamiltonian ratchets have so far mainly focused on so-called “diffusive Hamiltonian ratchets”, where the directed transport results from trajectories ergodically diffusing⁴ into such momentum-asymmetric chaotic seas [76, 182, 163].

We here take a different route, and study a system where the ratchet effect is based on integrable trajectories. The integrable ratchet effect has only been studied in the kicked rotor, where the ratchet effect occurs along the momentum axis (one speaks of accelerator ratchet [183, 184, 185]). The system that we study is a sine potential modulated in amplitude and phase in the fashion of the gating ratchet [186, 180]. In the simplest case of a single frequency of modulation, we determine modulation parameters such that the phase space of the system presents a regular island that travels between the sites of the periodic potential while periodically stopping in each site. This is to our knowledge the first study of such a non-diffusive ratchet effect along position space.

This chapter presents our study of this effect. The first section (Sec. 4.1) concerns the classical dynamics in this system. We then detail our method to determine modulation parameters for the integrable ratchet effect to emerge, and we then characterize the system. In the second section (Sec. 4.2), we consider quantum transport of wave functions in this Floquet system. Finally, we present experiments where we observed this non-diffusive ratchet effect with BECs in the modulated optical lattice.

The study presented in this chapter is the result of a quite personal work that I have been doing on the ratchet effect since my pre-thesis internship at LCAR in 2019. A publication is in preparation:

[65] N. Dupont, L. Gabardos, F. Arrouas, B. Peaudecerf, J. Billy and D. Guéry-Odelin, *Matter wave transport from non-diffusive Hamiltonian ratchet effect*, In preparation, (2022)

⁴We stress that, for Hamiltonian systems, this chaotic diffusion is deterministic.

4.1 Designing a non-diffusive Hamiltonian ratchet in classical mechanics

In this section, we detail our method to determine, in a classical Hamiltonian system, modulation parameters of the sine potential in order for the system to feature a non-diffusive ratchet effect in position space.

4.1.1 Hamiltonian system considered and statement of the problem

Our system. We consider a classical particle of mass m in a one-dimensional sine potential that is modulated in amplitude and phase with one harmonic at the same frequency. The corresponding time-dependent Hamiltonian can be written

$$H(x, p, t) = \frac{p^2}{2m} - [1 + \varepsilon_0 \cos(2\pi\nu t)] \frac{V_0}{2} \cos\left[\frac{2\pi x}{d} + \varphi_0 \cos(2\pi\nu t + \Delta\phi) + \Delta\varphi\right], \quad (4.6)$$

with the fixed spatial periodicity d , and the adjustable modulation parameters,

- V_0 , the average amplitude of the potential,
- ε_0 , the amplitude of amplitude modulation,
- φ_0 , the amplitude of phase modulation,
- ν , the frequency of modulation,
- and $\Delta\phi$, the relative phase between the phase and amplitude modulations.

The parameter $\Delta\varphi$ is a constant spatial phase that we set to

$$\Delta\varphi = -\varphi_0 \cos(\Delta\phi), \quad (4.7)$$

in order for the spatial origin $x = 0$ to correspond to a minimum of the potential at time $t = 0$. As we have already seen in Chap. 1, one can look for a scaling of the Hamiltonian (4.6) such that the classical dynamics depends on fewer parameters. Following the procedure summarized Sec. 1.4.1 (p. 34), we get

$$\tilde{H}(\tilde{x}, \tilde{p}, \tilde{t}) = \frac{\tilde{p}^2}{2} - \gamma [1 + \varepsilon_0 \cos(\tilde{t})] \cos[\tilde{x} + \varphi_0 \cos(\tilde{t} + \Delta\phi) + \Delta\varphi], \quad (4.8)$$

with

$$\tilde{x} = \frac{2\pi}{d} x, \quad \tilde{t} = 2\pi\nu t, \quad \tilde{p} = \frac{d\tilde{x}}{d\tilde{t}} = \frac{1}{md\nu} p, \quad \text{and} \quad \tilde{H} = \frac{1}{md^2\nu^2} H, \quad (4.9)$$

and the scaled amplitude of the potential $\gamma = V_0/2md^2\nu^2$. The scaled dynamics effectively depends on the four modulation parameters $\{\gamma, \varepsilon_0, \varphi_0, \Delta\phi\}$ (with $\Delta\varphi$ still fixed by Eq. (4.7)).

Correspondence with the gating ratchet. Our Hamiltonian (4.8) is a known system from the ratchet community, called the *gating ratchet*. To understand this designation, we perform the Galilean transformation to switch from the inertial reference frame to the frame of the phase-modulated potential:

$$\tilde{x}' = \tilde{x} + \varphi_0 \cos(\tilde{t} + \Delta\phi) + \Delta\varphi. \quad (4.10)$$

In this non-inertial frame, the lattice is stationary, and the particle experiences the pseudo force

$$\tilde{F}'(\tilde{t}) = -m\varphi_0 \cos(\tilde{t} + \Delta\phi). \quad (4.11)$$

In this system, the amplitude-modulated potential barriers between sites act as opening and closing gates whose period can be correlated with the modulated pseudo force (4.11) to induce ratchet transport. This system has been theoretically studied in the Brownian case [186], as well as experimentally in the deterministic case with dissipation [180, 164]. We here consider this system in the Hamiltonian regime as a candidate for the emergence of a non-diffusive ratchet effect.

Statement of the problem. In order to design such a non-diffusive Hamiltonian ratchet (*i.e.* with a transport based on quasi-periodic trajectories in the phase space), we ask the question: Are there modulation parameters $\{\gamma, \varepsilon_0, \varphi_0, \Delta\phi\}$ such that a classical particle starting at rest at the bottom of a site ends up in the bottom of the next site after one modulation period ($T = 1/\nu$)? Mathematically put, we are looking for modulation parameters such that the trajectory $(\tilde{x}(\tilde{t}), \tilde{p}(\tilde{t}))$ starting in

$$\begin{pmatrix} \tilde{x}(0) \\ \tilde{p}(0) \end{pmatrix} = \begin{pmatrix} 0 \\ 0 \end{pmatrix} \quad \text{goes to} \quad \begin{pmatrix} \tilde{x}(2\pi) \\ \tilde{p}(2\pi) \end{pmatrix} = \begin{pmatrix} 2\pi \\ 0 \end{pmatrix}, \quad (4.12)$$

where we arbitrarily aim for a positive ratchet displacement. From the periodicity of the potential, a direct consequence of this hypothetical trajectory is that $\tilde{x}(\tilde{t} = 2\pi n) = 2\pi n$ with $n \in \mathbb{N}$, resulting in a constant⁵ ratchet current $J = 1$ (Eq. (4.1)).

⁵At least stroboscopically constant, *i.e.* when evaluated after an integer number of modulation periods.

4.1.2 Search for modulation parameters

We are looking for modulation parameters $\{\gamma, \varepsilon_0, \varphi_0, \Delta\phi\}$ such that a classical particle described by the Hamiltonian (4.8) follows a trajectory passing by the two phase space points of Eq. (4.12).

From the correspondence with the gating ratchet discussed above, we simplify the problem by reducing the set of parameters: we set the relative phase $\Delta\phi$ between the amplitude and phase modulations to a value that optimizes the gating effect in this system. With the gating potential (4.8), the most efficient way [180] to induce a positive ratchet current is to have $\Delta\phi = \pi/2$ (*i.e.* a phase quadrature between the amplitude and phase modulations). In this case, the pseudo force becomes $\tilde{F}'(\tilde{t}) = m\varphi_0 \sin(\tilde{t})$, which is maximally positive (resp. negative) a quarter of a period before the instant at which the potential barrier between neighboring sites is minimum (resp. maximum), resulting in a configuration that globally favors a positive ratchet transport. Our Hamiltonian becomes

$$\tilde{H}(\tilde{x}, \tilde{p}, \tilde{t}) = \frac{\tilde{p}^2}{2} - \gamma [1 + \varepsilon_0 \cos(\tilde{t})] \cos[\tilde{x} - \varphi_0 \sin(\tilde{t} + \Delta\phi)], \quad (4.13)$$

with a set of modulation parameters reduced to $\{\gamma, \varphi_0, \varepsilon_0\}$.

To determine values for these three parameters, we note that, for the periodic trajectory (4.12) that we are looking to induce, the initial and final conditions have the same mechanical energy (evaluated by the Hamiltonian (4.13)), which is the global minimum of mechanical energy for this system:

$$\tilde{H}(2\pi n, 0, 2\pi n) = -\gamma(1 + \varepsilon_0), \quad (4.14)$$

with $n \in \mathbb{Z}$. Our search for modulation parameters can thus be expressed as a minimization problem, where we want to minimize, as a function of $\{\gamma, \varepsilon_0, \varphi_0\}$, the increase of mechanical energy over one modulation period for a trajectory starting in $(\tilde{x}(0), \tilde{p}(0)) = (0, 0)$ and ending in the neighboring site⁶. We define the function to minimize:

$$g(\gamma, \varepsilon_0, \varphi_0) = \begin{cases} \tilde{H}_{\gamma, \varepsilon_0, \varphi_0}[\tilde{x}(2\pi), \tilde{p}(2\pi), 2\pi] - \tilde{H}_{\gamma, \varepsilon_0, \varphi_0}[\tilde{x}(0), \tilde{p}(0), 0] & \text{if } \pi < \tilde{x}(2\pi) < 3\pi \\ \text{a large number} & \text{otherwise,} \end{cases} \quad (4.15)$$

where the condition is set to force the particle to change site. We proceed numerically to minimize $g(\gamma, \varepsilon_0, \varphi_0)$, with numerical integration⁷ of the trajectories $(\tilde{x}(t), \tilde{p}(t))$.

⁶One must be careful with this condition for the restatement of our problem, as, for instance, an absence of modulation $(\varepsilon_0, \varphi_0) = (0, 0)$ results in a constant trajectory $(\tilde{x}(\tilde{t}), \tilde{p}(\tilde{t})) = (0, 0)$ that also trivially minimizes the variation of mechanical energy.

⁷We use the Runge-Kutta ‘‘RK4’’ method to integrate classical dynamics.

Nelder-Mead algorithm. To tackle this minimization problem, we use Nelder-Mead [187] method^{8,9}: given a function $f(\mathbf{u}) : \mathbb{R}^N \mapsto \mathbb{R}^+$ to be minimized and a guess $\mathbf{u}^{(0)}$, this iterative method consists in considering a polytope of $N + 1$ vertices \mathbf{u}_i initialized in the neighborhood of $\mathbf{u}^{(0)}$. The function f is evaluated at each vertex, which are then iteratively moved from the one that maximizes f to the one that minimizes f until they all converge toward the same local minimum for f . The Nelder-Mead method is an efficient alternative to gradient-descent methods when the gradient of the function to be minimized cannot be written explicitly, as it is the case for us with $f(\mathbf{u}) = g(\gamma, \varepsilon_0, \varphi_0)$ (Eq. (4.15)). As is generally the case when employing iterative methods of optimization, we want our initial guess to be in the vicinity of a global optimum.

Initial guess. To be able to minimize Eq. (4.15), we minimally require an initial guess such that the particle is located in the next site after one modulation period. To find such initial guesses, we start by maximizing the energy transferred to the particle at the beginning of the modulation by making our initial guess correspond to a modulation frequency that is resonant with the harmonic frequency ν_0 at the bottom of the potential wells. For the Hamiltonian (4.13), the frequency of modulation is hidden in the scaled amplitude $\gamma = V_0/2md^2\nu^2$. From the potential of the unscaled Hamiltonian (4.6), we find $\nu_0 = \sqrt{V_0/2md^2}$, and we see that $\gamma = 1$ is the scaled amplitude corresponding to a resonant modulation at the bottom of the wells. We therefore set $\gamma = 1$ as our initial guess for this parameter.

To determine initial guesses for the amplitudes of modulation $(\varepsilon_0, \varphi_0)$, we compute maps showing, after one modulation period, the position and the momentum of a particle starting at in $(\tilde{x}(0), \tilde{p}(0)) = (0, 0)$ as a function of $(\varepsilon_0, \varphi_0)$. Such maps are shown in Fig. 4.2, for $\varepsilon \in [0, 1]$ (bounded so that the amplitude of the potential does not get negative, as required by the optical lattice setup in our experiment ; Sec. 2.4) and $\varphi_0 \in [0, \pi]$ (corresponding to a peak-to-peak modulation of up to one spatial period). We use these maps to initialize $(\varepsilon_0, \varphi_0)$ to values such that $\tilde{x}(2\pi) \approx 2\pi$ and $\tilde{p}(2\pi) \approx 0$.

Figure 4.2 features an interesting behavior identified with a dashed black line. This linear¹⁰ region corresponds to values of $(\varepsilon_0, \varphi_0)$ such that $\tilde{x}(2\pi) \approx \pi$ and $\tilde{p}(2\pi) \approx 0$. In words, they are modulation parameters such that the particle starting in $(\tilde{x}(0), \tilde{p}(0)) = (0, 0)$ is brought to the top of the potential barrier, at the border between two lattice sites, and finishes there at rest. For our problem, we want to overcome this barrier of potential, and stop at the bottom of the following well. In Fig. 4.2, we see that this can be achieved for amplitudes of phase modulation φ_0 larger than those bringing the particle to a stop at the top of the potential (*i.e.* larger amplitudes for the pseudo force (4.11)). To the right of the dashed line, one sees a rather vast region of $(\varepsilon_0, \varphi_0)$ values such that $\tilde{x}(2\pi) \approx 2\pi$ and $\tilde{p}(2\pi) \approx 0$. We identify with solid black lines an example of good initialization $(\varepsilon_0, \varphi_0)$ for the algorithm.

⁸Using the open-source Python library SciPy.

⁹We note that this problem could have very well been addressed using the formalism of optimal-control theory presented in Chap. 3. However, we ourselves were introduced to this field only after having found working modulation parameters for our non-diffusive Hamiltonian ratchet.

¹⁰That is actually not trivial.

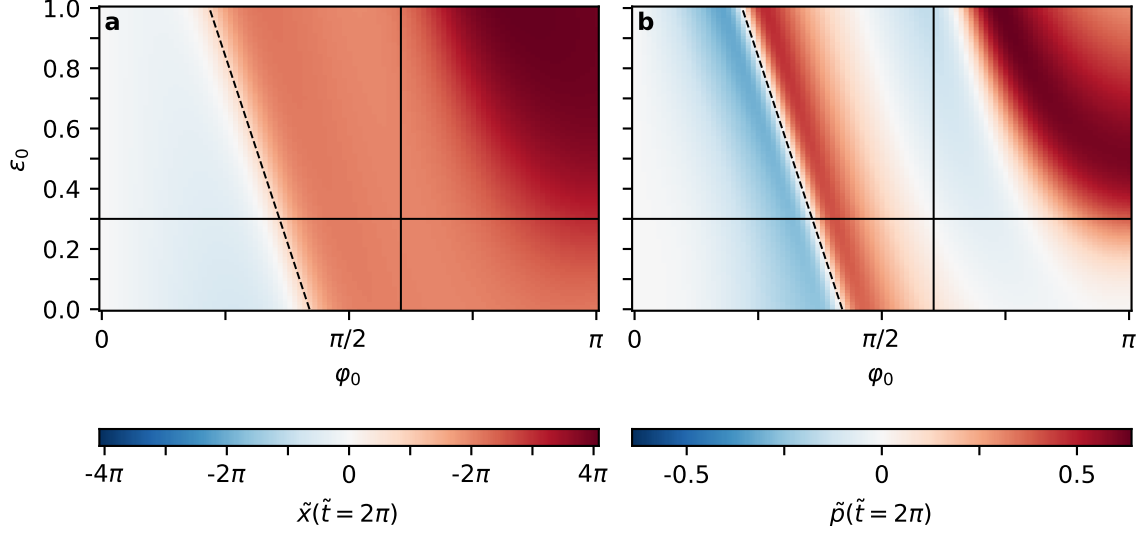


Figure 4.2 | Parameter maps for initial guess determination in the search for ratchet modulation parameters. (a) Position \tilde{x} and (b) momentum \tilde{p} after one modulation period for a particle starting in $(\tilde{x}(0), \tilde{p}(0)) = (0, 0)$ and described by the Hamiltonian (4.13) with the scaled potential amplitude $\gamma = 1$ (see text). The solid black lines in $(\epsilon_0, \varphi_0) = (0.3, 1.9)$ mark a parameter pair for an initial guess (see text), and the dashed black line marks a region of parameters for which the particle ends up resting at the top of the potential barrier between the central well and the next one.

4.1.3 Results of classical mechanics

Using the method detailed in the previous section, we converge to the modulation parameters

$$(\gamma, \epsilon_0, \varphi_0) = (1.2, 0.3, 1.7). \quad (4.16)$$

This solution for the problem that we set ourselves in Sec. 4.1.1 (p. 103) is not unique, and others can be found using the same method. In the rest of this chapter, we however focus on parameters (4.16). For these modulation parameters, we draw in Fig. 4.3(a,b) the position $\tilde{x}(\tilde{t})$ and the momentum $\tilde{p}(\tilde{t})$ over three modulation periods for the particle starting in $(\tilde{x}(0), \tilde{p}(0)) = (0, 0)$. As required, we get a periodic evolution, with a particle that travels one site per modulation period: $\tilde{x}(2\pi n) = 2\pi n$ ($n \in \mathbb{N}$). As explained in the introduction of this chapter, the general ratchet effect is intriguing as no global net force derives from a periodic potential (Eq. (4.3)). In the specific case of our periodic ratchet, we have the stronger fact that the average force exerted per modulation by the potential on the ratcheting particle is zero *along its trajectory*:

$$\left\langle \tilde{F}(\tilde{x}(\tilde{t}), \tilde{t}) \right\rangle_{2\pi} = \frac{1}{2\pi} \int_0^{2\pi} \tilde{F}(\tilde{x}(\tilde{t}), \tilde{t}) d\tilde{t} = 0. \quad (4.17)$$

This is illustrated numerically in Fig. 4.3(c) where we plot, as a function of time, the instantaneous force $\tilde{F}(\tilde{x}(\tilde{t}), \tilde{t})$ exerted by the potential on the particle in $\tilde{x}(\tilde{t})$, as well as the average of

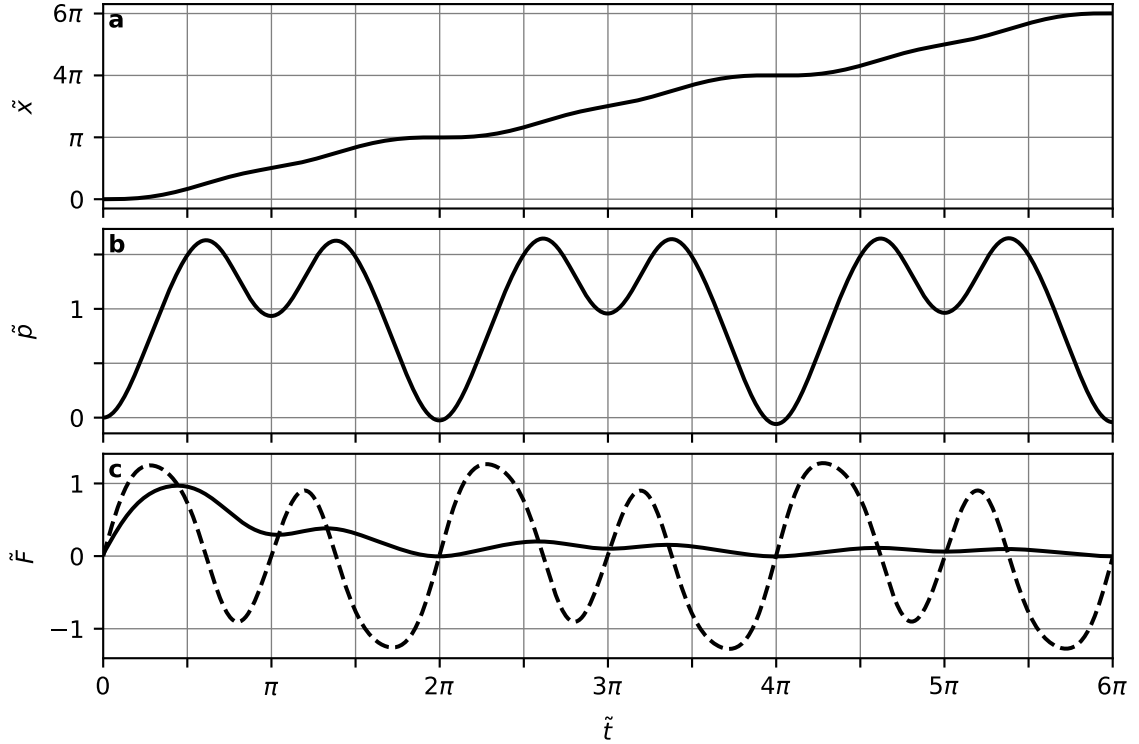


Figure 4.3 | Classical non-diffusive ratchet trajectory. (a) Position \tilde{x} as a function of time \tilde{t} for the particle starting at rest at the bottom of the central well. (b) Momentum \tilde{p} as a function of time for that same particle. (c) Instantaneous (dashed black line) and integrated average (solid black line) force $\tilde{F}(\tilde{x}(\tilde{t}), \tilde{t})$ as a function of time. We show three modulation periods, with modulation parameters $(\gamma, \varepsilon_0, \varphi_0) = (1.2, 0.3, 1.7)$.

this force from $\tilde{t} = 0$ up to that time. We see that this accumulated average is zero for $\tilde{t} = 2\pi n$ ($n \in \mathbb{N}$). This observation is also directly deduced from the conditions (4.12) that we imposed on the generated trajectory. Indeed, having $\tilde{p}(0) = \tilde{p}(2\pi)$ implies, from Hamilton equations and the fundamental theorem of calculus,

$$-\frac{\partial \tilde{H}}{\partial \tilde{x}} = \dot{\tilde{p}} \quad \Rightarrow \quad \int_0^{2\pi} -\frac{\partial \tilde{H}}{\partial \tilde{x}} d\tilde{t} = \tilde{p}(2\pi) - \tilde{p}(0) \quad (4.18)$$

$$\Leftrightarrow \int_0^{2\pi} \tilde{F}(\tilde{x}(\tilde{t}), \tilde{t}) d\tilde{t} = 0 \quad (4.19)$$

This is a key difference between our periodic system and diffusive systems¹¹, as well as between our spatial ratchet and the accelerator ratchet, also based on periodic trajectories, but ratcheting along the momentum axis¹² in a kicked-rotor system.

¹¹For diffusive Hamiltonian ratchet based on a chaotic sea bounded in momentum, one has $\langle F \rangle_t$ only going to zero asymptotically in time.

¹²With $p(nT) - p((n-1)T) \neq 0 \Rightarrow \langle F \rangle_T \neq 0$.

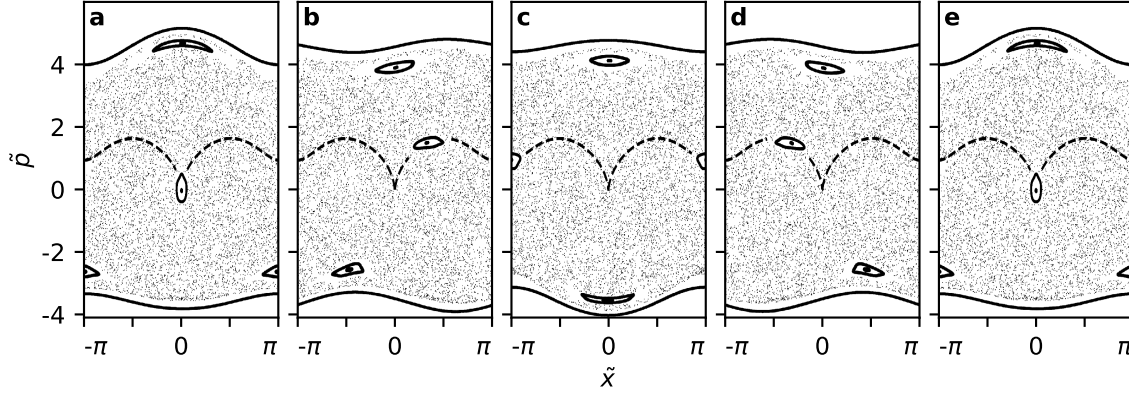


Figure 4.4 | Subperiod evolution of the stroboscopic phase portrait and ratcheting island. (a-e) Stroboscopic phase portraits for the same Hamiltonian (4.13) with $(\gamma, \varepsilon_0, \varphi_0) = (1.2, 0.3, 1.7)$ and the sub-stroboscopic observation times $\tilde{t}_0 = 0, 0.25, 0.5, 0.75$ and 1. In each panel, we artificially draw in continuous time the phase space trajectory at the center of the ratcheting island (dashed black line). See Sec. 1.1.2 and Fig. 1.2 for details on the procedure.

We also compute the stroboscopic phase portrait (Sec. 1.1.2) for our ratchet modulation parameters (4.16). In Fig. 4.4, we draw five portraits associated with the sub-stroboscopic¹³ observation times $\tilde{t} = 0, 0.25, 0.5, 0.75$ and 1. We see that the determination of modulation parameters such that the trajectory starting in $(\tilde{x}(0), \tilde{p}(0)) = (0, 0)$ periodically ratchets to the next site amounts to a “regularization” of the center of the phase space for this ratchet system. Indeed, we see that we generated a regular island that goes through one site of the potential per modulation period¹⁴, with the highly non-trivial fact that this island finds itself resting at the center of the sites periodically [188]. This is to our knowledge the first study of such a ratcheting regular island along the x axis. We also note from Fig. 4.4 that the rest of the phase portrait is greatly chaotic, which will later allows us to distinguish between evolutions carried by the regular ratcheting island and diffusive behavior in the chaotic sea.

We have so far considered classical mechanics in this system. In the next section, we study the transport of a wave function along this ratchet island.

4.2 Quantum ratchet transport along regular classical trajectories

4.2.1 A Floquet system

Given the modulation parameters $(\gamma, \varepsilon_0, \varphi_0) = (1.2, 0.3, 1.7)$, the scaled classical dynamics governed by the Hamiltonian (4.13) is completely determined, and represented by the phase space depicted in Fig. 4.4. We now consider wave function transport in this ratchet system. As introduced in Chap. 1, quantum dynamics in such scaled systems depends on an effective reduced Planck constant \hbar_{eff} . For our scaling (p. 102), we have

¹³See Sec. 1.1.2 and Fig. 1.2 for details.

¹⁴*i.e.* a regular island with a winding number $w = 1$ (Sec. 1.1.2).

$$\hbar_{\text{eff}} = 2\frac{\nu_L}{\nu}, \quad (4.20)$$

with ν the unscaled modulation frequency and $\nu_L = h/2md^2$ a characteristic quantum frequency in Bloch systems (Sec. 1.2). As discussed in Sec. 1.4.1, \hbar_{eff} sets the typical extent of quantum states with respect to the scaled phase space of the system. As we are interested in studying transport along the ratchet island that we designed in the previous section, we place our study “at the onset” of the semi-classical regime (see Sec. 1.4.1 and below), for values of \hbar_{eff} such that the minimal extent of the quantum states is of the order of the area of the engineered ratcheting island. We recall that in the semi-classical regime, Floquet states are, in general, either localized on regular phase space structures or spread over the chaotic sea (see Sec. 1.4.1 and [86, 87, 69]). By “at the onset of the semi-classical regime”, we mean that the values of \hbar_{eff} that we will consider will be small enough for quantum dynamics to be strongly affected by underlying phase space structures, but not be small enough for more than one Floquet state to be localized on the ratcheting island.

The quantum analogue of the periodic trajectory at the center of the ratcheting island (see Figs. 4.3 and 4.4) is the Floquet state $|\varphi_r\rangle$ that can be associated with this island, and we refer to it as the ratcheting Floquet state. For a given value of \hbar_{eff} , we compute the Floquet states $|\varphi_m\rangle$ by diagonalizing the Floquet operator (Sec. 1.3.2) around the sub-stroboscopic observation time $\tilde{t}_0 = 0$, *i.e.* when the ratcheting island is centered in the phase space (Fig. 4.4). We then identify the ratcheting Floquet state $|\varphi_r\rangle$ as the one with the greatest overlap with the ground state $|\phi_0\rangle$ of the static potential, a state itself centered in the phase space:

$$|\varphi_r\rangle = \arg \max_{|\varphi_m\rangle} \left\{ |\langle \phi_0 | \varphi_m \rangle|^2 \right\}. \quad (4.21)$$

To quantify transport in a quantum state, we also define the expected transport between times \tilde{t}_0 and \tilde{t}_1 as the integral over this time interval of the averaged momentum¹⁵. For an arbitrary state $|\psi\rangle$, the expected transport can be written as

$$\Delta \tilde{x}_{\tilde{t}_0, \tilde{t}_1}(|\psi\rangle) = \int_{\tilde{t}_0}^{\tilde{t}_1} \langle \hat{p} \rangle_{\psi(\tilde{t})} d\tilde{t}. \quad (4.22)$$

with \hat{p} the scaled momentum operator. In the semi-classical regime, one expects Floquet states associated with regular structures to evolve as their associated structure, and, in particular for the ratcheting Floquet state, $\Delta \tilde{x}_{0, 2\pi n}(|\varphi_r\rangle) \sim 2\pi n$. While this is generally true (see below), one has to account for Floquet state mixing which can complexify the picture for certain values of \hbar_{eff} .

¹⁵This definition is, among other things, motivated by our TOF imaging setup (Sec. 2.3), through which we measure the momentum distribution of the quantum state evolving in our lattice.

4.2.2 Influence of the effective Planck constant and Floquet state mixing

We show in Fig. 4.5 numerical results of quantum transport in the ratcheting island as a function of $1/\hbar_{\text{eff}}$ (*i.e.* as a function of a classical scaling action in the system ; see Sec. 1.4.1). We plot in Fig. 4.5(a,b) two quantities as a function of $1/\hbar_{\text{eff}}$: first, the overlap $|\langle\phi_0|\varphi_r\rangle|^2$ between the ratcheting Floquet state and the ground state of the static potential. This overlap somehow quantifies the “centrality” of $|\varphi_r\rangle$ in the phase space (as well as our upcoming ability to experimentally load the ratcheting Floquet state from the ground state of the optical lattice in order to observe ratchet transport). Second, we plot the expected transport per period $\Delta\tilde{x}_{0,2\pi}(|\varphi_r\rangle)$ of the ratcheting Floquet state. Having fixed the classical scaled dynamics (and, in particular, fixing $\gamma = V_0/2md^2\nu^2$), the limit $1/\hbar_{\text{eff}} \rightarrow 0 \Leftrightarrow \nu \rightarrow 0$ (Eq. 4.20) corresponds to a vanishing amplitude of the potential. In this radically deep quantum limit, both $|\varphi_r\rangle$ and $|\phi_0\rangle$ tend to the resting plane wave¹⁶: their overlap tends to one and the transport of $|\varphi_r\rangle$ in the vanishing potential tends to zero (Fig. 4.5(a,b)). As $1/\hbar_{\text{eff}}$ varies, both $|\langle\phi_0|\varphi_r\rangle|^2$ and $\Delta\tilde{x}_{0,2\pi}(|\varphi_r\rangle)$ display rather sharp non-monotonic fluctuations ascribed to the phenomenon of Floquet state mixing (which we now introduce ; the description of Fig. 4.5 is continued shortly below).

Floquet state mixing. As a parameter of the Hamiltonian is varied, the energy levels in the quasi-energy spectrum vary at different rates giving rise to the generic phenomenon of avoided crossings. This effect results in the coupled state mixing into reshaped orthogonal Floquet states near the crossing. We illustrate this phenomenon in Fig. 4.6 for realistic parameters, in the interval of $1/\hbar_{\text{eff}}$ identified in Fig. 4.5(a,b) by the gray shaded area, around a sharp drop of both $|\langle\phi_0|\varphi_r\rangle|^2$ and $\Delta\tilde{x}_{0,2\pi}(|\varphi_r\rangle)$. In Fig. 4.6(a), we draw a zoom of the quasi-energy spectrum (Sec. 1.3.2) where relevant Floquet levels have been identified from their overlap with the Floquet states¹⁷ shown in panels (c,d). In Fig. 4.6(b), we again plot $|\langle\phi_0|\varphi_r\rangle|^2$ in this small interval of $1/\hbar_{\text{eff}}$. This quantity displays two drops that were not resolved in Fig. 4.5. These drops correspond to the two consecutive avoided crossings observed in panel (a), at which the ratcheting Floquet state $|\varphi_r\rangle$ is strongly reshaped (as one can see from the Husimi representations of Fig. 4.6(c-e)). Surprisingly, we observe in Fig. 4.5(b) that there are even values of \hbar_{eff} such that the periodic transport of the ratcheting Floquet state becomes negative (even though the scaled classical dynamics still remains unchanged, with the ratcheting island going in the positive direction). As a matter of fact, there are such values of \hbar_{eff} in the zoom region of Fig. 4.6, and we see from the Husimi representations shown in panels (c-e) that negative transport in $|\varphi_r\rangle$ results from couplings with other Floquet states having weights in the negative momentum part of phase space.

Going back to Fig. 4.5, we draw on panels (c-e) the Husimi representations of $|\phi_0\rangle$ (blue) and $|\varphi_r\rangle$ (green) for the three values of $1/\hbar_{\text{eff}}$ identified on panel (a,b). At $\hbar_{\text{eff}} \approx 0.79 \approx 1/1.27$, Fig. 4.5(d) is an example of a semi-classical, phase-space-centered and island-shaped $|\varphi_r\rangle$, with

¹⁶See for instance Sec. 1.2.2.

¹⁷The Floquet states shown in Fig. 4.6(c,d) have themselves been identified by their overlap with the ground state $|\phi_0\rangle$.

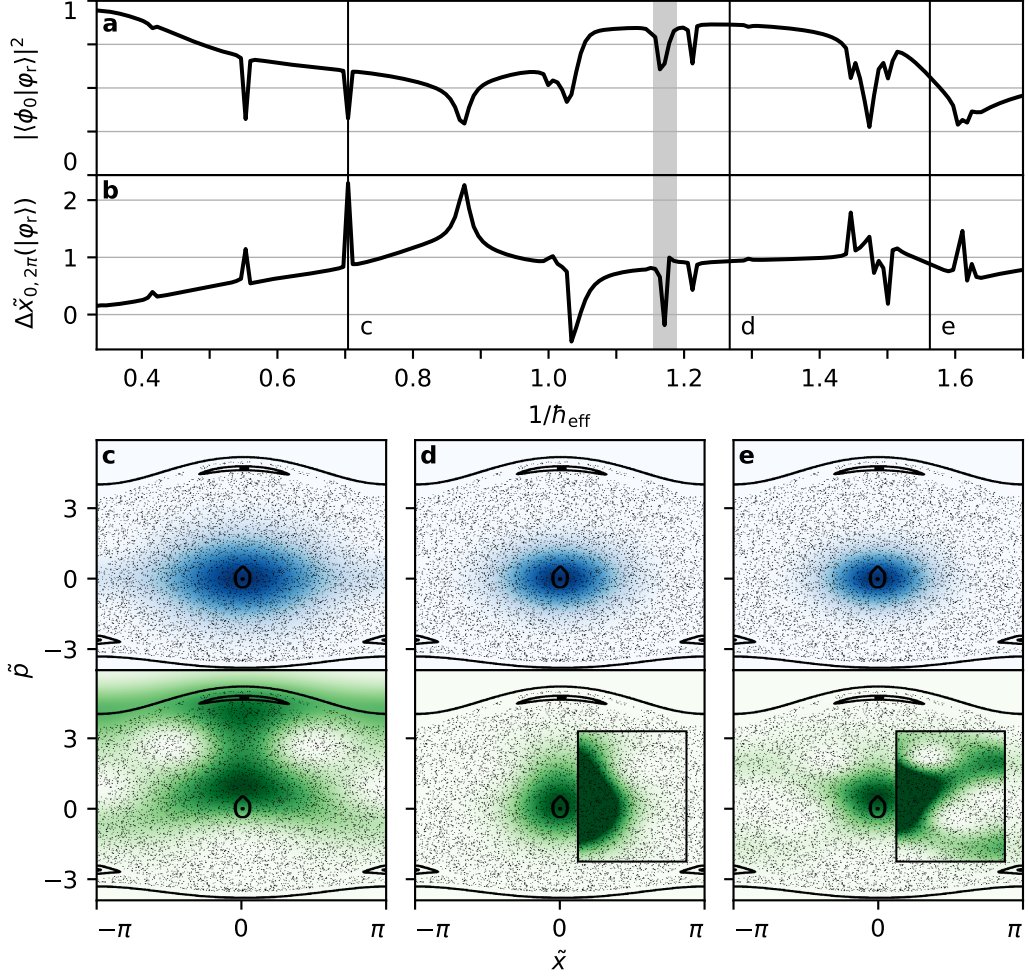


Figure 4.5 | Ratcheting Floquet state and influence of the effective Planck constant. (a) Overlap between the ratcheting Floquet state $|\varphi_r\rangle$ and the ground state $|\phi_0\rangle$ of the potential as a function of $1/\hbar_{\text{eff}}$. (b) Periodic expected transport $\Delta\tilde{x}_{0,2\pi}$ of $|\varphi_r\rangle$ as a function of $1/\hbar_{\text{eff}}$. (c-e) Stroboscopic phase portraits and Husimi representations (Sec. 1.4.1) of $|\phi_0\rangle$ (top, blue) and $|\varphi_r\rangle$ (bottom, green) for the values of $1/\hbar_{\text{eff}}$ identified by the vertical black lines on the panels (a,b) (with $1/\hbar_{\text{eff}} \approx 0.704, 1.27$ and 1.56 for (c-e) resp.). The Husimi functions in the inset of panels (d,e) are truncated to a quarter of their respective overall maximum value to reveal details. The gray shaded area in panels (a,b) corresponds to the interval of $1/\hbar_{\text{eff}}$ studied in Fig. 4.6. The Hamiltonian of the system is given by Eq. (4.13) with parameters $(\gamma, \varepsilon_0, \varphi_0) = (1.2, 0.3, 1.7)$.

a ground state overlap of $|\langle\phi_0|\varphi_r\rangle|^2 \approx 0.86$ and a periodic transport of $\Delta\tilde{x}_{0,2\pi}(|\varphi_r\rangle) \approx 0.93$. On the other hand, Fig. 4.5(c) and (e) correspond to values of \hbar_{eff} where a wave function (such as the ground state of the static lattice) placed in the ratcheting island will evolve out of it (towards a mode of high momentum¹⁸ for Fig. 4.5(c) and over the chaotic sea for Fig. 4.5(e)).

This concludes our numerical study (both classical and quantum mechanical) about this non-diffusive Hamiltonian ratchet. In the following section, we apply our analysis of the influence of \hbar_{eff} and the observations of Fig. 4.5 to experimentally observe ratchet transport of matter

¹⁸Quantum ratchet effects based on such couplings with Floquet states associated with large momentum have *e.g.* been studied in [189, 190].

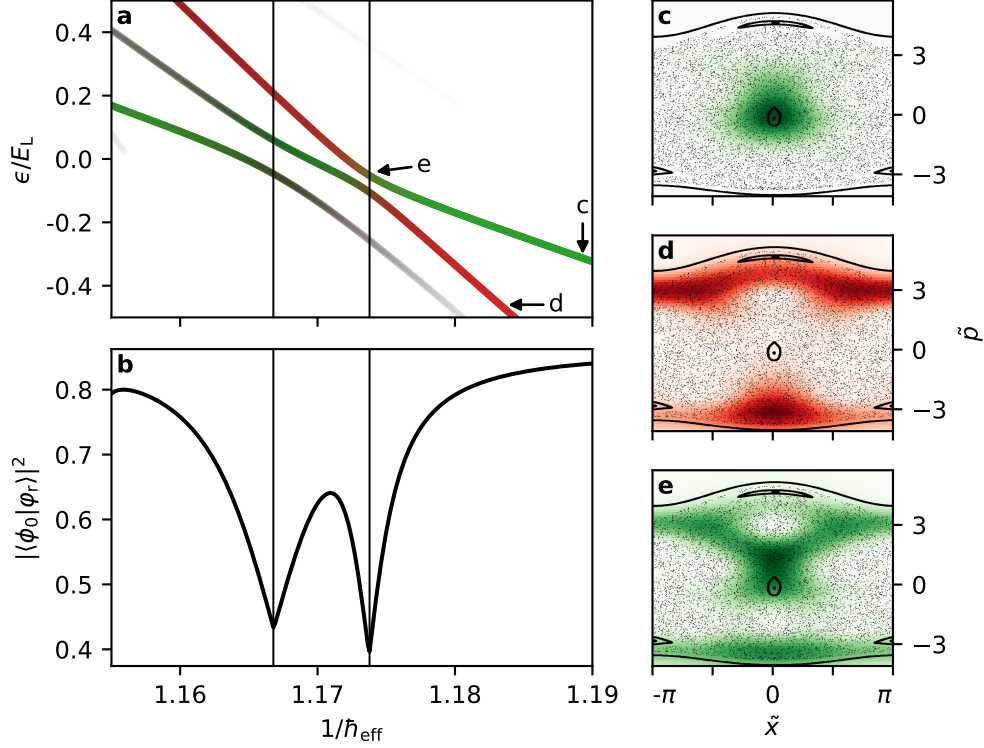


Figure 4.6 | Floquet state mixing phenomenon illustrated on the ratcheting Floquet state. (a) Portion of the quasi-energy spectrum as a function of $1/\hbar_{\text{eff}}$ for the modulated Hamiltonian (4.13) with parameters $(\gamma, \varepsilon_0, \varphi_0) = (1.2, 0.3, 1.7)$. ϵ denotes the quasi-energy that we plot reduced by the characteristic quantum energy scale of the potential $E_L = \hbar^2/2md^2$ (Secs. 1.2 and 1.3.2). The Floquet states associated with the quasi-energy marked by the letters (c) and (d) are identified from their overlap with the ground state of the potential (see text). The colors green and red are associated with these states, and the spectrum is in return colored depending on the overlaps with these states (see Sec. 1.3.2 for method details). For all values of \hbar_{eff} , the most green quasi-energy corresponds to the ratcheting Floquet state $|\varphi_r\rangle$ according to Eq. (4.21). (b) Overlap between the ratcheting Floquet state and the ground state $|\phi_0\rangle$ of the potential. The black vertical lines in (a,b) mark the position of the two avoided crossings seen in (a) corresponding to the two drops in ground state overlap seen in (b) (see text). (c-e) Stroboscopic phase portraits and Husimi representations of the three states associated with the quasi-energies identified in (a).

waves along the ratcheting island that we engineered in Sec. 4.1.

4.3 Experimental ratchet transport of matter waves

In this last section, we present experiments of non-diffusive ratchet transport of BECs in the optical lattice. We focus on the two values of the effective reduced Planck constant $\hbar_{\text{eff}} \approx 0.79 \approx 1/1.27$ and $0.64 \approx 1/1.56$, which respectively correspond to the numerical simulations of Fig. 4.5(d) and (e). For both values, we see in Fig. 4.5(b) that the periodic transport of the ratcheting Floquet state is approximately one. However, their projection on lattice ground state (Fig. 4.5(a)) is quite different, with $|\langle \phi_0 | \varphi_r \rangle|^2 \approx 0.86$ for $\hbar_{\text{eff}} \approx 0.79$, while we only have

$|\langle \phi_0 | \varphi_r \rangle|^2 \approx 0.56$ for $\hbar_{\text{eff}} \approx 0.64$ (resulting from a mixing with a Floquet state from the chaotic sea in this case).

In Sec. 4.3.1, we first present, for these two values of \hbar_{eff} , experiments of ratchet transport from the lattice ground state. In a second set of experiments (Sec. 4.3.2), we use the quantum-optimal control protocol detailed in Chap. 3 to prepare the ratcheting Floquet states and enhance ratchet transport and the periodicity of the evolution.

4.3.1 Transport from the ground state

The time-dependent Hamiltonian (4.13) studied in the two previous sections is directly implementable on our experiment of BECs in a one-dimensional optical lattice introduced in Chap. 2. To determine the experimental parameters for the modulation, we follow this procedure:

- (i) We determine a value of \hbar_{eff} at which we want to perform the experiment of ratchet transport (Sec. 4.2). As we require a given scaled phase space associated with the modulation parameters $(\gamma, \varepsilon, \varphi_0) = (1.2, 0.3, 1.7)$, we broadly set the lattice beams intensity in order to have the lattice depth $s_0 = 4\gamma/\hbar_{\text{eff}}^2$ (as $\gamma = s\nu_L^2/\nu^2$ and $\hbar_{\text{eff}} = 2\nu_L/\nu$; see p. 34). We can quickly verify the consistency of our settings by performing a ‘‘Kapitza-Dirac calibration’’ of the lattice (Sec. 2.4.2).
- (ii) We precisely calibrate the lattice depth s_0 using our usual method of ground state translation (Sec. 2.4.2 and [112, 113]). As $\gamma = s_0(\nu_L/\nu)^2$, we set the value of the modulation frequency to $\nu = \nu_L\sqrt{s_0/\gamma}$, which fixes in return the true value of the effective Planck constant $\hbar_{\text{eff}} = 2\nu_L/\nu$ at which the experiment will be performed.
- (iii) We perform the ratchet transport experiment (see below).

After obtaining the BECs (Sec. 2.2.3), we adiabatically load them into the ground state of the optical lattice at the calibrated depth s_0 . We then modulate the depth and phase of the lattice to realize the Hamiltonian (4.13) during a given amount of time, before proceeding to TOF imaging (Sec. 2.3.2) allowing us to measure the momentum distribution of the atomic state in the lattice right before the TOF. For this experiment, we sample the evolution with four observations per modulation period.

We start by showing results of ratchet transport from the ground state of the lattice at $\hbar_{\text{eff}} \approx 0.79$ (the value of Fig. 4.5(d) associated to a semi-classical behavior). In Fig. 4.7(a-d), we show next to each other the stroboscopic phase portraits and the absorption images at corresponding sub-stroboscopic times during the first modulation period. In order to compare the momentum of the ratcheting island to that of the momentum components of the diffraction images, the classical dynamics in the phase portraits of Fig. 4.7(a-d) has been unscaled using

$$p/\hbar k_L = \tilde{p}/\hbar_{\text{eff}}, \quad (4.23)$$

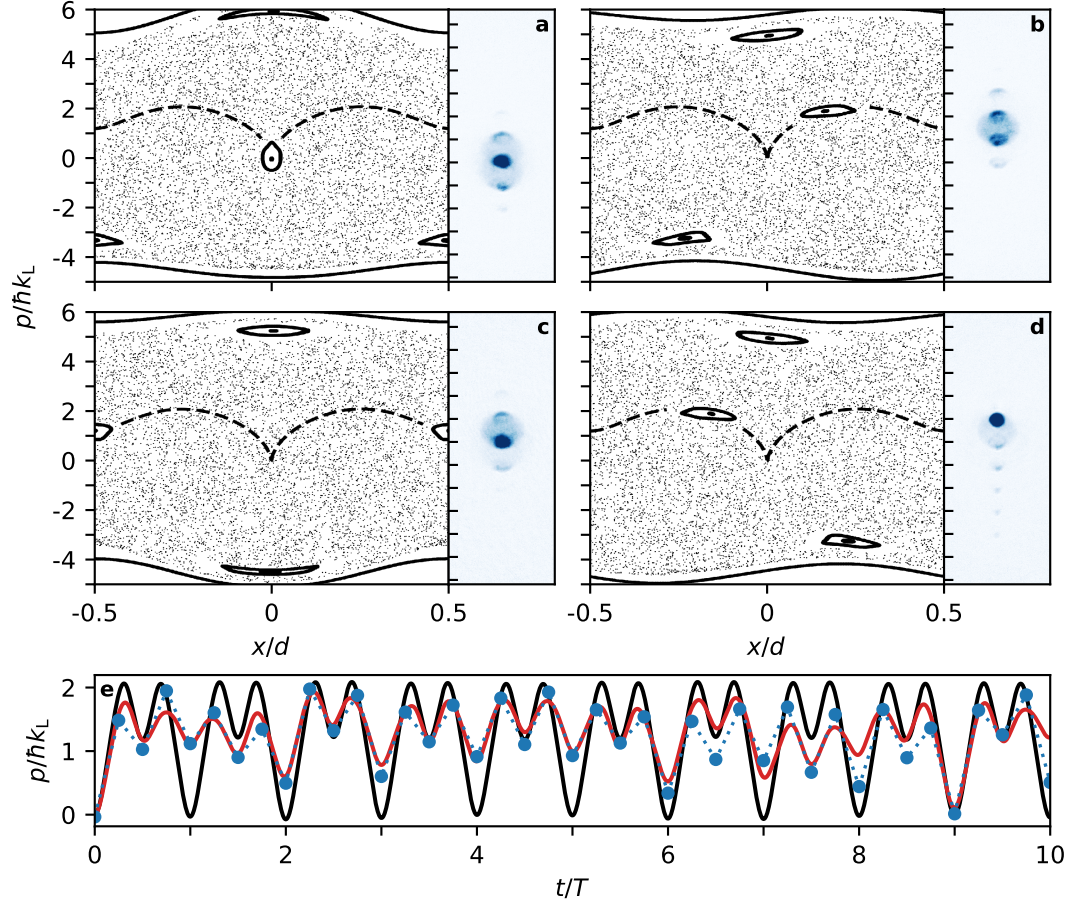


Figure 4.7 | Semi-classical non-diffusive ratchet transport from the ground state. (a-d) Stroboscopic phase portraits (left) and experimental TOF absorption images (right) at sub-period observation times $\tilde{t} = (n + r) \times 2\pi$, with $n \in \mathbb{N}$ and $r = 0, 0.25, 0.5$ and 0.75 for (a) to (d) respectively. The period shown for the experimental images is $n = 0$, implying that (a) is the momentum distribution of the lattice ground state. (e) Momentum as a function of time, showing the experimental (blue markers linked with dotted lines) and numerical (plain red line) average of the momentum distribution with the ground state as the initial state, as well as the momentum of the classical trajectory at the center of the ratcheting island (plain black line).

an expression that can be deduced from Eqs. (4.9) and (4.20) (with $k_L = 2\pi/d$). The great qualitative agreement observed between the momentum of the island and that of the momentum peaks in the diffraction pattern illustrates the semi-classicality of the observed ratchet transport, as well as its non-diffusive nature over this first period (this is demonstrated for longer times below). In Fig. 4.7(e), we compare three momentum evolutions: the experimental average momentum measured from the diffraction patterns, the corresponding numerical simulation for the evolution from the ground state, and the momentum of the classical trajectory at the center of the ratcheting island (as in Fig. 4.3(b), although unscaled using Eq. (4.23)). This plot further illustrates the semi-classicality of this ratchet transport.

The experimentally measured moment distributions (used to plot Fig. 4.7(e)) are shown in Fig. 4.8(a), as well as the corresponding numerically obtained momentum distributions. This

evolution is to be compared with the same experiment performed for the other value of the effective Planck constant $\hbar \approx 0.64$. Numerical and experimental momentum evolutions for this experiment are shown in Fig. 4.8(b). While the scaled phase space is fixed and the initial state is in both cases the ground state of the static lattice, we observe a strong difference between the momentum evolutions for these two experiments. For $\hbar \approx 0.79$ in panel (a), we observe a quasi-periodic evolution with a rather constant momentum dispersion. This semi-classical evolution results from the ground state $|\phi_0\rangle$ of the static lattice being well projected onto the ratcheting Floquet state $|\varphi_r\rangle$ for this values of \hbar_{eff} (as seen in Fig. 4.5(d)). In the case of $\hbar \approx 0.64$ shown in Fig. 4.8(b), the momentum distribution is initially rather narrow before quickly widening, never to return to a configuration close to that of the initial situation. This is emblematic of a diffusion in the chaotic sea, which results from a situation where $|\varphi_r\rangle$ is partially delocalized over the chaotic sea (as seen in Fig. 4.5(e) and discussed in Sec. 4.2). This observation is of purely quantum nature: although the atoms are initially at the center¹⁹ of the regular island, we here obtain a quantum evolution diverging from its classical counterpart.

From the sub-stroboscopic sampling of the momentum evolution, we compute the expected transport (4.22). We plot this quantity in Fig. 4.8(c). In the case of experiment (a), we get a transport of approximately 10 lattice sites in 10 modulation periods, as was expected from Fig. 4.5. We also show this transport in the strongly aperiodic case of experiment (b). The overall great agreement between experiments and numerical simulation shows our successful implementation of the ratchet Hamiltonian (4.13), as well as our ability to precisely set and determine modulation parameters in the experiment (notably thanks to our fine calibrations of the lattice depths ; Sec. 2.4.2).

Transport reversal. A key feature of the ratchet effect is the ability to reverse the direction of the transport [163, 164]. For our Hamiltonian (4.13), this direction is imposed by the sign of the phase quadrature between the modulations of amplitude and phase. One expects the opposition of the phase modulation ($\varphi(t) = -\varphi_0 \sin(t) \rightarrow +\varphi_0 \sin(t)$) to result in a negative ratchet transport. In Fig. 4.8(c), we label (a') the integrated transport obtained experimentally (blue dots) and numerically (red line) for the parameters $(\gamma, \varepsilon, \varphi_0) = (1.2, 0.3, -1.7)$ and $\hbar_{\text{eff}} \approx 0.77$ (*i.e.* close to the experiment of panel(a)). We measure for this experiment a ratchet transport of approximately -10 sites in 10 modulation periods, a symmetric ratchet transport.

These results demonstrate the observation of quantum transport along a ratcheting island in the phase space of our system. We have also observed how Floquet state mixing can complexify the loading of the ratcheting phase space region, as this phenomenon reshapes the ratcheting Floquet state. In the following section, we present a last experiment in which we use quantum-optimal control to optimize the loading of this state.

¹⁹We also highlight that $\hbar_{\text{eff}}^{(a)} > \hbar_{\text{eff}}^{(b)}$ (corresponding to Fig. 4.5(d,e) resp.), meaning that the phase space extent of the initial state in panel (b) is *smaller* than that of panel (a), the latter yielding nevertheless a more semi-classical behavior.

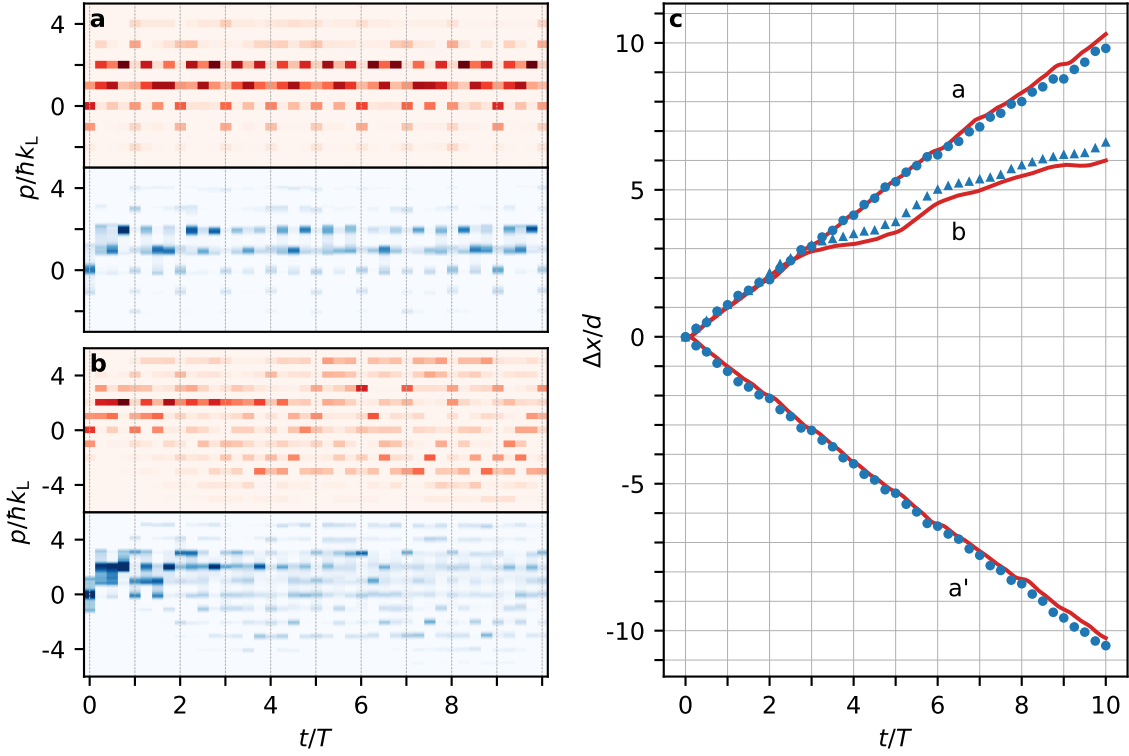


Figure 4.8 | Experiments of ratchet transport from the ground state of the lattice. (a) Top: Numerical simulation of the momentum evolution during the ratchet modulation as a function of time for $\hbar_{\text{eff}} \approx 0.79$ (corresponding to Fig. 4.5(d)). Bottom: Corresponding experimental integrated absorption images. (b) Same as (a) for $\hbar_{\text{eff}} \approx 0.64$ (corresponding to Fig. 4.5(e)). (c) Expected numerical (solid red line) and experimental (blue markers) transport (see text) for data (a) and (b) as a function of time. Data (a') is approximately the reversed ratchet transport of (a), with $\varphi_0 \rightarrow -\varphi_0$ and $\hbar_{\text{eff}} \approx 0.77$ (see text).

4.3.2 Preparation of the ratcheting Floquet state using quantum-optimal control

To improve the transport of a quantum state in a ratcheting island (as well as the periodicity of its evolution), the Floquet state $|\varphi_r\rangle$ associated with the island must be prepared as the initial state for the modulation. To do so, we use the quantum-optimal control (QOC) protocol detailed in Chap. 3. As in that chapter, we use the lattice phase $\varphi(t)$ as our control parameter, and we target $|\varphi_r\rangle$ from the ground state $|\phi_0\rangle$ of the static lattice at depth of work. For this experiment, between the steps (ii) and (iii) of the experimental procedure presented in the previous section (p. 113), we add the following steps:

- (ii.i) Having set all the modulation parameters, we numerically determine $|\varphi_r\rangle$ by diagonalizing the Floquet operator, and selecting among its eigenstates the one that maximizes the overlap with the lattice ground state $|\phi_0\rangle$ (itself centered in the phase space).
- (ii.ii) Using our QOC algorithm (Sec. 3.1.3), we numerically compute the control field $\varphi(t)$ that drives $|\phi_0\rangle$ to $|\varphi_r\rangle$. We set the control duration to $t_c = 1.75 T_0$ (see Sec. 3.1.4), and

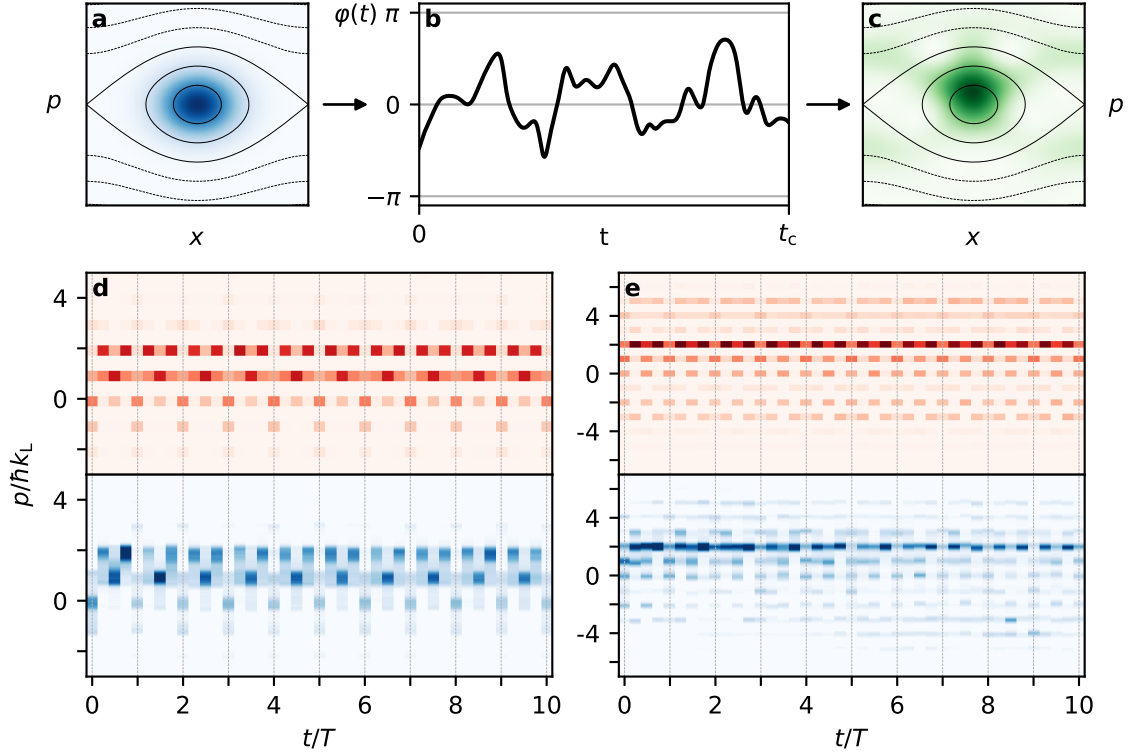


Figure 4.9 | Ratchet transport experiments of ratcheting Floquet states prepared by QOC. (a-c) Sketch of the QOC protocol to prepare the ratcheting Floquet state $|\varphi_r\rangle$ from the ground state $|\phi_0\rangle$ at $\hbar_{\text{eff}} \approx 0.64$. (a) Husimi representation of $|\phi_0\rangle$ in the phase space of the static lattice. (b) Lattice phase evolution that drives $|\phi_0\rangle$ to $|\psi_{\text{QOC}}\rangle$ with the fidelity $\mathcal{F}_{\text{num}} = |\langle\varphi_r|\psi_{\text{QOC}}\rangle|^2 \approx 0.996$. (c) Same as (a) for the prepared state $|\psi_{\text{QOC}}\rangle$. (d) Top: Numerical simulation of the momentum evolution of $|\psi_{\text{QOC}}\rangle$ during the ratchet modulation as a function of time for $\hbar_{\text{eff}} \approx 0.77$ (corresponding to Fig. 4.6(d) and Fig. 4.8(a)). Bottom: Corresponding experimental integrated absorption images. (e) Same as (d) for $\hbar_{\text{eff}} \approx 0.64$ (corresponding to Fig. 4.5(e) and Fig. 4.8(b)).

the algorithm converges to control fields that numerically prepare the state $|\psi_{\text{QOC}}\rangle$ with numerical fidelity to the target $\mathcal{F}_{\text{num}} = |\langle\varphi_r|\psi_{\text{QOC}}\rangle|^2 > 0.995$

The experimental sequence then consists in an adiabatical loading of $|\varphi_0\rangle$ (Sec. 2.4.1), the QOC preparation with the computed control field, the ratchet modulation for a given amount of time and finally the TOF imaging. As in the previous section, we take four images of the momentum distribution of the atoms per modulation period.

We sketch in Fig. 4.9(a-c) the QOC procedure applied to this ratchet study for $\hbar_{\text{eff}} \approx 0.64$. This value corresponds to the case of the poor ratchet state loading of Fig. 4.5(e) and Fig. 4.8(b). In Fig. 4.9(d,e), we show numerical simulations and experimental results of optimized ratchet transport using QOC. The values of \hbar_{eff} in Fig. 4.9(d,e) approximately correspond to the two values of this parameter previously studied in Fig. 4.8(a,b) (see the caption). While Fig. 4.8(a) already presented a clear regular ratchet transport, we see that the use of QOC enhances the periodicity of the evolution of the momentum distribution (as one expects from the evolution of a Floquet state). Comparing Fig. 4.9(e) with Fig. 4.8(b), one sees in this case an evident

improvement of periodicity. Interestingly, the momentum evolution of Fig. 4.9(e) display a broad momentum dispersion from the beginning of the modulation, corresponding to $|\varphi_r\rangle$ being partially delocalized over the chaotic sea for this value of \hbar_{eff} (Fig. 4.5(e)).

These results further demonstrate our experimental observation of matter waves ratcheting along a regular structure in the phase space of the modulated optical lattice. They also give another example of Floquet state preparations from QOC, in addition to the results of Sec. 3.4.

Conclusion

The ratchet effect is the intriguing emergence of a directed transport of particle in the *global* absence of net force. In this chapter, we presented the first study and experimental implementation of a Hamiltonian ratchet system that features a non-diffusive ratchet effect along space. Following an introduction on the ratchet effect, we presented the method that allowed to determine modulation parameters to observe this new kind of ratchet effect in a sine potential modulated in amplitude and phase. After having determined such modulation parameters, we characterized classical dynamics in this system. Interestingly, it follows from the quasi-periodicity of the ratcheting trajectories that, for this kind of ratchet, no net force is exerted on the particles *locally*, along their trajectories. In a second stage, we studied quantum mechanics in this ratchet system as a function of the effective reduced Planck constant \hbar_{eff} , and discussed the phenomenon of Floquet state mixing that can complexify the semi-classical picture for given values of \hbar_{eff} .

Following these numerical studies, we experimentally implemented this system using our setup of Bose-Einstein condensates in a controlled one-dimensional optical lattice (Chap. 2). We performed experiments of ratchet transport from the ground state of the optical lattice and experimentally observed the ratchet effect of matter waves. Finally, we optimized, using quantum-optimal control (QOC), the loading of the Floquet state associated with the ratcheting island even at values of \hbar_{eff} for which Floquet state mixing couples the island with the chaotic sea. Following our results on QOC presented in the previous chapter, these experiments give another example of application of QOC to quantum simulation in a Floquet system, this time in a study of the ratchet effect.

Part III

Beyond the one-body wave function

Chapter 5 - Emergence of a tunable supercrystalline order in a Floquet-Bloch system

Spectacular. You appear to understand how a portal affects forward momentum, or to be more precise, how it does not. Momentum, a function of mass and velocity, is conserved between portals. In layman's terms, speedy thing goes in, speedy thing comes out.

GLaDOS (Portal, 2007)

Contents

Introduction	123
5.1 Modulation regime and typical observations	125
5.2 An effective tight-binding model	126
5.2.1 Modeling the Floquet bands	128
5.2.2 Adding the interactions	131
5.2.3 Stability	135
5.2.4 Estimation of the interaction parameter	137
5.2.5 Results of the model and predictions	138
5.3 Experimental results	140
5.3.1 Band-mapping method and quasi-momentum of the decadal diffraction peaks	140
5.3.2 Tuning the momenta of the instabilities	142
5.3.3 Nucleation time	143
5.3.4 Survival of the instability	144
5.3.5 Amplitude modulation	145
5.4 Discussion on the realized state	146
5.4.1 Truncated-Wigner simulations	146
5.4.2 Shared features and differences between supersolids and the state emerging in our system	148
Conclusion	149

Introduction

In the last two chapters, we presented results on the control and the transport of the *one-body* wave function of BECs in a one-dimensional optical lattice. In both these studies, we captured the dynamics of the BECs in the lattice with the Schrödinger equation. In this linear framework, we designed efficient control fields for the preparation of non-trivial quantum states (Chap. 3), and determined the right modulation parameters to observe ratchet transport of matter waves along regular classical trajectories in the optical lattice (Chap. 4). In both studies, we obtained very good agreements between the experiments and numerical simulations, while completely neglecting the repulsive interatomic interactions in the system. This is made possible by the weak interaction regime of our one-dimensional system combined with the short timescales of the experiments presented so far (typically a few hundreds of microseconds). In this final chapter, we present experiments performed over longer timescales that take us out of the one-body formalism: the emergence of a supercrystalline order through spontaneous four-wave mixing in the phase modulated optical lattice.

Four-wave mixing is an emblematic consequence of the introduction of interactions in a wave theory. In non-linear optical media, it leads to the production of photon pairs, correlated in momentum and energy according to conservation laws. As a direct consequence, the effect strongly depends on the relation of dispersion of the media. Four-wave mixing is an essential tool in quantum optics, notably for the generation of entangled states. In its formalism, one speaks of *input* and *output* channels for the wave states before and after the process. In quantum gases, the same phenomenon is at work through two-body interactions [191, 90]. At equilibrium, it is at the root of the production of momentum-correlated atom pairs [192, 193, 194]. In direct analogy with the optical parametric amplification, four-wave mixing of matter waves can also be parametrized [195]. A way to achieve it in Bloch systems is by engineering the band structures with a periodic modulation of an external parameter of the system¹.

Using ultracold atoms in modulated optical lattices, parametric four-wave mixing has been studied in effective one-band systems [196, 197], for frequencies of lattice modulation low in comparison to the frequencies of interband transitions. The effect notably leads to the realization of staggered states [198, 199, 200, 201] with output channels located at the edge of the Brillouin zone.

In this chapter, we present experiments where we modulate our optical lattice at a frequency that couples the ground band with an excited band, but not at the quasi-momentum where the atoms are initially loaded. After tens of periods of modulation, we observe the emergence of new, narrow and macroscopically populated diffraction peaks, between the momentum components associated with the ground state. To understand these observations, we develop a two-level tight-binding model with interactions that allows us to study the dynamical stability of our system. As it turns out, we find sharp regions of dynamical instabilities located near the quasi-momenta at which our modulation couples the bands. These instabilities indicate narrow four-wave mixing

¹One speaks of Floquet engineering.

output channels in the Brillouin zone, where atoms colliding from $q = 0$ may accumulate. From the connection between the unstable modes and the avoided crossings, we deduce that we can tune the output channel quasi-momenta (and experimentally the momentum at which the structure emerges) by varying the position of the interband coupling in the Brillouin zone.

This last chapter is organized as follow: in the first section 5.1, we discuss the modulation regime of this study and present experiments with typical observations of the phenomenon. In the second section 5.2, we detail the development of an effective tight-binding model of two coupled bands that is able to reproduce the quasi-energy spectrum of our system. Following a perturbative Bogoliubov treatment of the interactions, we study the dynamical stability of our system for realistic parameters. We make a series of predictions from the behavior of the exponents of instability at the avoided-crossing. Section 5.3 presents experiments that test these predictions. The narrow diffraction patterns via which the new structures manifest hints at a preserved coherence in the emerging states. Moreover, the existence of closer diffraction peaks at adjustable momenta suggests, that a new, larger and controllable periodicity structures the BECs real space. We confirm these experimental hints in the last section 5.4 of this chapter by presenting results of Truncated-Wigner simulations, performed by Peter Schlagheck from the CESAM Research Unit in the University of Liège.

The research work presented in this chapter results from a collaboration for the numerical studies with Prof. Peter Schlagheck from the CESAM Research Unit at the University of Liège. A publication is in preparation:

- [66] N. Dupont, L. Gabardos, F. Arrouas, G. Chatelain, M. Arnal, J. Billy, P. Schlagheck, B. Peaudecerf, and D. Guéry-Odelin, *Emergence of a tunable supercrystalline order in a Floquet-Bloch system*, In preparation, (2022)

5.1 Modulation regime and typical observations

In this chapter, we study the behavior of a weakly interacting BEC in a phase-modulated optical lattice over many modulation periods. The atoms experience the lattice potential

$$V(x) = -s_0 \frac{E_L}{2} \cos[k_L x + \varphi_0 \cos(2\pi\nu t)]. \quad (5.1)$$

At a given lattice depth s_0 , we write $|\phi_{n,q}\rangle$ the n^{th} eigenstate of the static lattice ($\varphi_0 = 0$) at quasi-momentum q . Before the modulation, the atoms are adiabatically loaded in the ground state $|\phi_{n,q}\rangle = |\phi_{0,0}\rangle$ (Sec. 2.4.1). We then modulate the lattice in phase, with a moderate modulation amplitude φ_0 and a frequency ν that couples the ground band s to an excited band at $q \neq 0$. As the modulation does not resonantly couple $|\phi_{0,0}\rangle$ to another state of the static lattice², this situation results, in the Floquet picture, in a Floquet eigenstate $|\varphi_{m,q=0}\rangle$ that strongly resembles $|\phi_{0,0}\rangle$ for a given m . For instance at lattice depth $s_0 = 3.7$, the frequency of modulation³ $\nu = 2.9 \nu_L$ couples the lattice bands s and d at $q \approx 0.28$ (Fig. 5.1(a)). In this situation, a phase modulation of amplitude $\varphi_0 = 15^\circ$ gives

$$\max_j \{ |\langle \phi_{0,0} | \varphi_{j,0} \rangle|^2 \} = |\langle \phi_{0,0} | \varphi_{m,0} \rangle|^2 \approx 0.995, \quad (5.2)$$

with Husimi representations⁴ of $|\phi_{0,0}\rangle$ and $|\varphi_{m,0}\rangle$ displayed in Fig. 5.1. According to what we have studied so far in this thesis⁵, one expects the stroboscopic evolution of $|\phi_{0,0}\rangle$ to be almost static, as it is mainly projected over one Floquet eigenstate. Experimentally (Fig. 5.2(c-d)), for the first tens of periods of modulation, we essentially observe the ground state of the static lattice and indeed see no evolution of the characteristic diffraction patterns, with momentum components separated by $\hbar k_L = h/d$. However, after ~ 70 periods of modulation, we distinctly see new diffraction peaks appear in between the original ones, with momenta $\hbar k^* \neq \ell \times h/d$ (with $\ell \in \mathbb{Z}$). In the following, we refer to these peaks as “decimal peaks”. We note that the decimal peaks are observed both for a coupling between the bands s and d (Fig. 5.2(c)), and a coupling between the bands s and f (Fig. 5.2(c)), *i.e.* regardless the curvature of the excited band. In both cases, the TOF images clearly display the emergence of a smaller periodicity in the reciprocal space. Through Fourier analysis, this would indicate a spontaneous *in situ* structuring with a new step $d^* > d$.

In Bloch systems, the drift of the whole diffraction pattern in the resting frame of the lattice results from a variation of quasi-momentum (Sec. 1.2.1). This well known effect is at the root of the Bloch oscillation phenomenon (see for example [148, 79]), where the quasi-momentum of the system is swept adiabatically by the mean of a constant force. In our case, only a part of

²At least not by a realistic number of phonons considering the low amplitude of modulation ; see Sec. 1.3.2

³We recall the characteristic angular frequency of the lattice $\nu_L = h/2md^2 \approx 8.1$ kHz in our system ; see Sec. 2.4.

⁴Drawn with respect to the stroboscopic phase portrait (Sec. 1.1.2) of the driven system to inform incidentally on the degree of chaoticity for our modulation parameters.

⁵*i.e.* studying the evolution of the system with Schrödinger equation.

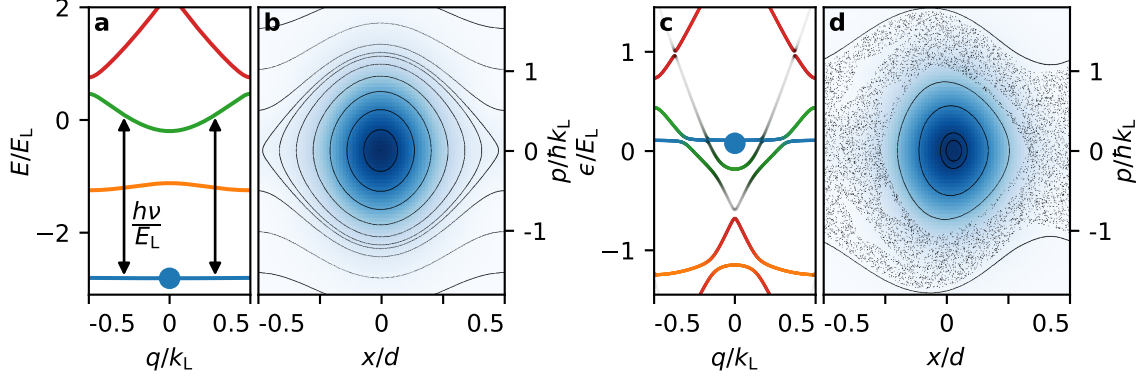


Figure 5.1 | Non-resonant modulation in the one-body wave function framework. (a) band structure of the static lattice (colored lines), with the point that corresponds to the initial state of the atoms (blue disk) and the energy of modulation (black arrows, only from the ground state) that leads to the spectrum (c). (b) Husimi representation of the ground state in the classical phase space of the static lattice. (c) Quasi-energy spectrum (colored lines) where the overlaps between the Floquet eigenstates and the eigenstates of the static lattice have been color coded (see Sec. 1.3.2) and projection of the atomic state (blue disk) at the beginning of the modulation. (d) Husimi representation of the Floquet state that maximizes the overlap with the ground state in the stroboscopic phase portrait for the modulated potential (5.1). Parameters are $s_0 = 3.7$ for all panels, and $\nu = 2.9\nu_L$ and $\phi_0 = 15^\circ$ for panels (c) and (d).

the atoms are observed in shifted but symmetric diffraction peaks (Fig. 5.2(c-d)), behaving as if a local force was selectively and symmetrically applied on some of the atoms. According to this observation, and inspired by previous studies on dynamical instabilities in Floquet system [196, 201], we attribute the emergence of the decimal peaks to short-range interactions in the system. More precisely, we interpret the emergent momentum peaks as originating from two-body collisions that occur between atoms of the lattice ground state $q = 0$ and result in atoms accumulating in $q = \pm q^*$, *i.e.* four-wave mixing of atomic wave functions from the center of the Brillouin zone scattering into quasi-momenta $q = \pm q^*$. In this framework, an initial seed is needed in the output channels of the mixing. In our case, this role is provided by fluctuations of thermal or quantum origin as will be discussed in Sec 5.4.1.

To account for the interactions in the system, we develop an effective tight-binding model with interactions. As the real system is driven by a phase modulation that couples the s band with an excited state at $q \neq 0$, we implement a two-band model with a coupling at the quasi-momentum where the modulation is resonant. We detail the development of this model in the following section.

5.2 An effective tight-binding model

We consider N bosons placed into a periodic lattice potential of L sites. Labelling two energy bands 0 and 1, we define, in the second quantization formalism, the effective Hamiltonian

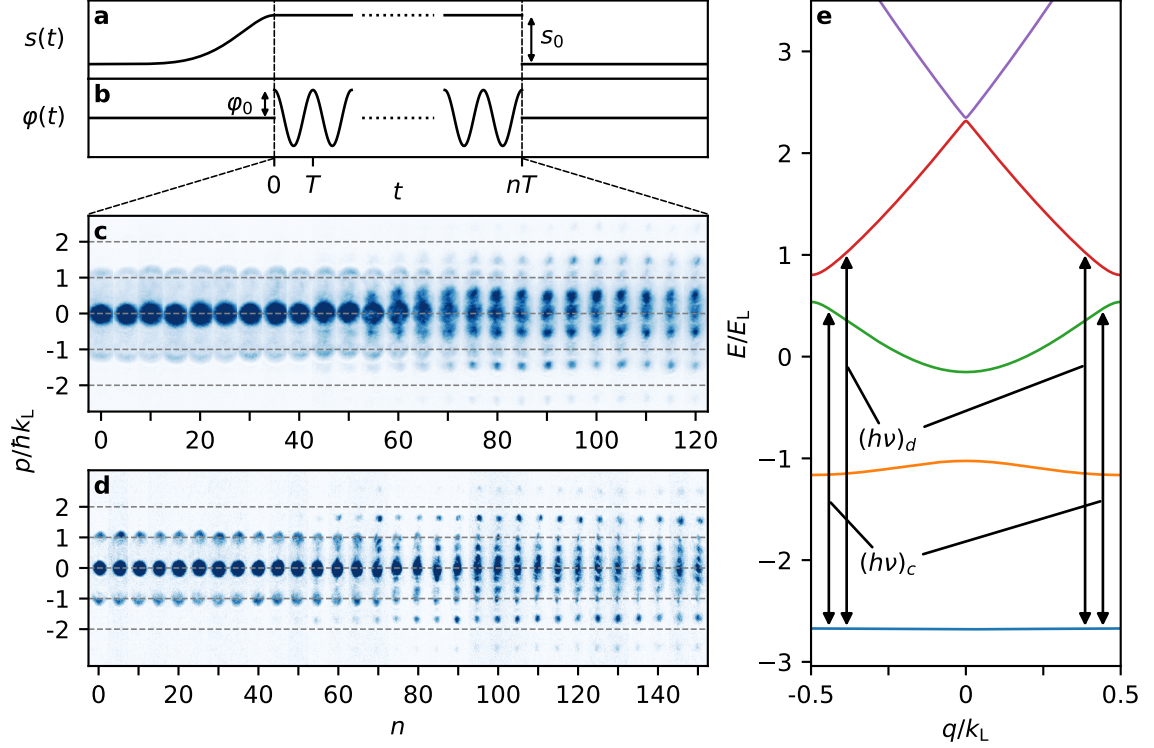


Figure 5.2 | Experimental protocol and nucleation of decimals peaks. (a) Time-evolution of lattice depth and (b) phase, showing the adiabatic loading to the ground state of the lattice, the phase modulation for an integer number of periods, and the lattice release for TOF. (c,d) Stacks of experimental absorption images ($t_{\text{TOF}} = 35$ ms) showing the stroboscopic evolutions of the momentum distribution as a function of the number n of periods T . Parameters for (c) are: BECs of $N = 5 \cdot 10^5$ atoms, $s_0 = 3.7 \pm 0.10$, $\varphi_0 = 15^\circ$, $\nu = 1/T = 25.5$ kHz. Parameters for (d) are: $N = 1 \cdot 10^5$ atoms, $s_0 = 3.4 \pm 0.10$, $\varphi_0 = 20^\circ$, $\nu = 30.0$ kHz. The upper value of the colormaps for the ODs (optical densities; Sec. 2.3) are truncated to reveal details. (e) Lattice band structure for average $\bar{s}_0 = 3.55$ and transitions from the ground state for the modulation (c) and (d).

$$\begin{aligned}
\hat{H}_{\text{eff}} &= \hat{H}_0 + \hat{H}_{\text{int}} & (5.3) \\
\hat{H}_0 &= -J_0 \sum_{j=0}^{L-1} \left(\hat{a}_{j+1}^\dagger \hat{a}_j + \hat{a}_j^\dagger \hat{a}_{j+1} \right) \\
&\quad - J_1 \sum_{j=0}^{L-1} \left(\hat{b}_{j+1}^\dagger \hat{b}_j + \hat{b}_j^\dagger \hat{b}_{j+1} \right) + \Delta E_1 \sum_{j=0}^{L-1} \hat{b}_j^\dagger \hat{b}_j \\
&\quad + iW \sum_{j=0}^{L-1} \left(\hat{b}_j^\dagger \hat{a}_j - \hat{a}_j^\dagger \hat{b}_j \right) \\
\hat{H}_{\text{int}} &= \frac{U}{2} \sum_{j=0}^{L-1} \hat{a}_j^{\dagger 2} \hat{a}_j^2,
\end{aligned}$$

where:

- our spatial coordinate is the lattice site j and the periodicity is $d = 1$,
- \hat{a}_j and \hat{b}_j (respectively \hat{a}_j^\dagger and \hat{b}_j^\dagger) are the annihilation (respectively creation) operators for the effective bands 0 and 1 on site j of the lattice,
- J_0 and J_1 are the tunneling amplitudes with neighboring sites for the two bands (in the sine-potential system that we want to model, we have a ground band with $J_0 > 0$ coupled with an higher energy band with a tunneling amplitude $|J_1| > |J_0|$),
- ΔE_1 offsets the energy of the band 1 with respect to the band 0, allowing us to tune the position of energy crossings in the Brillouin zone for the model,
- W is a coupling amplitude between the bands on site j ,
- U is an effective on-site interaction energy in the lowest band ($U_0 = U$, see below).

The interaction Hamiltonian \hat{H}_{int} here only takes into account the on-site two-body interactions for the band 0. One could include the interactions between an atom in band 0 and an atom in band 1 with a term of the form $U_{01} \sum_j \hat{a}_j^\dagger \hat{b}_j^\dagger \hat{b}_j \hat{a}_j / 2$, or the interactions between two atoms in band 1 with $U_1 \sum_j \hat{b}_j^\dagger \hat{b}_j^2 / 2$. However, as we are interested in modeling the *beginning* of the decimal peaks nucleation from atoms initially *almost all* in band 0, we will see that \hat{H}_{int} as written in Eq. (5.3) is sufficient to obtain our results (Sec. 5.2.5).

5.2.1 Modeling the Floquet bands

Setting aside the interactions for the moment, we show how \hat{H}_0 can model the two Floquet levels associated with the two lowest bands of the lattice that are coupled by the phase modulation (that is, for instance, the blue and green eigenvalues as a function of q in the spectrum of Fig. 5.1(c)). Doing so, we will determine realistic parameters for the model. As we consider a finite number L of lattice sites, the quasi-momentum q becomes a discrete quantity:

$$q = \frac{2\pi k}{L} \quad \text{with the integer } k = \left[-\frac{L}{2} + 1, \dots, \frac{L}{2} \right]. \quad (5.4)$$

In the limit $L \rightarrow \infty$, we retrieve a continuous quasi-momentum $q/k_L \in (-0.5, 0.5]$. We start by writing the annihilation operators in the reciprocal space, yielding Fourier modes \hat{c}_k and \hat{d}_k associated with the Bloch waves for our two bands:

$$\hat{c}_k = \sum_{j=0}^{L-1} \frac{e^{-i2\pi k j / L}}{\sqrt{L}} \hat{a}_j \quad \text{and} \quad \hat{d}_k = \sum_{j=0}^{L-1} \frac{e^{-i2\pi k j / L}}{\sqrt{L}} \hat{b}_j, \quad (5.5)$$

along with the inverse transformations

$$\hat{a}_j = \sum_k \frac{e^{i2\pi kj/L}}{\sqrt{L}} \hat{c}_k \quad \text{and} \quad \hat{b}_j = \sum_k \frac{e^{i2\pi kj/L}}{\sqrt{L}} \hat{d}_k, \quad (5.6)$$

where the summation boundaries for k have been defined in Eq. (5.4). The Hamiltonian \hat{H}_0 (Eq. (5.3)) becomes⁶

$$\begin{aligned} \hat{H}_0 = & \sum_k -2J_0 \cos\left(\frac{2\pi k}{L}\right) \hat{c}_k^\dagger \hat{c}_k + \sum_k \left(-2J_1 \cos\left(\frac{2\pi k}{L}\right) + \Delta E_1\right) \hat{d}_k^\dagger \hat{d}_k \\ & + \sum_k iW \left(\hat{d}_k^\dagger \hat{c}_k - \hat{c}_k^\dagger \hat{d}_k\right). \end{aligned} \quad (5.7)$$

We see that the eigenenergies of the uncoupled Bloch modes are cosine functions of the quasi-momentum, as expected for a tight-binding model:

$$\begin{aligned} E_0(k) &= -2J_0 \cos\left(\frac{2\pi k}{L}\right), \\ E_1(k) &= -2J_1 \cos\left(\frac{2\pi k}{L}\right) + \Delta E_1. \end{aligned} \quad (5.8)$$

The Hamiltonian (5.7) is now expressed as a sum over the Brillouin zone: $\hat{H}_0 = \sum_k \hat{H}_0(k)$, where the coupling Hamiltonian $\hat{H}_0(k)$ in the sub-space of quasi-momentum $q = 2\pi k/L$ reads

$$\hat{H}_0(k) = E_0(k) \hat{c}_k^\dagger \hat{c}_k + E_1(k) \hat{d}_k^\dagger \hat{d}_k + iW \left(\hat{d}_k^\dagger \hat{c}_k - \hat{c}_k^\dagger \hat{d}_k\right). \quad (5.9)$$

This Rabi Hamiltonian can be diagonalized by defining the mode \hat{u}_k and \hat{v}_k :

$$\begin{aligned} \hat{u}_k &= \cos\left(\frac{\theta(k)}{2}\right) \hat{c}_k - i \sin\left(\frac{\theta(k)}{2}\right) \hat{d}_k, \\ \hat{v}_k &= \sin\left(\frac{\theta(k)}{2}\right) \hat{c}_k + i \cos\left(\frac{\theta(k)}{2}\right) \hat{d}_k, \end{aligned} \quad (5.10)$$

where the mixing angle $\theta(k) \in [0, \pi)$ is defined by

$$\tan(\theta(k)) = \frac{2W}{E_0(k) - E_1(k)}. \quad (5.11)$$

⁶We use the relation $\sum_{j=0}^{L-1} e^{i2\pi j(k-k')/L} = L \delta_{k,k'}$.

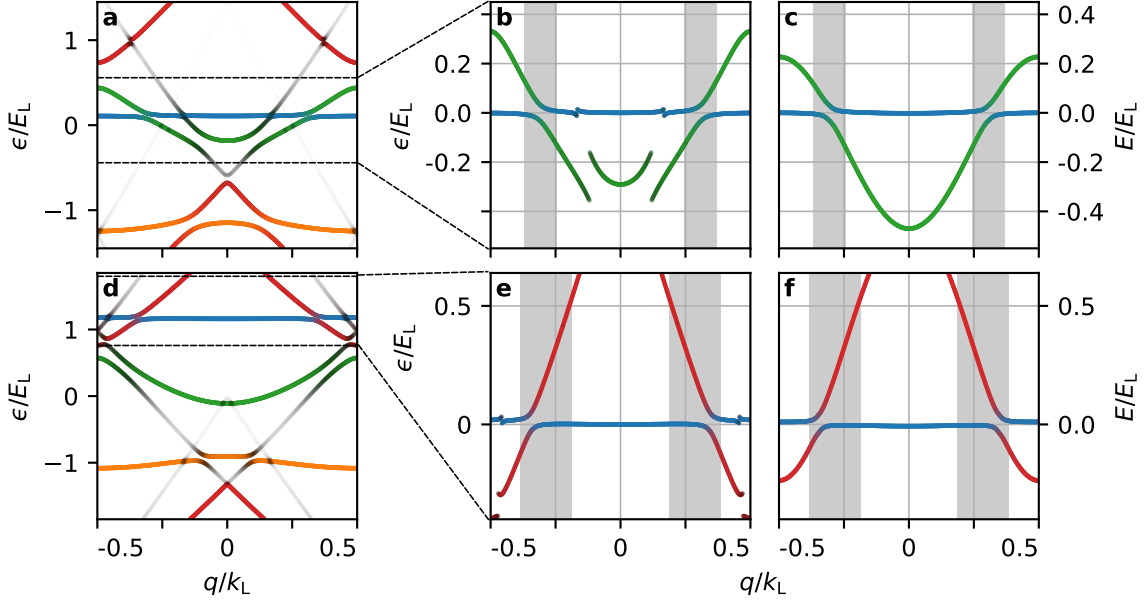


Figure 5.3 | Partial fits of Floquet spectra with the two-level tight-binding model. (a,d) Typical Floquet spectra (colored lines) to be partially modeled (see text). Parameters are $s_0 = 3.7$, $\nu = 23.5$ kHz and $\varphi_0 = 15^\circ$ for (a) and $s_0 = 3.4$, $\nu = 30.0$ kHz and $\varphi_0 = 15^\circ$ for (d). (b,e) Zooms on the modeled parts of (a-e) resp., each only displaying the quasi-energies of the 2 Floquet states onto which the coupled static bands are maximally decomposed. (c,f) Spectra of \hat{H}_0 , the Hamiltonian of the model (Eq. (5.3)) without interactions, with parameters adjusted to fit (b,e) The parameters for (c) are $(J_0, J_1, \Delta E_1, W) = (1.63 \cdot 10^{-3}, 1.73 \cdot 10^{-1}, -1.22 \cdot 10^{-1}, 3.11 \cdot 10^{-2}) \times E_L$ and the parameters for (f) are $(J_0, J_1, \Delta E_1, W) = (3.00 \cdot 10^{-3}, -2.75 \cdot 10^{-1}, 3.18 \cdot 10^{-1}, 3.81 \cdot 10^{-2}) \times E_L$. The gray areas in (b,c,e,f) indicate the intervals of quasi-momenta over which the fits are performed (see text).

In the following, we write θ with an implicit dependence on k to lighten the notation. We finally get

$$\hat{H}_0 = \sum_k \left(E_u(k) \hat{u}_k^\dagger \hat{u}_k + E_v(k) \hat{v}_k^\dagger \hat{v}_k \right) \quad (5.12)$$

with dressed energy levels

$$\begin{aligned} E_u(k) &= E_0(k) \cos^2 \left(\frac{\theta}{2} \right) + E_1(k) \sin^2 \left(\frac{\theta}{2} \right) + W \sin(\theta), \\ E_v(k) &= E_0(k) \sin^2 \left(\frac{\theta}{2} \right) + E_1(k) \cos^2 \left(\frac{\theta}{2} \right) - W \sin(\theta). \end{aligned} \quad (5.13)$$

With the effective dressed bands of Eq. (5.13), we can now fit the part of interest in the Floquet spectrum of the real system with the parameters J_0 , J_1 , ΔE_1 and W . This is done in the continuous quasi-momentum limit ($L \rightarrow \infty$). We draw in Fig. 5.3 the fit of two spectra for modulation parameters similar to those of the experiments of Fig. 5.2. As the frequency of

modulation can also couple the excited state to even higher bands (or, slightly, the ground band to higher bands through multi-phonon processes, see Sec. 1.3.2), we see in Fig. 5.3(b,e) that more than two avoided crossings are seen in the part of interest of the Floquet spectra. Therefore, we only perform the fits in intervals of quasi-momenta around the main avoided crossings. For this adjustment, the quasi-energies of the real system are also offsetted in order to have a zero eigenvalue in the center of the Brillouin zone for the Floquet state associated with the lower band of the model (as we only set an energy offset for band 1 in our model (5.3)). Figures 5.3(c,f) show the corresponding adjusted spectra of H_0 (with details presented in the figure caption). This method can be applied for other modulation parameters if they are moderate enough to identify effective static bands. Moreover, the results (5.9), (5.11) and (5.13) are general and can be used with other choices for the uncoupled energy levels $E_0(k)$ and $E_1(k)$, for instance with more paraboloid functions for the method to work at lower lattice depths, in a regime where the tight-binding approximation with only next-neighbor tunneling does not hold.

We can now add the interactions and study their effect in a model with two realistic coupled bands.

5.2.2 Adding the interactions

In Eq. (5.3), the presence of the interaction part \hat{H}_{int} , quartic in operators, complicates the diagonalization of the effective Hamiltonian \hat{H}_{eff} in order to determine how the system evolves. To handle the quartic terms, we use a perturbative approach in the fashion of N. Bogoliubov [202, 90]. We choose to present a detailed derivation of the equations of evolution for the perturbation modes in the Brillouin zone. Results are summarized at the end of the derivation (p. 136).

In the experimental situation (Fig. 5.2), the vast majority of atoms (with the exception of perhaps some thermal excitations) is initially in the ground state. In the model, the corresponding mode is \hat{c}_0 from Eq. (5.5). This mode therefore contains a large number of atoms $N_0 = \langle \hat{c}_0^\dagger \hat{c}_0 \rangle$, and only a small number of atoms $N^* = N - N_0$ populates the other modes:

$$N^* = \sum_{k \neq 0} \left(\langle \hat{c}_k^\dagger \hat{c}_k \rangle + \langle \hat{d}_k^\dagger \hat{d}_k \rangle \right) + \langle \hat{d}_0^\dagger \hat{d}_0 \rangle \ll N_0 \approx N. \quad (5.14)$$

The perturbative treatment then consists in an expansion in powers of the small parameter $\varepsilon = N^*/N$. Besides, the Bogoliubov prescription consists in replacing the macroscopically populated mode \hat{c}_0 by a scalar⁷: $\hat{c}_0 \simeq \sqrt{N_0} \simeq \sqrt{N}$. This prescription implies that we can decompose the mode \hat{a}_j as (from Eq. (5.6))

$$\hat{a}_j = \sqrt{n_0} + \delta \hat{a}_j, \quad (5.15)$$

⁷A more rigorous method can be found in [203, 204].

with $n_0 = N_0/L$ and

$$\delta\hat{a}_j = \sum_{k \neq 0} \frac{e^{i2\pi kj/L}}{\sqrt{L}} \hat{c}_k. \quad (5.16)$$

We note at this stage that, from these definitions, we have

$$\sum_{j=0}^{L-1} \delta\hat{a}_j = \sum_{k \neq 0} \hat{c}_k \delta_{0,k} = 0, \quad (5.17)$$

which is to say that the perturbation on band 0 is orthogonal to the mode of the condensate described by $\phi(j) = \sqrt{n_0}$:

$$\sum_{j=0}^{L-1} \phi^*(j) \delta\hat{a}_j = 0. \quad (5.18)$$

We also note that the number operator for the non-condensed modes can be written equivalently

$$\hat{N}^* = \sum_{j=0}^{L-1} \delta\hat{a}_j^\dagger \delta\hat{a}_j + \sum_{j=0}^{L-1} \hat{b}_j^\dagger \hat{b}_j. \quad (5.19)$$

We can now insert decomposition (5.15) into the \hat{H}_{eff} (5.3) and consider terms in successive powers of the perturbations (*i.e.* containing 0, 1 or 2 quantum fields).

Zeroth order. At lowest order, $H_{\text{eff}}^{(0)}$ is a function of the atom number:

$$H_{\text{eff}}^{(0)} = -2J_0 N_0 + \frac{N_0^2 U}{2L} \simeq -2J_0 N + \frac{N^2 U}{2L}, \quad (5.20)$$

where, in the second equation, we neglected second order corrections from perturbations⁸. Equation (5.20) is the energy of the condensate of approximately N atoms in the mode \hat{c}_0 . In particular, we can identify the chemical potential of the condensate:

$$\mu = \frac{\partial H_{\text{eff}}^{(0)}}{\partial N} = -2J_0 + nU. \quad (5.21)$$

⁸As $N_0 \simeq N - \hat{N}^*$, see Eq. (5.19)

First order. Injecting the decomposition (5.15) in \hat{H}_{eff} (5.3) yields the following first-order terms:

$$\begin{aligned}\hat{H}_{\text{eff}}^{(1)} &= \hat{H}_0^{(1)} + \hat{H}_{\text{int}}^{(1)} \\ \hat{H}_0^{(1)} &= -2J_0\sqrt{n_0} \sum_{j=0}^{L-1} (\delta\hat{a}_j^\dagger + \delta\hat{a}_j) + iW\sqrt{n_0} \sum_{j=0}^{L-1} (\hat{b}_j^\dagger - \hat{b}_j) \\ \hat{H}_{\text{int}}^{(1)} &= n_0^{3/2}U \sum_{j=0}^{L-1} (\delta\hat{a}_j^\dagger + \delta\hat{a}_j).\end{aligned}\tag{5.22}$$

However, from Eq. (5.17), the only contribution that does not cancel out is

$$H_{\text{eff}}^{(1)} \simeq iW\sqrt{n} \sum_{j=0}^{L-1} (\hat{b}_j^\dagger - \hat{b}_j),\tag{5.23}$$

where we have equated $n \simeq n_0$ (as it amounts to neglecting third-order terms) and neglected edge terms in rearranging the sums. We will make sense of this remaining term (5.23) shortly below.

Second order. The terms up to the second order in perturbations are

$$\begin{aligned}\hat{H}_{\text{eff}}^{(2)} &= \hat{H}_0^{(2)} + \hat{H}_{\text{int}}^{(2)} \\ \hat{H}_0^{(2)} &= -J_0 \sum_{j=0}^{L-1} (\delta\hat{a}_{j+1}^\dagger \delta\hat{a}_j + \delta\hat{a}_j^\dagger \delta\hat{a}_{j+1}) - J_1 \sum_{j=0}^{L-1} (\hat{b}_{j+1}^\dagger \hat{b}_j + \hat{b}_j^\dagger \hat{b}_{j+1}) + \Delta E_1 \sum_{j=0}^{L-1} \hat{b}_j^\dagger \hat{b}_j \\ \hat{H}_{\text{int}}^{(2)} &\simeq \frac{nU}{2} \sum_{j=0}^{L-1} (\delta\hat{a}_j^{\dagger 2} + \delta\hat{a}_j^2 + 4\delta\hat{a}_j^\dagger \delta\hat{a}_j).\end{aligned}\tag{5.24}$$

Here, another contribution needs to be considered: at zeroth order in Eq. (5.20), we defined the energy of the condensate $H_{\text{eff}}^{(0)}(N_0) \simeq H_{\text{eff}}^{(0)}(N)$. However the corrections in this last equation are of order two. Therefore, we may write

$$\hat{H}_{\text{eff}}^{(0)}(N_0) = \hat{H}_{\text{eff}}^{(0)}(N - \hat{N}^*) \simeq H_{\text{eff}}^{(0)}(N) + 2J_0\hat{N}^* - 2N\frac{\hat{N}^*U}{2L},\tag{5.25}$$

stopping the expansion at second order. This means that in order for our treatment to be consistent, we need to include in the second order Hamiltonian the extra term

$$\hat{H}_\mu^{(2)} = (2J_0 - nU)\hat{N}^* = -\mu\hat{N}^*, \quad (5.26)$$

where we recognized the chemical potential μ of the condensate (5.21). Equation (5.26) means that, in this approximation, the condensate is acting as a chemical potential for the perturbation modes.

Dynamics in $k = 0$. From Eqs. (5.23), (5.24) and (5.26), we can isolate the terms pertaining to the dynamics of the mode \hat{d}_0 (noting that $\sum_j \hat{b}_j = \sqrt{L}\hat{d}_0$ by definition (5.5)):

$$\hat{H}_{k=0}^{(2)} = iW\sqrt{N}(\hat{d}_0^\dagger - \hat{d}_0) + (-2J_1 + \Delta E_1 - \mu)\hat{d}_0^\dagger\hat{d}_0. \quad (5.27)$$

This is, in fact, a Rabi Hamiltonian for the mode \hat{d}_0 , driven by the coupling to the condensate mode $\hat{c}_0 \simeq \sqrt{N}$. This coupling is non resonant provided the energy difference $(-2J_1 + \Delta E_1 - \mu)$ is large compared to the coupling. We will make sure to consider such situations, as in Figs. 5.1 and 5.3.

Dynamics in $k \neq 0$. The dynamics of the other modes is also best viewed in momentum space. Rewriting the corresponding terms of Eq. (5.24) with the use of Eqs. (5.16), (5.6) and (5.10), we get

$$\hat{H}_{0,k \neq 0}^{(2)} = \sum_{k \neq 0} \left(E_u(k)\hat{u}_k^\dagger\hat{u}_k + E_v(k)\hat{v}_k^\dagger\hat{v}_k \right), \quad (5.28)$$

and, likewise for the interaction terms⁹:

$$\begin{aligned} \hat{H}_{\text{int},k \neq 0}^{(2)} = & \frac{nU}{2} \sum_{k \neq 0} \left\{ \left(\cos\left(\frac{\theta}{2}\right)\hat{u}_k + \sin\left(\frac{\theta}{2}\right)\hat{v}_k \right) \left(\cos\left(\frac{\theta}{2}\right)\hat{u}_{-k} + \sin\left(\frac{\theta}{2}\right)\hat{v}_{-k} \right) \right. \\ & + \left(\cos\left(\frac{\theta}{2}\right)\hat{u}_k^\dagger + \sin\left(\frac{\theta}{2}\right)\hat{v}_k^\dagger \right) \left(\cos\left(\frac{\theta}{2}\right)\hat{u}_{-k}^\dagger + \sin\left(\frac{\theta}{2}\right)\hat{v}_{-k}^\dagger \right) \\ & \left. + 4 \left(\cos\left(\frac{\theta}{2}\right)\hat{u}_k^\dagger + \sin\left(\frac{\theta}{2}\right)\hat{v}_k^\dagger \right) \left(\cos\left(\frac{\theta}{2}\right)\hat{u}_k + \sin\left(\frac{\theta}{2}\right)\hat{v}_k \right) \right\}. \end{aligned} \quad (5.29)$$

Finally, the chemical potential term for the perturbation may be written

$$\hat{H}_{\mu,k \neq 0}^{(2)} = -\mu \sum_{k \neq 0} \left(\hat{u}_k^\dagger\hat{u}_k + \hat{v}_k^\dagger\hat{v}_k \right). \quad (5.30)$$

⁹We here use the fact that $\theta(k) = \theta(-k)$ for the symmetric band structure of \hat{H}_0 , modeling our Floquet-Bloch system whose quasi-energy spectrum also presents that symmetry (*e.g.* Fig. 5.3) as it is a time-reversal symmetric system (see Eq. (5.1) and Sec. 1.2.2).

With the quadratic expression for $\hat{H}_{\text{eff},k \neq 0}^{(2)}$ (*i.e.* the sum of Eqs. (5.28), (5.29) and (5.30)), we can now study the dynamics of the modes $(\hat{u}_k, \hat{v}_k)_{k \neq 0}$ in the system.

5.2.3 Stability

Evolution of the perturbations. To study the stability of the system, we write the Heisenberg equations for the evolution of the fields $\hat{u}_{k \neq 0}$ and $\hat{v}_{k \neq 0}$ from their commutation with $\hat{H}_{\text{eff},k \neq 0}^{(2)}$. In the following, we stop specifying that this study of dynamical stability is performed away from $k = 0$. We remind that the operators \hat{c}_k and \hat{d}_k , as well as \hat{u}_k and \hat{v}_k , have bosonic commutation relations. We have $[\hat{u}_k, \hat{v}_{k'}] = [\hat{u}_k, \hat{v}_{k'}^\dagger] = 0$ ($\forall k$) and $[\hat{u}_k, \hat{u}_{k'}^\dagger] = [\hat{v}_k, \hat{v}_{k'}^\dagger] = \mathbb{1}\delta_{k,k'}$. Important consequences for our derivation are

$$\left[\hat{u}_k, \hat{u}_k^\dagger \hat{u}_k \right] = \hat{u}_k, \quad \left[\hat{u}_k, \sum_{k'} \hat{u}_{k'}^\dagger \hat{u}_{k'} \right] = \hat{u}_k \quad \text{and} \quad \left[\hat{u}_k, \sum_{k'} \hat{u}_{k'}^\dagger \hat{u}_{-k'}^\dagger \right] = 2\hat{u}_{-k}^\dagger.$$

With these relations, we find that the differential equations for the evolution of \hat{u}_k and \hat{v}_k are:

$$\begin{aligned} i\hbar \frac{\partial \hat{u}_k}{\partial t} &\simeq \left[\hat{u}_k, \hat{H}_{\text{eff}}^{(2)} \right] & (5.31) \\ &\simeq A_{uu}(k)\hat{u}_k + A_{uv}(k)\hat{v}_k + B_{uu}(k)\hat{u}_{-k}^\dagger + B_{uv}(k)\hat{v}_{-k}^\dagger \\ i\hbar \frac{\partial \hat{v}_k}{\partial t} &\simeq \left[\hat{v}_k, \hat{H}_{\text{eff}}^{(2)} \right] \\ &\simeq A_{uv}(k)\hat{u}_k + A_{vv}(k)\hat{v}_k + B_{uv}(k)\hat{u}_{-k}^\dagger + B_{vv}(k)\hat{v}_{-k}^\dagger. \end{aligned}$$

The nomenclature for the coefficients is such that A couples the evolution of modes in the same quasi-momentum while B couples the evolution of modes at opposite quasi-momentum, with indices specifying the modes. From the parameters of the model, these coefficients read

$$\begin{aligned} A_{uu}(k) &= \tilde{E}_u(k) + 2nU \cos^2\left(\frac{\theta}{2}\right) & B_{uu}(k) &= nU \cos^2\left(\frac{\theta}{2}\right) & (5.32) \\ A_{vv}(k) &= \tilde{E}_v(k) + 2nU \sin^2\left(\frac{\theta}{2}\right) & B_{vv}(k) &= nU \sin^2\left(\frac{\theta}{2}\right) \\ A_{uv}(k) &= nU \sin(\theta) & B_{uv}(k) &= \frac{nU}{2} \sin(\theta), \end{aligned}$$

where we defined the energy levels of the coupled bands offsetted by the chemical potential $\tilde{E}_{u,v}(k) = E_{u,v}(k) - \mu$. In the following, we make implicit the dependence of $\tilde{E}_{u,v}$ (as well as that of the parameters of Eq. (5.32)) on the quasi-momentum $q = 2\pi k/L$. In Eq. (5.31), we see

that we get a set of four coupled differential equations. The last two can simply be obtained by complex conjugation of the first two and transforming¹⁰ $k \rightarrow -k$:

$$\begin{aligned} i\hbar \frac{\partial \hat{u}_{-k}^\dagger}{\partial t} &\simeq -B_{uu}\hat{u}_k - B_{uv}\hat{v}_k - A_{uu}\hat{u}_{-k}^\dagger - A_{uv}\hat{v}_{-k}^\dagger \\ i\hbar \frac{\partial \hat{v}_{-k}^\dagger}{\partial t} &\simeq -B_{uv}\hat{u}_k - B_{vv}\hat{v}_k - A_{uv}\hat{u}_{-k}^\dagger - A_{vv}\hat{v}_{-k}^\dagger. \end{aligned} \quad (5.33)$$

We write this system in a matrix format:

$$i\hbar \frac{\partial}{\partial t} \begin{pmatrix} \hat{u}_k \\ \hat{v}_k \\ \hat{u}_{-k}^\dagger \\ \hat{v}_{-k}^\dagger \end{pmatrix} = \mathcal{L}(k) \begin{pmatrix} \hat{u}_k \\ \hat{v}_k \\ \hat{u}_{-k}^\dagger \\ \hat{v}_{-k}^\dagger \end{pmatrix}, \quad (5.34)$$

where the matrix $\mathcal{L}(k)$ that governs the evolution of the modes reads

$$\mathcal{L}(k) = \begin{pmatrix} A_{uu} & A_{uv} & B_{uu} & B_{uv} \\ A_{uv} & A_{vv} & B_{uv} & B_{vv} \\ -B_{uu} & -B_{uv} & -A_{uu} & -A_{uv} \\ -B_{uv} & -B_{vv} & -A_{uv} & -A_{vv} \end{pmatrix}. \quad (5.35)$$

The spectrum of $\mathcal{L}(k)$ contains the information about the stability of the system, as discussed in the following summary box.

Result of the perturbative treatment of the interactions.

$\mathcal{L}(k)$ (5.35) is the coupling matrix for the differential equations (5.34) of the modes \hat{u}_k , \hat{v}_k , \hat{u}_{-k} , and \hat{v}_{-k} (which are the coupled Fourier modes of our perturbations (5.10)). Its diagonalization yields eigenmodes whose angular frequencies of evolution are the four eigenvalues $\lambda_i(k)$ of $\mathcal{L}(k)$. These eigenvalues contain the information about the stability of the system. Indeed, any perturbation at quasi-momentum $q = 2\pi k/L$ will have a stable oscillating behavior *if and only if* all four eigenvalues $\lambda_i(q)$ are real. On the other hand, if either of the $\lambda_i(q)$ has non-zero imaginary part along the Brillouin zone, we get a “complex frequency” associated to exponential growth of unstable modes at that quasi-momentum. In the following, we will compute and display the instability parameter

$$w(q) = \max_i \{|\text{Im}\{\lambda_i(q)\}|\}. \quad (5.36)$$

Evaluated for all quasi-momentum $-0.5 < q/k_L \leq 0.5$ (taken in the continuous limit

¹⁰Using once again the central symmetry of the band structure (see footnote p. 134), implying here $A_{\alpha\beta}(-k) = A_{\alpha\beta}(k)$ and $B_{\alpha\beta}(-k) = B_{\alpha\beta}(k)$ for all modes $\hat{\alpha}, \hat{\beta}$.

corresponding to $L \rightarrow \infty$), $w(q)$ informs us on the regions where to expect the growth of unstable modes in the Brillouin zone.

The matrix elements of $\mathcal{L}(k)$ (5.35) for the evaluation of $w(q)$ are computed using Eqs. (5.32), (5.13), (5.11) and (5.8).

To summarize, in Sec. 5.2.1, we developed a method to fit Floquet spectra of the real system and determine realistic parameters for the model. In this section, we explicitly obtained the elements of the evolution matrix for the perturbations in the Brillouin zone, allowing to determine regions of instability in the system through the parameter $w(q)$ (Eq. (5.36)). The only unknown quantity is the interaction parameter nU . In the next section, we discuss an estimation for this parameter.

5.2.4 Estimation of the interaction parameter

The interaction parameter nU in the effective one-dimensional model has to take into account two features from the real system:

- (i) the real system is a one-dimensional lattice of pancakes of atoms, highly confined in the lattice wells parallel to the lattice and loosely confined in perpendicular directions,
- (ii) the number of atoms per site is not constant along the lattice, with more atoms in the center of the hybrid trap than further away from it.

A heuristic formula obtained from [205, 201] allows us to estimate the interaction parameter n_0U_0 in the central, most populated lattice site:

$$n_0U_0 \simeq \hbar\Omega_{\perp} \sqrt{\frac{a_s}{\sqrt{2\pi}a_0}} \sqrt{n_0}, \quad (5.37)$$

where $\Omega_{\perp} \approx 2\pi \times 67$ Hz is the averaged angular frequency of the hybrid trap along the axes perpendicular to the lattice (see Sec. 2.2.4), $a_s \approx 5.23$ nm is the s -wave scattering length of ^{87}Rb , $a_0 = \sqrt{\hbar/m\omega_0}$ is the characteristic size of the ground state in each lattice site in the harmonic approximation (with $\omega_0 = \sqrt{s_0} \times 2\pi\nu_L$, see Sec. 1.4.1) and n_0 is the number of atoms in this central lattice site. Working with BECs of $N \approx 5 \cdot 10^5$ atoms in a hybrid trap with angular frequencies $(\Omega_x, \Omega'_y, \Omega'_z) \approx 2\pi \times (10.4, 66, 68)$ Hz, we can estimate [201, 66] $n_0 \approx 4.4 \cdot 10^3$ atoms in this central lattice site. There, we thus get for the interaction parameter (in units of E_L): $n_0U_0/E_L \approx 0.86$. This estimate gives us an upper bound for nU across the lattice, which permits to study the spectrum of $\mathcal{L}(q)$ (Eq. (5.35)) over a realistic range of interaction parameters.

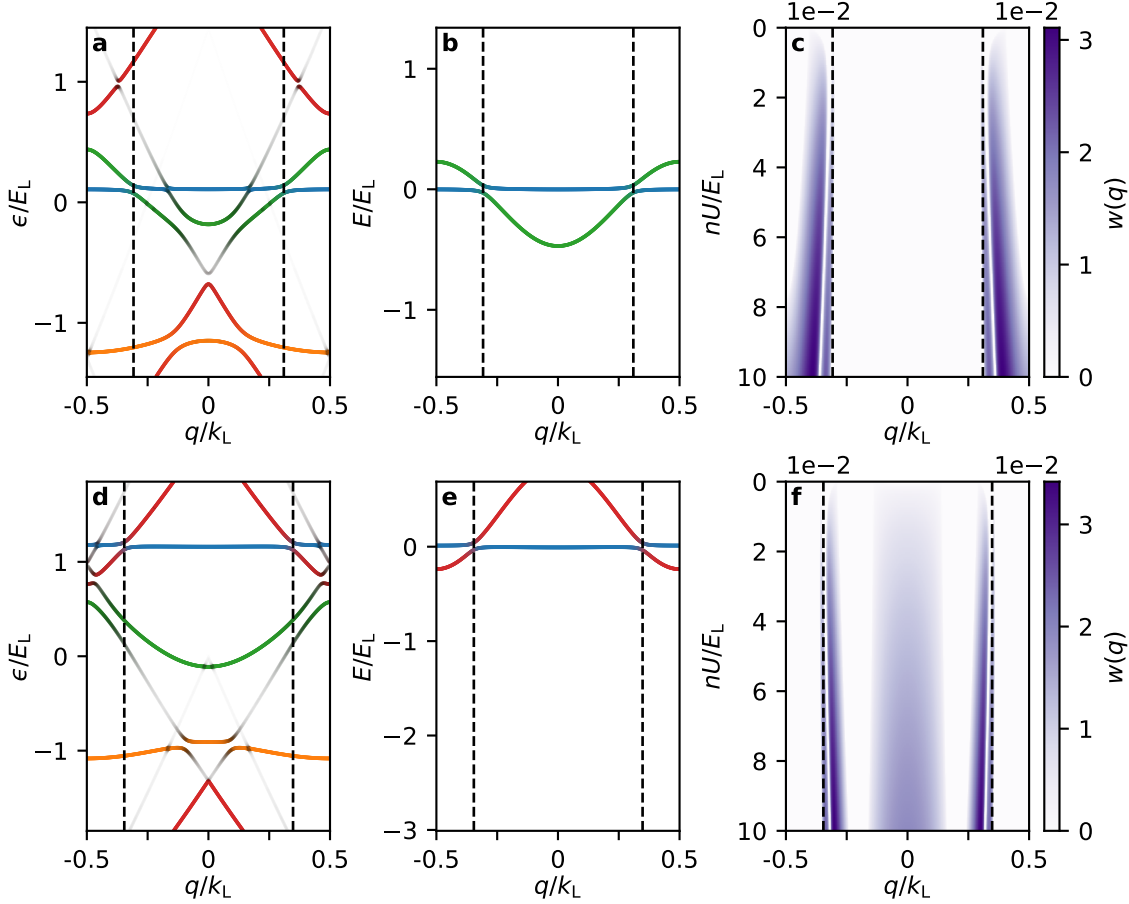


Figure 5.4 | Typical results of the two-band tight-binding model with interactions for realistic parameters. (a,d) Quasi-energy spectra. (b,e) Spectra of the effective Hamiltonian partially fitting (a,d) (see Sec. 5.2.1). (c,f) Corresponding instability parameter $w(q)$ (5.36) as a function of q and nU . Parameters for (a-c) correspond to those of Fig. 5.3(a-c) and parameters for (d-f) correspond to those of Fig. 5.3(d-f). The vertical black dashed lines mark the quasi-momenta of the avoided crossings. A closer look of the crossings can be seen in Fig. 5.3.

5.2.5 Results of the model and predictions

In the Secs. 5.2.1 and 5.2.4, we have determined realistic values for all the parameters of the tight-binding model and we are now able to study the stability of the system by computing the instability parameter $w(q)$ along the Brillouin zone. According to our estimation of the upper bound for the interaction parameter, we evaluate $w(q)$ in the realistic interval $nU \in [0, 0.1] E_L$. Figure 5.4 shows a summary of our approach, from the fit of the Floquet bands to the study of the spectrum of $\mathcal{L}(q)$. As nU is increased, we see emerging sharp stripes in quasi-momentum of non-zero values of $w(q)$, corresponding to region where $\mathcal{L}(q)$ has at least one complex eigenvalue and where instabilities are expected. Strikingly, these sharp regions are observed in the vicinity of the avoided crossings. As we will demonstrate in the next section of experimental results, the decimal peaks observed in the experiments can be traced back to these unstable regions in the Brillouin zone.

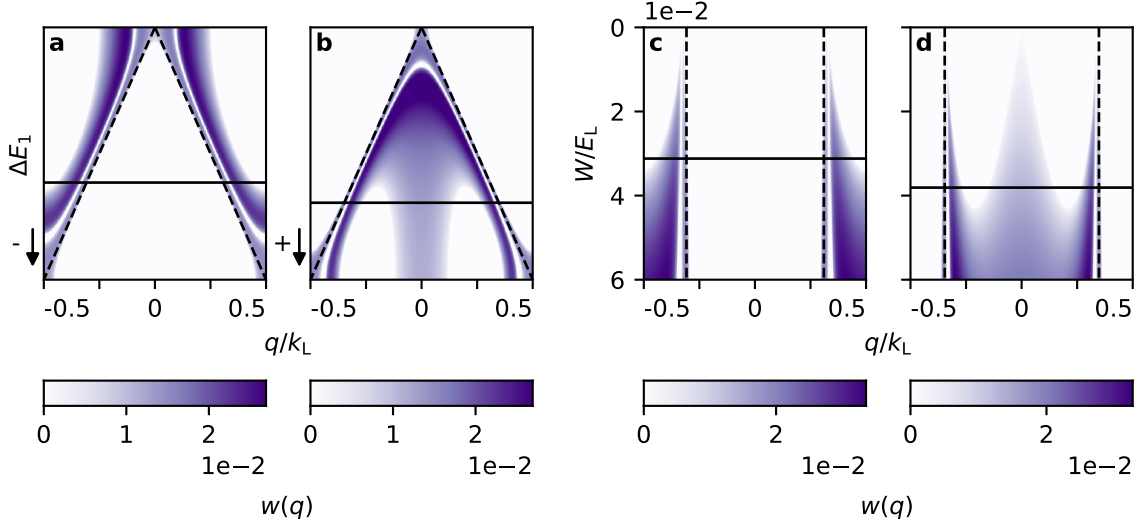


Figure 5.5 | Predictions from the two-band tight-binding model with interactions. Instability regions versus ΔE_1 and W with the interaction parameter value fixed to $nU = 0.05 E_L$. **(a)** Instability parameter $w(q)$ as a function of q and ΔE_1 for $J_1 > 0$ (the parameters J_0 , J_1 and W are those of the fit of Fig. 5.3(c)). The variation of ΔE_1 is such that the crossings position q' (oblique dashed black lines) varies linearly, that is $\Delta E_1(q') = -2J_0 \cos(q') + 2J_1 \cos(q')$, with $0 \leq q' \leq \pi$ from the top to the bottom of the panel. **(b)** Same for $J_1 < 0$, with parameters corresponding to Fig. 5.3(f). **(c)** $w(q)$ as a function of q and W for $J_1 > 0$ (the parameters J_0 , J_1 and ΔE_1 are those of the fit of Fig. 5.3(c)). **(d)** Same for $J_1 < 0$, with parameters corresponding to Fig. 5.3(f). The vertical dashed black lines mark the crossings position and the horizontal plain black line mark the value of the varied parameter corresponding to Fig. 5.4.

We see in Fig. 5.4 that the relative position of the unstable regions and the crossings depends on the curvature of the higher band 1 in the model. Indeed for $J_1 > 0$ (Fig. 5.4(c)), instabilities are observed outside the central region delimited by the crossings in the first Brillouin zone, while we observe them toward the inside this region for $J_1 < 0$ (Fig. 5.4(f)). This is a general trend of the model: for the regime of relative magnitude of $|J_0|$ and $|J_1|$ considered, instabilities are always observed away from the crossings, in the direction toward which the upper band grows (*i.e.* away from $p = 0$ in the unfolded band structure ; see for instance Sec. 2.4.3). However, we will see in the next section (Sec. 5.3.1) that these small shifts are not resolved experimentally.

In Fig. 5.4(f), one can distinguish a broad region of low instability centered in $q = 0$. This may indicate in that case a less pronounced destabilization of modes near $q = 0$.

Predictions. We can make a series of experimental predictions from the model.

(i) A first prediction follows from the apparent connection between the avoided crossings and the instability region. We further investigate this connection in Fig. 5.5, where we fix the interaction parameter to a realistic intermediate value of $nU = 0.05 E_L$ and we vary the energy offset ΔE_1 of the band 1. This changes the quasi-momenta at which the uncoupled levels of the model cross, and we see in Fig. 5.5(a,b) that the position of the instability regions follows this variation. Experimentally, the positions of the avoided crossings are mainly set by

the modulation frequency of the lattice (see Fig. 1.6). By tuning this parameter, we expect four-wave mixing to feed decimal peaks at momenta that will follow the variation of the quasi-momentum at which resonant coupling occurs. This experiment is presented in Sec. 5.3.2.

(ii) Another expected behavior directly stems from Fig. 5.4: we note that as nU increases, so do the maxima of the instability parameter $w(q)$. In the model, this is associated with shorter instability timescales. In the experiment, we can *decrease* the interaction parameter nU by reducing the number of atoms in the BECs (Sec. 2.2.4), which is expected to delay the decimal peaks nucleation. In Fig. 5.5(c,d), we also see that the variation of the coupling parameter W results in a similar trend. Experimentally, the main parameter on which W depends is the amplitude of modulation φ_0 . Therefore, we should measure a strictly decreasing nucleation timescale as φ_0 increases. These experiments are presented in Sec. 5.3.3.

(iii) A last prediction concerns the generality of the model. Since the effective model is blind to the coupling mechanism between the bands, we can for instance expect similar instabilities with another type of modulation. With our experimental setup, we can very well generate similar looking Floquet spectra by modulating the *depth* instead of the phase of the lattice (see for instance Fig. 1.6). As a result, we expect to observe the nucleation of decimal peaks in depth-modulated optical lattices with similar modulation parameters.

We present experimental results in the next section. We start in 5.3.1 by measuring the quasi-momentum of the experimental decimal peaks to confirm the connection with the instability regions observed in the spectrum of $\mathcal{L}(q)$. In the rest of the section, we test our series of predictions.

5.3 Experimental results

5.3.1 Band-mapping method and quasi-momentum of the decimal diffraction peaks

In the previous section, we developed a tight-binding model that predicts the growth of instability modes in the neighborhood of the avoided crossings in the quasi-energy spectrum. Following this result, we perform a band-mapping experiment to access the quasi-momentum of the decimal peaks (observed in for example in Fig. 5.2) in order to confirm that it matches that of the instabilities predicted by the model. A reminder on the band-mapping technique is provided in Sec. 2.4.3.

Figure 5.6 shows a band-mapping experiment for the same modulation parameters as in Fig. 5.2(c). Comparing Fig. 5.6(c) and Fig. 5.2(c), we see how the TOF images are simplified through band-mapping. Indeed, as the atoms from the ground state only populate the plane wave of zero momentum after band-mapping, the rest of the signal stands out. In Fig. 5.6(d-f), we sketch the effect of the band-mapping process on the spectra of the system at different times. In panel (d), we place markers on the bands at the avoided crossings (in the model, these

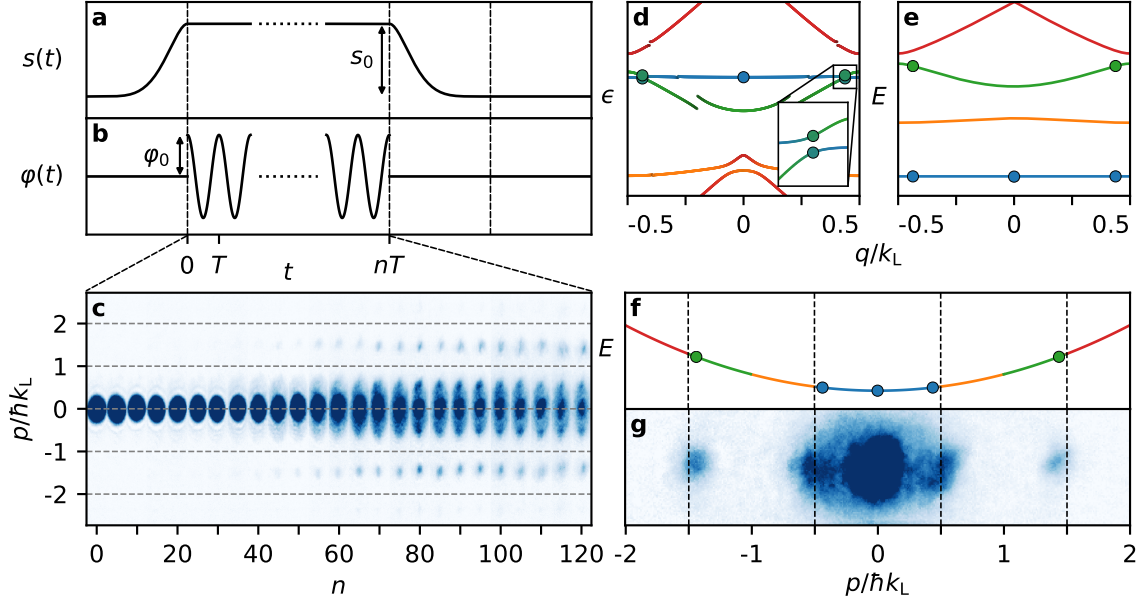


Figure 5.6 | Measurement of the quasi-momentum of the decimal peaks through band-mapping. (a) Depth of the lattice along time: adiabatical loading at s_0 , held constant during the experiment, adiabatical unloading to band map (see text) and switch off for TOF imaging. (b) Phase of the lattice along time, sine-modulated with amplitude φ_0 for an integer number n of periods T . (c) Stack of experimental absorption images for increasing n , with $s_0 = 3.70 \pm 0.10$, $\varphi_0 = 15^\circ$, $\nu = 1/T = 25.5$ kHz and $t_{\text{TOF}} = 35$ ms. (d) Corresponding quasi-energy spectrum (colored lines), with BEC (disk in $q = 0$) and instability (disks in $q \neq 0$) modes. (e-f) Band structures of the lattices of depth $s_0 = 3.7$ for (e) and $s_0 = 0$ for (f) (solid colored lines) and follow-up of the modes (see text) with the same color code. (f-g) Borders of the Brillouin zone (black dotted lines). (g) Absorption image after $n = 80$ periods of data (c). The upper value of the colormaps for the ODs are truncated to reveal details.

markers correspond to states in the modes \hat{u}_q and \hat{v}_q at the crossing) and a marker in $q = 0$ that corresponds to the atoms in the ground state that initially macroscopically populate one Floquet state (see Fig. 5.1). When we stop the modulation (panel (e)), the populated states are projected on the Bloch eigenstates of the static lattice. Figures 5.6(f-g) correspond to the situation at the end of the band-mapping. We compare the position of the markers in the unfolded relation of dispersion with a TOF image from Fig. 5.6(c) after the nucleation of the decimal peaks. The agreement between the momentum of the markers and the position of the momentum peaks in the diffraction pattern confirms that, as predicted by the model, the quasi-momentum q^* of the observed decimal peaks is related to the quasi-momentum of the avoided crossings in the quasi-energy spectrum. In the unfolded band structure, the model however predicts unstable modes with a slightly higher absolute momentum than the unfolded quasi-momentum of the crossings (Sec. 5.2.5). This trend has not been clearly observed in the experiments and we suspect that we cannot resolve this phenomenon due to the non-zero momentum dispersion of our atomic clouds, which translates in diffraction peaks of finite width.

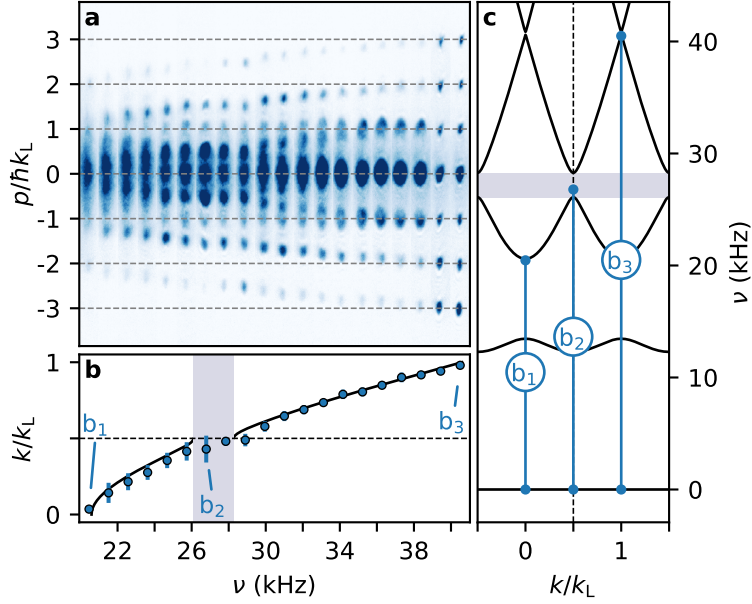


Figure 5.7 | Instability displacement with the modulation frequency. (a) Stack of experimental absorption images after $n = 100$ periods, averaged over 3 realizations, for an increasing modulation frequency ν , with $s_0 = 3.57 \pm 0.10$, $\varphi_0 = 15^\circ$ and $t_{\text{TOF}} = 35$ ms. The upper value of the colormaps for the ODs are truncated to reveal details. (b) Average instability position (in terms of the reduced quasi-momentum k/k_L of the unfolded band structure) extracted from the fitted drift of the four $1 \leq |p|/\hbar k_L \leq 3$ orders of diffraction over all realizations (blue dots, errorbars correspond to the standard deviation of the 12-point sample) and calculated position of the resonant coupling as a function of the modulation frequency (solid black line). (c) Transition diagram from the lowest band s over the first two Brillouin zones (solid black lines) and addressed transitions for data b_1 , b_2 and b_3 (blue dots and solid lines). In (b-c) the gap between the transitions s - d and s - f (grey shaded area) and edge of the first Brillouin zone (black dotted line) are represented.

5.3.2 Tuning the momenta of the instabilities

To further demonstrate that the quasi-momenta of the decimal peaks follows that of the avoided crossings, we tune the position of the crossings in the Floquet spectrum. This is simply achieved by varying the frequency ν of the phase modulation and taking TOF images after the nucleation of the decimal peaks. To this end, we fix the observation time at $n = 100$ periods for similar parameters as in Fig. 5.2. In Fig. 5.7, we compare, as a function of ν , the measured reduced wave number k/k_L of the emerging peaks with the unfolded quasi-momentum at which ν couples the bands. We vary ν from ~ 20.5 to ~ 40.5 kHz, resulting in a complete scan of the transitions s to d through s to f over the whole Brillouin zone (see Fig. 5.7(c)).

We observe that the decimal peaks in Fig. 5.7(a) follow the position of the avoided crossings in the quasi-momentum space (Fig. 5.7(b)), and even through the gap where the crossing transitions from the band pair (s, d) to the pair (s, f). Although this is globally in very good agreement with the predictions of the model, such a smooth correspondence over the whole Brillouin zone is not trivial as our interpretation of the model is valid when studying the instability at $q \neq 0$ (see Sec. 5.2).

This experiment demonstrates our ability to tune the position of the unstable modes in the quasi-momentum space, *i.e.* the quasi-momentum of the output channels for the four-wave mixing occurring at $q = 0$. Considering the experiment of Fig. 5.7, one can argue that the determination of the quasi-momenta of the decimal peaks as a function of ν would have been easier with a band-mapping before the measurements (as in Sec. 5.3.1). However, we here decided not to band-map in order to display the periodicity of both the ground state and the decimal peaks. Doing so, the results that we show in Fig. 5.7(a) suggest, from the momentum space, the coexistence of multiple spatial periodicities with a ratio of periods that can be tuned with the frequency of the phase modulation. At the end of this chapter (Sec. 5.4.1), we discuss numerical simulations that have been performed on this system, which corroborate the emergence of new spatial periodicities in the system.

5.3.3 Nucleation time

The two-band model (Sec. 5.2) can provide the position of unstable modes in the Brillouin zone and the magnitude of the exponents that characterize their growth, but it cannot provide the full kinetics of the mode growth nor their subsequent evolution. However, as hinted by Fig. 5.6(c), the full dynamics of the mode growth is readily accessible experimentally. In this section, we study the behavior of the nucleation time versus the amplitude φ_0 of the phase modulation and the initial number N of atoms in the BECs.

To easily extract the population of atoms in the decimal diffraction peaks, we once again perform band-mapping. The data analysis is presented in Fig. 5.8. For a given run (e.g. Fig. 5.8(a)), we count, as a function of the modulation time, the fraction of atoms in a set of lateral decimal peaks that are clearly visible. We do not take into account the decimal peaks that are too close to the central BEC, as the proximity with this highly populated region makes difficult to extract the populations in the emerging structures. We fit the fraction of atoms in the lateral decimal peaks in time with the sigmoid growth curve:

$$\pi^*(t) = \frac{\pi_0^*}{1 + e^{-(t-t_n)/\tau}}, \quad (5.38)$$

where:

- π_0^* is the value of the plateau, *i.e.* the final fraction of atoms in the decimal peaks considered,
- t_n is the time of half-maximum, which we choose to define the nucleation time,
- τ is the characteristic growth time of the instability.

For a frequency that couples the bands s and d , we plot in Fig. 5.8(b) the growths of the atomic populations in the lateral order and the results of the fit for φ_0 ranging from 10° to 20° . The extracted nucleation times t_n are shown in Fig. 5.8(c) together with data corresponding to a resonant modulation between the bands s and f . Fig. 5.8(d) shows a similar experiment, but

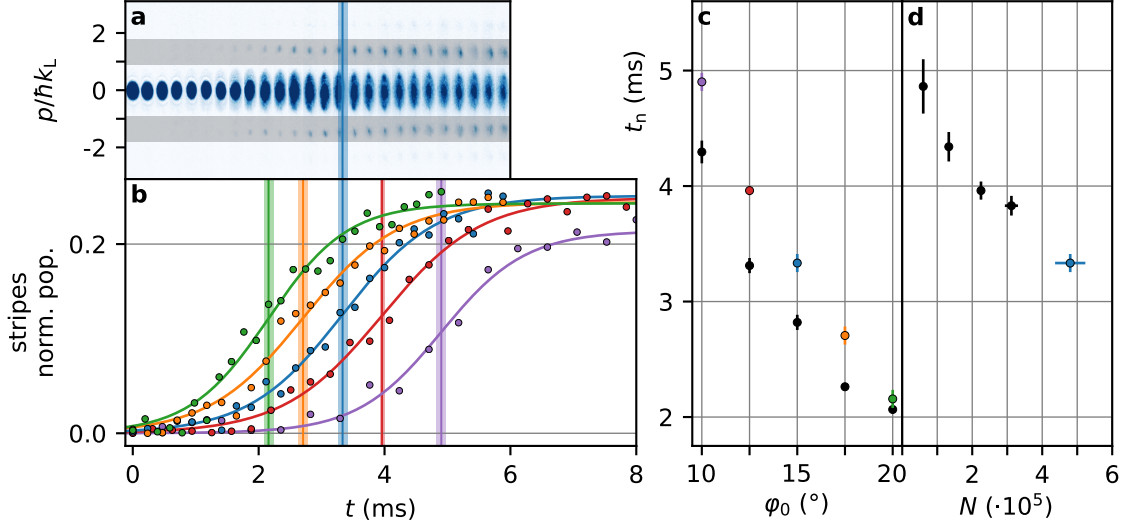


Figure 5.8 | Measurement of the nucleation time of the instability. (a) Stack of absorption images after band-mapping for an increasing time of modulation, for $s_0 = 3.70 \pm 0.20$, $\nu = 25.5$ kHz (coupling bands s - d), $\varphi_0 = 15^\circ$ and $N = (4.8 \pm 0.4) \cdot 10^5$ atoms in the BECs. The number of atoms in the grey stripes (here for $1 \lesssim |p|/(\hbar k_L) \lesssim 2$) is used to determine the nucleation time t_n (blue vertical line, with a surrounding blue shaded area corresponding to one standard deviation on the fit). The upper value of the colormaps for the ODs are truncated to reveal details. (b) Growth curves extracted from data as in (a), with the purple, red, blue, orange, and green data corresponding to $\varphi_0 = \{10^\circ, 12.5^\circ, 15^\circ, 17.5^\circ, 20^\circ\}$ respectively. The sigmoid fitting curves are shown and t_n is displayed as in (a). (c) t_n as a function of the modulation amplitude for data (b) (colored dots) and for $\nu = 30.5$ kHz and $s_0 = 3.56 \pm 0.20$ (black dots, coupling bands s - f). (d) Same as (c) as a function of the number of atoms N in the BEC for $\nu = 25.5$ kHz and $s_0 = 3.58 \pm 0.30$, for a fixed modulation amplitude $\varphi_0 = 15^\circ$. The blue marker/line in every panels corresponds to the same experiment. Error bars correspond vertically to one standard deviation on the fit and horizontally to one standard deviation over 4 independent measurements of the atom number.

as a function of the initial number N of atoms in the BECs for a frequency of modulation that couples the bands s and d . In the experiment, we reduce the number of atoms in the BECs during a holding time prior to the lattice loading (Sec. 2.2.4).

Results in Fig. 5.8 show that the nucleation time decreases with φ_0 and N . These trends are in agreement with the predictions of the tight-binding model (Sec. 5.2.5): by increasing φ_0 , we mainly increase the coupling W between the bands, which leads to larger instability exponents. The variation of the nucleation time with N is qualitatively expected as well, as the initial interaction energy in the condensate increases with N , and is also associated with a stronger instability. We note that these results are similar to those obtained for the single-band Bogoliubov instability leading to staggered states [201].

5.3.4 Survival of the instability

Using the same experimental procedure as for the study of the nucleation time of the decimal peaks, we observe the behavior of the instability over a longer period of time. Figure 5.9 shows

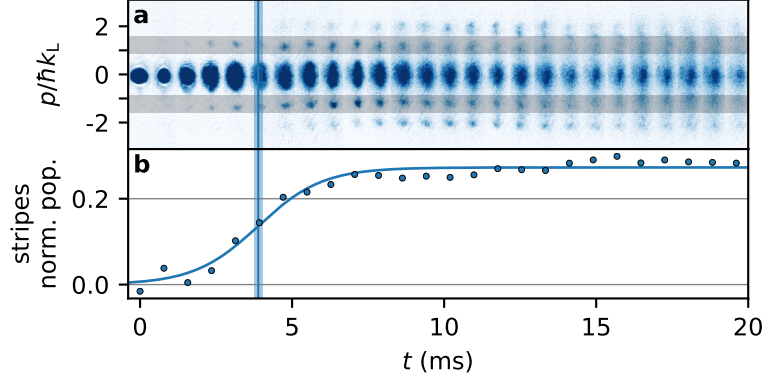


Figure 5.9 | Survival time of the nucleated pattern for $s_0 = 3.8 \pm 0.1$, $\nu = 25.5$ kHz, $\varphi_0 = 15^\circ$ and $N \approx 5 \cdot 10^5$ atoms. **(a)** Stack of absorption images after band-mapping. The upper value of the colormaps for the ODs are truncated to reveal details. **(b)** Growth of the population of atoms in the instability regions. Same analysis as Fig. 5.8

the result of the experiment for a large number of atoms and a coupling between the bands s and d . We see that the emerging patterns remain visible even $\sim 2 t_n$ (~ 8 ms ~ 200 modulation periods) after their appearance ($t_n \sim 4$ ms). Beyond that, we observe some heating, typical in modulated systems, that blurs the signal as a whole. We come back to the disappearance of the decimials peaks in Sec. 5.4.1.

5.3.5 Amplitude modulation

A last experiment suggested by the tight-binding model is the amplitude modulation of the lattice with similar lattice depth and frequency of modulation. Indeed, as the effective model is of static nature, it does not distinguish between phase and amplitude modulations. As the amplitude modulation of the real system can produce comparable Floquet spectra (see Fig. 5.10(a) below), four-wave mixing should trigger similar results in a depth-modulated lattice. Our amplitude-modulated potential is

$$V(x, t) = -s_0 \frac{E_L}{2} [1 + \varepsilon_0 \cos(2\pi\nu t)] \cos(x). \quad (5.39)$$

Results are shown in Fig. 5.10. On panels (a,b), we plot the quasi-energy spectrum and its fit from the two-band tight-binding model. As we see, the pair $(s_0, \nu/\nu_L) = (3.2, 2.84)$ couples the bands s and d close to the edge of the Brillouin zone. panel (c) shows the instability parameter $w(q)$, predicting unstable modes near the edge of the Brillouin zone for realistic interaction parameters nU (Sec. 5.2.4). Experimentally (panel (e)), we indeed observe the emergence of diffraction peaks in between those associated to the lattice ground states (panel (d)). The emerging peaks have momentum slightly below half integer values of $\hbar k_L$, which is consistent with predictions made from $w(q)$ (panel (c)). This experiment highlights the generality of the phenomenon studied in this chapter, and the relevance of the two-level model that predicts

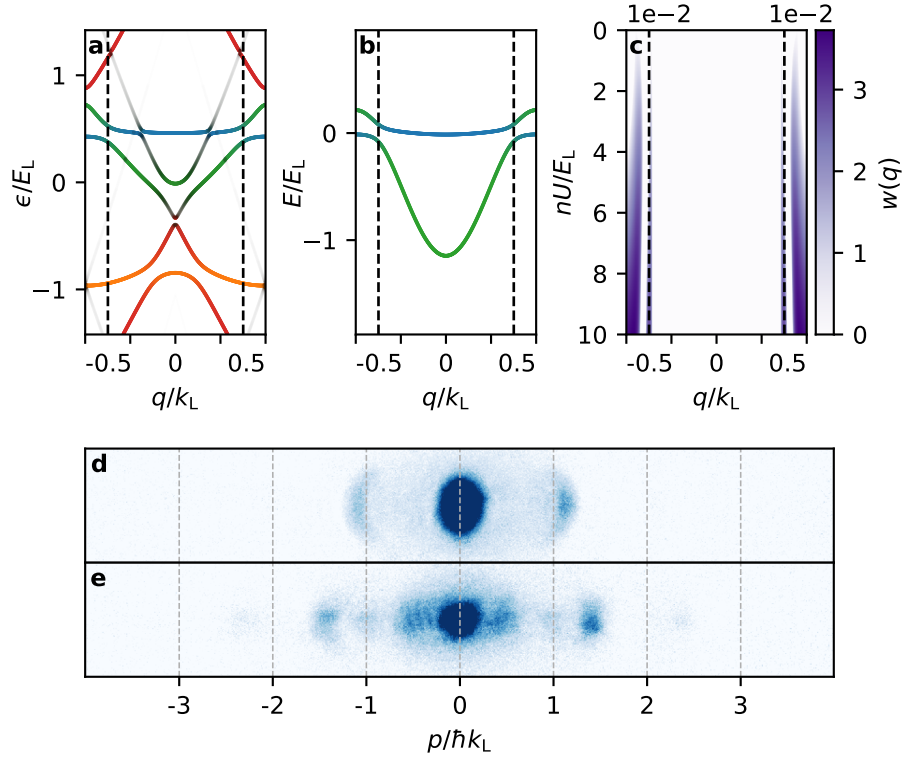


Figure 5.10 | Instability nucleation through amplitude modulation of the lattice. (a) Quasi-energy spectrum (colored lines) for the amplitude modulation of Eq. (5.39) with parameters $s_0 = 3.2$, $\varepsilon_0 = 0.325$ and $\nu = 2.84\nu_L$. (b) Spectrum of the two-band tight-binding model partially fitting (a). (c) Instability parameter $w(q)$ over the Brillouin zone as a function of nU . (d) TOF absorption image of the ground state of the static lattice of depth $s_0 = 3.2 \pm 0.1$ at the beginning of the modulation with $N \approx 4 \cdot 10^5$ atoms. (e) TOF absorption image of the atom cloud after $n = 60$ periods of modulation with $\nu = 23.05$ kHz, corresponding to the spectrum (a). The upper value of the colormaps for the ODs are truncated to reveal details.

the instabilities regardless the nature of the interband coupling (in this case the kind of lattice modulation employed).

5.4 Discussion on the realized state

5.4.1 Truncated-Wigner simulations

As discussed previously (Sec. 5.3.3), our two-level tight-binding model (Sec. 5.2) is able to predict trends on the timescale of the instability produced by four-wave mixing, but it is not suitable to study the kinetics of the phenomenon. To do so, one needs to make a simulation of the modulated system that takes into account both the interactions between the particles and fluctuations, either of thermal or quantum nature, to work as a seed for the spontaneous four-wave mixing process and feed the modes that eventually start to grow. To face these requirements, Truncated-Wigner (TW) simulations [201] were performed by our collaborator Peter

Schlagheck from the University of Liège. Through TW simulations, one is able to mimic quantum fluctuations by averaging over the integration of many independent trajectories with slightly different initializations. The simulations were performed with a realistic harmonic confinement (sec. 2.2.4) superimposed to the lattice potential.

These simulations are performed with $N = 1 \cdot 10^5$ atoms in the phase-modulated lattice (Eq.(5.1)), with parameters $s_0 = 3.4$, $\nu = 30$ kHz (which couples the bands s and f at $q = 0.36 k_L$) and $\varphi_0 = 20^\circ$. These parameters are similar to those of the experiments featured in this chapter. These simulations reproduce what we observe experimentally, namely an absence of evolution for the first milliseconds of modulation, followed by the nucleation of momentum components at decimal multiples of $\hbar k_L$, and later a disappearance of the patterns (as experimentally shown in Fig. 5.9). In Figs. 5.11 and 5.12, we present typical results of TW simulations on the state of the system after a fixed $t = 5$ ms of lattice modulation.

First in Fig. 5.11, we present details on the reduced one-body density matrix $\hat{\rho}^{(1)}$ of atomic ensemble after the nucleation of the instability. panel (a) displays the eigenvalues of $\hat{\rho}^{(1)}$. The greatest eigenvalue corresponds to the initially populated state at $q = 0$ (closely alike the lattice ground state, see Sec. 5.1). We then see two eigenvalues emerging from the rest. This manifests the emergence of two condensed mode in the mixed state. panels (b-d) shows successively the momentum representation of the states associated with these three greatest eigenvalues. Focusing on the emerging modes (Fig. 5.11(d-e)), we see that the two secondary condensate wave functions are symmetric and antisymmetric combinations of plane waves $\langle x | \chi_{\pm q^* / k_L} \rangle \propto e^{\pm i q^* x}$ (Sec. 1.2.1), with $q^* \approx q = 0.36$, the quasi-momentum of the avoided crossings for our modulation parameter (see above). These modes are coherently populated by four-wave mixing during the evolution of the atoms in the modulated lattice.

With $\hat{\rho}^{(1)}$, we can also verify that the apparition of these modes translates to the emergence of a periodicity d^* larger than the lattice step d . Figure 5.12 features a study of spatial correlations in the atomic ensemble. On panel (a), we show, as a function of the lattice site j , the atomic density distribution computed within the s band. On the two individual TW trajectories displayed, we see evidence of a new structuration on a scale of about 3 sites. This is in agreement with the expected quasi-momentum at which the instability occurs, as a resonant modulation at $q/k_L = 0.36$ leads to a spacing $d^*/d \simeq 1/0.36 \simeq 2.8$. The phase reference of the density modulation appears random for each trajectory, so the modulation washes out on the spatial density averaged over many TW realizations. Nevertheless, we can recover evidence of the spatial density modulation in the averaged state by computing the normalized density-density correlation function $g^{(2)}(j) = \langle n_0 n_j \rangle / (\langle n_0 \rangle \langle n_j \rangle)$, between the central and the j^{th} site of the lattice. This is plotted in Fig. 5.12(b). It reveals clear density oscillations across the lattice which signal the emergence of a new long-range order. Still within the ground band, we can also compute a normalized coherence $g^{(1)}(j) = \langle \hat{a}_0^\dagger \hat{a}_j \rangle / (\langle n_0 \rangle \langle n_j \rangle)^{1/2}$. We plot $g_j^{(1)}$ in Fig. 5.12(c). It displays a modulations at long-range with the same period. These last two panels show that coherent emergent states with a new period d^* coexist with the initial condensate of period d . As we briefly discuss in the next section, there are shared features between supersolids and the exotic state that we realize in the modulated lattice.

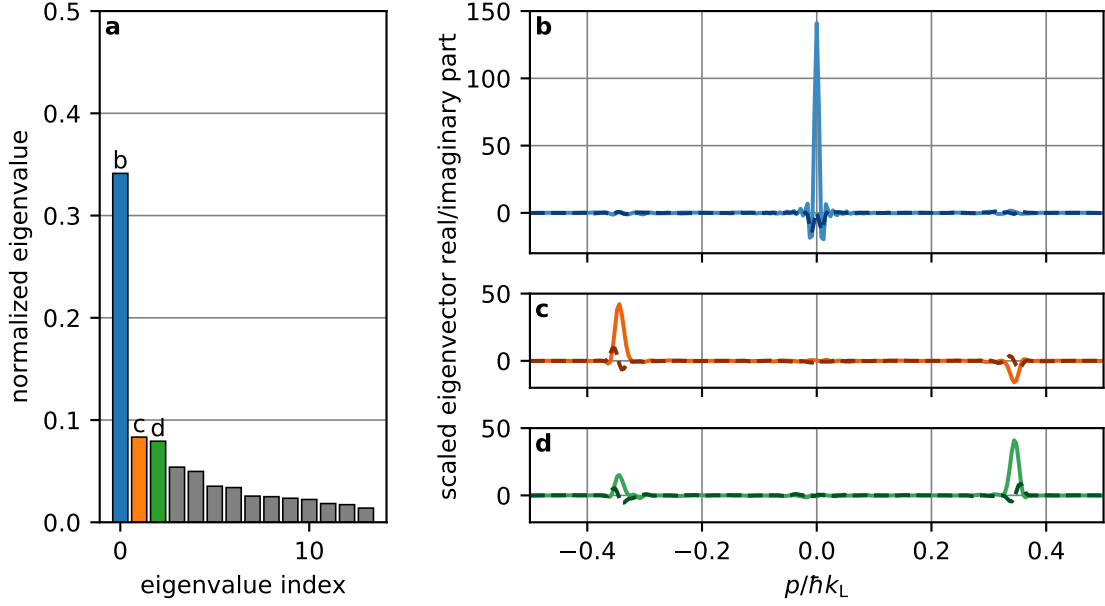


Figure 5.11 | Structure of the reduced one-body density matrix after nucleation of the instability. (a) Ordered eigenvalues of the reduced one-body density matrix normalized by the total number N of atoms. The eigenvalues identified by color and letter are shown in panel (b-d). (b-d) s band components of the eigenstates identified in (a) (scaled by the square roots of the associated eigenvalues) plotted in the momentum space, displayed by plotting their real parts (solid colored lines) and imaginary part (dashed colored line). Parameters are $s_0 = 3.4$, $\varphi_0 = 20^\circ$, $\nu = 30$ (kHz) and $N = 1 \cdot 10^5$ atoms.

5.4.2 Shared features and differences between supersolids and the state emerging in our system

In this last section, we discuss common features between supersolids and the emerging state in our system, as well as differences that make reluctant to use the work supersolid in our case. Briefly introduced, supersolidity is the emergence of a crystalline order within a coherent superfluid phase [206]. This mysterious state of matter was first introduced near 1960 (see [207, 208, 209]). Its existence was first discussed and debated in the context of ^4He [210]. It was only in 2017, in the field of ultracold atoms, that conclusive observations of supersolidity were made. To bring out supersolid features, these pioneering experiments relied on different experimental techniques involving spin-orbit coupling [211], cavity-mediated long-range interactions [212], and later long-range dipolar interactions in ultracold erbium and dysprosium gases [213, 214]. Three key requirements [206] for a quantum state to be dubbed supersolid are

- (i) a long range modulation of the spatial density accompanied by
- (ii) a preserved coherence in the modes associated with the large density oscillations, and
- (iii) the realization of a stable and stationary state (possibly the ground state of the system).

In our case, requirements (i) and (ii) are respectively demonstrated by the oscillations observed in the $g^{(2)}$ and $g^{(1)}$ correlations function (Fig. 5.12). However, as hinted by the disappearance of

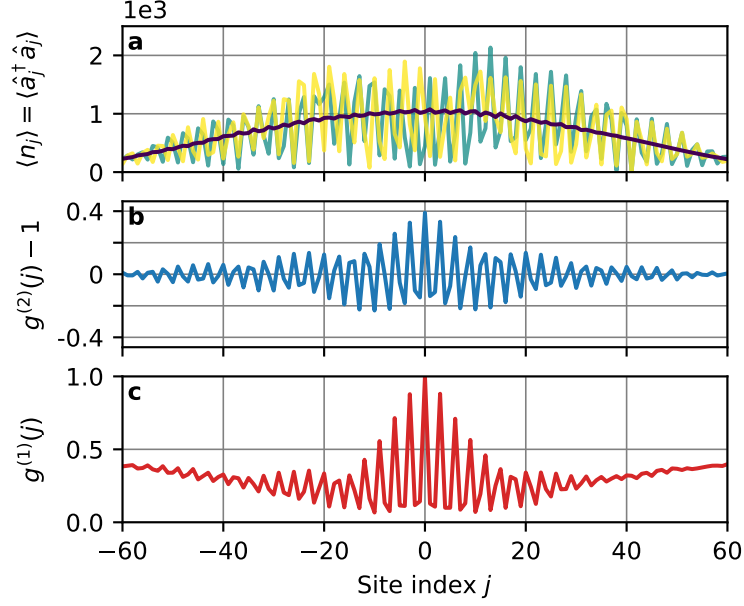


Figure 5.12 | Correlations and coherence after nucleation of the instability. (a) Spatial density distribution in the s band as a function of the site index j . Two individual TW trajectories (dashed and dotted lines) exhibit a clear periodic modulation of the density, which is washed out in the average of 1000 trajectories (thick line). (b) Average density-density correlation function $g^{(2)}(j)$ between the central site and the j^{th} site in the s band. (c) Average amplitude correlation function $g^{(1)}(j)$ between the central site and the j^{th} site in the s band. Parameters are $s_0 = 3.4$, $\varphi_0 = 20^\circ$, $\nu = 30$ (kHz) and $N = 1 \cdot 10^5$ atoms.

the emerging structure for long modulation times (observed both in the experiments (Fig. 5.9) and in the TW simulations [66]), the state that emerges in our system is not a steady state strictly speaking. This is the reason why we avoid to use the term of supersolidity, and prefer to speak of the transient emergence of supercrystalline order.

Conclusion

In this last chapter, we presented results on the observation and control of a supercrystalline order emerging from short-range interatomic interactions in the phase-modulated optical lattice. By loading the ground state of the lattice and modulating its phase at a frequency that couples the ground band to an excited state in $q \neq 0$, we make the peculiar observation of momentum components emerging between the diffraction peaks associated with the ground state.

To model this situation, we develop an effective two-level tight-binding model with interactions to study the stability of the system. With the two-band model, we obtain instability regions symmetric in quasi-momentum that are much narrower than what can be found with one-band systems [199, 201, 197]. These instabilities are populated by pairs of atoms from the BEC at $q = 0$ that coherently scatters into $q = \pm q^*$ (the output channels of the four-wave mixing process at stake). We find that these output channels follows the quasi-momentum of

the avoided-crossings in the Floquet spectrum, so their quasi-momenta can be tuned by the frequency of lattice modulation. Through several experiments, we confirm the connection between the instability regions of the model, the avoided crossings in the quasi-energy spectrum and the emerging structures observed in TOF images. We demonstrate how the periodicity and the nucleation timescale of the emerging momentum peaks can be tuned by engineering the Floquet spectrum.

To quantitatively account for the kinetics of four-wave mixing, a numerical study of this problem has to go beyond a mean-field treatment of the interactions. Such analysis were performed by Peter Schlagheck with Truncated-Wigner simulations, typical results of which were presented in the end of this chapter.

This work opens unexplored routes to generate exotic tunable states in higher dimensions and/or other lattice geometries. A publication on this work is in preparation [66].

General conclusion

“Audi panem quid meliora.” Ça veut rien dire, mais je trouve que ça boucle bien.

Roi Loth (Kaamelott, Livre IV, Episode 1)

This manuscript features part of the results that I obtained during my PhD in the Cold Atoms group at *Laboratoire Collisions, Agrégats et Réactivité* (LCAR, Toulouse) between 2019 and 2022. Using Bose-Einstein condensates (BECs) of ^{87}Rb in a controllable one-dimensional optical lattice, my PhD work concerned the development and implementation of quantum state control methods and their application to quantum simulation in a Floquet-Bloch system (*i.e.* a system periodic in space and time). In this conclusion, I begin with a brief summary of this work, and I then discuss perspectives opened by this thesis and the results of our group these last three years.

Summary

Quantum-optimal control of matter waves in a one-dimensional optical lattice. In the first study presented in this manuscript (Chap. 3), we used the formalism of quantum-optimal control (QOC) to compute the way in which to continuously shift the optical lattice in order to arbitrarily control the motional state of the BECs in the lattice. Using this protocol, we first prepared specific momentum distributions, for which the success of the preparation could be assessed with a single time-of-flight (TOF) observation of the atoms, as shown in Fig. 6.1(a). We then targeted more involved quantum state, the preparation of which we had to certify by implementing a dedicated state tomography algorithm based on likelihood maximization. Using these tools, we demonstrated our ability to prepare Gaussian states that we squeezed in position up to more than a factor of four, an example of states unattainable by more conventional methods such as adiabatic approaches. I conclude this first chapter of results with the presentation of an experiment providing a proof-of-principle of QOC application to quantum simulation in a Floquet system. We demonstrated how the optimization on the initial state in a study of dynamical tunneling in the depth-modulated lattice resulted in clearer signals of tunneling oscillations. See [63, 64] for our publications on this subject.

Non-diffusive Hamiltonian ratchet in space. I detailed in Chap. 4 the design of an integrable ratchet effect in a sine potential whose amplitude and phase modulations are correlated. This

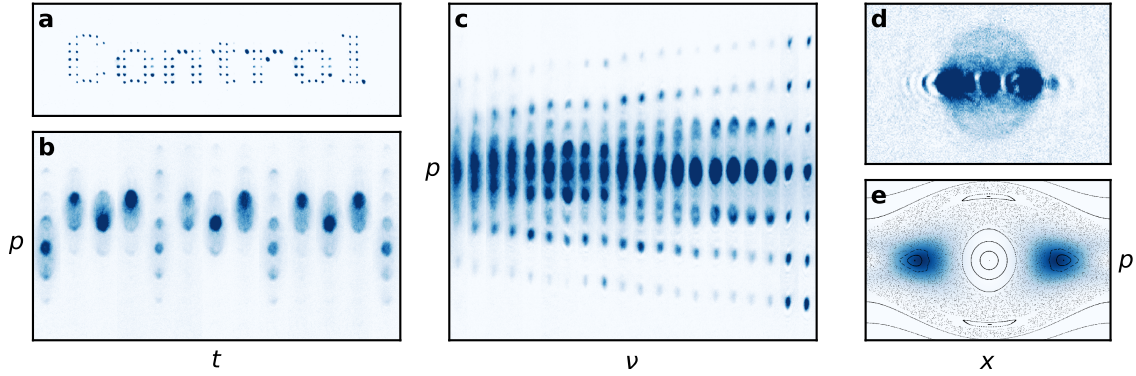


Figure 6.1 | Summary figure of my PhD work. (a) Horizontal stack of independent TOF absorption images showing our control over the BEC momentum distribution in the optical lattice. This panel refers to [63, 64] and Chap. 3. (b) Horizontal stack of TOF absorption images showing the momentum evolution of the ratcheting Floquet state (here prepared by quantum-optimal control) over three ratchet periods. This panel refers to [65] and Chap. 4. (c) Horizontal stack of TOF absorption images showing the momenta at which emerge a transient supercrystalline structure as a function of the lattice phase modulation frequency. This panel refers to [66] and Chap. 5. (d) TOF absorption image featuring a scattering halo between the momentum components $\pm 4\hbar k_L$ (diffractions orders are not well resolved for this TOF shortened to 8 ms in order to reveal the halo). This panel refers to [62]. (e) Stroboscopic phase portrait and Husimi representation of a Floquet state (localized on regular islands) involved in CAT in this system. This panel refers to [61].

kind of ratchet effect consists in the emergence of a directed current of particles along quasi-periodic trajectories, with the noteworthy detail that these integrable trajectories periodically stop in each lattice site. After having presented our method to determine the modulation parameters for this classical mechanics effect to emerge, I discussed wave function transport along these classical trajectories: as a parameter of the system is varied (in our case the effective Planck constant¹), Floquet state mixing couples in a non-monotonous way the ratcheting region of phase space with the chaotic sea. The identification of this effect allowed us to determine optimal experimental parameters to observe the effect, and the chapter ends with the presentation of experiments where we observed the transport of matter waves along the ratcheting structures in the classical phase space (Fig. 6.1(b)). A publication on this study is in preparation [65].

Emergence of a tunable supercrystalline order in a Floquet-Bloch system. In the last part of this manuscript (Chap. 5), I presented the study of an effect that goes beyond one-body physics in our system: the transient emergence of a supercrystalline phase resulting from short-range interactions in the shaken optical lattice. In these experiments, we initially loaded the ground state (at quasi-momentum $q = 0$) of the lattice before applying a phase modulation that couples the ground band to an excited band away from the center of the Brillouin zone (at $|q| \neq 0$, resulting in avoided crossings between the two bands involved at $\pm q$). Experimentally, after tens of modulation periods, we observed the nucleation of additional momentum components in the TOF images. To understand this phenomenon, we developed a two-band tight-binding model with on-site interactions. Through a Bogoliubov treatment of the interactions, we found

¹Which is the only free parameter left once the classical phase space is fixed..

the presence of instability regions near the quasi-momenta of the avoided crossings. Through Floquet engineering of the avoided crossings, we demonstrated a control on these unstable modes (namely their periodicity, as shown in Fig. 6.1(c), and nucleation timescale) resulting from spontaneous four-wave mixing. A publication on this study is in preparation [66].

Research not featured in this manuscript. I have contributed to two other research axes during my thesis, which I did not include in this manuscript for concision. The two following paragraphs briefly summarize these results:

Observations of chaos-assisted tunneling (CAT) resonances. CAT [88, 155, 154, 89] is a type of dynamical tunneling (Sec. 3.4) where the tunneling between the two regular regions is carried by two Floquet states mainly localized on these regions (Fig. 6.1(e)), as well as by a third Floquet state mainly delocalized over a chaotic sea. Under the variation of a parameter of the system, the phenomenon of Floquet-state mixing (described in Sec. 4.2) leads to CAT resonances [88], associated with a non-monotonic variation of the tunneling frequencies in that three-level system. In this sense, the mixing chaotic state can assist, or on the contrary freeze, dynamical tunneling in the system. In our work [61], we were the first to unambiguously observe such a resonance of CAT using BECs in the depth-modulated optical lattice. This work results from a collaboration with M. Martinez, G. Lemarié and B. Georgeot from the *Laboratoire de Physique Théorique* (Toulouse) and O. Giraud and D. Ullmo from the *Laboratoire de Physique Théorique et Modèles Statistiques* (Paris). For numerical and theoretical details on this work, see the thesis of M. Martinez [69]. For experimental details, see the theses of M. Arnal [67] and G. Chatelain [68].

Observation and control of quantized scattering halos. When BECs are released from an optical lattice to perform a TOF, atoms can undergo two-body collisions at the beginning of the TOF [62] resulting in well visible scattering halos in the images [107, 215, 216, 62]. In our experiment, the low relative kinetic energy between the colliding pair results in spherical s -wave scattering [90] (Fig. 6.1(d)), and the momentum quantization implied by the lattice periodicity (Sec. 1.2.1) results in a quantization of the possible relative momentum for the colliding atoms, thus leading to the observation of scattering halos of quantized diameter. In our work [62], we showed how one can control the momentum characteristics of these quantized halos: from a perturbative treatment of the collisions, one obtains that the number of atoms in the halos is proportional to the product of the colliding momentum component populations [62]. Thus, controlling halo momentum amounts to control the momentum probability distributions² of the state in the lattice before the TOF. In our work [62], we demonstrated such control with a systematic technique that relies on a sudden lattice shift φ_0 followed by a precisely timed evolution τ in the lattice of depth s_0 . By determining optimal triplet (φ_0, τ, s_0) , we managed to control the atomic populations in the momentum components to the best of what is achievable from the evolution of a

²We point out that these results were obtained before our implementation of QOC in the experiment. This study on quantized scattering halos was actually our gateway to QOC.

translated state in the static lattice, and thereby demonstrated our ability to control the scattering halos in the reciprocal space. This work results from a collaboration with P. Schlagheck from the CESAM research unit at the University of Liège. Details on this study [62] can be found in the thesis of G. Chatelain [68].

Some prospects

Several lines of research are opened by these works. I highlight three of them here:

QOC for qudit computation. A qubit, the famous building block of quantum processors, can be defined as the superposition of two discrete quantum levels $|\psi\rangle = c_0|0\rangle + c_1|1\rangle$, with $c_0, c_1 \in \mathbb{C}$ and $|c_0|^2 = |c_1|^2 = 1$. A d -qudit [217, 218] is the generalization in d dimensions of the two-dimensional qubit: $|\psi_d\rangle = \sum_{n=1}^d c_n|n\rangle$, with $c_n \in \mathbb{C}$ and $\sum_{n=1}^d |c_n|^2 = 1$. In that regard, we remark that the external quantum states of BECs in Bloch systems (with their discretized Hilbert space) can be considered as qudits in momentum space. In Chap. 3 and [63, 64], we used QOC with the phase of the lattice as a control parameter $u(t)$, of which we computed the optimal evolution to drive an initial state $|\psi_a\rangle$ to a final state $|\psi_b\rangle$:

$$|\psi_a\rangle \xrightarrow{u(t)} |\psi_b\rangle. \quad (6.1)$$

One can try to go further and compute the optimized control field $u(t)$ in order to connect one-to-one the elements of two bases of the Hilbert space:

$$\left\{ \begin{array}{c} |\psi_{a,1}\rangle \\ \vdots \\ |\psi_{a,d}\rangle \end{array} \right\} \xrightarrow{u(t)} \left\{ \begin{array}{c} |\psi_{b,1}\rangle \\ \vdots \\ |\psi_{b,d}\rangle \end{array} \right\}, \quad (6.2)$$

with, for example in our system, a mapping between the plane waves $|\psi_{a,i}\rangle = |\chi_\ell\rangle$ and the Bloch eigenstates $|\psi_{b,i}\rangle = |\phi_n\rangle$ (see Sec. 1.2) for some relation $n = \sigma(\ell)$ between ℓ and n . Operations such as Eq. (6.2) correspond to unitary transformations, and allow one to design quantum gates acting on the qudits. Through this control approach, one does not have to compute the numerous matrix elements of the transformation (6.2), but only to optimize the control field $u(t)$. From here, one can implement basic quantum computing algorithms as for instance a version of the Deutsch algorithm [219] with a single qudit.

This application directly benefits from our implementation of QOC on the experiment. The connections with our work are here multiple, as, after the application of quantum processing operations, it will be necessary to measure the qudit. The maximum-likelihood state tomography technique implemented in Chap. 3 is well suited for this task.

QOC for quantum sensing. From our implementation of QOC, we can also design protocols for quantum sensing, *i.e.* the accurate measurement of an external parameter. A possible approach is to engineer a control field $u(t)$ in order to maximize, as a function of an external parameter to be measured, the rate at which diverge the different evolutions of a same initial state. Preliminary numerical results have been obtained for our setup in order to measure *e.g.* the lattice depth or a small magnetic force. Proof-of-concept experiments of quantum sensing will soon be realized by the group.

Long-range chaos-assisted tunneling. In our study of CAT [61], we have observed coupling resonances between pairs of regular islands of the same lattice site (Fig. 6.1). As a generalization of the effect, it has been predicted [220] that when the chaotic sea extend between lattice sites, there exists an harmonically decreasing coupling $t(n) \propto 1/n$ between the regular structures of a given site and the regular structures in the n^{th} neighboring site. This slowly decreasing behavior of longer-range couplings can for instance be opposed with the exponentially decreasing coupling to neighboring sites in the case of the static lattice. Our observations of CAT resonances pave the way for a study of long-range chaos-assisted tunneling.

New experimental setup. Finally, our group is building a new experiment of ^{87}Rb BECs in the newly built facility at LCAR. On this new setup, the implementation of optical lattices of higher dimensionality is planned. The developments presented in this manuscript are readily applicable to be utilized and further studied on systems of higher dimensionality.

These perspectives will be addressed during the theses of F. Arrouas and N. Ombredane, PhD students recently arrived in the group.

Part IV

Appendices

Appendix A - Rubidium 87 D₂ line

This appendix refers to the Chap. 2. We present in Fig. A.1 the detail of the ⁸⁷Rb D₂ line, and we identify the transitions that we work with during the cooling sequence (Sec. 2.2). In a magnetic field gradient, the transition frequency between states $|F = 1, m_F = -1\rangle$ and $|F = 2, m_F = -1\rangle$ (on which microwave evaporation is based) decreases as the magnetic field increases, hence the negative detuning $\delta_{\text{MW}}(t)$ in Fig. A.1 (see Sec. 2.2.2). We remind that more information on the cooling sequence can be found in previous theses of our group [93, 94, 115, 67, 68].

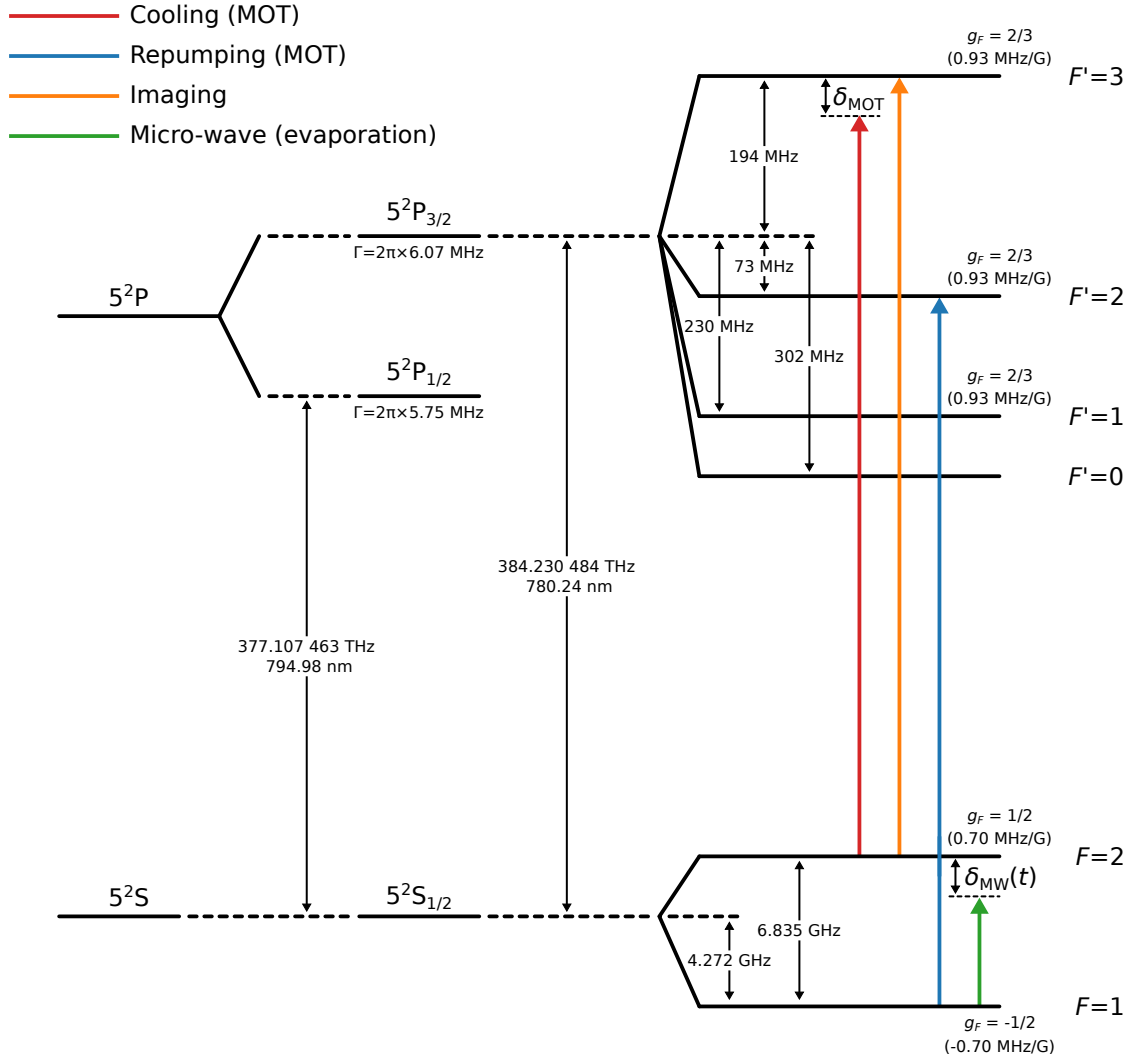


Figure A.1 | Rubidium 87 D₂ line. During the MOT loading (Sec. 2.2.1), the cooling beam is red-detuned by a quantity $\delta_{\text{MOT}} \approx 2\Gamma$, with the spontaneous decay rate $\Gamma \approx 2\pi \times 6.07$ MHz (FWHM). The micro-wave frequency sweep $\delta_{\text{MW}}(t)$ is discussed in Sec. 2.2.2. The data in this figure are taken from [99].

Appendix B - Dipole beams preparation and control

This appendix refers to the Chap. 2. We list the main elements that allow to prepare and control the dipole trap. We then present the optical diagram for the preparation of the dipole beams that constitute the trap in which Bose-Einstein condensation is achieved.

Dipole beams. The laser for the dipole trap is a monomode ALS-IR-1064-20-I-SF from Azurlight Systems, with wavelength $\lambda = 1064$ nm and maximum power $P = 20$ W. We operate it at $P = 17$ W. The two beams that make the dipole trap are focused at the same point in the cell. Their waist is $w_0 = 45$ μm with maximum power $P \approx 4$ W each. At the end of the evaporation in the dipole trap, their power is $P_f \approx 20$ mW each.

AOMs. The control of the dipole beams is the same for both beams. A radio frequency (RF) generator QMODP_{140,68-B-45-03} drives an acousto-optic modulator MQ_{40-B5A2-L1064-WSc} (both components are from AA Opto-Electronic). This RF generator has an input channel that allows to vary the intensity of the driving RF and control the power of the diffracted beam. To prevent interference between the dipole beams, we work with opposite diffracted orders ± 1 (see Fig. B.2).

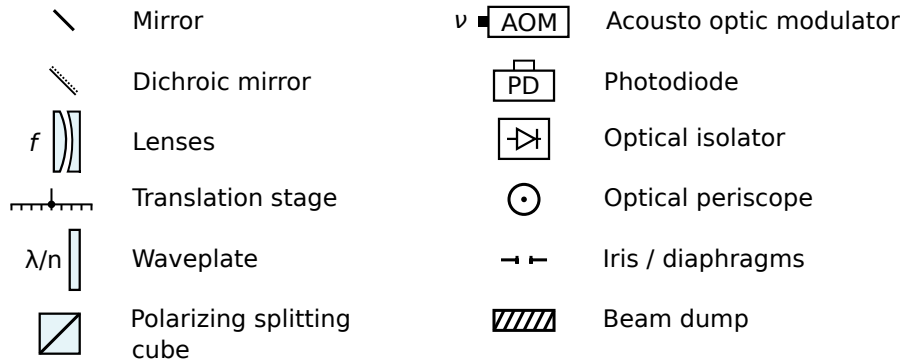


Figure B.1 | Legend for the optical diagram.

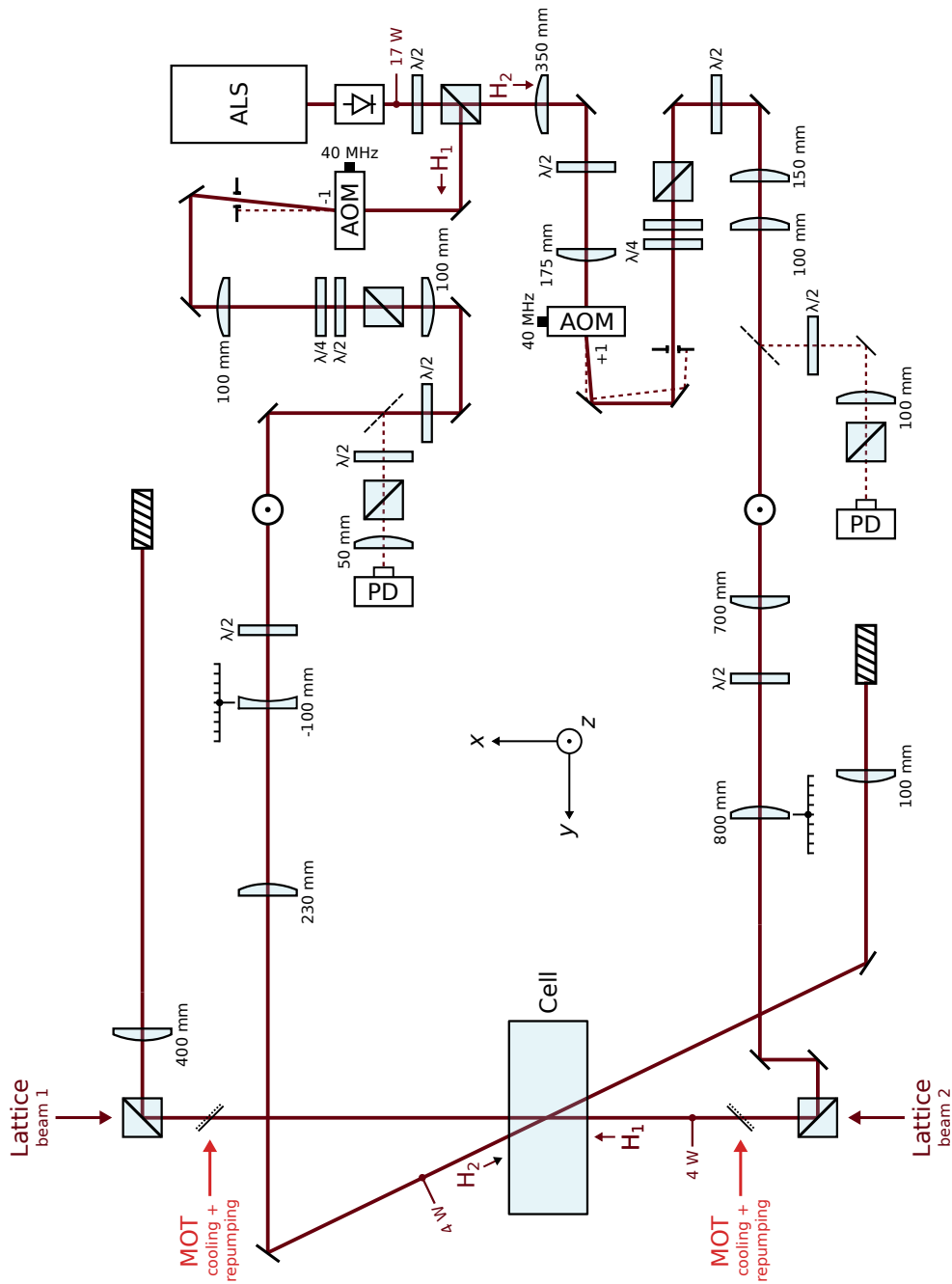


Figure B.2 | Optical diagram for the dipole beams. This figure completes Fig. C.2 of App. C. See Fig. B.1 for the legend. Adapted from [67].

Appendix C - Lattice beams preparation and control

This appendix refers to the Chap. 2. We list the major components that constitute the optical lattice. We then present in Fig. C.2 the optical diagram for the preparation of the laser beams for the optical lattice. We remind the lattice dipole potential locally experienced by the atoms:

$$V(x, t) = -A(t) \times s_0 \frac{E_L}{2} \cos(k_L x + \varphi(t)). \quad (\text{C.1})$$

with the lattice wavenumber $k_L = 2\pi/d$.

Lattice beams. The laser is a monomode YLR-15-1064-LP-SF from IPG Photonics. Its wavelength is $\lambda = 1064$ nm and it has maximum a power $P = 15$ W. At their focal point on the crossed dipole trap, the counterpropagating beams have maximum power $P = 2.3$ W and waist $w_0 = 150$ μm . The corresponding Rayleigh length is $x_R \approx 66.4$ mm, large compared to the lattice spacing $d = \lambda/2 = 532$ nm.

Amplitude control. The acousto-optic modulator (AOM) for the control of the lattice depth $A(t) \times s_0$ is placed before the beam splitting. It is a AA Opto-Electronic MQ80-A0.3-L1064-Z20-WLg driven by a radio frequency (RF) generator AA Opto-Electronic MODA80-B4-43. This latter component has a $[0, 5]$ V modulation input acting on the amplitude of the RF that goes to the AOM, and its effect on the diffracted beam power is linear on the range $[1.3, 3.3]$ V where we operate it [67]. We trigger an arbitrary waveform generator (AWG) (Keysight 33611A) during the sequence to control that input and therefore the lattice depth. We present in Fig. C.1 the Bode plot for the amplitude modulation of the lattice (measured using a photodiode with a sampling rate of 150 MHz placed before the cell on the lattice beam 2, see Fig. C.2). We see that we have approximately no loss in the amplitude of the depth modulation up to $\nu = 100$ kHz, a bound below which every experiments presented in this manuscript are performed.

Phase control. We control the lattice phase $\varphi(t)$ with one AOM per beam placed after the splitting. These AOMs are two AA Opto-Electronic MT200-A0.5-1064. By controlling the relative phase between their driving RFs, we control the relative phase between the diffracted beams. We generate their driving RF ourselves using AWGs, frequency doublers, filters and amplifiers (see [94, 115, 67]). We drive them at 160 MHz, *i.e.* slower than their nominal driving frequency of 200 MHz. The two AWGs are:

Beam 1: a Keysight 33612A with two channels. The first channel generates the AOM driving RF and the second channel modulates *internally* the phase of the first channel.

Beam 2: a Keysight 33611A to generate the AOM driving RF.

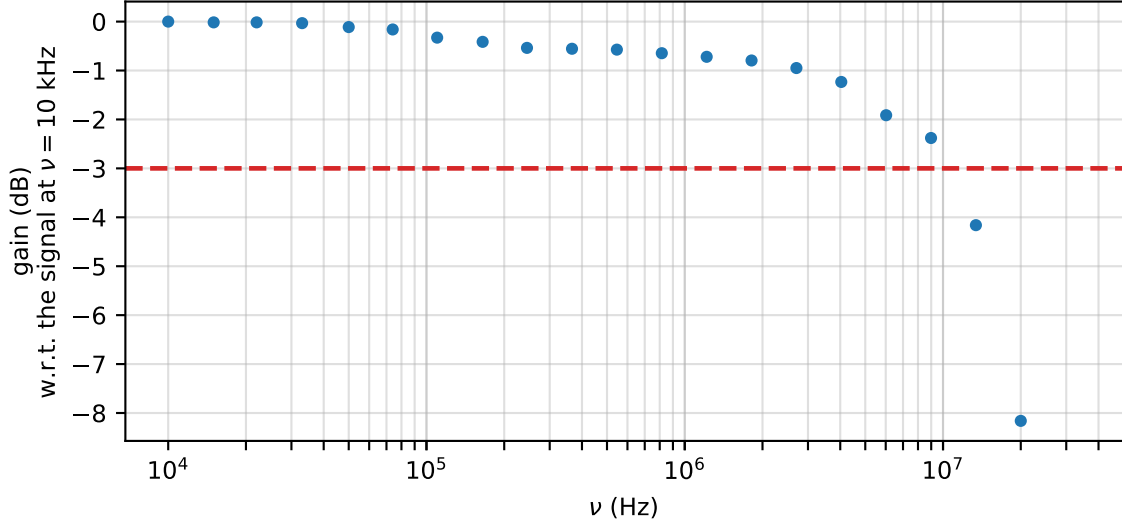


Figure C.1 | Bode plot for the amplitude modulation of the lattice. The frequency at -3 dB is $\nu_0 \approx 10$ MHz.

These two AWGs are synchronized with each other, as well as with the AWG that controls $A(t)$.

We are yet to implement an optical monitoring of the phase between the lattice beams from a beat signal. However, the result of two experiments allow us to estimate the cutoff frequency for the phase modulation of the lattice. On one hand, from electrical beat between the phase-modulated beam 1 RF and the unmodulated beam 2 RF, we measured an electrical cutoff frequency $\nu_{0,\text{elec}} \gtrsim 3$ MHz for the phase modulation of the beam 1 RF [68]. On the other hand, we measured the renormalization of the lattice depth in a fast phase-modulated optical lattice [198, 199, 113]. This effect, that depends on the amplitude of the phase-modulation, was measured up to $\nu = 500$ kHz [113, 67]. We therefore estimate the cutoff frequency for the phase modulation of the lattice to be somewhere in the range $[0.5, 3]$ MHz.

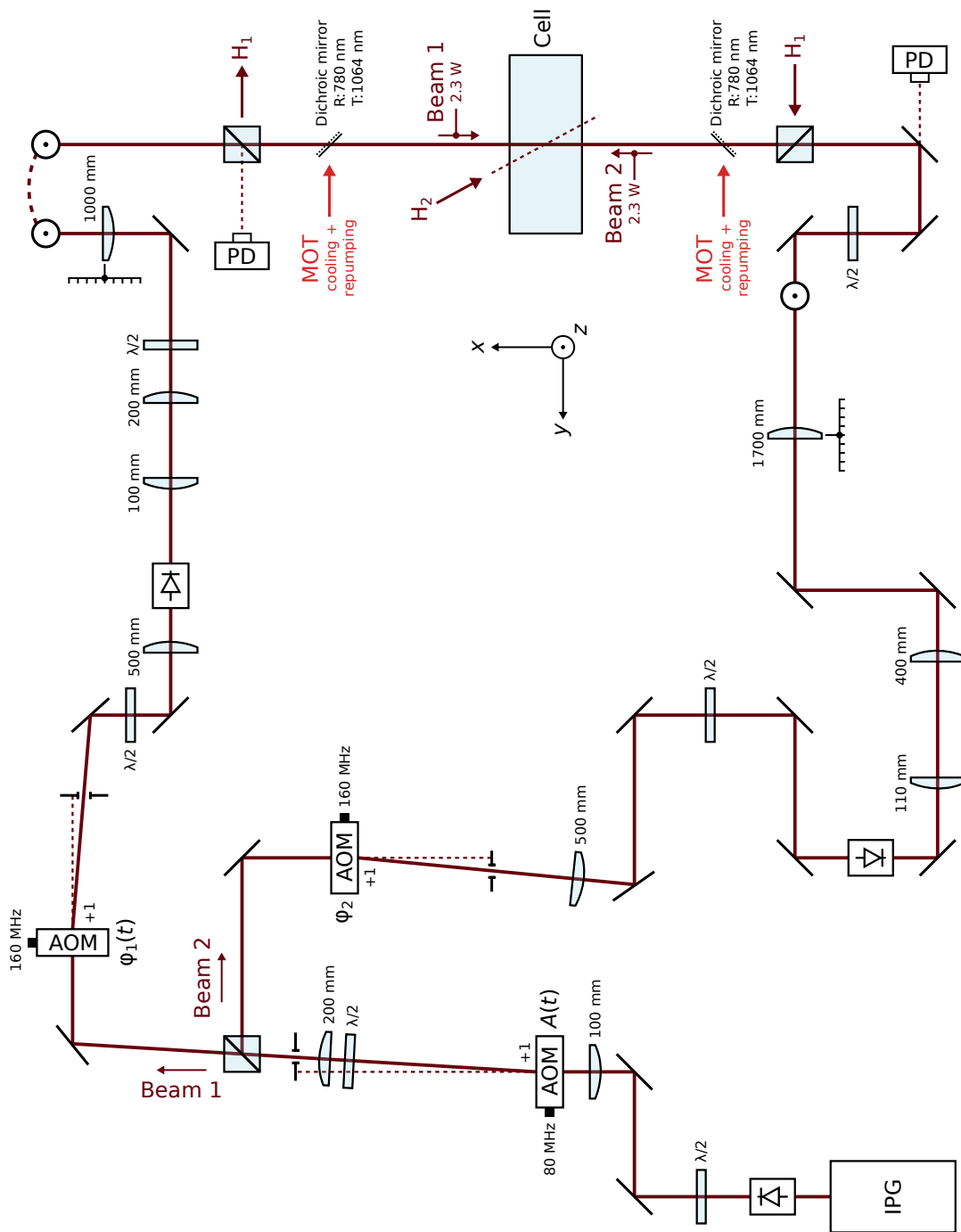


Figure C.2 | Optical diagram for the lattice beams that completes Fig. B.2 of App. B. See Fig. B.1 for the legend. Adapted from [67].

Appendix D - Effect of the control duration in our QOC protocol

This appendix refers to the Chap. 3. We present a brief study of the experimental effect of the control duration t_c in our QOC protocol. This study consists in targeting the state of Fig. 3.5(a):

$$|\psi\rangle = \frac{1}{\sqrt{2}} (|\chi_{-1}\rangle + |\chi_1\rangle), \quad (\text{D.1})$$

for different control times $t_c \in [0.75, 8] T_0$ and two lattice depth $s_0 = 2.55 \pm 0.10$ and $s_0 = 5.5 \pm 0.2$. Results are shown in Fig. D.1.

As discussed in Sec. 3.1.4, the lower bound on the control duration is of theoretical nature and consists in the lowest time needed for the target state to become reachable from the initial state. In the lattice, the dynamics of the atoms is dictated by the band structure. The initial state that we use for QOC protocols is generally the ground state of the lattice. The relevant timescale with respect to which the control duration needs to be sufficiently long is the largest inter-band transition period from the lattice ground state, *i.e.* T_0 as defined in Eq. (3.34).

For too long control times, experimental fluctuations have more time to accumulate. This is illustrated in Fig. D.1, as we observe a decreasing fidelity when t_c increases. For the lattice depth $s_0 \approx 5.5$ (at which we performed most of the experiments in Chap. 3), we also observe larger fluctuations in the prepared state the longer the control time. Our rule of thumb is to set the control duration to the shortest time for which the numerical algorithm converged satisfactorily.

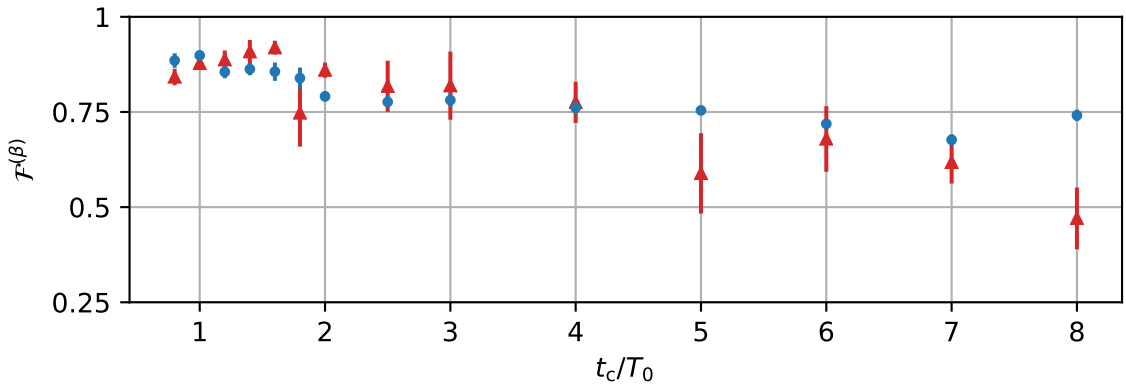


Figure D.1 | **Effect of the control duration** when targeting the state $(|\chi_1\rangle + |\chi_{-1}\rangle)/\sqrt{2}$. Fidelity $\mathcal{F}^{(\beta)}$ (3.36) between the momentum distributions of the numerical and experimental states prepared by QOC as a function of the scaled control duration t_c/T_0 for two lattice depth ($s_0 = 2.55 \pm 0.10 \rightarrow T_0 \approx 87 \mu\text{s}$ (blue dots) and $s_0 = 5.5 \pm 0.2 \rightarrow T_0 \approx 59 \mu\text{s}$ (red triangles)). Error bars correspond to one standard deviation over a 10-realization statistics.

Appendix E - Additional optimal control preparations

This appendix refers to the Chap. 3. We present three additional experiments that we have chosen to put in appendix in order to lighten the reading of that chapter. The three experiments featured in this appendix are (E.1) a preparation of the plane wave $|\chi_6\rangle$ from the resting plane wave $|\chi_0\rangle$, (E.2) a qualitative demonstration of our ability to control the relative phases between three momentum components and (E.3) the preparation and measurement of rotated squeezed Gaussian states.

E.1 Momentum distribution control from the resting BEC

In Chap. 3, we demonstrate the efficiency of QOC for computing the manner in which to continuously shift the optical lattice in time in order to prepare arbitrary quantum states in our Bloch system. In the experiments presented in that chapter, the control stage always follows an adiabatical lattice loading (see Sec. 2.4.1), so the initial condition is the ground state of the lattice. We present in Fig. E.1 an experiment illustrating that this choice is somewhat arbitrary, and that control fields can as well be computed and experimentally applied to prepare a target starting from the resting BEC (*i.e.* the plain wave $|\chi_0\rangle$, see Secs. 1.2.1 and 2.4.1). Indeed, we manage to prepare the 6th momentum component with fidelity $\mathcal{F}_{\text{exp}}^{(\beta)} = 0.85 \pm 0.06$ (averaged over 10 realizations with one standard deviation as uncertainty), *i.e.* as reliably as for the equivalent preparations of the Sec. 3.2.2 achieved from the ground state of the lattice.

E.2 Control of the relative phases between three momentum components

We here extend the experiment of Sec. 3.3.1 and further display our ability to control the argument of the $c_{q,\ell}$ coefficients. We here target three-momentum component superpositions with specific relative phases between the plane wave coefficients:

$$\begin{aligned} |\psi_{\text{T}}^{(\text{a})}\rangle &= \frac{1}{\sqrt{3}} (|\chi_{-2}\rangle + |\chi_0\rangle + |\chi_2\rangle) \\ |\psi_{\text{T}}^{(\text{b})}\rangle &= \frac{1}{\sqrt{3}} (|\chi_{-2}\rangle + e^{2i\pi/3} |\chi_0\rangle + e^{4i\pi/3} |\chi_2\rangle) \\ |\psi_{\text{T}}^{(\text{c})}\rangle &= \frac{1}{\sqrt{3}} (e^{2i\pi/3} |\chi_{-2}\rangle + |\chi_0\rangle + e^{2i\pi/3} |\chi_2\rangle) \end{aligned} \quad (\text{E.1})$$

Experimental results are shown in Fig. E.2. For each of these states, we show the experimentally measured evolution of the momentum distribution in the static lattice following the state preparation. We also present the theoretical evolutions of the numerically prepared states. We

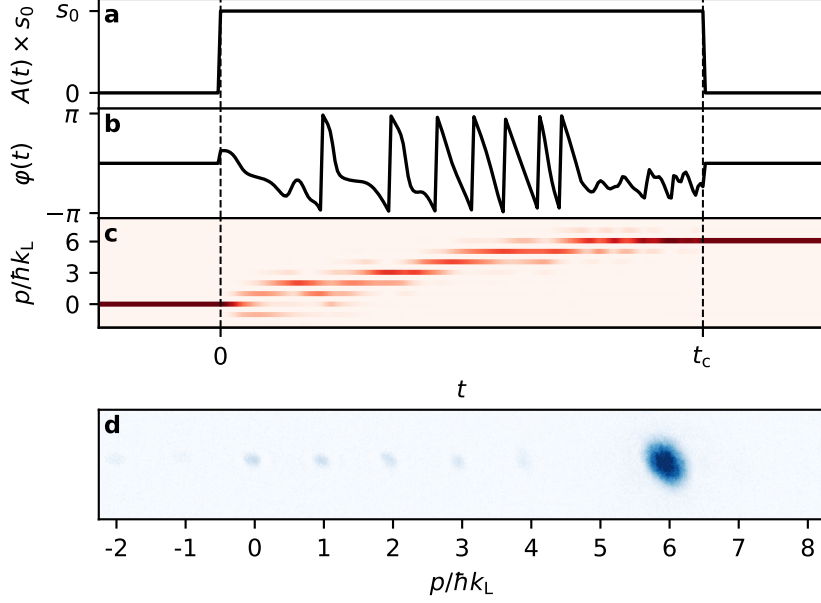


Figure E.1 | Experimental preparation of the plane wave with momentum $p = 6 \hbar k_L$ from the resting BEC. (a) Depth of the lattice as a function of time. (b) Phase of the lattice as function of time, optimized for the preparation of the plane wave $|\chi_6\rangle$ from $|\chi_0\rangle$ using QOC in the interval $0 \leq t \leq t_c$. The numerical fidelity for this control field is $\mathcal{F}^{(\beta)} \approx 0.977$ (see Sec. 3.2.1). (c) Numerical simulation of the momentum distribution in the lattice as function of time. (d) Experimental TOF absorption image after the preparation. The colormap for the OD is truncated to 0.8 of its maximum value (which saturates the center of the sixth momentum order) to see preparation defects. Parameters are $s_0 = 5.23 \pm 0.10$, $t_c = 3.25 T_0$ (see Sec. 3.1.2) and $t_{\text{TOF}} = 30$ ms.

observe good qualitative agreement between the experimental and theoretical data, which allows us to identify the prepared superposition. Our general control on the c_ℓ coefficients is asserted when we target and reconstruct phase space distributions (see Secs. 3.3.4 and 3.3.5 as well as following section).

E.3 Squeezed and rotated Gaussian states

This last section refers to Sec. 3.3. As a final example of optimal control preparation of Gaussian states, we present the rotation of squeezed Gaussian states. For a rotation angle θ (defined positive from the x axis to the p axis), the plane wave coefficients of a rotated squeezed Gaussian state can be written as:

$$c_\ell^{(\xi, \theta)}(u, v) = \left(\frac{\text{Re}\{A\}}{\pi} \right)^{1/4} e^{iuv/2} e^{-ilu} e^{-A(l-v)^2/2}, \quad (\text{E.2})$$

with

$$A = \frac{\cosh(r) - \sinh(r) e^{2i\theta}}{\cosh(r) + \sinh(r) e^{2i\theta}} \quad \text{and} \quad r = \frac{1}{4} \ln \left(\frac{s}{4\xi^4} \right).$$

We focus on a rather large squeezing $\xi = 1/3$ (as compared to the experiments of Sec. 3.3.5),

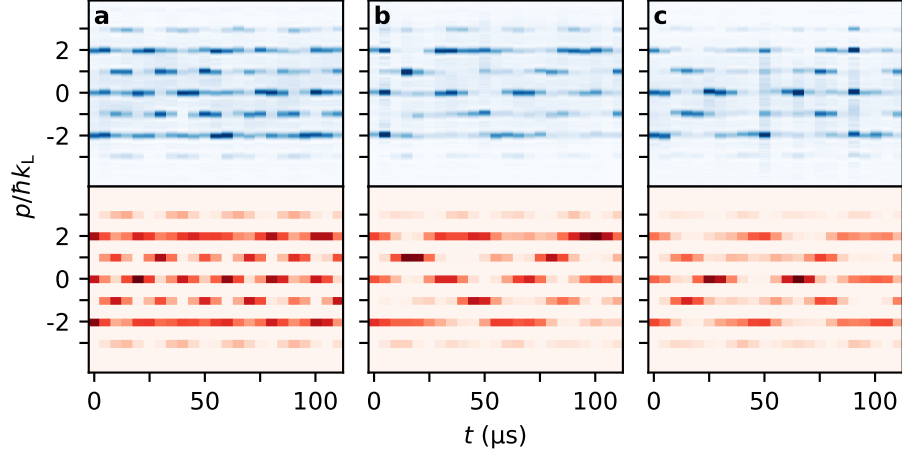


Figure E.2 | Preparation of three-momentum component states. (a,b,c) Preparation of the superpositions $|\psi_T^{(a)}\rangle$, $|\psi_T^{(b)}\rangle$, and $|\psi_T^{(c)}\rangle$ (see Eq. (E.1)) respectively. Top: stack of integrated experimental images showing the evolution of the momentum distribution during a subsequent 110 μs holding time in a static lattice after applying the control field $\varphi(t)$ for the preparation of the target. Bottom: numerical propagation of the expected prepared state in a static lattice. For all three prepared states, the dimensionless lattice depth is $s_0 = 5.7 \pm 0.2$.

phase space-centered states with $(u, v) = (0, 0)$ and we target the two rotation angles $\theta = \pm\pi/4$. As for most of our targets in Secs. 3.3.4 and 3.3.5, the control duration is fixed to $t_c = 1.75 T_0$ and we reconstruct the experimentally prepared states from the data of its evolution in the static lattice as detailed in 3.3.3. In Fig. E.3 we compare the Husimi representations of the numerically prepared and experimentally reconstructed states. In both cases, the QOC algorithm converged to a control field preparing the target with quantum fidelity $\mathcal{F}_{\text{num}} > 0.995$. For $\theta = \pi/4$ (Fig. E.3(a)), the experimental fidelity to the numerically prepared state is $\mathcal{F}_{\text{exp}} = 0.88$ with purity $\gamma = 0.89$ (see Sec. 3.3.3). For $\theta = -\pi/4$ (Fig. E.3(b)), we have $\mathcal{F}_{\text{exp}} = 0.89$ and $\gamma = 0.88$.

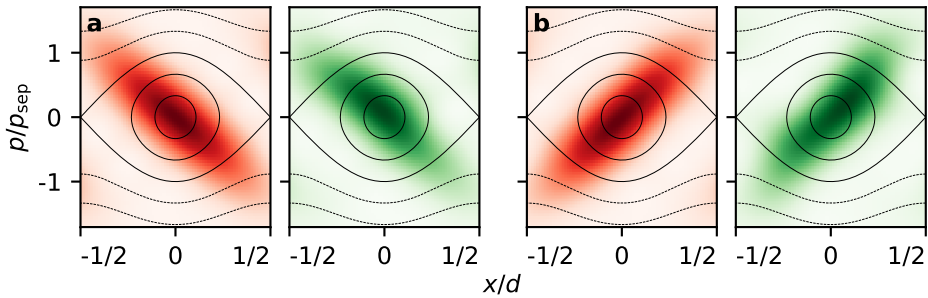


Figure E.3 | Preparation and measurement of rotated squeezed Gaussian states. (a-b) Husimi representations in the phase space of the static lattice. Left (red): state $|\psi_{\text{QOC}}\rangle$ numerically prepared by optimal control. Right (blue): density matrix $\hat{\rho}_{\text{ML}}$ reconstructed from experimental data by likelihood maximization. The squeezing parameter for both targets is $\xi = 1/3$ and the rotation angles are $\theta = \pm\pi/4$ for (a,b) respectively. The lattice depth during the experiments is $s_0 = 5.45 \pm 0.30$. See text for fidelities and purities.

Appendix F - Résumé du manuscrit en français

Introduction

L'usage de la lumière et de champs magnétiques afin de contrôler les degrés de liberté externes des atomes (c'est-à-dire leur position et vitesse) a révolutionné le domaine de la physique atomique. Tirant parti du développement des lasers dans les années 1960, les techniques de piégeage et de refroidissement d'atomes [1, 2, 3] ont permis aux expérimentateurs d'atteindre un niveau de contrôle sans précédent sur les systèmes atomiques. Grâce à ces méthodes, il est possible de refroidir des ensembles atomiques proche du zéro absolu, jusqu'à des températures auxquelles une description quantique de la matière devient nécessaire. Un résultat emblématique de ce domaine d'étude est celui de la condensation de Bose-Einstein, une transition de phase quantique au travers de laquelle un gaz de bosons passe d'un ensemble de particules décrit classiquement par la statistique de Maxwell-Boltzmann à une fonction d'onde macroscopiquement peuplée par les atomes du gaz et dont l'évolution est gouvernée par la mécanique quantique: un condensat de Bose-Einstein (CBE).

La condensation de Bose-Einstein a été atteinte pour la première fois en 1995, dans les groupes de E. Cornell et C. Wieman [6] puis dans celui de W. Ketterle [7]. Cette prouesse expérimentale, récompensée par le prix Nobel de physique en 2001, marque la naissance du domaine de recherche sur les gaz quantiques, en constante croissance depuis lors. Ces gaz d'atomes ultrafroids, qui peuvent être de nature bosonique ou fermionique, constituent une plateforme hautement versatile avec laquelle étudier la mécanique quantique. En effet:

- L'utilisation de lasers et de champs magnétiques permet la réalisation d'une grande variété de potentiels [8, 9] dans lesquels étudier l'évolution de ces systèmes quantiques. Il est par exemple possible de manipuler jusqu'à l'atome unique à l'aide de pinces optiques [10, 11] ou de réaliser des potentiels périodiques dans l'espace (dits de Bloch) finement contrôlables à l'aide *e.g.* de réseau optique [12] et de modulateurs spatiaux de lumière (*spatial light modulators*) [13, 14].
- En modulant périodiquement dans le temps ces potentiels artificiels (on parle alors de systèmes de Floquet), il devient possible de réaliser des hamiltoniens effectifs d'intérêt pour l'étude d'un système particulier [15, 16]. Une telle ingénierie de Floquet permet par exemple de créer des effets de magnétisme artificiel pour les atomes neutres [17, 18].
- Les effets des interactions entre particules quantiques peuvent être étudiés grâce aux résonances de Feshbach [19], qui permettent, pour les systèmes d'atomes ultrafroids, de contrôler la force et le signe des interactions à courtes portées entre les atomes. En outre,

d'autres systèmes sont développés afin d'étudier des effets d'interaction à plus longue portée, comme notamment les gaz dipolaires [20, 21, 22] et les systèmes d'atomes de Rydberg [23, 24, 25].

Le haut degré de contrôle qu'il est possible d'atteindre grâce aux expériences de gaz quantiques revêt un intérêt particulier pour les deux domaines que sont la simulation quantique et la métrologie quantique.

Le domaine de la simulation quantique [26, 27] vise à émuler des systèmes quantiques complexes sur des systèmes plus simples à observer et à contrôler. Cette idée a initialement été proposée par R. Feynman en 1982 [28] et a depuis été mise en œuvre sur de nombreux systèmes, comme par exemple les circuits supraconducteurs [29], les systèmes photoniques [30], les ions piégés [31] et les atomes neutres ultrafroids [32, 33, 34]. Nous nous intéressons dans ce manuscrit à cette dernière plateforme avec laquelle ont été réalisées, ces vingt dernières années, des expériences phare dans le domaine de la simulation quantique. On peut notamment citer la réalisation du modèle de Bose-Hubbard en trois dimensions, grâce à laquelle a été observée la transition entre une phase superfluide et un isolant de Mott [35], l'observation de la localisation d'Anderson en une [36, 37], deux [38, 39] et trois dimensions [40, 41, 42] dans des systèmes avec un désordre artificiel et la transition de Berezinskii-Kosterlitz-Thouless dans un gaz quantique confiné à deux dimensions [43, 44].

Un autre domaine fondamental qui bénéficie du haut niveau de contrôle offert par les gaz quantiques est celui de la métrologie quantique. Un exemple clé des avantages que recèle la manipulation d'un système quantique à des fins de métrologie est donné par les états comprimés, qui permettent d'atteindre des sensibilités de mesure de plus en plus proche des limites fondamentales dictées par le principe d'incertitude d'Heisenberg [45, 46]. C'est notamment le cas avec les états comprimés de photons pour la spectroscopie [47] et l'interférométrie [48, 49], et d'importants efforts sont fournis pour tirer parti de la compression d'états quantiques de matière dans le domaine de l'interférométrie avec des ondes de matières [50, 51, 52, 53, 54, 55].

Ces différents champs d'application encouragent le développement de nouvelles méthodes afin de contrôler et de manipuler les systèmes d'atomes froids. Plusieurs approches modernes sont proposées, parmi lesquelles les boucles de rétroaction [56], les raccourcis vers l'adiabaticité [57], l'apprentissage machine [58] et le contrôle optimal appliqué aux systèmes quantiques [59, 60].

Le groupe de recherche Atomes Froids dans lequel j'ai réalisé mon doctorat au Laboratoire Collisions, Agrégats et Réactivité (LCAR, Toulouse) travaille dans le domaine de la simulation quantique et du développement de techniques pour le contrôle de systèmes d'atomes ultrafroids. Le travail de thèse rapporté dans ce manuscrit porte à la fois sur le développement de telles méthodes et sur leur application pour la simulation quantique dans un système de Floquet-Bloch (c'est-à-dire un système périodique à la fois dans le temps et l'espace). Dans l'équipe Atomes Froids du LCAR, nous travaillons sur une expérience avec laquelle nous réalisons des CBE de ^{87}Rb que nous plaçons ensuite dans un réseau optique unidimensionnel. Le long de l'axe du réseau, les atomes (qui peuvent être décrits par une fonction d'onde unique) font l'expérience d'un potentiel sinusoïdal dont nous pouvons contrôler la profondeur et la phase de manière arbitraire

au cours du temps à l'aide de modulateurs acousto-optiques. Ce système relativement simple constitue une plateforme idéale sur laquelle développer de nouvelles méthodes pour le contrôle d'états quantiques, ainsi que pour l'expérimentation sur la dynamique d'ondes de matière dans un potentiel sinusoïdal finement contrôlable dans le temps, et cela dans un régime de faibles interactions interatomiques.

Ce manuscrit de thèse est organisé de la manière suivante:

Partie 1. Nous commençons par une première partie de méthodes, composée des chapitres 1 et 2. Dans le **Chapitre 1**, nous présentons des rappels de théorie pour l'étude de la dynamique d'une fonction d'onde dans un système de Floquet-Bloch. Dans le **Chapitre 2**, nous présentons notre montage expérimental pour l'obtention de CBE, ainsi que le réseau optique et la manière dont nous le contrôlons, ce qui nous permet de réaliser dans le laboratoire le système décrit au premier chapitre.

Partie 2. La seconde partie présente deux études expérimentales pour lesquelles les échelles de temps des expériences nous permettent de négliger les interactions interatomiques dans les CBE. Le **Chapitre 3** porte sur la mise en place d'un protocole de contrôle optimal quantique afin de contrôler arbitrairement l'état quantique externe des CBE dans le réseau optique (c'est-à-dire leur état de mouvement). Dans le **Chapitre 4**, nous détaillons l'étude, à la fois théorique et expérimentale, d'un effet *ratchet* (ou rochet) non-diffusif (c'est-à-dire le long de trajectoires classiques non-chaotiques) dans un système hamiltonien.

Partie 3. La troisième et dernière partie de ce manuscrit est composée du **Chapitre 5** où nous nous plaçons dans un régime expérimental dans lequel il n'est plus possible de négliger les interactions entre les atomes qui constituent le CBE. Nous y présentons l'étude de l'émergence d'une nouvelle structuration des atomes dans le réseau optique modulé en phase, qu'il nous est possible de contrôler par l'ingénierie, dans l'espace des impulsions, d'instabilités dynamiques dues à un phénomène de mélange à quatre ondes.

Nous dressons ci-après un bref résumé de ces cinq chapitres.

Chapitre 1 : Éléments de théorie pour l'étude d'une fonction d'onde dans un potentiel unidimensionnel

Dans ce premier chapitre, nous rappelons des éléments de théorie pour étudier la dynamique d'une fonction d'onde dans un potentiel unidimensionnel $V(x, t)$ dont les paramètres peuvent dépendre du temps. La forme générale de potentiel qui nous intéresse dans ce manuscrit est la suivante :

$$V(x, t) = -A(t) \frac{V_0}{2} \cos \left(\frac{2\pi x}{d} + \varphi(t) \right). \quad (\text{F.1})$$

avec V_0 l'amplitude typique du potentiel (par la suite, on donne cette profondeur en unité de l'énergie caractéristique E_L via le paramètre $s_0 = V_0/E_L$; voir p. 18), d sa périodicité spatiale, $A(t)$ une fonction de modulation de l'amplitude du potentiel et $\varphi(t)$ une fonction de modulation de sa phase.

Nous adressons dans un premier temps le cas d'une particule classique dans un tel potentiel. Après un bref rappel de mécanique classique hamiltonienne, nous introduisons la notion d'espace des phases position-impulsion, un outil puissant qui encapsule la dynamique du système. Dans le cas d'un potentiel statique unidimensionnel ($A(t) = 1$ et $\varphi(t) = 0$ dans l'Éq. (F.1)), le tracé de l'espace des phases (x, p) permet d'afficher de manière concise la dynamique d'un système (voir Fig. 1.1, p. 14), qui est dans ce cas complètement intégrable. À l'inverse, lorsque le potentiel varie dans le temps, des trajectoires chaotiques peuvent exister dans l'espace des phases, qui devient un espace (x, p, t) car l'évolution d'une configuration (x, p) dépend du potentiel à l'instant t . Nous terminons cette partie de mécanique classique avec la notion de *portrait de phase stroboscopique* : dans le cas particulier où la dépendance du potentiel est périodique dans le temps (*i.e.* $V(x, t+T) = V(x, t)$), on peut considérer des sections $(x, p, t_0 + nT)$ de l'espace des phases et ainsi tracer un portrait de phase stroboscopique (voir Fig. 1.2, p. 15 pour un schéma de la procédure). La figure F.1 présente deux exemples de portraits de phase stroboscopiques qui correspondent aux cas du potentiel sinusoïdal modulé périodiquement en amplitude (panneaux (a)) :

$$A(t) = 1 + \varepsilon_0 \cos(2\pi\nu t) \quad \text{et} \quad \varphi(t) = 0, \quad (\text{F.2})$$

ou en phase (panneaux (b)) :

$$A(t) = 1 \quad \text{et} \quad \varphi(t) = \varphi_0 \cos(2\pi\nu t). \quad (\text{F.3})$$

On y voit la coexistence de trajectoires intégrables (ou "régulières", identifiables par des traits continus) et de trajectoires chaotiques (identifiables par une "mer chaotique" de points dispersés). Lorsque chaos et intégrabilité ainsi coexistent, on parle de dynamique mixte.

La suite de ce premier chapitre traite de la dynamique d'une fonction d'onde dans un potentiel périodique dans l'espace et éventuellement modulé dans le temps. Nous commençons par rappeler le théorème de Bloch, qui énonce que les fonctions d'ondes $\psi_q(x, t)$ qui évoluent dans un potentiel de période spatiale d s'écrivent, dans un sous-espace donné de quasi-moment q , comme le produit d'une onde plane et d'une fonction d'amplitude de périodicité spatiale d . En conséquence directe de cette périodicité, ces fonctions d'ondes dans un système de Bloch s'écrivent sous la forme de leur série de Fourier

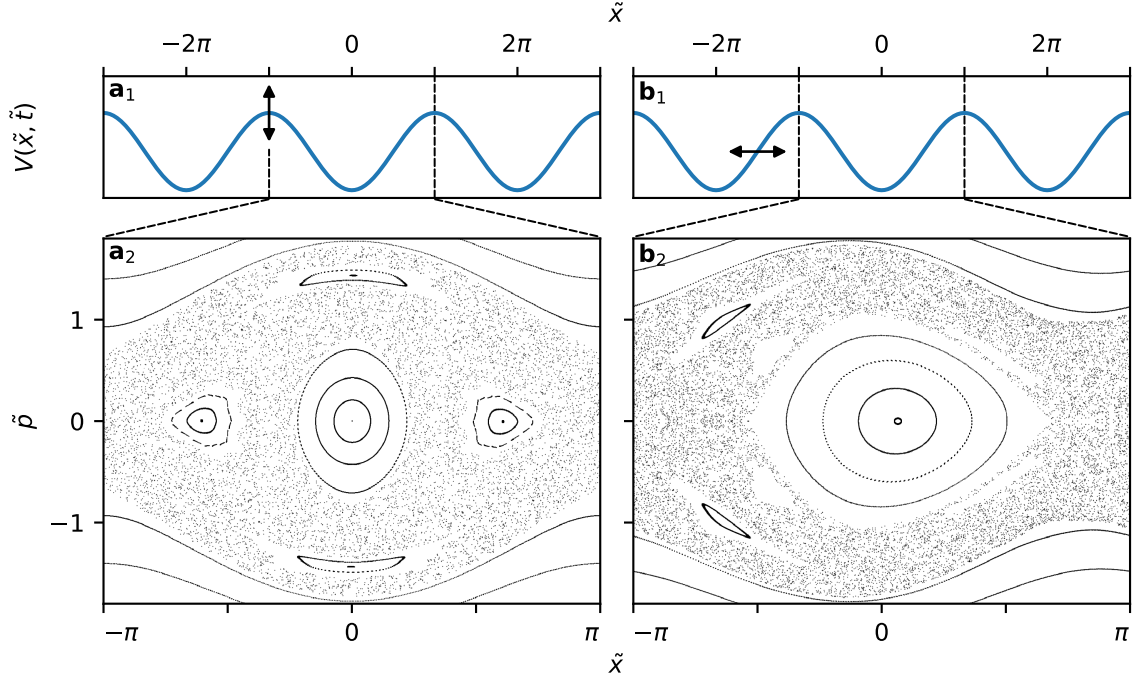


Figure F.1 | Exemples de portraits de phase stroboscopiques. En haut : potentiels sinusôdaux, modulés périodiquement dans le temps, représentés sur trois périodes spatiales. En bas : portraits de phase stroboscopiques correspondants, représentés sur une période spatiale. **(a)** Modulation de l’amplitude du potentiel, une configuration associée aux Éqs. (F.1) et (F.2), avec les paramètres de modulation $\gamma = 0.375$, $\varepsilon_0 = 0.24$ et un temps de référence pour l’observation sous-stroboscopique $\hat{t}_0 = 0$. **(b)** Modulation de la phase du potentiel, associée aux Éqs. (F.1) et (F.3), avec $\gamma = 0.44$, $\varphi_0 = 2\pi/24 = 15^\circ$ et $\hat{t}_0 = 0$. Les grandeurs “tildées” adimensionnées et le paramètre γ sont obtenus à partir des grandeurs dimensionnées en suivant la procédure résumée p. 34.

$$\psi_q(x, t) = \sum_{\ell \in \mathbb{Z}} c_{q,\ell}(t) \frac{e^{i(\ell k_L + q)x}}{\sqrt{d}}, \quad (\text{F.4})$$

avec le nombre d’onde du potentiel (F.1) $k_L = 2\pi/d$ et les coefficients des ondes planes $c_{q,\ell}(t) \in \mathbb{C}$, $\sum_{\ell} |c_{q,\ell}(t)|^2 = 1$. À l’aide du théorème de Bloch, on peut chercher les états propres associés à un potentiel périodique (dits états propres de Bloch) sous la forme (F.4), et nous donnons une méthode numérique pour calculer la structure de bande du potentiel sinusôdal statique à partir du spectre de l’hamiltonien, comme montré sur la figure F.2(a) (ainsi qu’avec plus de détails sur le figure 1.5, p. 22).

Nous poursuivons avec l’étude de l’évolution temporelle d’un état arbitraire $|\psi_q(t_0)\rangle$ dans un tel système. Dans le cas d’indépendance temporelle du potentiel, l’évolution d’un tel état est complètement déterminée par sa décomposition sur les états propres de Bloch à l’instant t_0 . Ce n’est plus le cas lorsque l’on considère un potentiel qui dépend du temps de manière arbitraire. Nous exposons néanmoins une approche numérique pour calculer cette évolution, en construisant de manière itérative un opérateur d’évolution sur des intervalles de temps suffisamment brefs, lors desquels il est peut être valide de considérer constant le potentiel. Nous adressons

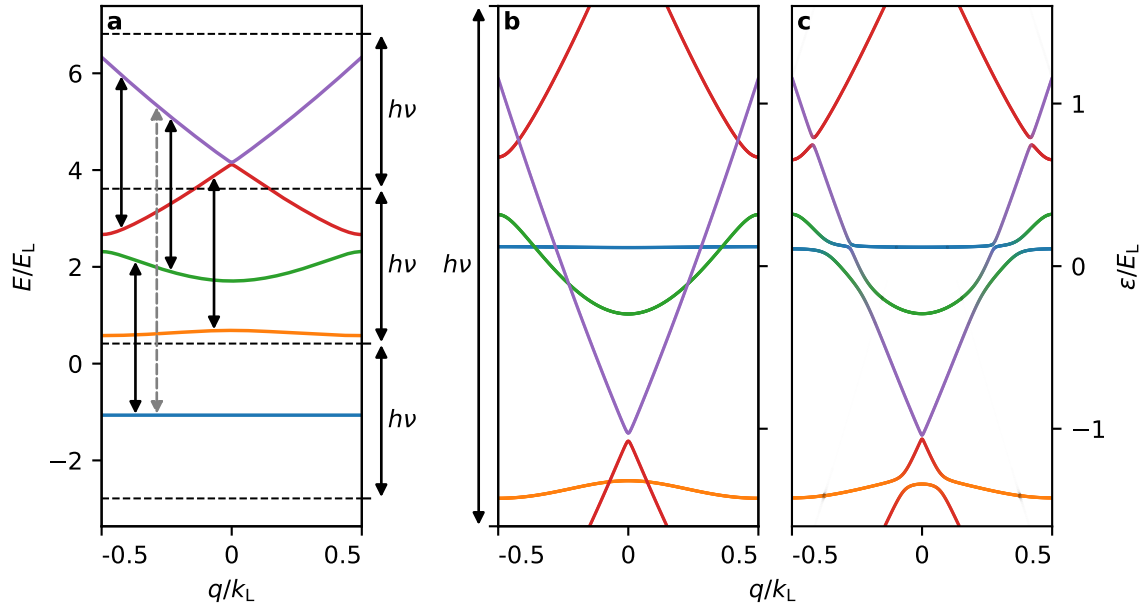


Figure F.2 | Structure de bande et spectres de quasi-énergie. (a) Structure de bande (lignes colorées continues) pour le potentiel sinusoïdal statique de profondeur $s_0 = 4$. Les cinq bandes de plus basse énergie sont en bleu, orange, vert, rouge et violet respectivement. Les flèches sont placées aux quasi-moments où les bandes sont séparées par une énergie $|E_{i,q} - E_{j,q}| = k \times h\nu$ correspondant à l'énergie de transition associée aux spectres de Floquet des panneaux (b) et (c) (avec $k = 1$ en noir et trait continu et $k = 2$ en gris et tireté). Ces flèches ne sont montrées que pour $q < 0$ par souci de lisibilité. Les lignes tiretées horizontales marquent la périodicité énergétique des spectres de Floquet des panneaux (b) et (c). (b,c) Spectres de quasi-énergie pour le potentiel sinusoïdal modulé périodiquement en amplitude au cours du temps (Éq. (1.40), p. 26), pour deux amplitudes de modulation ε_0 différentes et autres paramètres communs $s_0 = 4$ and $\nu = 4\nu_L$ (voir p. 18). Les amplitudes de modulation sont $\varepsilon_0 = 0$ (b) et $\varepsilon_0 = 0.15$ (c).

ensuite le cas particulier des systèmes de Floquet, pour lesquels la dépendance temporelle du potentiel est périodique. On s'intéresse dans ce cas à l'opérateur d'évolution sur une période de modulation (l'opérateur de Floquet), et nous montrons comment ses états propres (dits de Floquet) permettent d'étudier de façon stroboscopique la dynamique d'un état quantique dans un tel système, à la manière des états propres de l'hamiltonien dans le cas statique. Nous détaillons notamment comment calculer et représenter le spectre de quasi-énergie associé à un opérateur de Floquet, dont la périodicité en quasi-énergie est similaire, dans l'espace des énergies, à la notion de zone de Brillouin pour un spectre associé à un potentiel périodique dans l'espace. La figure F.2(b,c) montre des exemples de spectres de quasi-énergie, où les quasi-énergies sont représentées en fonction de la projection entre leur état de Floquet associé et les états de Bloch de plus basse énergie (qui correspondent aux bandes du panneau (a) ; une procédure détaillée dans la section 1.3.2).

Pour terminer ce premier chapitre, nous considérons la représentation d'états quantiques dans l'espace des phases d'un système dynamique. Nous expliquons dans cette section comment, en conséquence du principe d'incertitude d'Heisenberg $\Delta x \Delta p \geq \hbar/2$, la constante de Planck réduite \hbar limite l'étendue minimale que peut avoir la distribution d'un état quantique

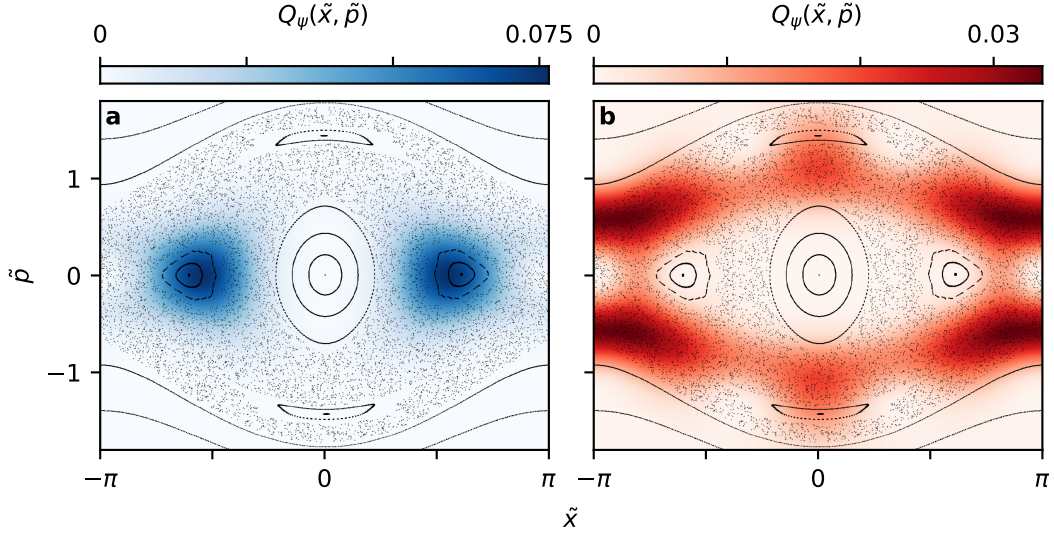


Figure F.3 | Représentations de Husimi d'états de Floquet-Bloch dans le cas du potentiel sinusoïdal modulé en amplitude (Éqs. (F.1), p. 176) avec les paramètres $\gamma = 0.375$, $\varepsilon_0 = 0.24$ and $\hbar_{\text{eff}} = 0.2$ (voir l'adimensionnement p. 18). (a) Un état de Floquet-Bloch localisé sur des îlots réguliers. (b) Un état de Floquet-Bloch délocalisé sur la mer chaotique.

dans l'espace des phases. Nous introduisons les quasi-distributions de probabilité de Wigner (figure 1.7, p. 30) et de Husimi (figure 1.8, p. 32) pour représenter un état dans l'espace des phases, ainsi que la notion de constante de Planck effective \hbar_{eff} , un paramètre qui permet de régler la prévalence des effets quantiques dans la dynamique d'un système (figure 1.8, p. 32). Enfin, nous montrons comment les outils introduits dans ce premier chapitre permettent de représenter, pour un système de Floquet-Bloch, les états de Floquet vis-à-vis du portrait de phase stroboscopique (Fig. F.3), c'est-à-dire vis-à-vis de la dynamique classique du système.

Chapitre 2 : Montage expérimental

Nous présentons dans ce deuxième chapitre l'expérience de refroidissement d'atomes de ^{87}Rb développée par l'équipe Atomes Froids au LCAR qui nous permet de réaliser au laboratoire les systèmes étudiés au chapitre 1. Cette expérience, en fonctionnement depuis 2016, a déjà fait l'objet d'exhaustives descriptions dans les thèses de mes prédécesseurs [93, 94, 115, 67, 68], et nous choisissons, par souci de concision, de ne procéder ici qu'à une succincte description de ce montage expérimental.

Nous commençons par un bref rappel de notions sur la condensation de Bose-Einstein, et revenons sur la longueur d'onde de de Broglie thermique

$$\Lambda_T = \sqrt{\frac{2\pi\hbar^2}{mk_B T}}, \quad (\text{F.5})$$

une quantité qui rend compte de la longueur d'onde typique des atomes de masse m dans un gaz à température T (avec k_B la constante de Boltzmann). La condensation de Bose-Einstein a lieu lorsque $\Lambda_T \geq l = n^{-1/3}$, avec l la distance moyenne entre les atomes dans le gaz et n la densité du gaz. L'enjeu d'une expérience d'atomes ultrafroids est donc de refroidir un gaz d'atomes tout en conservant suffisamment importante la densité n , de sorte à ce que la longueur d'onde de de Broglie thermique devienne supérieure à la distance moyenne entre les particules. Pour le piège dans lequel sont maintenus les atomes dans notre expérience, on calcule (voir p. 40) que la température critique en dessous de laquelle il nous faut refroidir le gaz est d'environ 130 nK.

L'expérience de l'équipe Atomes Froids au LCAR permet d'obtenir des CBE composés d'approximativement $5 \cdot 10^5$ atomes de ^{87}Rb toutes les 22 secondes. La séquence de refroidissement atomique peut être décomposée en trois parties : une première étape de refroidissement dans un piège magnéto-optique, suivie d'une étape d'évaporation micro-onde dans un piège magnétique avant une dernière étape d'évaporation dans un piège dipolaire dans lequel la condensation de Bose-Einstein est atteinte. Afin de rendre davantage robuste l'obtention des CBE sur l'expérience, nous avons durant ma thèse changé la géométrie du piège dipolaire dans lequel cette dernière étape de refroidissement a lieu. Cette modification, avec les ancienne et nouvelle géométries, est schématisée sur la figure 2.1 (p. 44). Nous caractérisons cette nouvelle géométrie, et donnons les fréquences harmoniques du piège dans lequel se trouvent les CBE à la fin de la séquence de refroidissement.

Nous détaillons ensuite comment nous sommes capables de remonter à la distribution d'impulsion de l'ensemble atomique au cours des expériences via un système d'imagerie par absorption (figure 2.2, p. 47) réalisée après un temps de vol. Lorsque nous souhaitons mesurer cette distribution d'impulsion, nous coupons subitement tous les pièges, et les atomes qui commencent à chuter sous l'effet de la gravité entrent en expansion. Après un temps d'expansion suffisamment long, la mesure de la dispersion spatiale du nuage atomique reflète directement la dispersion en vitesse qu'avaient les atomes avant la coupure du piège. Pour un nuage thermique (*i.e.* avant transition vers un CBE), nous décrivons comment la mesure de cette expansion en fonction de la durée du temps de vol permet de mesurer la température du nuage. Pour un CBE, l'imagerie du nuage après un temps de vol revient à échantillonner statistiquement, en représentation impulsion, la fonction d'onde macroscopiquement partagée par les atomes condensés.

Nous poursuivons avec la présentation du réseau optique unidimensionnel qui nous permet de réaliser les potentiels étudiés au chapitre 1 : ce réseau est formé par l'interférence de deux faisceaux laser contrapropageants dont la longueur d'onde $\lambda = 1064$ nm est fortement désaccordée vers le rouge par rapport à la transition atomique D_2 du ^{87}Rb (voir appendice A). Cela crée, pour les atomes, un potentiel dipolaire [8, 79] attractif vers les maxima d'intensité de l'interférence lumineuse, résultant en un potentiel sinusoïdal le long de l'axe de propagation des faisceaux. À l'aide de trois modulateurs acousto-optiques, nous pouvons contrôler l'intensité du réseau optique (et donc sa profondeur) ainsi que sa phase (voir appendice C). Tel que discuté ci-dessus, notre système d'imagerie après temps de vol nous permet d'accéder à la distribution en impulsion des atomes dans le réseau optique. Travaillant avec des CBE (*i.e.* des fonctions

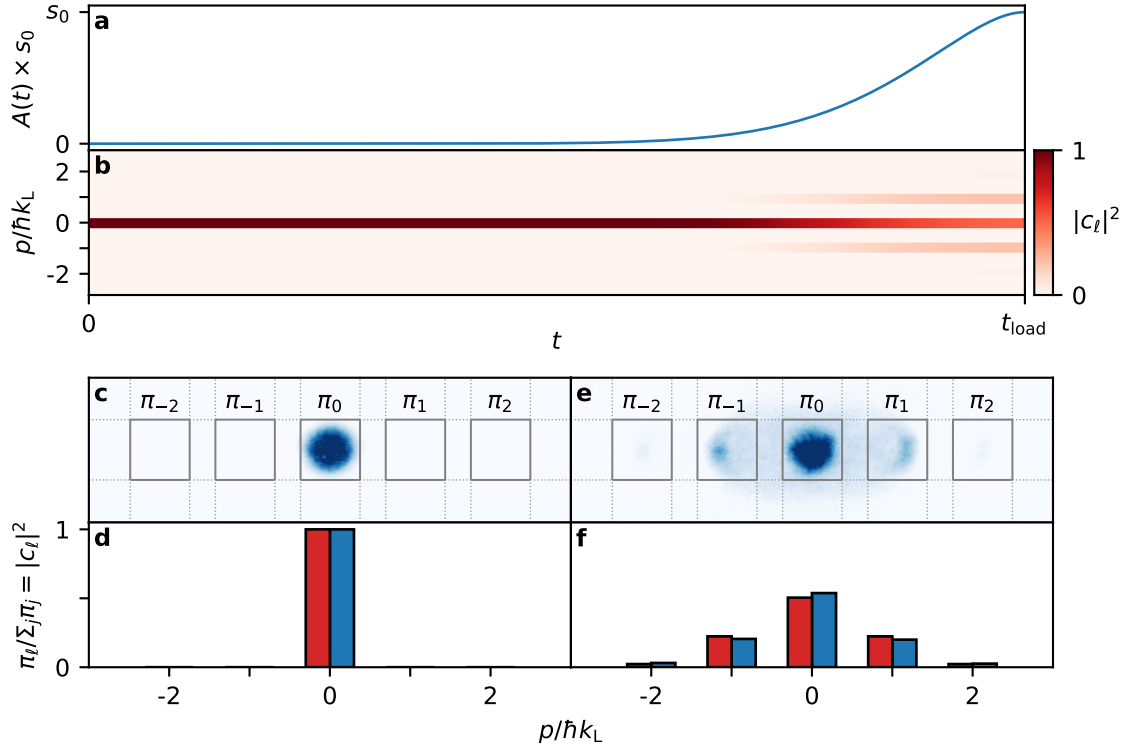


Figure F.4 | Chargement adiabatique du réseau optique et diffraction d’onde de matière. (a) Rampe de profondeur du réseau optique pour le chargement adiabatique de l’état fondamental du réseau optique de profondeur s_0 (voir texte). (b) Simulation numérique de la distribution d’impulsion au cours du chargement adiabatique du réseau. (c) (respectivement (e)) Image d’absorption expérimentale après temps de vol montrant les atomes avant (respectivement après) le chargement du réseau optique. Les rectangles gris délimitent les régions dans lesquelles les populations dans les ondes planes $|c_\ell|^2$ sont extraites. (f) (respectivement (e)) Diagramme en barres comparant les populations expérimentales (bleu) et théoriques (rouge) des ondes planes avant (respectivement après) le chargement du réseau optique. La profondeur du réseau est ici $s_0 = 8.06 \pm 0.10$, la durée du temps de vol est $t_{\text{TOF}} = 35$ ms et les cartes de couleurs pour les images d’atomes sont tronquées à 0.8 de leur valeur maximale respective afin de révéler les détails.

d’ondes) dans un système de Bloch, nous remontons ainsi aux modules carrés des coefficients des ondes planes $|c_{q,\ell}|^2$, comme montré sur la figure F.4 (dans un cas pour lequel $q = 0$).

Je conclus ce chapitre de présentation de l’expérience avec quelques techniques expérimentales usuelles lorsqu’on travaille avec des atomes froids dans un réseau optique, à savoir :

- une technique de chargement adiabatique de l’état fondamental du réseau optique (c’est-à-dire de l’état propre de Bloch de plus basse énergie) (figure F.4),
- deux méthodes pour calibrer, l’une rapidement [108] et l’autre finement [112, 113], la profondeur du réseau optique (voir figures 2.5 et 2.6, p.54 et 56),
- la méthode dite de *band-mapping* afin d’imager la structure de bande du réseau optique [107, 114, 79] (voir figure 2.7, p. 57).

Les trois chapitres suivants présentent une partie des résultats de recherche auxquels j'ai contribué durant ma thèse. Le reste de ces résultats publiés (à savoir les premières observations de résonance d'effet tunnel assisté par le chaos [61] et une étude du contrôle des halos de collisions quantifiés en impulsion qui apparaissent sur les figures de diffraction [62]) sont détaillés dans les thèses de M. Arnal [67] et G. Chatelain [68].

Chapitre 3 : Contrôle optimal quantique d'ondes de matières dans un réseau optique unidimensionnel

Ce chapitre s'inscrit dans le développement de méthodes pour le contrôle de l'état quantique d'un système d'atomes ultrafroids. Nous y détaillons la mise en place d'un protocole de contrôle optimal pour calculer la façon dont nous devons déplacer le réseau optique au cours du temps afin de contrôler arbitrairement l'état externe des CBE dans le réseau.

Nous commençons le chapitre par une introduction à la théorie du contrôle optimal quantique. Étant donné un système dont l'équation d'évolution est paramétrisée :

$$\dot{\mathbf{x}}(t) = \mathbf{f}(\mathbf{x}(t), \mathbf{u}(t), t), \quad (\text{F.6})$$

avec $\mathbf{x}(t)$ le vecteur d'état du système, $\mathbf{u}(t)$ un vecteur de paramètres et \mathbf{f} la fonction d'évolution, la théorie du contrôle optimal permet de calculer le champ de contrôle optimal $\mathbf{u}^*(t)$ qui amène le système d'un état initial $\mathbf{x}(t_0 = 0)$ à un état cible $\mathbf{x}(t_c)$ (avec t_c la durée du contrôle) tout en minimisant une fonctionnelle de coût. La détermination du champ de contrôle optimal s'énonce à l'aide du principe du maximum de Pontryagin que nous rappelons (voir section 3.1.1). Dans notre cas, nous souhaitons amener un état initial $|\psi_0\rangle$ (généralement l'état fondamental du réseau optique que nous savons préparer de manière fiable comme illustré sur la figure F.4) le plus proche possible d'une certaine cible, avec la phase du réseau optique $\varphi(t)$ comme unique champ de contrôle, le tout en un temps de contrôle fixé. Nous tâchons donc de maximiser une fidélité \mathcal{F} entre l'état préparé et la cible. La détermination du champ de contrôle optimal n'est généralement pas simple, et nous recourons à une approche numérique itérative de montée de gradient sur cette fidélité. Nous détaillons notre méthode dans les sections 3.1.2 et 3.1.3, et notre algorithme numérique est résumé p. 72.

Nous présentons dans la suite de ce chapitre une série d'expériences qui démontre notre capacité de contrôle de l'état externe des CBE dans le réseau optique.

Contrôle de la distribution en impulsion. Une première section de résultats (section 3.2) concerne le contrôle de la distribution en impulsion du CBE. Dans notre système de Bloch où la fonction d'onde du CBE s'écrit selon l'Éq. F.4, nous ciblons dans cette section¹ des ensembles

¹Ici dans le sous-espace de quasi-moment $q = 0$.

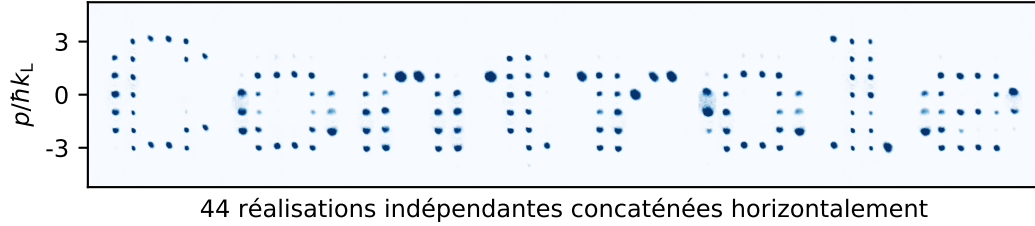


Figure F.5 | “Control” écrit avec des diffractions d’ondes de matière. Concaténation de 44 images d’absorption expérimentales obtenues après temps de vol, chaque colonne montrant la distribution en impulsion des atomes après application d’un champ de contrôle préalablement calculé via le formalisme du contrôle optimal quantique pour la réalisation d’une superposition équiprobable donnée de composantes d’impulsion.

donnés de probabilités $\{|c_\ell|^2\}$ (*i.e.* des ensembles donnés de nombre réels). Nous sommes ainsi capables de préparer :

- des ondes planes spécifiques, c’est-à-dire des états où tous les atomes sont mesurés dans le même ordre de diffraction (ce que nous démontrons jusqu’à une impulsion du paquet d’onde de $10 \hbar k_L$, voir Fig. 3.3, p.76),
- des superpositions équiprobables de composantes d’impulsion, comme illustré sur la figure F.5 (ainsi qu’avec davantage de détails sur la figure 3.4, p. 78),
- une superposition arbitraire de composantes d’impulsion (également sur la figure 3.4, p. 78).

Contrôle complet de l’état quantique. Nous nous intéressons dans un second temps au contrôle complet de l’état quantique externe des CBE selon l’axe du réseau, c’est-à-dire au contrôle de l’ensemble de nombres complexes $\{c_{q,\ell}\}$. Se pose ici la question de la certification des préparations : étant donné que nous n’accédons, par nos mesures après temps de vol, qu’aux modules carrés des coefficients $|c_{q,\ell}|^2$, comment attester de la réalisation d’un état donné présentant une certaine relation de phase entre ses coefficients $c_{q,\ell}$?

Nous démontrons premièrement un tel contrôle complet d’état quantique en préparant des cibles pour lesquelles il est simple de remonter aux phases relatives entre les coefficients $c_{q,\ell}$, avec:

- La préparation des superpositions des ondes planes d’impulsion $\pm 1 \hbar k_L$ (dans le sous-espace de quasi-moment $q = 0$) avec pour phase relative $\arg\{c_{-1}/c_1\} = \Delta\phi = j \times \pi/8$ et $j \in \{0, 1, \dots, 15\}$ (voir figure 3.5, p. 81). Alors que la mesure des états préparés au terme de la préparation donne le même résultat (c’est-à-dire environ 50 % des atomes dans les ordres de diffraction associés aux impulsions $\pm 1 \hbar k_L$), les évolutions subséquentes des distributions d’impulsion de ces états dans le réseau optique maintenu statique diffèrent fortement les unes des autres. L’ajustement de cette évolution avec pour paramètre ajustable la phase relative effectivement préparée entre les composantes d’impulsion nous permet de

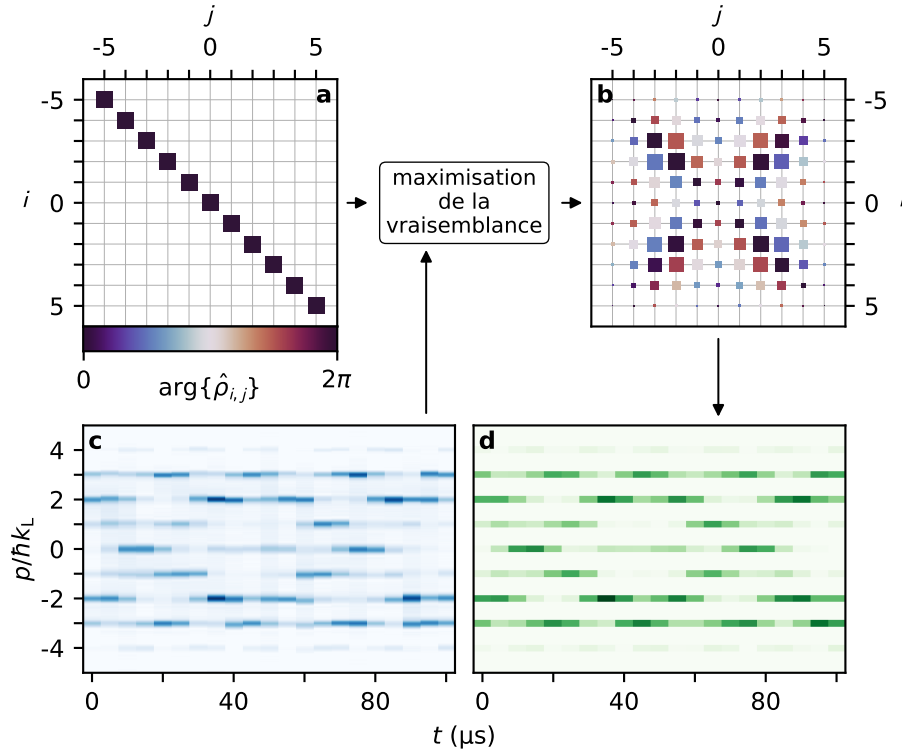


Figure F.6 | Reconstruction d'un état quantique dans un système de Bloch par maximisation de la vraisemblance. (a-b) Matrices densité $\hat{\rho}$ avec $\arg\{\hat{\rho}_{i,j}\}$ encodé en couleur et $|\hat{\rho}_{i,j}|$ encodé en taille (pas à l'échelle entre les panneaux). (a) Matrice identité $\mathbb{1}_{d_H}/d_H$ (où d_H est la dimension de l'espace de Hilbert, avec $d_H = 11$ ici) comme matrice densité d'essai. (b) Matrice densité de plus grande vraisemblance. (c) Concaténation d'images d'absorption expérimentales intégrées acquises durant l'évolution de l'état préparé dans le réseau maintenu statique à la profondeur $s = 5.5 \pm 0.5$. (d) Simulation numérique de l'évolution de l'état de plus grande vraisemblance dans le même réseau statique.

remonter à celle-ci. Ces mesures sont proches de ce que nous ciblons (voir figure 3.5, p. 81), démontrant un contrôle complet des états quantiques préparés dans ce cas simple.

- La préparation d'états propres du réseau (figure 3.6, p. 83). Étant donné que nous ciblons ici des états stationnaires du système, l'absence d'évolution atteste la bonne préparation. Nous préparons aussi des superpositions données de deux états propres du réseau, et observons une seule fréquence d'évolution pour les ordres de diffraction, qui est associée à la différence entre les énergies propres des états propres superposés.

Pour aller plus loin et démontrer notre capacité à préparer de manière arbitraire des états quantiques donnés, nous mettons en place un protocole dédié de reconstruction d'états par maximisation de vraisemblance. À nouveau, nous nous servons de l'évolution de la distribution en impulsion de l'état expérimentalement préparé lorsque celui-ci est maintenu dans le réseau statique au terme de la préparation. L'idée est de déterminer l'état théorique le plus susceptible de donner cette évolution, cette fois-ci de façon systématique. Notre approche itérative (inspirée de [138, 140, 141]) est résumée p. 86 et illustrée sur la figure F.6.

Nous appliquons cette méthode de reconstruction à plusieurs préparations. Nous com-

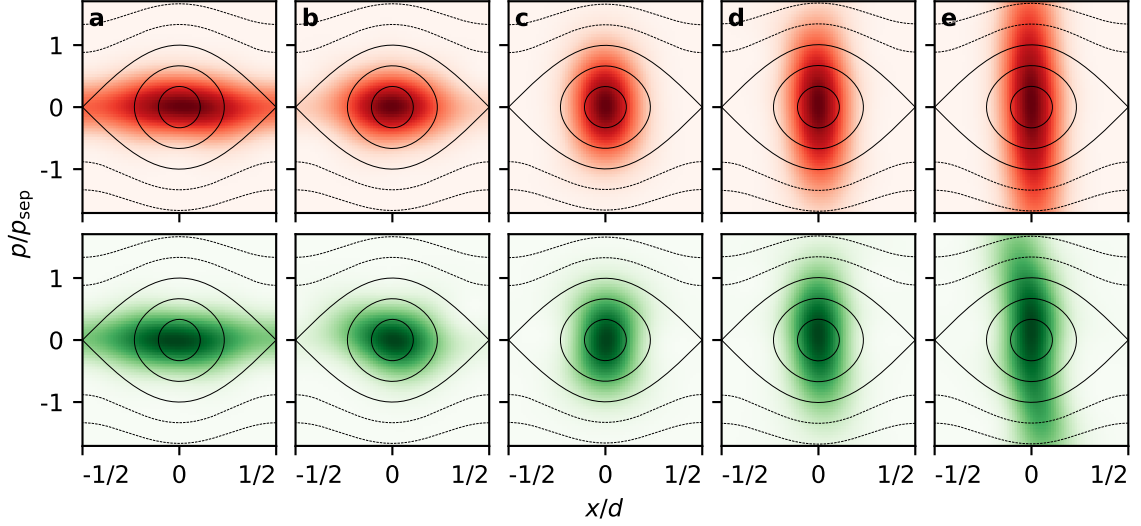


Figure F.7 | Préparation expérimentale et reconstruction d'états gaussiens comprimés. (a-e) Représentations de Husimi dans l'espace des phases du réseau statique. En haut (rouge) : états théoriques préparés par l'application du champ de contrôle préalablement calculé via le formalisme du contrôle optimal quantique pour la réalisation d'une compression donnée. En bas (vert) : états reconstruits de plus grande vraisemblance avec les mesures expérimentales (obtenue via la procédure illustrée sur la figure F.6). Les cartes de couleurs pour chaque fonction de Husimi vont de 0 à la valeur maximale que prend cette fonction sur l'espace des phases. Les facteurs de compressions sont $1/\xi = (0.44, 0.62, 1.65, 2.75, 4.34)$ pour (a-e) respectivement. Les fidélités des états reconstruits aux états théoriques sont $\mathcal{F}_{\text{exp}} = (0.99, 0.96, 0.98, 0.93, 0.75)$ et la pureté des états reconstruits est $\gamma = (1.00, 1.00, 1.00, 0.92, 0.72)$ (voir section 3.3.3, p. 82).

mençons par cibler des translations ainsi que des superpositions d'états gaussiens non comprimés dans l'espace des phases associé à chaque site du réseau optique. On définit l'absence de compression comme le rapport d'aspect position-impulsion de l'état gaussien qui est l'état fondamental des potentiels harmoniques approximant localement le fond des puits du réseau optique sinusoidal, c'est à dire un état dont les écarts-types en position Δx_0 et en impulsion Δp_0 s'écrivent, dans un réseau de profondeur s_0 :

$$k_L \Delta x_0 = s_0^{-1/4} \quad \text{et} \quad \Delta p_0 / \hbar k_L = s_0^{1/4} / 2. \quad (\text{F.7})$$

Les résultats de ces expériences sont présentés dans le section 3.3.4 (voir figure 3.8, p. 88). Nous poursuivons avec la préparation d'état gaussiens comprimés. Dans un réseau optique de profondeur s_0 , on associe à un état d'écart-type en position Δx le facteur de compression $\xi = \Delta x / \Delta x_0$. On prépare ainsi des états gaussiens comprimés en impulsion ($\xi > 1$) ainsi que des états comprimés en position ($\xi < 1$) dans un réseau de profondeur $s_0 \approx 5.5$. Ces résultats sont montrés sur la figure F.7. Nous démontrons notamment notre capacité à préparer fidèlement ($\mathcal{F}_{\text{exp}} \geq 0.75$) des états comprimés en position jusqu'à un facteur $1/\xi = 4.34$. Il s'agit, d'après nos connaissances, de la première réalisation d'un tel état, qui est impossible à obtenir de façon adiabatique. On peut en effet chercher la profondeur effective s_{eff} à laquelle l'état fondamental du réseau possède la même dispersion en position que celle réalisée expérimentalement. D'après

l'Éq. F.7, on trouve $s_{\text{eff}} = s_0/\xi^4 \approx 2000$. On note qu'il nous faudrait sur l'expérience du LCAR un laser de puissance $P \approx 750$ W pour réaliser un réseau de cette profondeur !

Nous avons également réalisé des états comprimés et inclinés dans l'espace des phases. Ces préparations et reconstructions sont présentées, ainsi que deux autres expériences mises de côté afin de fluidifier la lecture de ce chapitre, dans l'appendice E.

Application à la simulation quantique. Nous concluons ce premier chapitre de résultats par la présentation d'une expérience où nous appliquons notre protocole de préparation d'états quantiques à une étude d'effet tunnel dynamique [142, 89] dans le réseau modulé en amplitude. L'effet tunnel dynamique est une généralisation de l'effet tunnel usuel, où l'impossibilité classique du transport ne relève pas d'un défaut d'énergie mécanique (comme dans le cas usuel) mais de la traversée de surfaces KAM [89] dans un espace des phases présentant une dynamique mixte (c'est-à-dire de la traversée d'orbites régulières, classiquement impossible car impliquant une violation du principe de détermination ; voir section 1.1). L'effet tunnel dynamique peut avoir lieu dans un tel système lorsque deux états de Floquet non-dégénérés occupent les mêmes régions régulières du portrait de phase. Dans une telle situation, une particule quantique initialisée dans l'une de ces régions se mettra à osciller, avec une fréquence d'oscillation proportionnelle à la différence de quasi-énergie entre les états de Floquet impliqués.

Nous réalisons ici une expérience d'effet tunnel dynamique où nous initialisons, grâce au contrôle optimal quantique, les CBE dans l'idéale superposition des deux états de Floquet associés à ce phénomène pour des paramètres donnés de modulation d'amplitude du potentiel sinusoïdal. On compare cette approche optimale avec une approche plus traditionnelle [154, 155, 61] de translation soudaine du réseau optique afin de charger une des régions régulières entre lesquelles l'effet tunnel dynamique a lieu. Cette méthode simple est limitée en ceci qu'une translation de l'état fondamental du réseau statique ne se projette que partiellement dans le sous-espace composé des deux états de Floquet qui entraînent l'effet tunnel dynamique, ainsi que par l'asymétrie des projections sur ces deux états. Les résultats de cette comparaison de méthodes sont présentés sur la figure 3.13, p. 95, où nous observons une nette amélioration du signal d'oscillation tunnel à l'aide du contrôle optimal.

Publications en lien avec ce chapitre. Les travaux présentés dans ce chapitre résultent d'une collaboration avec Dominique Sugny du Laboratoire Interdisciplinaire de Carnot Bourgogne (Dijon). Ces études ont fait l'objet de deux publications :

- [63] N. Dupont, G. Chatelain, L. Gabardos, M. Arnal, J. Billy, B. Peaudecerf, D. Sugny and D. Guéry-Odelin, *Quantum State Control of a Bose-Einstein Condensate in an Optical Lattice*, PRX Quantum, 2:040303, (2021)
- [64] N. Dupont, F. Arrouas, L. Gabardos, N. Ombredane, J. Billy, B. Peaudecerf, D. Sugny and D. Guéry-Odelin. *Phase-space distributions of Bose-Einstein condensates in an optical lattice: Optimal shaping and reconstruction*, actuellement en processus de revue (2022)

Chapitre 4 : Ratchet hamiltonien non-diffusif

La deuxième étude présentée dans ce manuscrit traite d'un effet *ratchet* (rochet) non-diffusif dans un système hamiltonien. L'effet *ratchet* est l'émergence d'un courant de particules dans un potentiel duquel aucune force nette n'est dérivée [161, 162, 163]. Dans ce travail, nous corrélons les modulations d'amplitude et de phase du potentiel sinusoïdal afin de faire émerger, dans l'espace des phases du système, une îlot de trajectoires régulières qui transite d'un site au suivant en s'arrêtant périodiquement au centre du site. Nous présentons ici les premières étude théorique et réalisation expérimentale d'un tel effet *ratchet* déterministe, non-dissipatif et porté par des trajectoires non-chaotiques entraînant un déplacement linéaire dans l'espace pour des particules initialement au repos². Avec ce système, nous faisons l'observation expérimentale d'un transport linéaire et non-diffusif d'ondes de matière dans le réseau optique.

Dans ce chapitre, nous considérons l'hamiltonien suivant, associé à un potentiel sinusoïdal modulé en amplitude et en phase :

$$H(x, p, t) = \frac{p^2}{2m} - [1 + \varepsilon_0 \cos(2\pi\nu t)] \frac{V_0}{2} \cos\left[\frac{2\pi x}{d} + \varphi_0 \cos(2\pi\nu t + \Delta\phi) + \Delta\varphi\right]. \quad (\text{F.8})$$

Nous commençons par chercher des paramètres de modulation $(V_0, \varepsilon_0, \varphi_0, \nu, \Delta\phi, \Delta\varphi)$ tels qu'une particule classique initialisée au repos au fond d'un site de ce potentiel se retrouve, après une période de modulation, au repos au fond du prochain site. L'intérêt d'une telle modulation est qu'elle peut alors être répétée pour entraîner un transport directif. Nous développons une méthode systématique pour déterminer de tels paramètres (section 4.1) et nous convergions vers le jeu

$$(\gamma, \varepsilon_0, \varphi_0, \Delta\phi, \Delta\varphi) = (1.2, 0.3, 1.7, \pi/2, 0), \quad (\text{F.9})$$

qui est celui que nous étudions dans le reste du chapitre (avec l'amplitude dynamique adimensionnée $\gamma = V_0/2md^2\nu^2$). Ces paramètres donnent un exemple de la dynamique classique que nous requérons, comme présenté sur les portraits de phase stroboscopiques de la figure F.8 (voir aussi la figure 4.3, p. 107). De manière plus forte encore que l'absence de force nette globale inhérente aux systèmes présentant l'effet *ratchet*, on obtient ici, pour la trajectoire périodique au centre de l'îlot de transport, une absence de force nette *le long de la trajectoire sur chaque période* (voir notamment la figure 4.3, p. 107).

Nous poursuivons ce chapitre avec l'étude du transport quantique le long de l'îlot *ratchet* de cet espace des phases. On montre comment ce transport dépend la constante de Planck

²L'effet *ratchet* que nous étudions système se rapproche de l'effet *ratchet* "accélérateur" [183, 184, 185] observé dans le système du rotateur frappé (*kicked rotor*) avec lequel il est possible de faire émerger un transport non-diffusif, cette fois le long de l'axe des impulsions, en déplaçant savamment le potentiel sinusoïdal entre les flashes du potentiel.

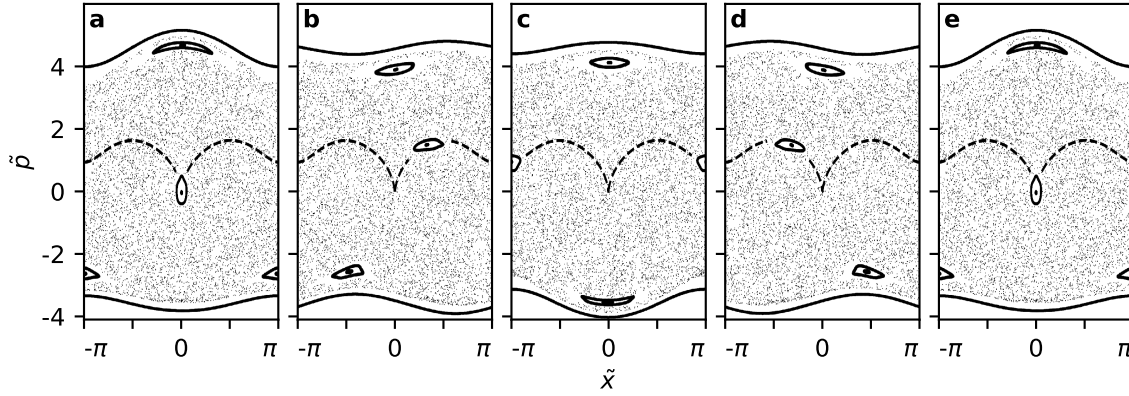


Figure F.8 | Évolution sous-stroboscopique du portrait de phase stroboscopique d'un système présentant un effet *ratchet* régulier. (a-e) Portraits de phase stroboscopiques associés à l'hamiltonien (F.8) (avec les paramètres de l'Éq. (F.9)) et les références de temps d'observation sous-stroboscopique $\nu t_0 = 0, 0.25, 0.5, 0.75$ et 1 . On représente sur chaque panneau la trajectoire au centre de l'îlot *ratchet* pour tout temps (ligne noire tiretée).

effective introduite au chapitre 1 (avec ici $\hbar_{\text{eff}} = h/mvd^2$), en ceci que ce paramètre règle la surface relative entre l'étendue minimale que peuvent avoir les états dans l'espace des phases et les structures classiques dans ce dernier. L'analyse de ce transport en fonction de $1/\hbar_{\text{eff}}$ (c'est-à-dire proportionnellement à l'action classique dans le système, voir section 1.4) est présentée sur la figure F.9. On y représente :

- la projection de l'état fondamental du réseau statique avec l'état de Floquet associé à l'îlot *ratchet* (une sorte de mesure de la centricité de cet état de Floquet, stroboscopiquement stationnaire comme le transport classique dont nous avons fait l'ingénierie en début de chapitre) (panneau (a)),
- le transport périodique de cet état de Floquet (panneau (b)),
- les représentations de Husimi de l'état fondamental du réseau statique et de l'état de Floquet *ratchet* pour les trois valeurs de \hbar_{eff} identifiées en sur les panneaux (a) et (b).

On observe une dépendance non-monotone de ces métriques de transport semi-classique en fonction de \hbar_{eff} . Cet effet est lié au phénomène de mélange d'états de Floquet (et notamment avec des états de Floquet localisés dans la mer chaotique) que nous présentons dans la section 4.2.2 et illustrons sur la figure 4.6, p 112.

Fort de ces analyse, nous procédons enfin à des expériences de transport de CBE dans le réseau optique dont nous corrélons les modulations d'amplitude et de phase afin de réaliser l'hamiltonien *ratchet* (Éq. (F.8)), ce dans un premier temps à partir de l'état fondamental du réseau statique. Ces expériences sont réalisées pour les deux valeurs de \hbar_{eff} correspondant aux panneaux (d) et (e) de la figure F.9, c'est-à-dire dans un cas idéal pour observer un transport *ratchet* semi-classique et dans un cas davantage défavorable à l'observation de ce transport contrôlé. Le cas favorable est présenté sur la figure F.10, où nous observons un très bon accord entre l'expérience et la simulation numérique des dynamiques à la fois quantique et classique (ce

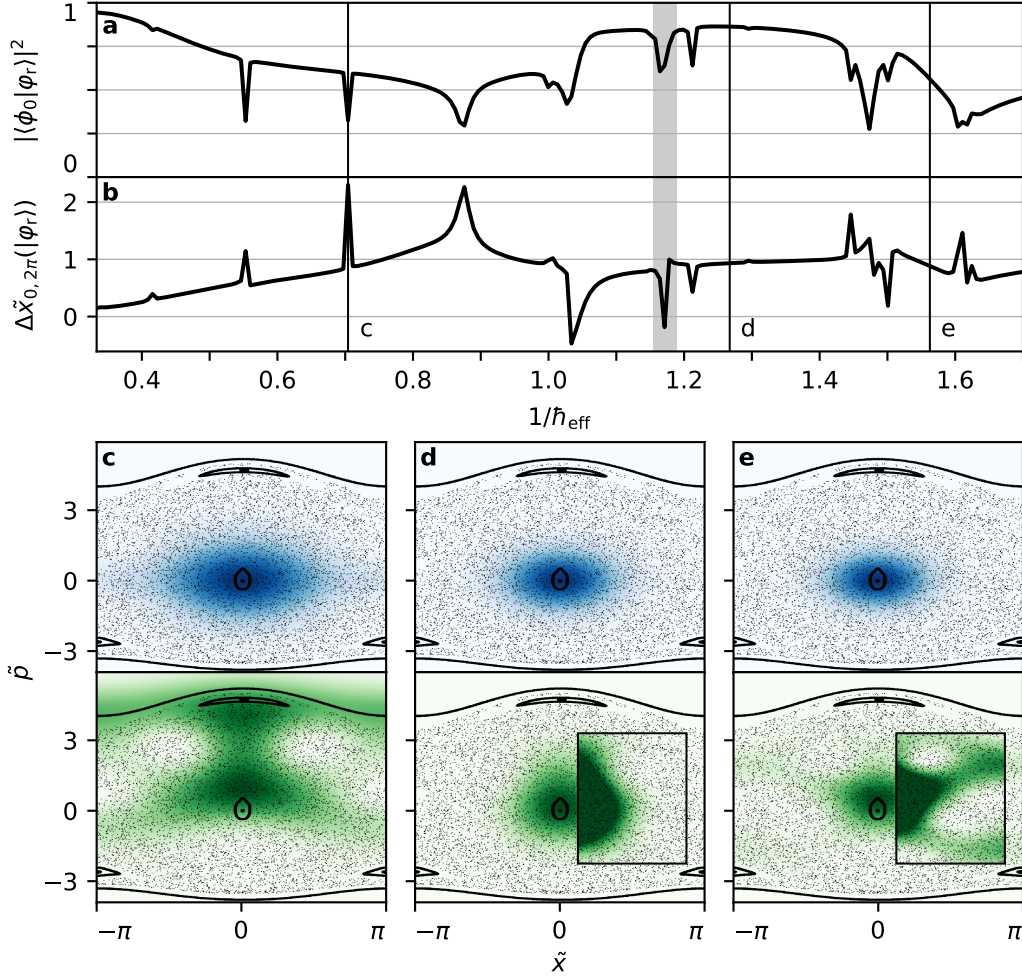


Figure F.9 | Influence de la constante de Planck effective sur le transport *ratchet*. (a) Projection entre l'état de Floquet $|\varphi_r\rangle$ associé à l'îlot *ratchet* et l'état fondamental du réseau static $|\phi_0\rangle$ en fonction de $1/\hbar_{\text{eff}}$. (b) Transport périodique $\Delta\tilde{x}_{0,2\pi}$ de $|\varphi_r\rangle$ sur une période de modulation (voir Éq. 4.22, p. 109) en fonction de $1/\hbar_{\text{eff}}$. (c-e) Représentations de Husimi de $|\phi_0\rangle$ (en haut, bleu) et de $|\varphi_r\rangle$ (en bas, vert) vis-à-vis du portrait de phase stroboscopique du système pour les valeurs de $1/\hbar_{\text{eff}}$ identifiées sur les panneaux (a,b). Les fonctions de Husimi dans les encadrés sont tronquées à un quart de leur valeur maximale afin de visualiser les détails. La zone grisée des panneaux (a,b) marque l'intervalle de $1/\hbar_{\text{eff}}$ sur lequel le phénomène de mélange d'états de Floquet est étudié (voir figure 4.6). Les grandeurs "tildées" adimensionnées sont obtenues à partir des grandeurs dimensionnées en suivant la procédure résumée p. 34.

qui s'explique par la semi-classicalité attendue pour le transport à cette valeur de \hbar_{eff}). La comparaison du transport pour les deux valeurs de \hbar_{eff} étudiées expérimentalement est présentée sur la figure 4.8, p. 116. Pour la valeur de \hbar_{eff} correspondant à la figure F.9(d), nous observons une évolution quasi-périodique de la distribution en impulsion. Pour la valeur de \hbar_{eff} correspondant à la figure F.9(e), nous mesurons une forte croissance aperiodique de la dispersion en impulsion, associée à une fuite vers la mer chaotique (comme suggéré par la représentation de Husimi de l'état Floquet *ratchet* illustré sur la figure F.9(e)).

Dans un second et dernier temps, nous appliquons notre protocole de contrôle optimal

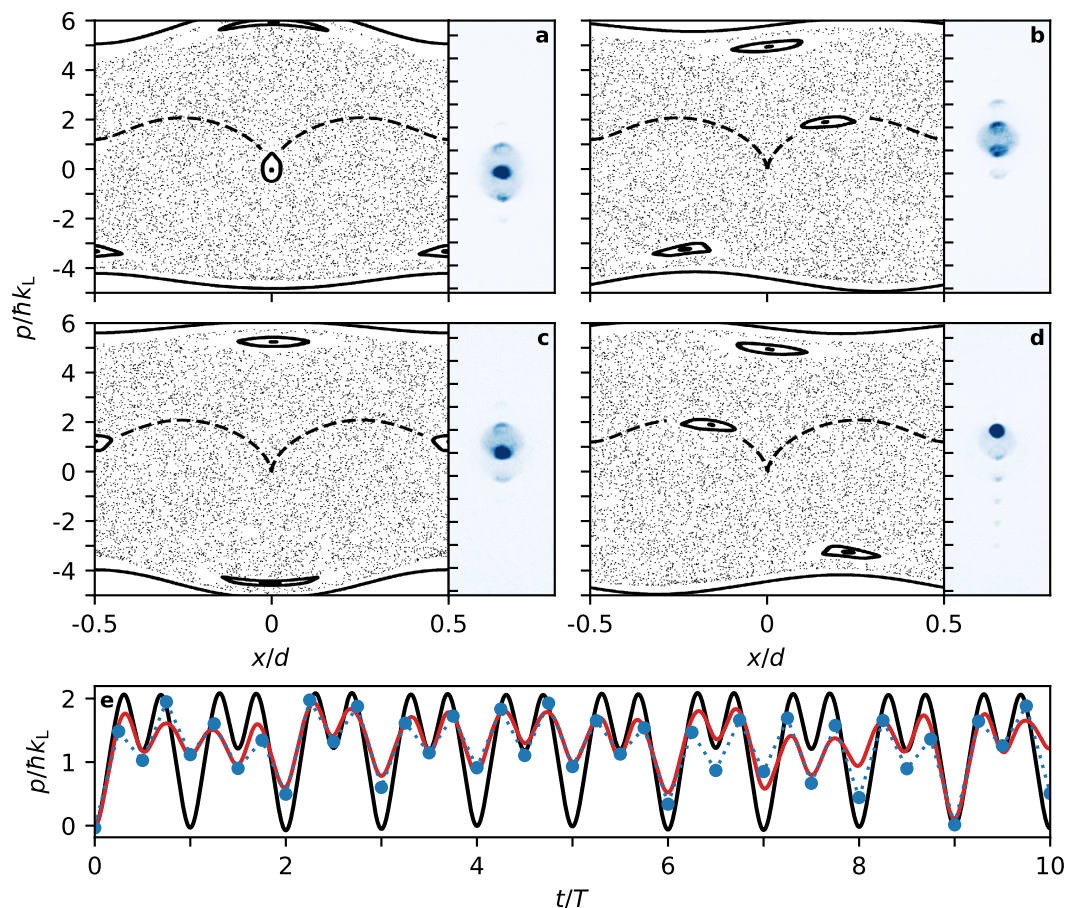


Figure F.10 | Transport *ratchet* semi-classique et non-diffusif à partir de l'état fondamental du réseau optique. (a-d) Portraits de phase stroboscopiques (à gauche) et images d'absorption expérimentales après temps de vol (à droite) pour les temps sous-stroboscopiques $\nu t = n + r$, avec $n \in \mathbb{N}$ et $r = 0, 0.25, 0.5$ et 0.75 pour les panneaux (a) à (d) respectivement. Les images expérimentales ont été prises lors de la première période de modulation $n = 0$. (e) Quantité de mouvement en fonction du temps, montrant la valeur moyenne de la distribution d'impulsion expérimentale (bleu) et numérique (rouge) ainsi que la quantité de mouvement de la trajectoire au centre de l'îlot ratchet (noir).

quantique mis en place dans le chapitre 3 afin d'optimiser le transport *ratchet*. Nous ciblons alors, avant l'application de la modulation, l'état de Floquet associé à l'îlot de transport (voir figure F.9(c-e)). Ces résultats sont présentés sur la figure 4.9, p. 117. Nous montrons comment le protocole de contrôle optimal quantique permet de restaurer la périodicité du transport *ratchet*, et ce, même dans le cas de fort couplage avec la mer chaotique (figure F.9(e)).

Publication en lien avec ce chapitre. L'étude présentée dans ce chapitre résulte d'un travail de recherche que je mène sur l'effet ratchet depuis mon stage de pré-thèse réalisé au LCAR en 2019. Une publication est en cours de préparation :

- [65] N. Dupont, L. Gabardos, F. Arrouas, B. Peaudecerf, J. Billy and D. Guéry-Odelin, *Matter wave transport from non-diffusive Hamiltonian ratchet effect*, In preparation, (2022)

Chapitre 5 : Émergence d'un ordre supercrystallin de pas accordable dans un système de Floquet-Bloch

La dernière étude que nous présentons dans ce manuscrit se place dans un régime dans lequel il n'est plus possible de négliger les interactions entre les atomes du CBE. Nous y démontrons comment, dans un réseau optique modulé sinusoïdalement en phase à une fréquence couplant la bande fondamentale à une bande excitée du système, les interactions interatomiques à courte-portée peuvent entraîner, sur de longs temps d'expérience, l'émergence d'un ordre supercrystallin de pas accordable via un processus de mélange à quatre ondes contrôlé. Cette travail s'inscrit dans l'étude des instabilités dynamiques dans un système de Floquet-Bloch [198, 199, 196, 201, 197].

Nous illustrons sur la figure F.11 le protocole typique pour les expériences présentées dans ce chapitre, ainsi que les observations qui en résultent. On commence par charger l'état fondamental du réseau optique en $q = 0$. Celui-ci est ensuite modulé en phase à une fréquence qui couple la bande fondamentale à une bande excitée (ici la bande 2 ou 3) en $q \neq 0$. Sur les premières dizaines de périodes de modulation, on observe inchangée, ou peu s'en faut, la distribution en impulsion de l'état fondamental du réseau statique (comme on peu s'y attendre étant donné que la modulation n'est pas résonante pour la bande fondamentale en $q = 0$, là où sont initialement chargés les atomes). Cependant après un certain temps d'expérience³, on observe la nucléation d'ordres de diffraction entre les ordres associés à l'état fondamental du réseau statique, à des valeurs d'impulsion $\hbar k^*$ qui ne sont pas des multiples entiers du quantum d'impulsion $\hbar k_L = h/d$ (de nouveaux ordres de diffractions qu'on qualifie de "décimaux"). Cette nouvelle périodicité plus fine dans l'espace réciproque (observée après temps de vol) suggère l'émergence d'une structuration avec un pas d^* supérieur à la périodicité d du réseau optique.

Pour comprendre ce phénomène, nous modélisons ce système à l'aide d'un système effectif à deux bandes couplées, fortement liées et avec interactions. Dans un formalisme de seconde quantification, ce système est régi par l'hamiltonien effectif $\hat{H}_{\text{eff}} = \hat{H}_0 + \hat{H}_{\text{int}}$, où

$$\begin{aligned} \hat{H}_0 = & -J_0 \sum_{j=0}^{L-1} \left(\hat{a}_{j+1}^\dagger \hat{a}_j + \hat{a}_j^\dagger \hat{a}_{j+1} \right) - J_1 \sum_{j=0}^{L-1} \left(\hat{b}_{j+1}^\dagger \hat{b}_j + \hat{b}_j^\dagger \hat{b}_{j+1} \right) \\ & + \Delta E_1 \sum_{j=0}^{L-1} \hat{b}_j^\dagger \hat{b}_j + iW \sum_{j=0}^{L-1} \left(\hat{b}_j^\dagger \hat{a}_j - \hat{a}_j^\dagger \hat{b}_j \right), \end{aligned} \quad (\text{F.10})$$

et

³De l'ordre de la milliseconde, là où la période de modulation du réseau optique est de l'ordre de la dizaine de microsecondes.

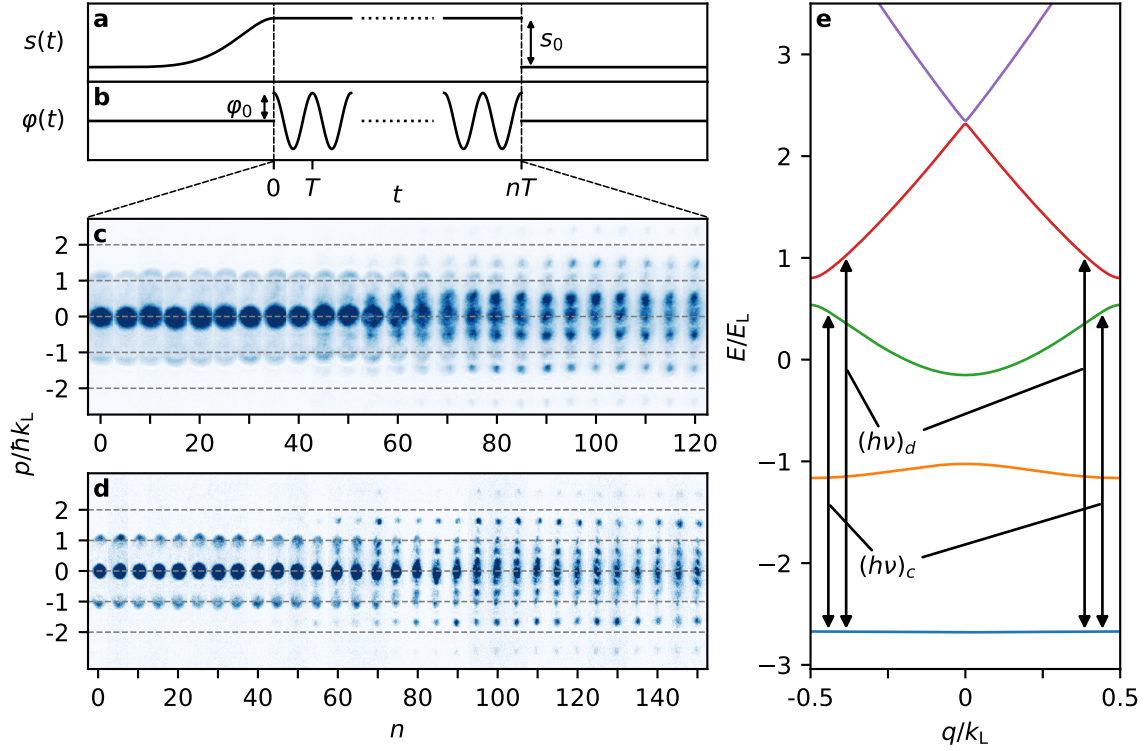


Figure F.11 | Protocole expérimental et observation typique de nucléation d'ordres décimaux. (a) Profondeur $s(t)$ et (b) phase $\varphi(t)$ du réseau optique au cours du temps, montrant le chargement adiabatique de l'état fondamental du réseau, la modulation de phase pour un nombre entier de périodes et l'extinction du réseau pour l'imagerie par temps de vol. (c,d) Concaténation d'images d'absorption expérimentales après temps de vol montrant l'évolution stroboscopique de la distribution en impulsion en fonction du nombre n de périodes de modulation T . Les paramètres expérimentaux sont donnés sur la figure 5.2, p. 127. (e) Structure de bande du réseau statique à la profondeur des expériences (lignes colorées) et principales transitions induites sur la bande fondamentale par les modulations des expériences (c) et (d) (flèches noires).

$$\hat{H}_{\text{int}} = \frac{U}{2} \sum_{j=0}^{L-1} \hat{a}_j^{\dagger 2} \hat{a}_j^2, \quad (\text{F.11})$$

avec L le nombre de sites peuplés du réseau, \hat{a}_j et \hat{b}_j les opérateurs de créations sur les deux bandes au site j , J_0 et J_1 les amplitudes tunnel des bandes, ΔE_1 un décalage d'énergie pour la bande modélisant le niveau excité, W l'amplitude de couplage entre les bandes et U le paramètre d'interaction sur site pour la bande initialement peuplée. Nous montrons dans un premier temps comment, les interactions mises de côté, l'hamiltonien \hat{H}_0 permet de modéliser les spectres de quasi-énergie des systèmes modulés à la manière des expériences de la figure F.11. Ce processus de modélisation est détaillé sur la figure 5.3, p. 130 (et peut être observé sur la figure F.12 ci-dessous).

Nous procédons ensuite à un traitement perturbatif des interactions à la manière de Bogoliubov [202, 90], que nous présentons en détail. Nous obtenons un jeu de quatre équations

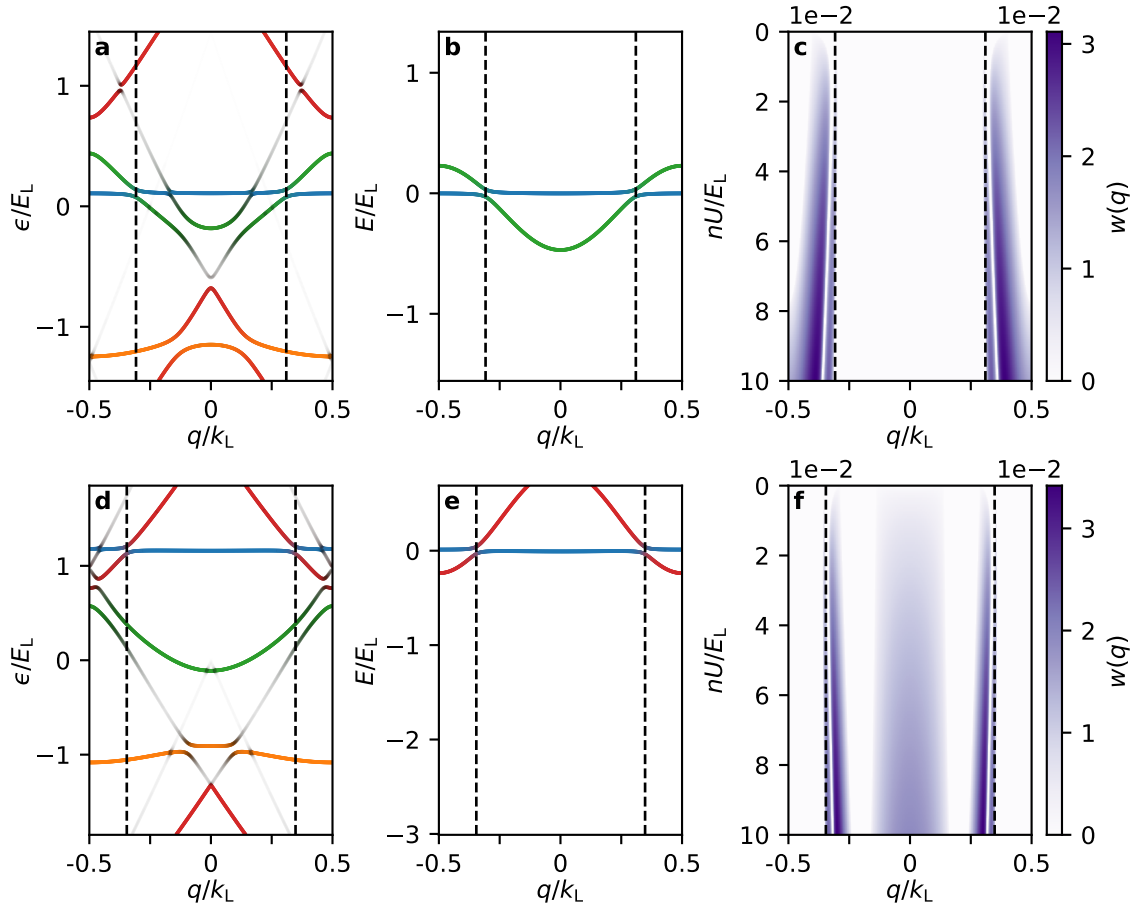


Figure F.12 | Résultats de l'étude de la stabilité du système pour des paramètres de modèle réalistes. (a,d) Spectres de quasi-énergie. (b,e) Spectres de l'hamiltonien H_0 , avec paramètres ajustés afin de reproduire le comportement des spectres (a,d) aux abords des croisements principaux de la bande associé à l'état fondamentale (bleu). (c,f) Paramètre d'instabilité $w(q)$ correspondant, tracé en fonction de q et du paramètre d'interaction nU (voir section 5.2.4, p. 137, avec n le nombre d'atomes par site du réseau, supposé ici ne pas dépendre de l'indice du site). Les lignes verticales noires tiretées marquent la position des croisements évités.

d'évolution d'Heisenberg couplées pour les perturbations le long de la zone de Brillouin. L'étude du spectre $\lambda_i(q)$ (avec $i = 1, 2, 3, 4$) de la matrice de couplage de ces équations différentielles d'ordre 1 nous permet de déterminer les régions de la zone de Brillouin où le système présente des instabilités dynamiques (via le paramètre $w(q) = \max_i \{ |\text{Im}\{\lambda_i(q)\}| \}$, voir résumé p. 136). Cette analyse renseigne sur les quasi-moments en lesquels on peut s'attendre à ce que se peuplent des modes dynamiquement instables. La figure F.12 présente le résultat de cette modélisation. On y observe le comportement général qui ressort de notre étude, à savoir que de fines régions d'instabilité sont localisées au voisinage des croisement évités dans les spectres de \hat{H}_0 (qui modélisent eux-mêmes les spectres de quasi-énergie du système réel).

Nous poursuivons avec une série de prédictions sur le comportement des pics de diffraction décimaux en fonction des paramètres du système (voir section 5.2.5, p. 138). Notamment, on s'attend à ce que la fréquence de modulation du potentiel, qui a pour principale conséquence de

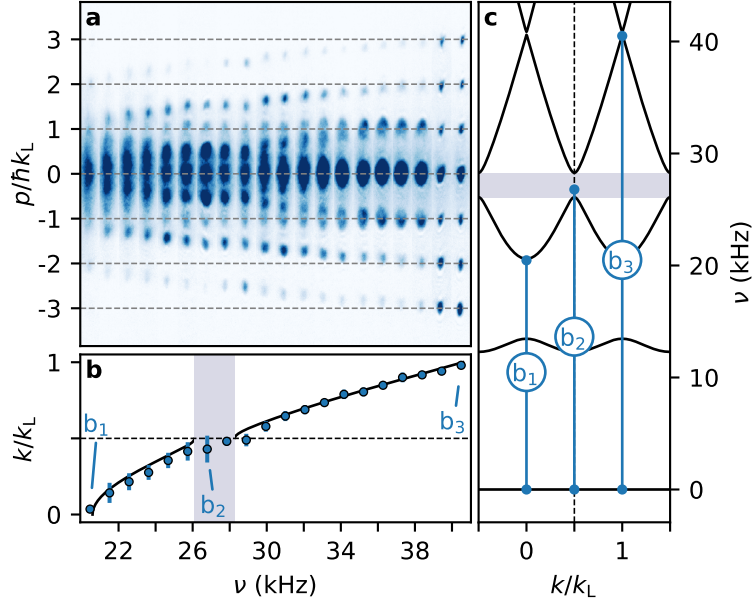


Figure F.13 | Déplacement de l'instabilité avec la fréquence de modulation. (a) Concaténation d'images d'absorption expérimentales (post temps de vol et moyennées sur 3 réalisations), après un nombre fixe de $n = 100$ périodes de modulation, en fonction de la fréquence de modulation ν . (b) Comparaison entre la position moyenne de l'instabilité (en terme du quasi-moment réduit k/k_L dans la structure de bande dépliée) extraite à partir d'un ajustement de la position des quatre ordres décimaux dans l'intervalle $1 \leq |p|/\hbar k_L \leq 3$ (points bleus, les barres d'erreur correspondant à un écart-type sur la statistique de 12 points) et le quasi-moment de résonance entre les bandes d'intérêt (ligne noire) en fonction de ν . (c) Diagramme de transition à partir de la bande fondamentale tracé sur les deux premières zones de Brillouin (lignes noires) et transitions adressées pour les données b_1 , b_2 et b_3 (bleu). Voir figure 5.7, p. 142, pour davantage de détails.

déplacer les croisements évités dans la zone de Brillouin (comme suggéré par le graphe F.11(e)), nous permette d'accorder la position des pics décimaux dans les figures de diffraction (voir figure 5.5, p. 139).

Nous présentons à une série d'expériences qui confirment ces prédictions (voir section 5.3), comme illustré sur la figure F.13 dans le cas énoncé ici du déplacement des motifs émergents en fonction de la fréquence de modulation du potentiel. Ces expériences confirment nos prédictions, et la justesse de notre modèle à deux bandes fortement liées avec interactions.

Pour conclure, nous discutons de la nature de l'état réalisé dans le système, et confrontons l'hypothèse de l'émergence d'un ordre *in-situ* de période d^* supérieur au pas d du réseau optique. Pour évaluer ces points, des simulations *Truncated-Wigner* [201] ont été réalisées par notre collaborateur Peter Schlagheck de l'Université de Liège. Ces simulations confirment l'émergence d'une structuration à longue portée dans le système, présentant une période $d^* \approx 2\pi/q^*$ (avec q^* le quasi-moment des instabilités). De façon inhérente aux simulations *Truncated-Wigner* (de par la considération *in fine* d'une moyenne sur de nombreuses trajectoires simulées), cette structuration est invisible sur la densité *in-situ*, mais peut être retrouvée en calculant une corrélation d'ordre deux (voir figure 5.12, p. 149). Ces simulations pointent aussi que la cohérence est

préservée dans les modes instables, comme suggéré en premier lieu expérimentalement par l'observation des pics décimaux sur les figures de diffraction.

Ce travail résulte d'une collaboration avec Peter Schlagheck de l'unité de recherche CESAM à l'Université de Liège. Une publication est en préparation :

- [66] N. Dupont, L. Gabardos, F. Arrouas, G. Chatelain, M. Arnal, J. Billy, P. Schlagheck, B. Peaudecerf, and D. Guéry-Odelin, *Emergence of a tunable supercrystalline order in a Floquet-Bloch system*, In preparation, (2022)

Bibliography

- [1] William D. Phillips. Nobel Lecture: Laser cooling and trapping of neutral atoms. *Rev. Mod. Phys.*, 70:721–741, Jul 1998.
- [2] Claude N. Cohen-Tannoudji. Nobel Lecture: Manipulating atoms with photons. *Rev. Mod. Phys.*, 70:707–719, Jul 1998.
- [3] Steven Chu. Nobel Lecture: The manipulation of neutral particles. *Rev. Mod. Phys.*, 70:685–706, Jul 1998.
- [4] A. Einstein. Quantentheorie des einatomigen idealen Gases. 1924.
- [5] A. Einstein. Quantentheorie des einatomigen idealen Gases, II. 1, 1925.
- [6] M. H. Anderson, J. R. Ensher, M. R. Matthews, C. E. Wieman, and E. A. Cornell. Observation of Bose-Einstein Condensation in a Dilute Atomic Vapor. *Science*, 269(5221):198–201, 1995.
- [7] K. B. Davis, M. O. Mewes, M. R. Andrews, N. J. van Druten, D. S. Durfee, D. M. Kurn, and W. Ketterle. Bose-Einstein Condensation in a Gas of Sodium Atoms. *Phys. Rev. Lett.*, 75:3969–3973, Nov 1995.
- [8] R. Grimm, M. Weidemüller, and Y. B. Ovchinnikov. Optical Dipole Traps for Neutral Atoms. volume 42 of *Advances In Atomic, Molecular, and Optical Physics*, pages 95–170. Academic Press, 2000.
- [9] Dan M. Stamper-Kurn and J.H. Thywissen. Chapter 1 - Experimental Methods of Ultracold Atomic Physics. In Kathryn Levin, Alexander L. Fetter, and Dan M. Stamper-Kurn, editors, *Ultracold Bosonic and Fermionic Gases*, volume 5 of *Contemporary Concepts of Condensed Matter Science*, pages 1–26. Elsevier, 2012.
- [10] Jérôme Beugnon, Charles Tuchendler, Harold Marion, Alpha Gaëtan, Yevhen Miroshnychenko, Yvan R. P. Sortais, Andrew M. Lance, Matthew P. A. Jones, Gaëtan Messin, Antoine Browaeys, and Philippe Grangier. Two-dimensional transport and transfer of a single atomic qubit in optical tweezers. *Nature Physics*, 3(10):696–699, Oct 2007.
- [11] T. Grunzweig, A. Hilliard, M. McGovern, and M. F. Andersen. Near-deterministic preparation of a single atom in an optical microtrap. *Nature Physics*, 6(12):951–954, Dec 2010.
- [12] Markus Greiner and Simon Fölling. Optical lattices. *Nature*, 453(7196):736–738, Jun 2008.
- [13] S. Bergamini, B. Darquie, M. Jones, L. Jacubowicz, A. Browaeys, and P. Grangier. Holographic generation of micro-trap arrays for single atoms. In *International Quantum Electronics Conference, 2004. (IQEC)*, pages 1132–1133, 2004.
- [14] F. Nogrette, H. Labuhn, S. Ravets, D. Barredo, L. Béguin, A. Vernier, T. Lahaye, and A. Browaeys. Single-Atom Trapping in Holographic 2D Arrays of Microtraps with Arbitrary Geometries. *Phys. Rev. X*, 4:021034, May 2014.

- [15] N. Goldman and J. Dalibard. Periodically Driven Quantum Systems: Effective Hamiltonians and Engineered Gauge Fields. *Phys. Rev. X*, 4:031027, Aug 2014.
- [16] André Eckardt. Colloquium: Atomic quantum gases in periodically driven optical lattices. *Rev. Mod. Phys.*, 89:011004, Mar 2017.
- [17] Y.-J. Lin, R. L. Compton, K. Jiménez-García, J. V. Porto, and I. B. Spielman. Synthetic magnetic fields for ultracold neutral atoms. *Nature*, 462(7273):628–632, Dec 2009.
- [18] Jean Dalibard, Fabrice Gerbier, Gediminas Juzeliūnas, and Patrik Öhberg. Colloquium: Artificial gauge potentials for neutral atoms. *Rev. Mod. Phys.*, 83:1523–1543, Nov 2011.
- [19] Cheng Chin, Rudolf Grimm, Paul Julienne, and Eite Tiesinga. Feshbach resonances in ultracold gases. *Rev. Mod. Phys.*, 82:1225–1286, Apr 2010.
- [20] T Lahaye, C Menotti, L Santos, M Lewenstein, and T Pfau. The physics of dipolar bosonic quantum gases. *Reports on Progress in Physics*, 72(12):126401, nov 2009.
- [21] Mingwu Lu, Nathaniel Q. Burdick, Seo Ho Youn, and Benjamin L. Lev. Strongly Dipolar Bose-Einstein Condensate of Dysprosium. *Phys. Rev. Lett.*, 107:190401, Oct 2011.
- [22] K. Aikawa, A. Frisch, M. Mark, S. Baier, A. Rietzler, R. Grimm, and F. Ferlaino. Bose-einstein condensation of erbium. *Phys. Rev. Lett.*, 108:210401, May 2012.
- [23] Antoine Browaeys, Daniel Barredo, and Thierry Lahaye. Experimental investigations of dipole–dipole interactions between a few Rydberg atoms. *Journal of Physics B: Atomic, Molecular and Optical Physics*, 49(15):152001, jun 2016.
- [24] Hannes Bernien, Sylvain Schwartz, Alexander Keesling, Harry Levine, Ahmed Omran, Hannes Pichler, Soonwon Choi, Alexander S. Zibrov, Manuel Endres, Markus Greiner, Vladan Vuletić, and Mikhail D. Lukin. Probing many-body dynamics on a 51-atom quantum simulator. *Nature*, 551(7682):579–584, Nov 2017.
- [25] Antoine Browaeys and Thierry Lahaye. Many-body physics with individually controlled Rydberg atoms. *Nature Physics*, 16(2):132–142, Feb 2020.
- [26] J. Ignacio Cirac and Peter Zoller. Goals and opportunities in quantum simulation. *Nature Physics*, 8(4):264–266, Apr 2012.
- [27] Ehud Altman, Kenneth R. Brown, Giuseppe Carleo, Lincoln D. Carr, Eugene Demler, Cheng Chin, Brian DeMarco, Sophia E. Economou, Mark A. Eriksson, Kai-Mei C. Fu, Markus Greiner, Kaden R.A. Hazzard, Randall G. Hulet, Alicia J. Kollár, Benjamin L. Lev, Mikhail D. Lukin, Ruichao Ma, Xiao Mi, Shashank Misra, Christopher Monroe, Kater Murch, Zaira Nazario, Kang-Kuen Ni, Andrew C. Potter, Pedram Roushan, Mark Saffman, Monika Schleier-Smith, Irfan Siddiqi, Raymond Simmonds, Meenakshi Singh, I.B. Spielman, Kristan Temme, David S. Weiss, Jelena Vučković, Vladan Vuletić, Jun Ye, and Martin Zwierlein. Quantum Simulators: Architectures and Opportunities. *PRX Quantum*, 2:017003, Feb 2021.
- [28] Richard P. Feynman. Simulating physics with computers. *International Journal of Theoretical Physics*, 21(6):467–488, Jun 1982.
- [29] John Clarke and Frank K. Wilhelm. Superconducting quantum bits. *Nature*, 453(7198):1031–1042, Jun 2008.
- [30] Alán Aspuru-Guzik and Philip Walther. Photonic quantum simulators. *Nature Physics*, 8(4):285–291, Apr 2012.

- [31] R. Blatt and C. F. Roos. Quantum simulations with trapped ions. *Nature Physics*, 8(4):277–284, Apr 2012.
- [32] Maciej Lewenstein, Anna Sanpera, Veronica Ahufinger, Bogdan Damski, Aditi Sen(De), and Ujjwal Sen. Ultracold atomic gases in optical lattices: mimicking condensed matter physics and beyond. *Advances in Physics*, 56(2):243–379, 2007.
- [33] Immanuel Bloch, Jean Dalibard, and Sylvain Nascimbène. Quantum simulations with ultracold quantum gases. *Nature Physics*, 8(4):267–276, Apr 2012.
- [34] Immanuel Bloch. Quantum simulations come of age. *Nature Physics*, 14(12):1159–1161, Dec 2018.
- [35] M. Greiner, O. Mandel, T. Esslinger, T. W. Hänsch, and I. Bloch. Quantum phase transition from a superfluid to a Mott insulator in a gas of ultracold atoms. *Nature*, 415(6867):39–44, Jan 2002.
- [36] Juliette Billy, Vincent Josse, Zhanchun Zuo, Alain Bernard, Ben Hambrecht, Pierre Lugan, David Clément, Laurent Sanchez-Palencia, Philippe Bouyer, and Alain Aspect. Direct observation of Anderson localization of matter waves in a controlled disorder. *Nature*, 453(7197):891–894, Jun 2008.
- [37] Giacomo Roati, Chiara D’Errico, Leonardo Fallani, Marco Fattori, Chiara Fort, Matteo Zaccanti, Giovanni Modugno, Michele Modugno, and Massimo Inguscio. Anderson localization of a non-interacting Bose–Einstein condensate. *Nature*, 453(7197):895–898, Jun 2008.
- [38] Isam Manai, Jean-Fran çois Clément, Radu Chicireanu, Clément Hainaut, Jean Claude Garreau, Pascal Szriftgiser, and Dominique Delande. Experimental Observation of Two-Dimensional Anderson Localization with the Atomic Kicked Rotor. *Phys. Rev. Lett.*, 115:240603, Dec 2015.
- [39] Donald H. White, Thomas A. Haase, Dylan J. Brown, Maarten D. Hoogerland, Mojdeh S. Najafabadi, John L. Helm, Christopher Gies, Daniel Schumayer, and David A. W. Hutchinson. Observation of two-dimensional Anderson localisation of ultracold atoms. *Nature Communications*, 11(1):4942, Oct 2020.
- [40] Julien Chabé, Gabriel Lemarié, Benoît Grémaud, Dominique Delande, Pascal Szriftgiser, and Jean Claude Garreau. Experimental Observation of the Anderson Metal-Insulator Transition with Atomic Matter Waves. *Phys. Rev. Lett.*, 101:255702, Dec 2008.
- [41] F. Jendrzejewski, A. Bernard, K. Müller, P. Cheinet, V. Josse, M. Piraud, L. Pezzé, L. Sanchez-Palencia, A. Aspect, and P. Bouyer. Three-dimensional localization of ultracold atoms in an optical disordered potential. *Nature Physics*, 8(5):398–403, May 2012.
- [42] G. Semeghini, M. Landini, P. Castilho, S. Roy, G. Spagnolli, A. Trenkwalder, M. Fattori, M. Inguscio, and G. Modugno. Measurement of the mobility edge for 3D Anderson localization. *Nature Physics*, 11(7):554–559, Jul 2015.
- [43] Zoran Hadzibabic, Peter Krüger, Marc Cheneau, Baptiste Battelier, and Jean Dalibard. Berezinskii–kosterlitz–thouless crossover in a trapped atomic gas. *Nature*, 441(7097):1118–1121, Jun 2006.
- [44] P. Cladé, C. Ryu, A. Ramanathan, K. Helmerson, and W. D. Phillips. Observation of a 2d bose gas: From thermal to quasicondensate to superfluid. *Phys. Rev. Lett.*, 102:170401, Apr 2009.
- [45] Vittorio Giovannetti, Seth Lloyd, and Lorenzo Maccone. Quantum-Enhanced Measurements: Beating the Standard Quantum Limit. *Science*, 306(5700):1330–1336, 2004.

- [46] Vittorio Giovannetti, Seth Lloyd, and Lorenzo Maccone. Advances in quantum metrology. *Nature Photonics*, 5(4):222–229, Apr 2011.
- [47] E. S. Polzik, J. Carri, and H. J. Kimble. Spectroscopy with squeezed light. *Phys. Rev. Lett.*, 68:3020–3023, May 1992.
- [48] M. Tse, Haocun Yu, N. Kijbunchoo, A. Fernandez-Galiana, P. Dupej, L. Barsotti, C. D. Blair, D. D. Brown, S. E. Dwyer, A. Effler, M. Evans, P. Fritschel, V. V. Frolov, A. C. Green, G. L. Mansell, et al. Quantum-Enhanced Advanced LIGO Detectors in the Era of Gravitational-Wave Astronomy. *Phys. Rev. Lett.*, 123:231107, Dec 2019.
- [49] F. Acernese, M. Agathos, L. Aiello, A. Allocca, A. Amato, S. Ansoldi, S. Antier, M. Arène, N. Arnaud, S. Ascenzi, P. Astone, F. Aubin, S. Babak, P. Bacon, F. Badaracco, et al. Increasing the Astrophysical Reach of the Advanced Virgo Detector via the Application of Squeezed Vacuum States of Light. *Phys. Rev. Lett.*, 123:231108, Dec 2019.
- [50] Masahiro Kitagawa and Masahito Ueda. Squeezed spin states. *Phys. Rev. A*, 47:5138–5143, Jun 1993.
- [51] D.J. Wineland, J.J. Bollinger, W.M. Itano, and D.J. Heinzen. Squeezed atomic states and projection noise in spectroscopy. *Phys. Rev. A*, 50:67–88, Jul 1994.
- [52] J. Estève, C. Gross, A. Weller, S. Giovanazzi, and M.K. Oberthaler. Squeezing and entanglement in a Bose-Einstein condensate. *Nature*, 455(7217):1216–1219, Oct 2008.
- [53] B. Lücke, M. Scherer, J. Kruse, L. Pezzé, F. Deuretzbacher, P. Hyllus, O. Topic, J. Peise, W. Ertmer, J. Arlt, L. Santos, A. Smerzi, and C. Klempt. Twin Matter Waves for Interferometry Beyond the Classical Limit. *Science*, 334(6057):773–776, Oct 2011.
- [54] Tim Kovachy, Jason M. Hogan, Alex Sugarbaker, Susannah M. Dickerson, Christine A. Donnelly, Chris Overstreet, and Mark A. Kasevich. Matter Wave Lensing to Picokelvin Temperatures. *Phys. Rev. Lett.*, 114:143004, Apr 2015.
- [55] Alice Sinatra. Spin-squeezed states for metrology. *Appl. Phys. Lett.*, 120(12):120501, Mar 2022.
- [56] Seth Lloyd. Coherent quantum feedback. *Phys. Rev. A*, 62:022108, Jul 2000.
- [57] D. Guéry-Odelin, A. Ruschhaupt, A. Kiely, E. Torrontegui, S. Martínez-Garaot, and J. G. Muga. Shortcuts to adiabaticity: Concepts, methods, and applications. *Rev. Mod. Phys.*, 91:045001, Oct 2019.
- [58] P. B. Wigley, P. J. Everitt, A. van den Hengel, J. W. Bastian, M. A. Sooriyabandara, G. D. McDonald, K. S. Hardman, C. D. Quinlivan, P. Manju, C. C. N. Kuhn, I. R. Petersen, A. N. Luiten, J. J. Hope, N. P. Robins, and M. R. Hush. Fast machine-learning online optimization of ultra-cold-atom experiments. *Scientific Reports*, 6(1):25890, May 2016.
- [59] P. B. Wigley, P. J. Everitt, A. van den Hengel, J. W. Bastian, M. A. Sooriyabandara, G. D. McDonald, K. S. T. Y.-. J. O. U. R. Hardman, Steffen J. Glaser, Ugo Boscain, Tommaso Calarco, Christiane P. Koch, Walter Köckenberger, Ronnie Kosloff, Ilya Kuprov, Burkhard Luy, Sophie Schirmer, Thomas Schulte-Herbrüggen, Dominique Sugny, and Frank K. Wilhelm. Training Schrödinger’s cat: quantum optimal control. *The European Physical Journal D*, 69(12):279, Dec 2015.

- [60] Christiane P. Koch, Ugo Boscain, Tommaso Calarco, Gunther Dirr, Stefan Filipp, Steffen J. Glaser, Ronnie Kosloff, Simone Montangero, Thomas Schulte-Herbrüggen, Dominique Sugny, and Frank K. Wilhelm. Quantum optimal control in quantum technologies. Strategic report on current status, visions and goals for research in Europe. *EPJ Quantum Technology*, 9(1):19, Jul 2022.
- [61] M. Arnal, G. Chatelain, M. Martinez, N. Dupont, O. Giraud, D. Ullmo, B. Georgeot, G. Lemarié, J. Billy, and D. Guéry-Odelin. Chaos-assisted tunneling resonances in a synthetic Floquet superlattice. *Science Advances*, 6(38):eabc4886, 2020.
- [62] G Chatelain, N Dupont, M Arnal, V Brunaud, J Billy, B Peaudecerf, P Schlagheck, and D Guéry-Odelin. Observation and control of quantized scattering halos. *New Journal of Physics*, 22(12):123032, dec 2020.
- [63] N. Dupont, G. Chatelain, L. Gabardos, M. Arnal, J. Billy, B. Peaudecerf, D. Sugny, and D. Guéry-Odelin. Quantum State Control of a Bose-Einstein Condensate in an Optical Lattice. *PRX Quantum*, 2:040303, Oct 2021.
- [64] N. Dupont, F. Arrouas, L. Gabardos, N. Ombredane, J. Billy, B. Peaudecerf, D. Sugny, and D. Guéry-Odelin. Phase-space distributions of Bose-Einstein condensates in an optical lattice: Optimal shaping and reconstruction, 2022.
- [65] N. Dupont, L. Gabardos, F. Arrouas, B. Peaudecerf, J. Billy, and D. Guéry-Odelin. Matter wave transport from non-diffusive Hamiltonian ratchet effect. In preparation, 2022.
- [66] N. Dupont, L. Gabardos, F. Arrouas, G. Chatelain, M. Arnal, J. Billy, P. Schlagheck, B. Peaudecerf, and D. Guéry-Odelin. Emergence of a tunable supercrystalline order in a Floquet-Bloch system. In preparation, 2022.
- [67] Maxime Arnal. *Gaz quantique dans un potentiel périodique dépendant du temps : de la modulation perturbative aux résonances de l'effet tunnel assisté par le chaos*. PhD thesis, Université Toulouse III - Paul Sabatier, 2020.
- [68] Gabriel Chatelain. *Façonnage d'ondes de matière dans un réseau optique dépendant du temps : du chaos quantique au contrôle quantique*. PhD thesis, Université Toulouse III - Paul Sabatier, 2021.
- [69] Maxime Martinez. *L'effet tunnel assisté par le chaos comme nouvel outil pour la simulation quantique*. PhD thesis, Université Toulouse III - Paul Sabatier, 2021.
- [70] E. Ott. *Chaos in Dynamical Systems*. Cambridge University Press, 1993.
- [71] L. Reichl. *The Transition to Chaos*. Springer Cham, 3rd edition, 2021.
- [72] A. N. Kolmogorov. On conservation of conditionally periodic motions for a small change in Hamilton's function. *Doklady Akademii Nauk SSSR*, 98, 1954.
- [73] V. I. Arnold. Proof of a theorem of A. N. Kolmogorov on the preservation of conditionally periodic motions under a small perturbation of the Hamiltonian. *Russian Mathematical Surveys*, 18(5):9–36, 1963.
- [74] J. Moser. On invariant curves of area-preserving mappings of an annulus. *Nachr. Akad. Wiss. Göttingen Math.-Phys. Kl.*, 2:1–20, 1962.
- [75] R. Dubertrand, J. Billy, D. Guéry-Odelin, B. Georgeot, and G. Lemarié. Routes towards the experimental observation of the large fluctuations due to chaos-assisted tunneling effects with cold atoms. *Phys. Rev. A*, 94:043621, Oct 2016.

- [76] Holger Schanz, Marc-Felix Otto, Roland Ketzmerick, and Thomas Dittrich. Classical and Quantum Hamiltonian Ratchets. *Phys. Rev. Lett.*, 87:070601, 2001.
- [77] F. Bloch. Über die Quantenmechanik der Elektronen in Kristallgittern. *Zeitschrift für Physik*, 52(7):555–600, 1929.
- [78] N. W. Ashcroft and N. D. Mermin. *Solid State Physics*. Holt, Rinehart and Winston, 1976.
- [79] J. Dalibard. Des cages de lumière pour les atomes : la physique des pièges et des réseaux optiques, 2013.
- [80] G. Floquet. Sur les équations différentielles linéaires à coefficients périodiques. *Annales scientifiques de l'École Normale Supérieure*, 12, 1883.
- [81] E. Wigner. On the Quantum Correction For Thermodynamic Equilibrium. *Phys. Rev.*, 40:749–759, 1932.
- [82] R.L. Hudson. When is the Wigner quasi-probability density non-negative? *Reports on Mathematical Physics*, 6(2):249–252, 1974.
- [83] M. Hinarejos, A. Pérez, and M. C. Bañuls. Wigner function for a particle in an infinite lattice. *New Journal of Physics*, 14(10):103009, 2012.
- [84] K. Husimi. Some Formal Properties of the Density Matrix. *Proceedings of the Physico-Mathematical Society of Japan. 3rd Series*, 22(4):264–314, 1940.
- [85] B Bahr and H J Korsch. Quantum mechanics on a circle: Husimi phase-space distributions and semiclassical coherent state propagators. *Journal of Physics A: Mathematical and Theoretical*, 40(14):3959–3985, 2007.
- [86] M V Berry and M Robnik. Semiclassical level spacings when regular and chaotic orbits coexist. *Journal of Physics A: Mathematical and General*, 17(12):2413–2421, 1984.
- [87] O. Bohigas, S. Tomsovic, and D. Ullmo. Manifestations of classical phase space structures in quantum mechanics. *Physics Reports*, 223(2):43–133, 1993.
- [88] Steven Tomsovic and Denis Ullmo. Chaos-assisted tunneling. *Phys. Rev. E*, 50:145–162, Jul 1994.
- [89] S. Keshavamurthy and P. Schlagheck. *Dynamical tunneling: theory and experiment*. CRC Press, 2011.
- [90] C. Cohen-Tannoudji and D. Guéry-Odelin. *Advances in atomic physics*. World Scientific, 2011.
- [91] L. Pitaevskii and S. Stringari. *Bose-Einstein Condensation and Superfluidity*. Oxford University Press, 2016.
- [92] Ž. Gosar. Every cold atom. <https://everycoldatom.com/>.
- [93] Gabriel Condon. *Condensation de Bose-Einstein: des potentiels périodiques d'extension finie aux manipulations dans l'espace des phases*. PhD thesis, Université Toulouse III - Paul Sabatier, 2015.
- [94] Aéla Fortun. *Dynamique hors équilibre d'un condensat de Bose-Einstein dans un réseau dépendant du temps*. PhD thesis, Université Toulouse III - Paul Sabatier, 2016.
- [95] Harald F. Hess. Evaporative cooling of magnetically trapped and compressed spin-polarized hydrogen. *Phys. Rev. B*, 34:3476–3479, Sep 1986.

- [96] K. B. Davis, M.-O. Mewes, and W. Ketterle. An analytical model for evaporative cooling of atoms. *Applied Physics B*, 60(2):155–159, 1995.
- [97] J. Dalibard. Les interactions entre particules dans les gaz quantiques, 2020.
- [98] Ch. Buggle, J. Léonard, W. von Klitzing, and J. T. M. Walraven. Interferometric Determination of the s and d -Wave Scattering Amplitudes in ^{87}Rb . *Phys. Rev. Lett.*, 93:173202, Oct 2004.
- [99] D. A. Steck. Rubidium 87 D Line Data. <https://steck.us/alkalidata/rubidium87numbers.pdf>.
- [100] J. Dalibard. Une brève histoire des atomes froids, 2015.
- [101] W. Ketterle, K. B. Davis, M. A. Joffe, A. Martin, and D. E. Pritchard. High densities of cold atoms in a dark spontaneous-force optical trap. *Phys. Rev. Lett.*, 70:2253–2256, 1993.
- [102] J. Dalibard and C. Cohen-Tannoudji. Laser cooling below the Doppler limit by polarization gradients: simple theoretical models. *Journal of the Optical Society of America B*, 6:2023–2045, 1989.
- [103] T W Hijmans, O J Luiten, I D Setija, and J T.M. Walraven. Optical cooling of atomic hydrogen in a magnetic trap. *Journal of the Optical Society of America B: Optical Physics; (USA)*.
- [104] Gael Reinaudi. *Manipulation et refroidissement par évaporation forcée d'ensembles atomiques ultra-froids pour la production d'un jet intense dans le régime de dégénérescence quantique : vers l'obtention d'un "laser à atomes continu"*. PhD thesis, Université Pierre et Marie Curie - Paris VI, 2008.
- [105] Antoine Couvert. *Production et étude de lasers à atomes guidés, et de leur interaction avec des défauts contrôlés*. PhD thesis, Université Pierre et Marie Curie - Paris VI, 2009.
- [106] J Hecker Denschlag, J E Simsarian, H Häffner, C McKenzie, A Browaeys, D Cho, K Helmerson, S L Rolston, and W D Phillips. A bose-einstein condensate in an optical lattice. *Journal of Physics B: Atomic, Molecular and Optical Physics*, 35(14):3095–3110, 2002.
- [107] M. Greiner, I. Bloch, O. Mandel, T. W. Hänsch, and T. Esslinger. Exploring Phase Coherence in a 2D Lattice of Bose-Einstein Condensates. *Phys. Rev. Lett.*, 87:160405, Oct 2001.
- [108] Phillip L. Gould, George A. Ruff, and David E. Pritchard. Diffraction of atoms by light: The near-resonant Kapitza-Dirac effect. *Phys. Rev. Lett.*, 56:827–830, Feb 1986.
- [109] Yu. B. Ovchinnikov, J. H. Müller, M. R. Doery, E. J. D. Vredenburg, K. Helmerson, S. L. Rolston, and W. D. Phillips. Diffraction of a Released Bose-Einstein Condensate by a Pulsed Standing Light Wave. *Phys. Rev. Lett.*, 83:284–287, Jul 1999.
- [110] M. K. Oberthaler, R. M. Godun, M. B. d'Arcy, G. S. Summy, and K. Burnett. Observation of Quantum Accelerator Modes. *Phys. Rev. Lett.*, 83:4447–4451, 1999.
- [111] F. L. Moore, J. C. Robinson, C. F. Bharucha, Bala Sundaram, and M. G. Raizen. Atom Optics Realization of the Quantum δ -Kicked Rotor. *Phys. Rev. Lett.*, 75:4598–4601, Dec 1995.
- [112] A. Fortun, C. Cabrera-Gutiérrez, G. Condon, E. Michon, J. Billy, and D. Guéry-Odelin. Direct Tunneling Delay Time Measurement in an Optical Lattice. *Phys. Rev. Lett.*, 117:010401, Jun 2016.
- [113] C. Cabrera-Gutiérrez, E. Michon, V. Brunaud, T. Kawalec, A. Fortun, M. Arnal, J. Billy, and D. Guéry-Odelin. Robust calibration of an optical-lattice depth based on a phase shift. *Phys. Rev. A*, 97:043617, Apr 2018.

- [114] M. Köhl, H. Moritz, T. Stöferle, K. Günter, and T. Esslinger. Fermionic Atoms in a Three Dimensional Optical Lattice: Observing Fermi Surfaces, Dynamics, and Interactions. *Phys. Rev. Lett.*, 94:080403, Mar 2005.
- [115] Eric Michon. *Dynamique de condensats de Bose Einstein dans un réseau optique modulé en phase ou en amplitude*. PhD thesis, Université Toulouse III - Paul Sabatier, 2018.
- [116] Malcolm H. Levitt. Composite pulses. *Progress in Nuclear Magnetic Resonance Spectroscopy*, 18(2):61–122, 1986.
- [117] Genko T. Genov, Daniel Schraft, Thomas Halfmann, and Nikolay V. Vitanov. Correction of arbitrary field errors in population inversion of quantum systems by universal composite pulses. *Phys. Rev. Lett.*, 113:043001, Jul 2014.
- [118] H. J. Sussmann and J. C. Willems. 300 Years of Optimal Control: From The Brachystochrone to the Maximum Principle. *IEEE Control Systems Magazine*, pages 32–44, 1997.
- [119] L. S. Pontryagin. *Mathematical Theory of Optimal Processes*. CRC Press, 1987.
- [120] Richard Bellman. Dynamic Programming. *Science*, 153(3731):34–37, 1966.
- [121] Revaz V. Gamkrelidze. *Discovery of the Maximum Principle in Optimal Control*, pages 160–173. Birkhäuser Basel, Basel, 2003.
- [122] I. Michael Ross and Mark Karpenko. A review of pseudospectral optimal control: From theory to flight. *Annual Reviews in Control*, 36(2):182–197, 2012.
- [123] M. Hassan and H. Sirisena. Optimal control of queues in computer networks. In *ICC 2001. IEEE International Conference on Communications. Conference Record (Cat. No.01CH37240)*, volume 2, pages 637–641, 2001.
- [124] S. P. Sethi. *Optimal Control Theory - Applications to Management, Science and Economics*. Springer Charm, 2019.
- [125] Jesse A. Sharp, Kevin Burrage, and Matthew J. Simpson. Implementation and acceleration of optimal control for systems biology. *Journal of The Royal Society Interface*, 18(181):20210241, 2021.
- [126] U. Boscain, M. Sigalotti, and D. Sugny. Introduction to the Pontryagin Maximum Principle for Quantum Optimal Control. *PRX Quantum*, 2:030203, Sep 2021.
- [127] Jack Saywell, Max Carey, Mohammad Belal, Ilya Kuprov, and Tim Freegarde. Optimal control of Raman pulse sequences for atom interferometry. *Journal of Physics B: Atomic, Molecular and Optical Physics*, 53(8):085006, mar 2020.
- [128] S. van Frank, A. Negretti, T. Berrada, R. Bücker, S. Montangero, J.-F. Schaff, T. Schumm, T. Calarco, and J. Schmiedmayer. Interferometry with non-classical motional states of a Bose-Einstein condensate. *Nature Communications*, 5(1):4009, May 2014.
- [129] C. A. Weidner and Dana Z. Anderson. Experimental Demonstration of Shaken-Lattice Interferometry. *Phys. Rev. Lett.*, 120:263201, Jun 2018.
- [130] Xiaoji Zhou, Shengjie Jin, and Jörg Schmiedmayer. Shortcut loading a Bose-Einstein condensate into an optical lattice. *New Journal of Physics*, 20(5):055005, may 2018.

- [131] S. van Frank, M. Bonneau, J. Schmiedmayer, S. Hild, C. Gross, M. Cheneau, I. Bloch, T. Pichler, A. Negretti, T. Calarco, and S. Montangero. Optimal control of complex atomic quantum systems. *Scientific Reports*, 6(1):34187, Oct 2016.
- [132] Anirudh Acharya, Theodore Kypraios, and Mădălin Guță. A comparative study of estimation methods in quantum tomography. *Journal of Physics A: Mathematical and Theoretical*, 52(23):234001, may 2019.
- [133] D. Leibfried, D. M. Meekhof, B. E. King, C. Monroe, W. M. Itano, and D. J. Wineland. Experimental Determination of the Motional Quantum State of a Trapped Atom. *Phys. Rev. Lett.*, 77:4281–4285, Nov 1996.
- [134] C. Flühmann and J. P. Home. Direct Characteristic-Function Tomography of Quantum States of the Trapped-Ion Motional Oscillator. *Phys. Rev. Lett.*, 125:043602, Jul 2020.
- [135] Falk-Richard Winkelmann, Carrie A Weidner, Gautam Ramola, Wolfgang Alt, Dieter Meschede, and Andrea Alberti. Direct measurement of the Wigner function of atoms in an optical trap. *Journal of Physics B: Atomic, Molecular and Optical Physics*, 55(19):194004, sep 2022.
- [136] Christian Kokail, Rick van Bijnen, Andreas Elben, Benoît Vermersch, and Peter Zoller. Entanglement Hamiltonian tomography in quantum simulation. *Nature Physics*, 17(8):936–942, Aug 2021.
- [137] Giacomo Torlai, Guglielmo Mazzola, Juan Carrasquilla, Matthias Troyer, Roger Melko, and Giuseppe Carleo. Neural-network quantum state tomography. *Nature Physics*, 14(5):447–450, May 2018.
- [138] J. Řeháček, Z. Hradil, and M. Ježek. Iterative algorithm for reconstruction of entangled states. *Phys. Rev. A*, 63:040303, Mar 2001.
- [139] A. I. Lvovsky, H. Hansen, T. Aichele, O. Benson, J. Mlynek, and S. Schiller. Quantum State Reconstruction of the Single-Photon Fock State. *Phys. Rev. Lett.*, 87:050402, Jul 2001.
- [140] A I Lvovsky. Iterative maximum-likelihood reconstruction in quantum homodyne tomography. *Journal of Optics B: Quantum and Semiclassical Optics*, 6(6):S556, may 2004.
- [141] Samuel Deléglise, Igor Dotsenko, Clément Sayrin, Julien Bernu, Michel Brune, Jean-Michel Raimond, and Serge Haroche. Reconstruction of non-classical cavity field states with snapshots of their decoherence. *Nature*, 455(7212):510–514, Sep 2008.
- [142] Michael J. Davis and Eric J. Heller. Quantum dynamical tunneling in bound states. *The Journal of Chemical Physics*, 75(1):246–254, 1981.
- [143] Léo Van Damme. *Contrôle optimal de la dynamique des spins: Applications en Résonance Magnétique Nucléaire et en Information Quantique*. PhD thesis, Université de Bourgogne - Franche Comté, 2016.
- [144] L. M. Hocking. *Optimal control: an introduction to the theory with applications*. Oxford University Press, 1991.
- [145] Navin Khaneja, Timo Reiss, Cindie Kehlet, Thomas Schulte-Herbrüggen, and Steffen J. Glaser. Optimal control of coupled spin dynamics: design of NMR pulse sequences by gradient ascent algorithms. *Journal of Magnetic Resonance*, 172(2):296–305, 2005.
- [146] J Werschnik and E K U Gross. Quantum optimal control theory. *Journal of Physics B: Atomic, Molecular and Optical Physics*, 40(18):R175, sep 2007.

- [147] A.E. Bryson. *Applied Optimal Control: Optimization, Estimation and Control*. CRC Press, 1 edition, 1975.
- [148] M. Ben Dahan, E. Peik, J. Reichel, Y. Castin, and C. Salomon. Bloch Oscillations of Atoms in an Optical Potential. *Phys. Rev. Lett.*, 76:4508–4511, Jun 1996.
- [149] Rémy Battesti, Pierre Cladé, Saïda Guellati-Khélifa, Catherine Schwob, Benoît Grémaud, François Nez, Lucile Julien, and François Biraben. Bloch Oscillations of Ultracold Atoms: A Tool for a Metrological Determination of h/m_{Rb} . *Phys. Rev. Lett.*, 92:253001, Jun 2004.
- [150] S. Haroche. Synthèse et reconstruction d'états quantiques, 2010.
- [151] Bertrand Evrard, An Qu, Jean Dalibard, and Fabrice Gerbier. Observation of fragmentation of a spinor Bose-Einstein condensate. *Science*, 373(6561):1340–1343, 2021.
- [152] M. O. Brown, S. R. Muleady, W. J. Dworschack, R. J. Lewis-Swan, A. M. Rey, O. Romero-Isart, and C. A. Regal. Time-of-flight quantum tomography of single atom motion, 2022.
- [153] Serge Haroche and Jean-Michel Raimond. *Exploring the Quantum: Atoms, Cavities, and Photons*. Oxford University Press, 08 2006.
- [154] W. K. Hensinger, H. Häffner, A. Browaeys, N. R. Heckenberg, K. Helmerson, C. McKenzie, G. J. Milburn, W. D. Phillips, S. L. Rolston, H. Rubinsztein-Dunlop, and B. Upcroft. Dynamical tunnelling of ultracold atoms. *Nature*, 412(6842):52–55, Jul 2001.
- [155] Daniel A. Steck, Windell H. Oskay, and Mark G. Raizen. Observation of Chaos-Assisted Tunneling Between Islands of Stability. *Science*, 293(5528):274–278, 2001.
- [156] Gabriel Lippmann. La théorie cinétique des gaz et le principe de Carnot. In *Rapports présentés au congrès international de physique réuni à Paris en 1900 sous les auspices de la Société française de physique, rassemblés et publiés par Ch.-Éd. Guillaume et L. Poincaré, secrétaires généraux du congrès*, 1900.
- [157] G. Harmer and D. Abbott. The Feynman-Smoluchowski ratchet. <http://www.eleceng.adelaide.edu.au/Groups/parrondo/ratchet.html>.
- [158] Marian von Smoluchowski. Experimentell nachweisbare, der üblichen Thermodynamik widersprechende Molekularphänomene. *Physik. Zeitschr.*, 13(1069), 1912.
- [159] R. Feynman. The Feynman Lectures on Physics, Volume I, Chap. 46, Ratchet and pawl. https://www.feynmanlectures.caltech.edu/I_46.html.
- [160] J. M. R. Parrondo and P. Español. Criticism of Feynman's analysis of the ratchet as an engine. *American Journal of Physics*, 64(9):1125–1130, 1996.
- [161] S. Flach, O. Yevtushenko, and Y. Zolotaryuk. Directed Current due to Broken Time-Space Symmetry. *Phys. Rev. Lett.*, 84:2358–2361, 2000.
- [162] S. Denisov, S. Flach, A. A. Ovchinnikov, O. Yevtushenko, and Y. Zolotaryuk. Broken space-time symmetries and mechanisms of rectification of ac fields by nonlinear (non)adiabatic response. *Phys. Rev. E*, 66:041104, 2002.
- [163] Sergey Denisov, Sergej Flach, and Peter Hänggi. Tunable transport with broken space–time symmetries. *Physics Reports*, 538(3):77–120, 2014. Tunable transport with broken space–time symmetries.
- [164] Ralf Gommers. *Symmetry and Transport in Cold Atom Ratchets*. PhD thesis, University College London, 2007.

- [165] R. Dean Astumian and Peter Hänggi. Brownian motors. *Physics Today*, 55(11):33–39, 2002.
- [166] Peter Hänggi and Fabio Marchesoni. Artificial Brownian motors: Controlling transport on the nanoscale. *Rev. Mod. Phys.*, 81:387–442, 2009.
- [167] Peter Hänggi and Fabio Marchesoni. Introduction: 100 years of Brownian motion. *Chaos: An Interdisciplinary Journal of Nonlinear Science*, 15(2):026101, 2005.
- [168] Tian Yow Tsong and R.D. Astumian. Absorption and conversion of electric field energy by membrane bound ATPases. *Bioelectrochemistry and Bioenergetics*, 15(3):457–476, 1986.
- [169] Frank Jülicher, Armand Ajdari, and Jacques Prost. Modeling molecular motors. *Rev. Mod. Phys.*, 69:1269–1282, Oct 1997.
- [170] Debashish Chowdhury, Andreas Schadschneider, and Katsuhiko Nishinari. Traffic phenomena in biology: From molecular motors to organisms. In Andreas Schadschneider, Thorsten Pöschel, Reinhart Kühne, Michael Schreckenberg, and Dietrich E. Wolf, editors, *Traffic and Granular Flow'05*, pages 223–238, Berlin, Heidelberg, 2007. Springer Berlin Heidelberg.
- [171] Viviana Serreli, Chin-Fa Lee, Euan R. Kay, and David A. Leigh. A molecular information ratchet. *Nature*, 445(7127):523–527, Feb 2007.
- [172] Masayoshi Nishiyama, Etsuko Muto, Yuichi Inoue, Toshio Yanagida, and Hideo Higuchi. Substeps within the 8-nm step of the atpase cycle of single kinesin molecules. *Nature Cell Biology*, 3(4):425–428, 2001.
- [173] Peter Reimann. Brownian motors: noisy transport far from equilibrium. *Physics Reports*, 361(2):57–265, 2002.
- [174] C. Mennerat-Robilliard, D. Lucas, S. Guibal, J. Tabosa, C. Jurczak, J.-Y. Courtois, and G. Grynberg. Ratchet for cold rubidium atoms: The asymmetric optical lattice. *Phys. Rev. Lett.*, 82:851–854, Jan 1999.
- [175] P. Jung, J. G. Kissner, and P. Hänggi. Regular and chaotic transport in asymmetric periodic potentials: Inertia ratchets. *Phys. Rev. Lett.*, 76:3436–3439, Apr 1996.
- [176] M. Schiavoni, L. Sanchez-Palencia, F. Renzoni, and G. Grynberg. Phase control of directed diffusion in a symmetric optical lattice. *Phys. Rev. Lett.*, 90:094101, Mar 2003.
- [177] Gabriel G. Carlo, Giuliano Benenti, Giulio Casati, and Dima L. Shepelyansky. Quantum ratchets in dissipative chaotic systems. *Phys. Rev. Lett.*, 94:164101, Apr 2005.
- [178] Lei Wang, Giuliano Benenti, Giulio Casati, and Baowen Li. Ratchet Effect and the Transporting Islands in the Chaotic Sea. *Phys. Rev. Lett.*, 99:244101, Dec 2007.
- [179] I. Dana, V. Ramareddy, I. Talukdar, and G. S. Summy. Experimental Realization of Quantum-Resonance Ratchets at Arbitrary Quasimomenta. *Phys. Rev. Lett.*, 100:024103, Jan 2008.
- [180] R. Gommers, V. Lebedev, M. Brown, and F. Renzoni. Gating Ratchet for Cold Atoms. *Phys. Rev. Lett.*, 100:040603, Jan 2008.
- [181] S. Denisov, S. Kohler, and P. Hänggi. Underdamped quantum ratchets. *EPL (Europhysics Letters)*, 85(4):40003, feb 2009.
- [182] Holger Schanz, Thomas Dittrich, and Roland Ketzmerick. Directed chaotic transport in hamiltonian ratchets. *Phys. Rev. E*, 71:026228, Feb 2005.

- [183] Jiangbin Gong and Paul Brumer. Directed anomalous diffusion without a biased field: A ratchet accelerator. *Phys. Rev. E*, 70:016202, Jul 2004.
- [184] D. H. White, S. K. Ruddell, and M. D. Hoogerland. Experimental realization of a quantum ratchet through phase modulation. *Phys. Rev. A*, 88:063603, Dec 2013.
- [185] Clément Hainaut, Adam Rançon, Jean-François Clément, Jean Claude Garreau, Pascal Szriftgiser, Radu Chicireanu, and Dominique Delande. Ratchet effect in the quantum kicked rotor and its destruction by dynamical localization. *Phys. Rev. A*, 97:061601, Jun 2018.
- [186] M. Borromeo and F. Marchesoni. Noise-assisted transport on symmetric periodic substrates. *Chaos: An Interdisciplinary Journal of Nonlinear Science*, 15(2):026110, 2005.
- [187] J. A. Nelder and R. Mead. A Simplex Method for Function Minimization. *The Computer Journal*, 7(4):308–313, 01 1965.
- [188] T. Dittrich, R. Ketzmerick, M.-F. Otto, and H. Schanz. Classical and quantum transport in deterministic Hamiltonian ratchets. *Annalen der Physik*, 512(9-10):755–763, 2000.
- [189] Tobias Salger, Sebastian Kling, Tim Hecking, Carsten Geckeler, Luis Morales-Molina, and Martin Weitz. Directed Transport of Atoms in a Hamiltonian Quantum Ratchet. *Science*, 326(5957):1241–1243, 2009.
- [190] Christopher Grossert, Martin Leder, Sergey Denisov, Peter Hänggi, and Martin Weitz. Experimental control of transport resonances in a coherent quantum rocking ratchet. *Nature Communications*, 7(1):10440, Feb 2016.
- [191] L. Deng, E. W. Hagley, J. Wen, M. Trippenbach, Y. Band, P. S. Julienne, J. E. Simsarian, K. Helmerson, S. L. Rolston, and W. D. Phillips. Four-wave mixing with matter waves. *Nature*, 398(6724):218–220, Mar 1999.
- [192] K. Xu, Y. Liu, D. E. Miller, J. K. Chin, W. Setiawan, and W. Ketterle. Observation of Strong Quantum Depletion in a Gaseous Bose-Einstein Condensate. *Phys. Rev. Lett.*, 96:180405, May 2006.
- [193] Raphael Lopes, Christoph Eigen, Nir Navon, David Clément, Robert P. Smith, and Zoran Hadzibabic. Quantum Depletion of a Homogeneous Bose-Einstein Condensate. *Phys. Rev. Lett.*, 119:190404, Nov 2017.
- [194] Antoine Tenart, Gaétan Hercé, Jan-Philipp Bureik, Alexandre Dareaux, and David Clément. Observation of pairs of atoms at opposite momenta in an equilibrium interacting Bose gas. *Nature Physics*, 17(12):1364–1368, Dec 2021.
- [195] Gretchen K. Campbell, Jongchul Mun, Micah Boyd, Erik W. Streed, Wolfgang Ketterle, and David E. Pritchard. Parametric Amplification of Scattered Atom Pairs. *Phys. Rev. Lett.*, 96:020406, Jan 2006.
- [196] S. Lellouch, M. Bukov, E. Demler, and N. Goldman. Parametric Instability Rates in Periodically Driven Band Systems. *Phys. Rev. X*, 7:021015, May 2017.
- [197] K. Wintersperger, M. Bukov, J. Näger, S. Lellouch, E. Demler, U. Schneider, I. Bloch, N. Goldman, and M. Aidelsburger. Parametric Instabilities of Interacting Bosons in Periodically Driven 1D Optical Lattices. *Phys. Rev. X*, 10:011030, Feb 2020.
- [198] N. Gemelke, E. Sarajlic, Y. Bidet, S. Hong, and S. Chu. Parametric Amplification of Matter Waves in Periodically Translated Optical Lattices. *Phys. Rev. Lett.*, 95:170404, Oct 2005.

- [199] H. Lignier, C. Sias, D. Ciampini, Y. Singh, A. Zenesini, O. Morsch, and E. Arimondo. Dynamical Control of Matter-Wave Tunneling in Periodic Potentials. *Phys. Rev. Lett.*, 99:220403, Nov 2007.
- [200] E. Kierig, U. Schnorrberger, A. Schietinger, J. Tomkovic, and M. K. Oberthaler. Single-Particle Tunneling in Strongly Driven Double-Well Potentials. *Phys. Rev. Lett.*, 100:190405, May 2008.
- [201] E Michon, C Cabrera-Gutiérrez, A Fortun, M Berger, M Arnal, V Brunaud, J Billy, C Petitjean, P Schlagheck, and D Guéry-Odelin. Phase transition kinetics for a Bose Einstein condensate in a periodically driven band system. *New Journal of Physics*, 20(5):053035, may 2018.
- [202] P. Nozières and D. Pines. *The Theory of Quantum Liquids*, volume 2. CRC Press, 2018.
- [203] Y. Castin and R. Dum. Low-temperature Bose-Einstein condensates in time-dependent traps: Beyond the $U(1)$ symmetry-breaking approach. *Phys. Rev. A*, 57:3008–3021, Apr 1998.
- [204] Y. Castin. Mécanique quantique : seconde quantification et résolvente, 2011.
- [205] T. Paul, M. Hartung, K. Richter, and P. Schlagheck. Nonlinear transport of Bose-Einstein condensates through mesoscopic waveguides. *Phys. Rev. A*, 76:063605, Dec 2007.
- [206] M. Boninsegni and N. V. Prokof'ev. Colloquium: Supersolids: What and where are they? *Rev. Mod. Phys.*, 84:759–776, May 2012.
- [207] O. Penrose and L. Onsager. Bose-Einstein Condensation and Liquid Helium. *Phys. Rev.*, 104:576–584, Nov 1956.
- [208] A. F. Andreev and I. M. Lifshitz. Quantum theory of defects in crystal. 29(6), Dec 1969.
- [209] D. J. Thouless. The flow of a dense superfluid. *Annals of Physics*, 52(3):403–427, 1969.
- [210] M. H. W. Chan, R. B. Hallock, and L. Reatto. Overview on Solid 4He and the Issue of Supersolidity. *Journal of Low Temperature Physics*, 172(5):317–363, Sep 2013.
- [211] J.-R. Li, J. Lee, W. Huang, S. Burchesky, B. Shteynas, F. Ç. Top, A. O. Jamison, and W. Ketterle. A stripe phase with supersolid properties in spin-orbit-coupled Bose-Einstein condensates. *Nature*, 543(7643):91–94, Mar 2017.
- [212] J. Léonard, A. Morales, P. Zupancic, T. Esslinger, and T. Donner. Supersolid formation in a quantum gas breaking a continuous translational symmetry. *Nature*, 543(7643):87–90, Mar 2017.
- [213] G. Natale, R. M. W. van Bijnen, A. Patscheider, D. Petter, M. J. Mark, L. Chomaz, and F. Ferlaino. Excitation Spectrum of a Trapped Dipolar Supersolid and Its Experimental Evidence. *Phys. Rev. Lett.*, 123:050402, Aug 2019.
- [214] Matthew A. Norcia, Claudia Politi, Lauritz Klaus, Elena Poli, Maximilian Sohmen, Manfred J. Mark, Russell N. Bisset, Luis Santos, and Francesca Ferlaino. Two-dimensional supersolidity in a dipolar quantum gas. *Nature*, 596(7872):357–361, Aug 2021.
- [215] Nicholas R. Thomas, Niels Kjærgaard, Paul S. Julienne, and Andrew C. Wilson. Imaging of s and d Partial-Wave Interference in Quantum Scattering of Identical Bosonic Atoms. *Phys. Rev. Lett.*, 93:173201, Oct 2004.
- [216] Antoine Tenart, Cécile Carcy, Hugo Cayla, Thomas Bourdel, Marco Mancini, and David Clément. Two-body collisions in the time-of-flight dynamics of lattice Bose superfluids. *Phys. Rev. Research*, 2:013017, Jan 2020.

- [217] Z. Gedik, I. A. Silva, B. Çakmak, G. Karpat, E. L. G. Vidoto, D. O. Soares-Pinto, E. R. deAzevedo, and F. F. Fanchini. Computational speed-up with a single qudit. *Scientific Reports*, 5(1):14671, Oct 2015.
- [218] Martin Ringbauer, Michael Meth, Lukas Postler, Roman Stricker, Rainer Blatt, Philipp Schindler, and Thomas Monz. A universal qudit quantum processor with trapped ions. *Nature Physics*, 18(9):1053–1057, Sep 2022.
- [219] E.O. Kiktenko, A.K. Fedorov, A.A. Strakhov, and V.I. Man'ko. Single qudit realization of the deutsch algorithm using superconducting many-level quantum circuits. *Physics Letters A*, 379(22):1409–1413, 2015.
- [220] Maxime Martinez, Olivier Giraud, Denis Ullmo, Juliette Billy, David Guéry-Odelin, Bertrand Georgeot, and Gabriel Lemarié. Chaos-Assisted Long-Range Tunneling for Quantum Simulation. *Phys. Rev. Lett.*, 126:174102, Apr 2021.

Abstract: The field of quantum simulation aims at emulating complex quantum systems on platforms that are easier to control and observe. In the last twenty years, ultracold atoms in optical lattices have established themselves as a versatile controllable system for quantum simulation. The three experimental studies presented in this manuscript take place in the development of this field. They are performed using Bose-Einstein condensates (BECs) in a one-dimensional optical lattice that can be precisely controlled in amplitude and phase.

In the first study, we use the optimal control formalism to compute the way in which to continuously shift the lattice in order to arbitrarily shape the BEC distribution in the phase space of the system. We apply this method to different targets, among which squeezed Gaussian states more than four times narrower in position than the ground state of the system, as well as the ideal Floquet state superposition to perform quantum simulation of dynamical tunneling in the modulated lattice.

The second study concerns the realization of a non-diffusive Hamiltonian ratchet. The ratchet effect consists in the emergence of a directed current of particles in a system with no net force. In this second work, we correlate the amplitude and phase modulations of the lattice to produce, in the phase space of the system, a region of non-chaotic trajectories that travels between lattice sites, resting periodically in the center of each sites. We experimentally implement this system and observe non-diffusive ratchet transport of matter waves in the optical lattice.

Finally, we show how short-range interactions between atoms in the BECs lead to the emergence of a supercrystalline order in a sinusoidally modulated optical lattice for a modulation frequency coupling two energy levels. We develop a two-band tight-binding model which predicts that collisions occurring between the atoms of the BECs can lead to the growth of unstable Bogoliubov modes in the vicinity of avoided crossings in the quasi-energy spectrum of the modulated system. Interestingly, we experimentally demonstrate that the periodicity of the emergent order can be tuned through Floquet engineering of these crossings.

Résumé : Le domaine de la simulation quantique vise à émuler des systèmes quantiques complexes sur des systèmes plus simples à observer et à contrôler. Ces vingt dernières années, les gaz d'atomes ultrafroids sur réseau optique se sont démarqués comme une plateforme versatile et contrôlable pour la simulation quantique. Les trois études expérimentales présentées dans ce manuscrit s'inscrivent dans le développement de ce domaine. Elles sont réalisées avec des condensats de Bose-Einstein (CBE) placés dans un réseau optique unidimensionnel dont on peut contrôler finement la phase et l'amplitude.

Dans la première étude, nous utilisons le formalisme du contrôle optimal pour calculer la phase variable que doit avoir le réseau optique au cours du temps afin de préparer des distributions arbitraires de CBE dans l'espace des phases du système. Avec cette méthode, nous réalisons différents états, parmi lesquels des états gaussiens jusqu'à quatre fois plus comprimés en position que l'état fondamental du réseau optique, ou encore la superposition idéale d'états de Floquet pour faire une simulation quantique d'effet tunnel dynamique dans le réseau optique modulé.

La deuxième étude traite d'un effet *ratchet* (rochet) non-diffusif dans un système hamiltonien. L'effet *ratchet* est l'émergence d'un courant de particules dans un potentiel duquel aucune force nette n'est dérivée. Dans ce travail, nous corrélons les modulations d'amplitude et de phase du réseau afin de faire émerger, dans l'espace des phases du système, une région de trajectoires non-chaotiques qui transite d'un site au suivant en s'arrêtant périodiquement au centre du site. Nous réalisons expérimentalement ce système et observons le transport *ratchet* non-diffusif d'ondes de matière dans le réseau optique.

La dernière étude présentée dans cette thèse démontre comment, dans un réseau optique modulé sinusoidalement à une fréquence couplant deux bandes du système, les interactions à courte-portée entre atomes du CBE peuvent entraîner l'émergence d'un ordre supercristallin. Nous développons un modèle de bandes fortement liées à deux niveaux prédisant que les collisions interatomiques dans le CBE peuvent mener à la croissance de modes instables de Bogoliubov situés à proximité des croisements évités dans le spectre de quasi-énergie du système modulé. Notamment, nous montrons expérimentalement comment la périodicité de cet ordre émergent peut être accordée en procédant à l'ingénierie de Floquet de ces croisements.